Broadband Silicon Photonics Devices with Wavelength Independent Directional Couplers

A THESIS

submitted by

RAMESH K

for the award of the degree

of

DOCTOR OF PHILOSOPHY

DEPARTMENT OF ELECTRICAL ENGINEERING.
INDIAN INSTITUTE OF TECHNOLOGY MADRAS.

Tuesday 15th January, 2019

THESIS CERTIFICATE

This is to certify that the thesis titled **Broadband Silicon Photonics Devices with Wavelength Independent Directional Couplers**, submitted by **RAMESH K.**, to the Indian Institute of Technology Madras, for the award of the degree of **Doctor of Philosophy**, is a bonafide record of the research work done by him under my supervision. The contents of this thesis, in full or in parts, have not been submitted to any other Institute or University for the award of any degree or diploma.

Prof. Bijoy Krishna Das
Research Guide
Professor
Dept. of Electrical Engineering
IIT-Madras, 600 036

Place: Chennai, India

Date: Tuesday 15$^{\text{th}}$ January, 2019

There is nothing more purifying than knowledge

- Bhagavad Gita

Dedicated to my **Family**

for their eternal love and support

ACKNOWLEDGEMENTS

First and foremost, I am grateful to thank my supervisor Prof. Bijoy Krishna Das for introducing me to the interesting area of Silicon Photonics and for his motivation for upgrading my master's degree to the level of Ph.D. During our course of interaction in last few years, I have been deeply impressed with his advice, support, inspiration and encouragement in academic and non-academic activities. His unique way of approaching a problem in a systematic and out-of box thinking has a great impact on his students to overcome various obstacles and to produce high quality research-outputs. The present status of our *Integrated Optoelectronics Research Group, IIT Madras* with well developed research facilities is the result of his dedication and hard work over the last decade.

My doctoral committee guided me through all these years. I would like to acknowledge Prof. Amitava DasGupta, Prof. Anil Prabhakar, Dr. Ananth Krishnan and Dr. Manu Jaiswal for their continuous support and valuable comments during the review meetings.

My special thanks to Dr. Sujith Chandran (alumnus of our research group) for his encouragement, guidance and moral support throughout the completion of my Ph.D. His valuable suggestions, scientific inputs and personal helps as an elder brother have fueled me to accelerate my research work.

I express my thanks to Dr. Shantanu Pal, and Dr. Parimal Sah (alumni of our research group) for their support and motivation.

Heartfelt thanks to my fellow members Riddhi Nandi, Sumi R., Arnab Goswami and Meena B. Their cooperation, timely help and friendship shall always be remembered. I have learnt the initial steps of fabrication from Riddhi with strict DO's and DONT's, which helped me to handle dangerous chemicals and sophisticated machines independently and safely. Sumi's motivational words and songs refreshed me many

times during time-consuming fabrication and experimental works.

I thank my senior fellows Sakthivel, Siddharth Raveendran, Meenatchi Sundaram, Seetha Lakshmi, Sreevatsa Kuridi, Dadavali, Vivek P.S. and Saket Kausal for their academic and non-academic supports during my stay at IIT Madras. Special thanks to Sreevatsa for developing Lab-View programs to automate the experimental setups which helped all our labmates to complete their experiments with less efforts. A special mention of thanks to other IOLAB friends Mani Teja, Deepak, Sooraj M. S., Vishnu Krishna, Amrutha, Keerthana, Subhra Jyoti, Suvarna Parvathy, Ram Mohan, Pratyasa Priyadarshini, Vishnu V. G. and Agatya and Keerthana for their wishes and encouragements.

I must thank Mr. C. Rajendran (Sr. Tech.Superintendent), J. Prakash (Sr. Technician), Joseph, Venkatesh, Tamilarasan (Technicians) and other staff members for their technical support in MEMS & Microelectronics Lab. I would like to acknowledge the *Center for NEMS & Nanophotonics, IIT Madras* for providing all the necessary fabrication facilities.

A special mention of thanks to my friends Dhanesh, Meghna, Sanjay, Manu Balakrishnan, Bhadri and Nithin for their wishes and supports.

My deep gratitude to my sister Usha, brother-in-law Jayan, brother Suresh, sister-in-law Resmi and my nephews. Their unconditional love, support, and appreciation have always been my strength. Words are limited to thank my father Balakrishnan and my mother Sarojini, without their sacrifice and patience I would never have enjoyed so many opportunities. More importantly, their spiritual support and encouragement have given me the confidence to handle tough situations in life patiently and perfectly. I owe my deepest gratitude towards my better half Megha for her eternal support and understanding of my goals and aspirations. I am also indebted to my in-laws Manikandan and Soudamini, sister-in-law Sarigha for taking care of my personal life which allowed me to chase my dream.

ABSTRACT

KEYWORDS: Silicon Photonics, Integrated Optics, Silicon-on-Insulator, Waveguides, Directional Couplers, Microring Resonators, Mach-Zehder Interferometers, Thermo-optic Switch.

Integrated silicon photonics technology has revolutionized short-haul data communication (inter/intra-board and inter/intra-chip) by replacing bandwidth limited metal interconnects with high-speed optical interconnects. Silicon photonics devices with broad optical bandwidth are the futuristic demand to meet the gigantic speed requirements (> 1 Tbps) in datacenters and high performance computing. Microring resonators (MRRs) and Mach-Zehnder interferometers (MZIs) are the two important building blocks of an integrated silicon photonics chip (used in optical interconnect applications and in other allied fields like sensing and optical signal processing). Conventionally, both MRR and MZI structures are constructed with suitably designed directional couplers (DCs). In general, silicon photonics DC is wavelength dependent; this eventually limits the optical bandwidth of an integrated optical circuit designed with MRRs and MZIs. Thus there is a need of designing silicon photonics DC with scalable power splitting ratio operating uniformly over a broad wavelength range.

In this thesis work, we have studied the wavelength dependent coupling characteristics of DCs consisting of two single-mode rib waveguides as a function of waveguide width (W), slab height (h) and gap (G) between the coupled waveguides in silicon-on-insulator (SOI) substrate with a device layer thickness (H) of 220 nm. Solving the two lower order eigenmodes (supermodes) of a symmetric DC (constructed with two identical single-mode waveguides), we investigated their dispersion characteristics. In order to achieve a wavelength independent coupling, one needs to match the group indices of guided super-modes in DC. To design such a DC, we first calculated the wavelength dependent differential group index $\Delta n_g(\lambda)$ of supermodes by varying the cross-section design parameters. By analyzing the simulation results, a wavelength independent DC

(WIDC) geometry is optimized offering uniform coupling over C + L bands (1525 nm $\leq \lambda \leq$ 1625 nm). Wavelength independent performances of such DCs are shown to be tolerant against fabrication induced deviations ($\pm$ 30 nm) in waveguide/DC parameters (W, H, h and G); though the power spitting ratio varies a bit.

The proposed WIDC with a set of optimized design parameters, has been experimentally demonstrated using commercially available SOI substrate (device layer: 220 nm, BOX layer: 2 μm and handle wafer: 500 μm). A set of WIDCs with various power splitting ratios (0%-100%) were realized by changing the coupling length. The 3-dB coupling length of WIDC is measured to be ~ 5 μm which is found to be slightly longer than that of simulation result (~ 4 μm), which is attributed to the fabrication induced errors as mentioned earlier. However, all the demonstrated devices exhibit nearly uniform power splitting ratio with a measured ± 0.5 dB bandwidth of ~ 100 nm and insertion loss of ~ 1.2 dB.

After successful demonstration of WIDC based power splitters (2×2 and 1×4), we further extended the work towards the implementation of broadband MRRs and MZIs in TE-polarization covering C + L bands. The experimental results of MRRs have been analyzed for various ring radius (> 100 μm) and coupling lengths. The extinction ratio (ER~ 25 dB) and free-spectral range (FSR~ 0.8 nm) of a typical MRR with radius 100 μm are found to be nearly uniform over the entire operating band (1525 nm $\leq \lambda \leq$ 1625 nm). More compact WIDC based MRRs of radius ~ 25 μm are also realized in two step fabrication processes with deeply etched ring waveguide and adiabatically tapered shallow etched bus waveguides. Similarly, the balanced and unbalanced MZIs fabricated with WIDC based 3-dB power splitters also exhibit uniform extinction ratio of ~ 22 dB between cross- and bar-ports.

Finally, thermo-optic switching cells have been demonstrated with broadband MZIs (balanced and unbalanced). For thermo-optic switching, thin film Ti-microheaters were integrated in the slab region adjacent to one of the arms of the MZIs. A detailed theoretical study has been carried out to model the performance of metal-microheater integrated waveguide phase-shifters in terms of waveguide geometry and micro-heater positioning. The devices were characterized over a broad wavelength range (~ 100 nm) in TE-polarization with a nearly uniform extinction exceeding 22 dB and with a switching

time of ~ 5 μs. Average optical insertion loss is estimated to be ~ 2.4 dB and recorded electrical switching power is ~ 36 mW; which are again found to be nearly uniform over the above mentioned wavelength range of operation. The wavelength tunability of unbalanced MZI switches are measured to be 33 pm/mW. More importantly, the ON state switching temperature of the device is relatively low (~ 11K), making it suitable for large scale co-integration of electronics and photonics devices.

TABLE OF CONTENTS

LIST OF TABLES

xiv

LIST OF FIGURES

ABBREVIATIONS

Acronyms

C-Band	Conventional wavelength band ($\lambda \sim 1527$ to 1567 nm)
BOX	Buried Oxide
BW	Bandwidth
CE	Conventional Elements
CMOS	Complementary Metal Oxide Semiconductor
CWDM	Coarse Wavelength Division Multiplexing
DC	Directional Coupler
DI	De-ionized (water)
DSO	Digital Storage Oscilloscope
DUT	Device Under Test
EBL	Electron Beam Lithography
EL	Excess Loss
ER	Extinction Ratio
FBMS	Fixed Beam Moving Stage
FG	Function Generator
FSR	Free Spectral Range
F-MZI	Mach-Zehnder Interferometer integrated with Folded Waveguide Microheater
GC	Grating Coupler
GDS-II	Graphic Database System-II (mask file format)
HSQ	Hydrogen Silsesquioxane
ICPRIE	Inductively Coupled Plasma Reactive Ion Etching
IL	Insertion Loss
L-Band	Long wavelength band ($\lambda \sim 1567$ to 1607 nm)
OBW	Optical Bandwidth
OSA	Optical Spectrum Analyzer
PD	Photodetector

PMMA	Poly(methyl methacrylate)
MH	Microheater
MMI	Multi-Mode Interference
MRR	Microring Resonator
MZI	Mach-Zehder Interferometer
SEM	Scanning Electron Microscope
SMF	Single Mode Fiber
SMU	Source Measuring Unit
SOI	Silicon-on-Insulator
SR	Splitting Ratio
SWG	Sub-Wavelength Grating
S-MZI	Mach-Zehnder Interferometer integrated with Straight Waveguide Microheater
TE	Transverse Electric (polarization)
TM	Transverse Magnetic (polarization)
TOC	Thermo-Optic Coefficient
WDM	Wavelength Division Multiplexing
WIDC	Wavelength Independent Directional Coupler

Chemical Names

CHF_3	Tri-fluoro Methane
HF	Hydrofluoric Acid
HNO_3	Nitric Acid
H_2O	Water
H_2O_2	Hydrogen Peroxide
H_2SO_4	Sulphuric Acid
NH_4OH	Ammonium Hydroxide
SF_6	Sulfur Hexafluoride
Si	Silicon
SiO_2	Silicon dioxide
TCE	Tri-chloro Ethylene

Units

dB	decibel
dBm	decibel milli-watt
nm	nanometer
ns	nanosecond
K	Kelvin
μ**m**	micrometer
μ**W**	micro watt
μ**s**	microsecond
mW	milli watt
mbar	milli-Bar (of pressure)
ml	milli-liter (of fluid)
mTorr	milli-Torr (of pressure)
sccm	standard cubic centimeter per minute

NOTATIONS

n	Refractive index
$\mathbf{n}_{eff}$	Effective refractive index
ϵ	Permitivity
$\boldsymbol{\lambda}$	Wavelength
$\boldsymbol{\beta}$	Propagation constant
ϕ	Phase of the EM wave
L	Length (refers to device length, component length)
Γ	Overlap integral coefficient
$\boldsymbol{\alpha}$	Loss per unit length
$\boldsymbol{\kappa}$	Coupling coefficient
$\boldsymbol{g_w}$	Thermal conductivity per unit length of phase-shifter
$\boldsymbol{h_w}$	Heat capacitance per unit length of phase-shifter
$\boldsymbol{S_H}$	Thermal sensitivity
$\boldsymbol{\tau_{th}}$	Thermal time constant
$\mathcal{F}_H$	Figure of Merit of thermo-optic phase-shifter

CHAPTER 1

Introduction

Our literature survey reveals that wavelength dependent performance of a typical directional coupler (DC) limits the optical bandwidth of important silicon photonics components like microring resonator (MRR) and Mach-Zehnder interferometer (MZI). Within the scope of this Ph.D. work, we theoretically investigated coupling characteristics of a DC comprised of two single mode waveguides in silicon-on-insulator (SOI) platform followed by the design of a wavelength independent DC (WIDC) operating uniformly over a broad wavelength range of more than 100-nm near $\lambda = 1550$ nm in TE polarization. Broadband WIDCs with various power splitting ratios were demonstrated. The outcome of this results were further extended towards the demonstration of broadband 1×4 power splitters, microring resonators (MRRs), Mach-Zehnder interferometers (MZIs) and MZI based thermo-optic switches. Such devices are highly desired for broadband wavelength division multiplexing (WDM), reconfigurable signal switching/routing, add/drop filters, and many more applications. All the devices discussed in this thesis are designed, fabricated and characterized using in-house facilities available at IIT Madras. The research motivation including literature review, set of objectives and thesis organization have been presented in the following sections.

1.1 Motivation

Silicon photonics optical interconnects are being used in recent times to overcome the fundamental bandwidth bottleneck of metallic interconnects in very large scale integrated (VLSI) electronic chips. An optical interconnect by virtue of its higher carrier frequency offers higher data rate, lower latency, and lower power consumption, etc. In fact, the usages of optical interconnects started by installing long-haul optical fiber links since 80's of the previous century. Short-haul optical interconnects were emerged in early 2000's and progressively replacing the electrical interconnects in board-to-board

and intra/inter-chip data communications. In the past decade, the success of low-loss and complementary metal oxide-semiconductor (CMOS) compatible integrated optical waveguides led towards the implementation of photonics integrated circuits (PICs) for next generation on-chip communication and computing applications [1, 2]. Thus silicon photonics technology has been emerged to offer power- and cost-effective short-range optical interconnect solutions [3, 4, 5, 6]. A schematic block diagram of short-reach optical interconnect link has been displayed in Figure 1.1 [7]. The basic building blocks are laser sources, light distributors, optical modulators for electrical-to-optical conversion, and photodetectors for optical-to-electrical conversion. Silicon photonics technology has been evolved for integrating all these functionalities using silicon as optical medium and it is appropriately fueled by the existing silicon electronics infrastructure.
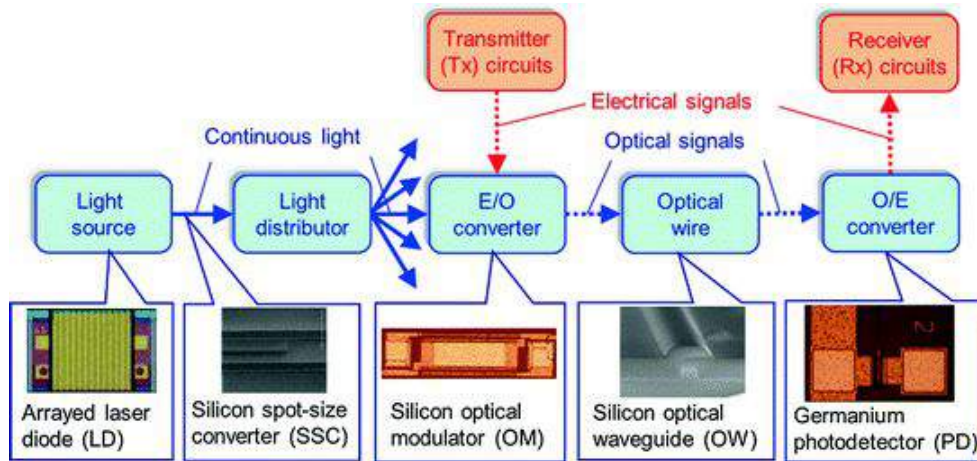
Figure 1.1: An outline scheme showing the basic building blocks of a silicon photonics optical interconnect. [7].

Today optical grade SOI substrates commercially produced and the silicon device layer is an excellent material platform for silicon photonics with its attractive optical, electro-optic, and thermo-optic properties.The SOI substrates facilitate compact and high density integration of photonic/optoelectronic circuits using existing CMOS foundry models [8, 9]. The broad transparency range of silicon covering the C and L communication bands, the large refractive index ($n_{Si} \sim 3.477$ at $\lambda = 1.55$ μm) and availability of high quality native oxide ($n_{SiO_2} \sim 1.477$ at $\lambda = 1.55$ μm) are the distinct properties that differentiate silicon from other integrated optical platforms such as LiNbO$_3$, III-V semiconductors and silica. The tighter confinement of light in the waveguide core region due to the high refractive index contrast between silicon core and

oxide/air cladding enables to scale down the device footprint to as small as few tens of μm^2. Moreover, the real and imaginary parts of refractive index of silicon crystal can be changed with the concentration of free carriers (electrons and holes). This (plasma dispersion effect) has been widely explored for high speed optical modulators and switches [10, 11]. Additionally, the large thermo-optic coefficient of silicon (1.86×10^{-4} K^{-1}) facilitates the active de-tuning of spectral characteristics as well as compensation of fabrication induced errors in device parameters, by means of monolithically integrated microheaters [12, 13, 14, 15]. Furthermore, Kerr nonlinear coefficient and Raman gain coefficient are respectively two and three orders of magnitude higher than that of silica fibers at communication wavelengths [16, 17]. The non-linear phenomena in silicon waveguides such as self-phase modulation (SPM) [18, 19], cross-phase modulation (XPM) [18, 20], stimulated Raman scattering (SRS) [21, 22], and four-wave mixing (FWM) [23, 24] have been widely investigated in recent years. Again, the silicon photonics device performance can be enhanced by hybrid and/or heterogeneous integration of III-V compound semiconductors, silicon nitride (SiN), silicon oxynitride (SiON), and other group-IV elements (Ge, Sn and C) [25, 26]. All the above factors, make silicon photonics a promising technology not only for high speed interconnect applications but also for high performance computing [27, 28], lab-on-chip bio-sensing [29, 30, 31, 32], solar harvesting [33, 34], quantum communication [35, 36], etc.
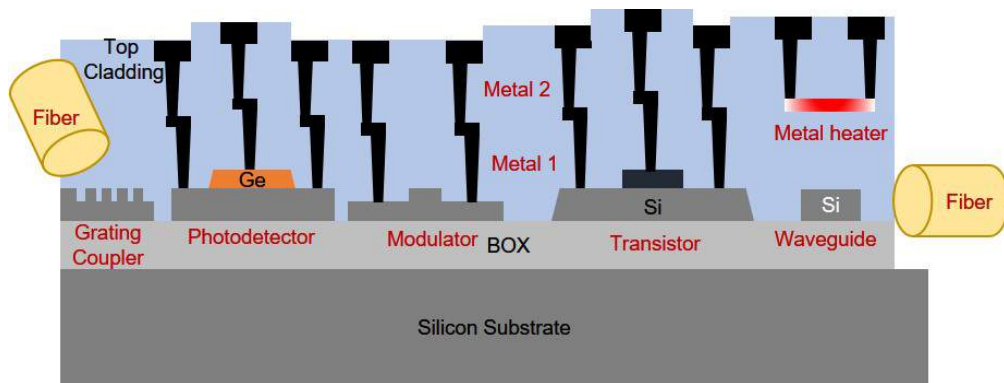
Figure 1.2: Scheme of a SOI based integrated silicon photonics circuit with important components like input/output fiber-grating couplers, Ge-photodetector, p-n/p-i-n modulator, silicon waveguide, metal heater, MOS transistor, etc. [37].

In the past couple of decades, there has been a boom in demonstrating individual silicon photonics components such as low-loss optical waveguides [38, 39, 40],

3

hybrid silicon lasers [41, 42], Raman lasers [43, 44], high-speed silicon modulators [45, 46, 47, 10], high-speed SiGe detector [48, 49, 50], and on-chip optical amplifiers [51, 52, 53, 54], etc. The research outcomes paved the way towards futuristic high-performance silicon photonics integrated circuits in which silicon VLSI electronics and nanophotonics components are co-integrated monolithically on a single silicon chip [55, 56, 57]. Cross-sectional schematic of such an integrated silicon photonics chip is shown schematically in Figure 1.2, where various CMOS photonics components such as grating couplers, p-n/p-i-n modulators, Ge photodetectors, waveguides, etc., are shown to be fabricated in the same active layer of transistors. Grating couplers and/or lensed-fibers are generally proposed for light coupling into and out of the device. The chip is electrically activated using metal-interconnects. Microheaters are also integrated in the same device layer to detune/reconfigure the optical characteristics of devices.

Liu *et al.* from Intel Corporation, demonstrated an 8-channel wavelength division multiplexing (WDM) circuit based high-speed silicon photonics transmitter test-chip capable of sending data at 200 Gb/s over single mode fiber [2]. This is regarded as the key milestone for future terabit transceivers of intra- and inter-chip interconnects [58, 59]. Very recently, Intel$^{®}$ has developed a high bandwidth optical transceiver module, 100G CWDM4 QSFP28 (100 Gb/s coarse WDM 4-lane quad small form-factor 28 Gb/s) for 100GbE optical links over single-mode fiber [60]. Riding on these features, currently the silicon photonics technology is being projected towards the demonstration of large-scale clouds and short-reach inter-datacenters with data rate 400 Gb/s and above. The speed and capacity of such optical interconnects are decided by the number of wavelength channels that can be accommodated in the WDM system and the operating speed of modulators per channel. The emerging IEEE 400 Gb/s (4×100 Gb/s) [61] standard optical interconnects need four-lane >100 Gb/s modulators. Such high-speed modulators often require advanced modulation schemes, complicated electrode design, hybrid integration of organic materials, high power consuming digital signal processing circuits, etc., [62, 63, 64, 65]. Integrated optical WDM is the key technology to scale up the capacity in optical communication and interconnects [2, 66, 67]. Figure 1.3(a) shows a silicon photonics WDM-based interconnect for datacenter applications proposed by Li *et al.* [58]. There are N servers with their transceivers interconnected by $N \times N$ switch matrix via single mode fibers. These WDM wavelength packets from the
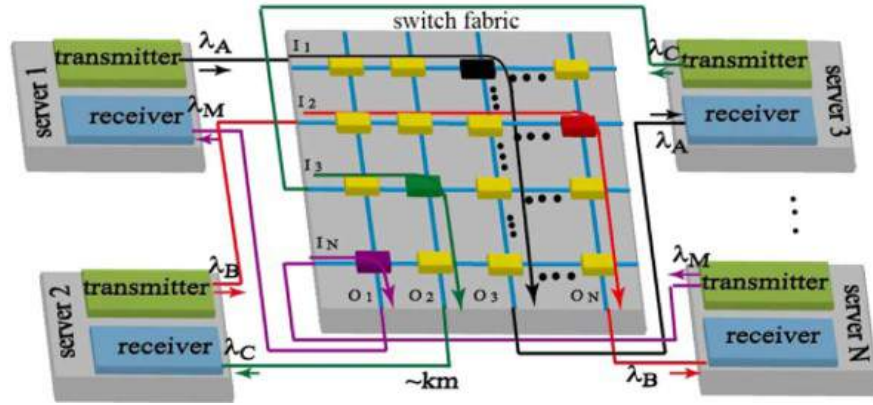
(a)
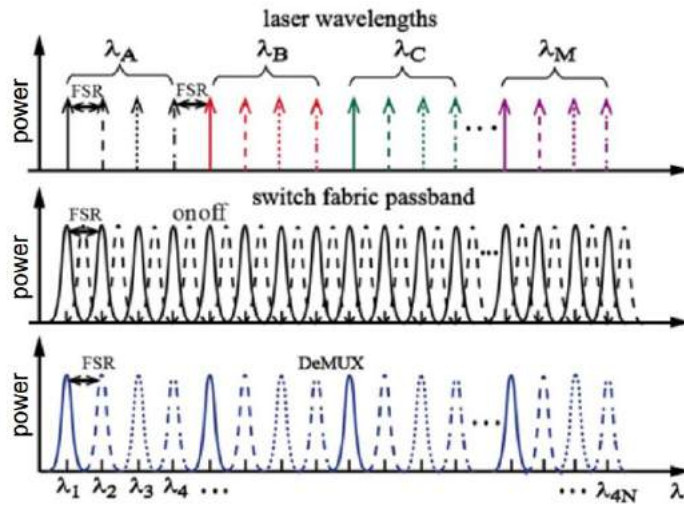
(b)

Figure 1.3: (a) Proposed scheme of a WDM silicon photonic interconnect for data-centers; (b) graphical representation of laser/channel wavelengths from the transmitters (upper), the switch fabric transmission bands at the "on" (solid) and "off" (dashed) states (middle), and the filter pass-bands of the DeMUX at the receiver (lower). The solid, dashed, dotted, and dashed-dotted arrows in the upper figure represent different wavelength channels from a single transmitter [58].

transceiver side are routed to any desired receiver through the switch matrix, where the optical path can be reconfigured using a CMOS control logic. Thus, individual switching elements require a minimum bandwidth of $(4N-1)\times$FSR to accommodate all the $4N$ λs, where FSR is the free spectral range between two neighboring wavelengths (see Figure 1.3(b)). The wavelength range of the proposed data center is 1300 nm to 1600 nm. The ideal switch fabric passband for ON/OFF state and the filter passband of the DeMUX are also shown in Figure 1.3(b), where the individual functional blocks are as-

sumed to have a broad optical bandwidth (OBW) to accommodate all the 4N wavelength channels. Hence broadband switching elements are the basic requirement of an optical interconnect to meet the future demand of high-speed data transmission. For instance, a silicon photonics WDM transceiver must have a flat transmission bandwidth of ~ 100 nm (~ 60 nm) to cover the entire 4 (40) channels of ITU CWDM (DWDM) channels in the 1510 nm to 1610 nm (1528 nm to 1568 nm) wavelength window. Fang *et. al* demonstrated a 32 channel arrayed waveguide grating (1×32 AWG) based 320 Gbps receiver with 200 GHz channel spacing [68]. However, the channel extinction ratio is highly non-uniform over the entire bandwidth of the de-multiplexer. MRR [69] and MZI [70] are the basic building blocks of many silicon photonics applications, especially for large scale switch fabrics shown in Figure 1.3(a). Both MRR and MZI structures are mostly constructed with suitably designed multimode-interferometers (MMIs) or directional couplers (DCs). In comparison with MMIs, DCs are more superior in-terms of coupling efficiency, less imbalance in output power, scalability and easiness of fabrication [71, 72, 73]. Moreover MMIs are highly sensitive to the position of input/output waveguides. An optical waveguide Y-junction is another alternative for power splitter/combiner, however, they are not suitable for large scale switching applications [74]. In this thesis we focus on 2×2 DCs designed with two single mode waveguides in SOI. In the following section we briefly discuss about the basic DC-based switch cell configurations and their switching characteristics.

1.1.1   Bandwidth Limitation of DC: Examples

Schematic representation of a typical add-drop MRR based switch cell is shown in Figure 3.1(b). Input wavelengths which are resonant to the ring appear at the drop port while those are non-resonant appear at the through port. An integrated microheater is used to tune the transfer function between the output ports. Figure 1.4(b) shows the schematic of ideal transfer function at the through port for "off" state and "on" state of the switch. The spectrum shows uniform extinction for all operating wavelengths with infinite 3-dB optical bandwidth. However, in practice, the optical bandwidth of a MRR is limited to few tens of nanometers. A fabricated MRR based add-drop multiplexer and its typical transmission characteristics at the through port and drop port of

6
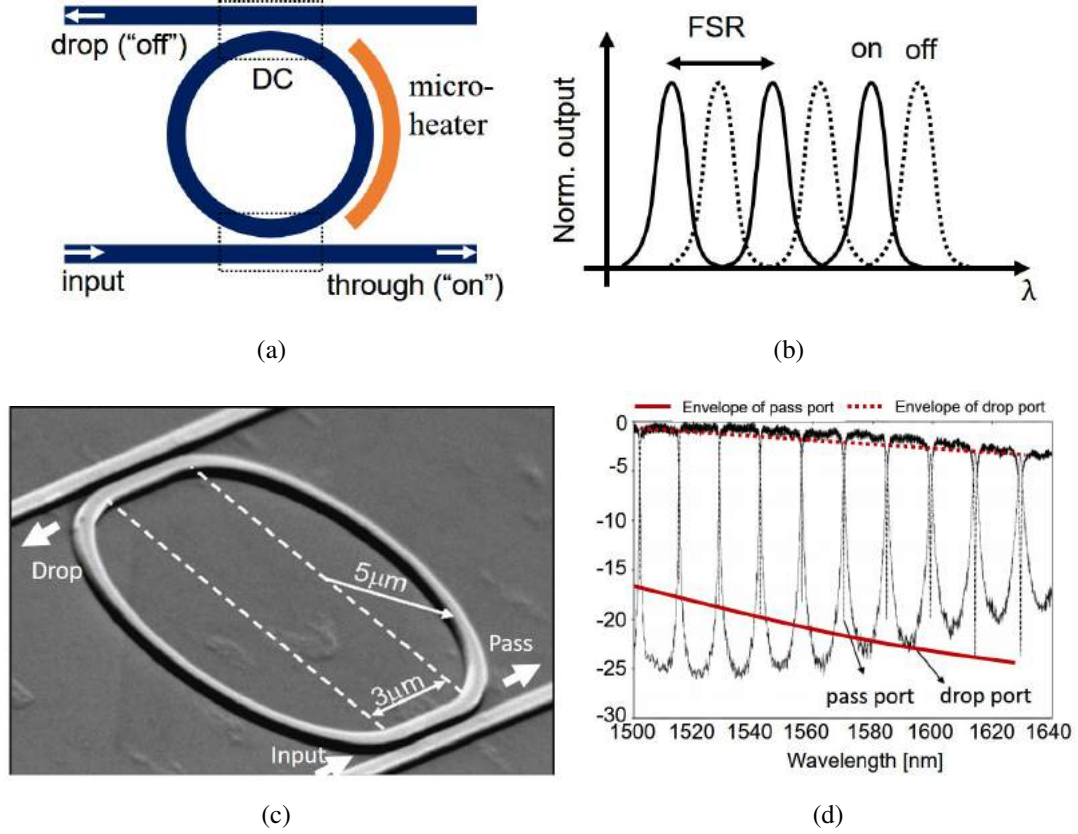
Figure 1.4: (a) Schematic of an add-drop MRR based switch cell and the corresponding ideal switching characteristics at the through port in (b). (c) SEM image of a fabricated add-drop MRR and (d) the corresponding transmission characteristics measured at the through- and drop- ports [75].

a demonstrated add-drop MRR (see SEM image in Figure 1.4(c)) are shown in Figure 1.4(d). It is evident that both the spectra have non-uniform extinction ratio (ER) over the entire range of wavelength (highlighted with red lines). This is because of the wavelength dependent coupling characteristics of DCs.

Though MRR based switches offer compact footprint (ring radius ~ 5 μm) and relatively low switching power, their sharp spectral response causes signal waveform distortion, unless channels are aligned critically to the resonant wavelength [77, 78, 79]. On the other hand, MZI based switches offer wide transmission band but require large footprint in the scale of millimeters [80, 81, 82]. Figure 1.5(a) shows schematic of a typical MZI (unbalanced arms) based switch cell. The two 3-dB DCs are being used for splitting and combing the optical signal. The ideal "off" state transfer function at the cross port switch is shown in Figure 1.5(b) as solid lines. At the same time, bar port follows a complementary transfer function. The transfer functions at the two output

7
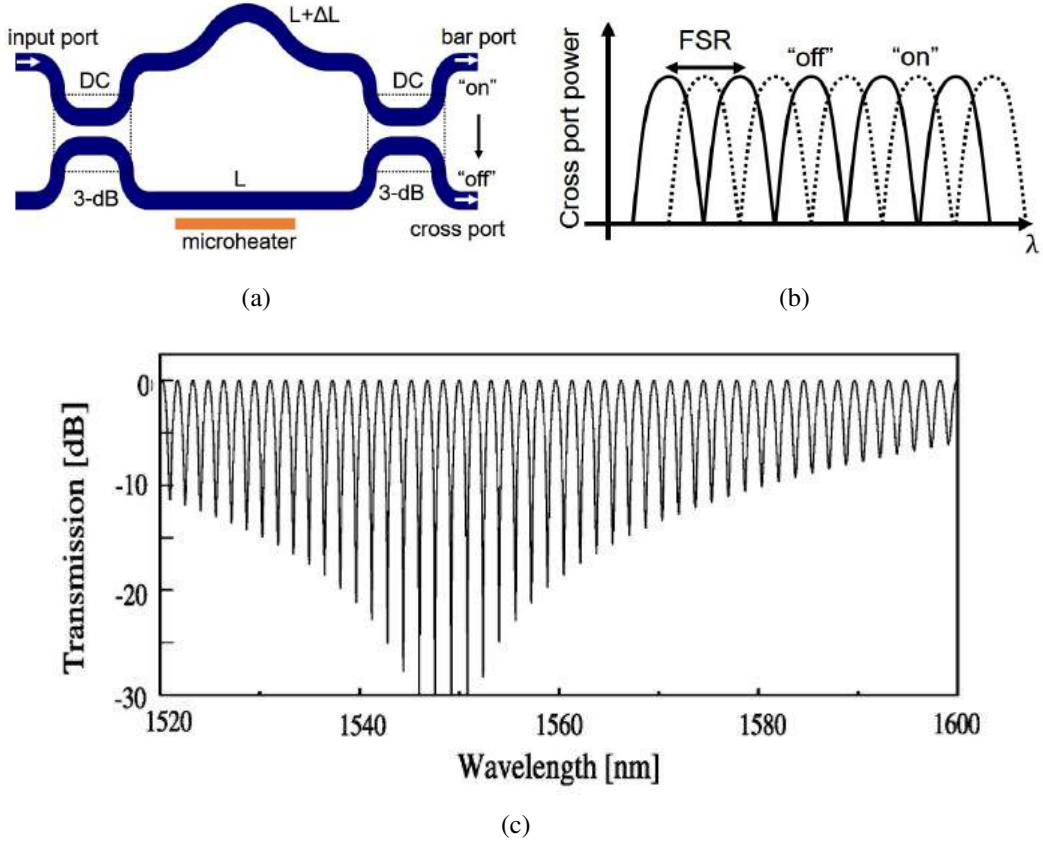
Figure 1.5: (a) Schematic of a 2×2 unbalanced MZI-based switch and (b) the transmission characteristics at Port 4 for "on" and "off" state of the switch (ideal case). (c) Actual wavelength dependent transmission characteristics calculated at Port 3. Waveguide parameters: width = 500 nm, height = 220 nm, gap of DC = 2.5 μm, effective $L_{DC} = 6.8$ μm, $\Delta L = 393.6$ μm [76].

ports can be interchanged by introducing a thermo-optic phase-shift of π using the integrated microheaters. Again, in actual case these transfer functions are highly modulated with wavelength dependent coupling characteristics of DCs coupling characteristics of DCs, the actual transfer function of MZIs are Figure 1.5(c) shows the actual transmission characteristics at the cross port of an MZI reported by Bhatt *et al.* in [76]. Again, the wavelength dependent envelope of the spectrum is due to the nonuniform coupling characteristics of the conventional DCs.

Typical 3D layout of a conventional 2×2 DC (power splitter) is shown in Figure 1.6(a), consisting of two single mode waveguides mutually coupled through their evanescent fields. Since the waveguide dimensions (W - width, H - height) and the separation (G - Gap) are in sub-wavelength range (typically in sub-micron scale), the coupling characteristics of a DC is strongly depends on the operating wavelength ($\lambda \sim$
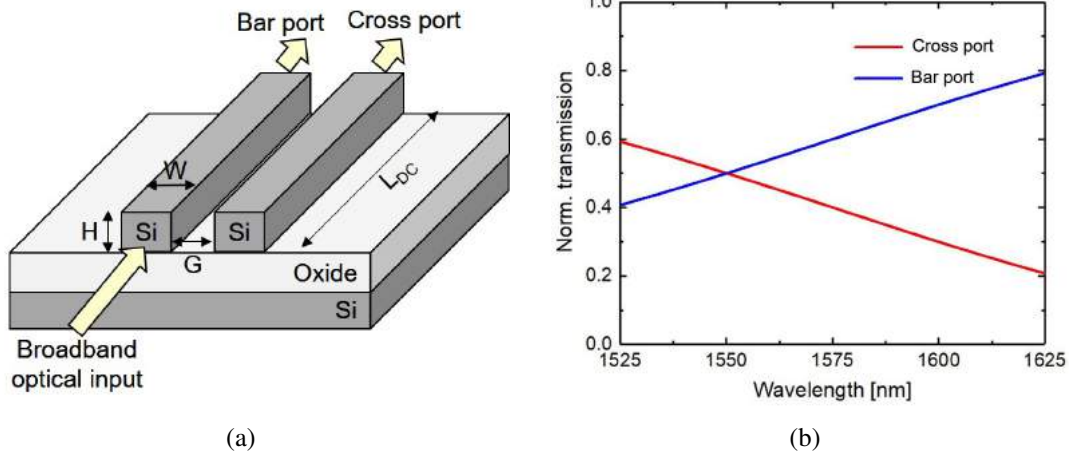
Figure 1.6: (a) Typical 3D scheme of a DC with two parallel coupled waveguides (W - width, H - height, G - Gap and L_{DC} - DC length) in SOI; (b) power splitting ratio at the bar port and cross port of a 3-dB DC ($L_{DC} = L_{3dB}$) designed at $\lambda = 1550$ nm corresponding to a broadband optical input (1525 nm $\leq \lambda \leq$ 1625 nm).

1550 nm) [83]. Typical wavelength dependent power splitting ratio at of a conventional DC designed for 3-dB power splitting at $\lambda = 1550$ nm are shown in Figure 1.6(b). This clearly indicate that the optical bandwidth of a DC is limited by the wavelength dependent coupling between the waveguides. This eventually limits the optical bandwidth of an integrated optical circuit designed with MRRs and MZIs [84, 85]. A detailed working principle of DC is given in Chapter 2.

1.1.2 Broadband DCs: Design Approaches

In recent years, various design approaches have been reported to enhance the bandwidth of DCs. In this section we briefly review some of the relevant efforts.

Approach - 1: The unbalanced MZI based structures are most popular [84, 86, 87] and is first proposed by Jinguji *et al.* in Ref [86] with low contrast waveguides. A schematic of a MZI based wavelength insensitive coupler is shown in Figure 1.7. k_1 and k_2 are the amplitude cross-coupling coefficients of individual DCs of lengths L_1 and L_2 respectively. The basic idea is to introduce an additional phase delay $\Delta\phi$ in one of the arms which compensate the wavelength dependent phase in the DCs. However, this design is not suitable for scalable power splitting ratio, since it requires adequate control over k_1, k_2 and ΔL. This concept has been borrowed in many recently reported broadband
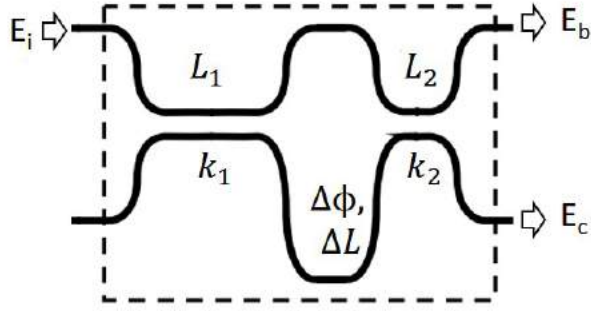
Figure 1.7: Scheme of a wavelength insensitive coupler proposed in [86].

optical switches [84, 88].

Approach - 2: Another approach using hybrid plasmonic waveguides has been proposed in Ref [89] and later demonstrated in Ref [90]. In this a hybrid plasmonic waveguide (HPWG) section is sandwiched between two symmetric DCs. Here, the HPWG section decouples the coupled waveguide modes in the first symmetric coupler. These two uncoupled waveguide modes travel with different phase constants in the HP section and again combine at the output symmetric coupler. With proper design of the lengths of the three sections, one can compensate for the wavelength dependent phase of the symmetric coupler with that of the HPWG section. This leads to wavelength independent operation near $\lambda = 1550$ nm. The measured power splitting ratio of a 3-dB coupler shows a $5 - 10$ % deviation over 60 nm wavelength range (1520 nm $\leq \lambda \leq$ 1580 nm). Though this approach is compact, metal deposition increases the complexity, insertion loss and cost of fabrication. Since metal is deposited on top of the waveguide, this works only for TM polarization (electric field in the vertical direction).

Approach - 3: Lu *et al.* proposed and demonstrated broadband DCs separately for TE and TM polarizations, using asymmetric-waveguide based phase control [91] (see Figure 1.9(a)). The cross-sectional view of the symmetric and phase control sections are shown in Figure 1.9(b) with waveguide design parameters. Here, wavelength dependent phase in the symmetric couplers are compensated by a small phase difference between the two uncoupled waveguides in the phase control section. The phase control section is comprised of two asymmetric waveguides and separated by relatively wider gap such that the waveguide modes propagate without coupling. The length of symmetric coupler L_1 and L_2 are separately optimized for TE mode and TM mode operations. Typical wavelength dependent power splitting ratio (obtained using MZI
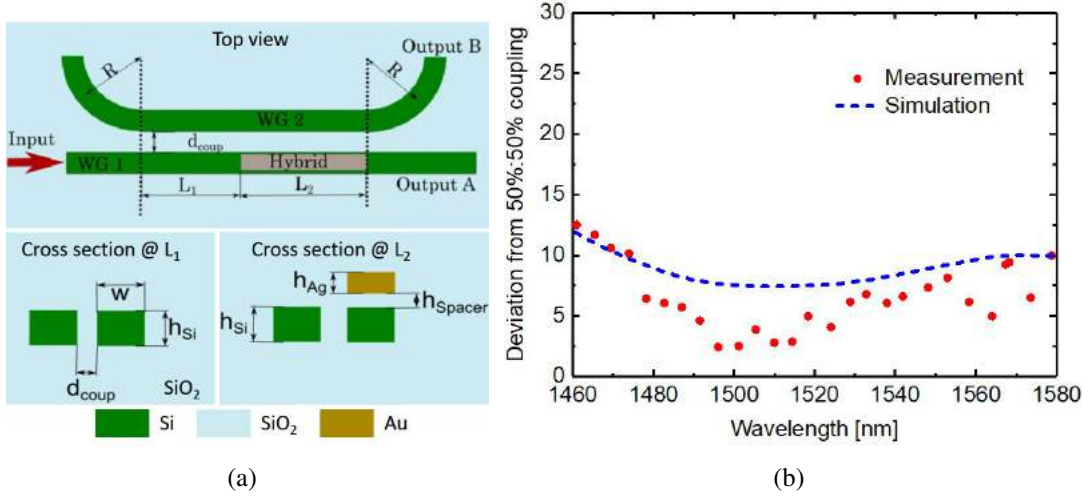
Figure 1.8: (a) Top view of the broadband directional coupler; (b) cross-sectional view of the coupling region showing the symmetric region at L_1 and the asymmetric hybrid plasmonic region at L_2 [89]; (c) deviation of the power coupling coefficient of a 3-dB coupler [90].

configuration [69]) measured for TE- and TM- mode couplers are shown in Figures 1.9(b) and 1.9(c) respectively. The footprint of the device (3-dB power splitter) is in the order of $20-40 \, \mu m^2$. However, these broadband power splitters require critical waveguide parameters and coupling length $> 15 \, \mu m$, and hence need further optimization for high Q MRRs. Also the presence of asymmetry in the coupler make the device less stable against temperature fluctuations (temperature sensitivity of DCs are discussed in Chapter 5).

Approach - 4: An alternate method to enhance the bandwidth of DC is the direct integration of sub-wavelength gratings (SWGs) in the coupling region of DC as proposed by Hailir in Ref [92] (Figure 1.10(a)). In this case, SWG embedded DC, the index perturbation in the coupling region changes the slope of the effective index of the fundamental (ϕ_1) mode while that of first order (ϕ_2) mode of DC is unaffected. This reduces the wavelength dependency in the power coupling strength between the waveguides. The transmission characteristics of a demonstrated 3-dB power coupler based on SWG DC [93] is shown in Figure 1.10(b). The device is compact in size (10-15 μm long) has exhibits nearly 100 nm bandwidth. However, they require adequate control over design parameters of SWGs (period, duty cycle, width, extension length of gratings to both sides of DC, etc.) and DC (waveguide width, gap, etch depth, etc). In addition to that, the measured insertion loss of such devices are 3-5 dB.
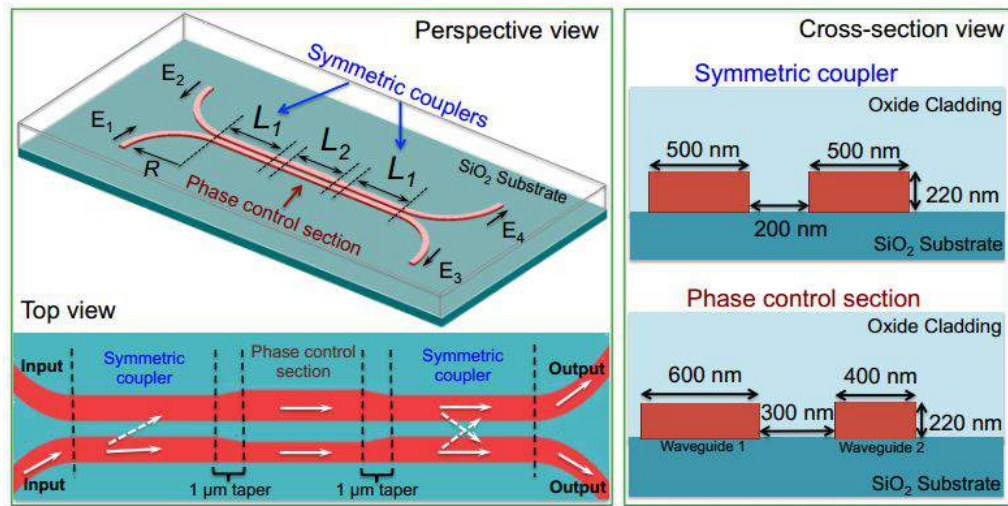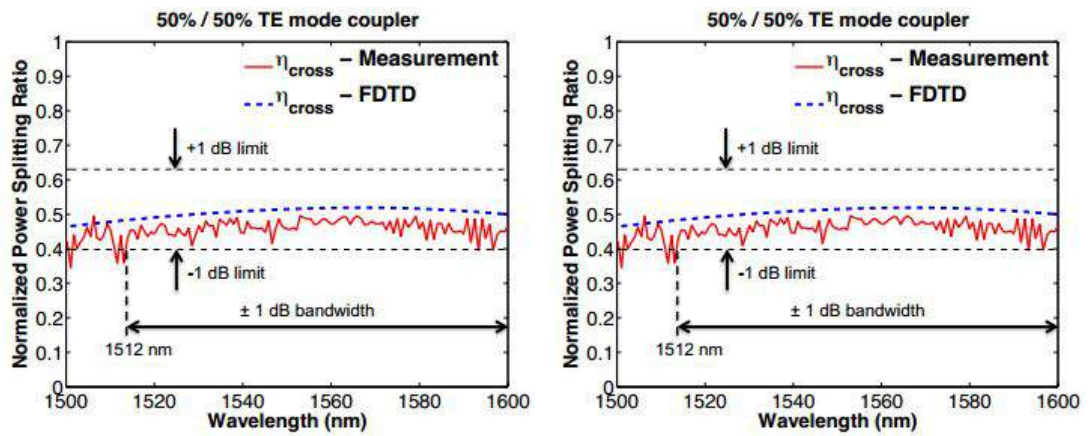
Figure 1.9: Scheme of a broadband silicon photonic directional coupler using asymmetric-waveguide based phase control [91].
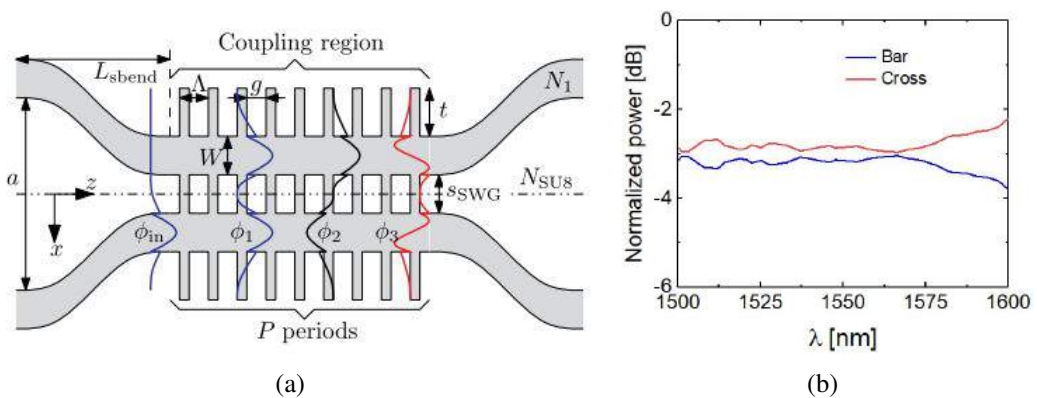
Figure 1.10: (a) Proposed scheme of a broadband directional coupler with dispersion engineered sub-wavelength structures [92]; (b) normalized optical powers for a fabricated SWG DC demonstrated in [93].

<div align="center">(a)   (b)</div>
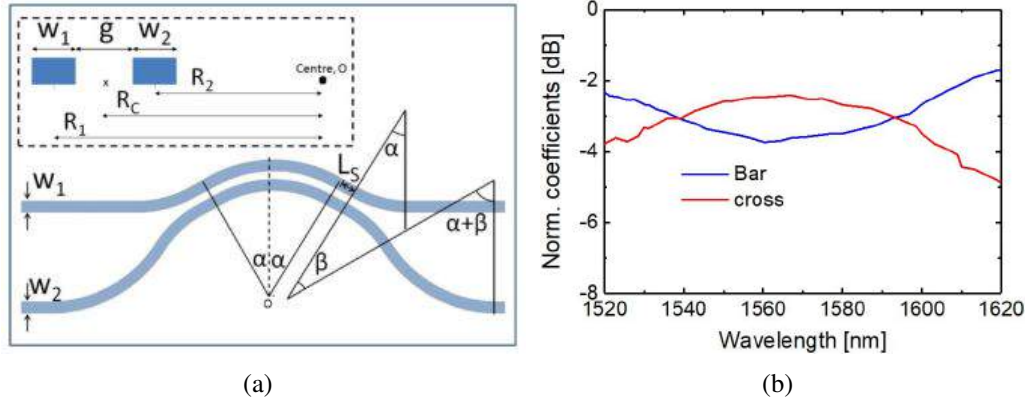
Figure 1.11: (a) Layout and design parameters of a curved DC for broadband operation; (b) Measured transmission characteristics at the bar- and cross- ports (W_1 = W_2 = 400 nm, gap g = 200 nm, radius R_c = 26 µm, L_c = 8.1 µm, L_s = 1.8 µm and $\alpha = \beta$) [94].

Approach - 5: More compact 3-dB power splitters are also reported with curved symmetric directional coupler [95, 96, 94]. The layout and design parameters of a 3-dB curved directional coupler are shown in Figure 1.11(a) [94], consisting of a central curved DC, a straight coupler region, and input/output access waveguides with different curvatures. The measured transmission characteristics at the two output (bar and cross) ports of a 3-dB splitter (W_1 = W_2 = 400 nm, gap g = 200 nm, radius R_c = 26 µm, L_c = 8.1 µm, L_s = 1.8 µm and $\alpha = \beta$) is shown in Figure 1.11(b). The 3 ± 1 dB bandwidth of the coupler is measured to be ~ 88 nm.

To conclude, all the above discussed approaches require extra design parameters to be controlled accurately for any decisive performances. Moreover, it appears not so easy task to design a DC with scalable power splitting ratio using these approaches. Thus there was need for detail investigation of a simple DC design for scalable power splitting and operating over a broad wavelength range for large-scale integrated photonic switching circuits discussed above.

1.2 Research Objective

With the view of above mentioned limitations, the objective of this PhD thesis was set to investigate the design/fabrication aspects thoroughly and to explore for a compact

design of DC in SOI platform operating uniformly over a wider wavelength range covering C + L bands (see Figure 1.12), such that power splitting ratio could be scaled by simply varying the device length. The best possible design of a DC (with the broadest possible optical bandwidth) could then be used to demonstrate wavelength independent MRRs and MZIs. The design results must be validated with experimental results by fabricating various passive/active device architectures (e.g., see Figure 1.13) using in house fabrication facilities available at IIT Madras. An integrated optical metal microheater design has been shown to observe wavelength independent switching characteristics. The access input/output waveguides are shown to be terminated with grating couplers to facilitate device characterizations using fiber optic probe station. The design and fabrication process parameters need to be optimized in accordance with the given specifications of a SOI substrate (device layer thickness $\sim$ 220 nm, buried oxide or BOX layer thickness $\sim$ 2 µm and handle wafer thickness $\sim$ 500 µm) commonly used in silicon photonics foundries.
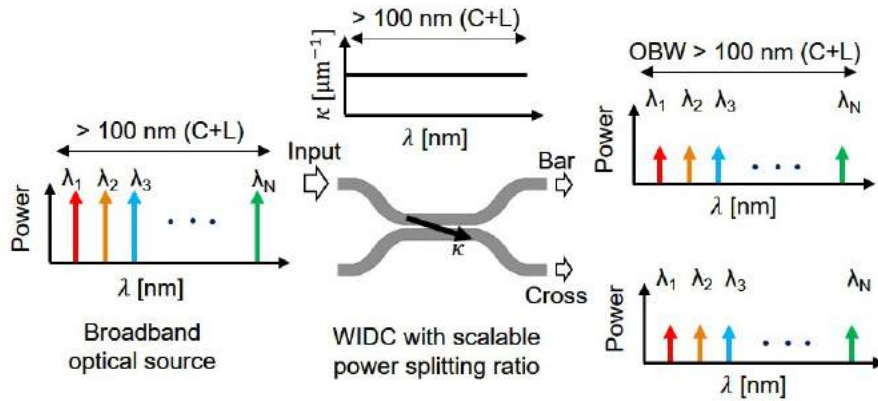
Figure 1.12: Schematic representation of the transmission characteristics of wavelength independent DC (WIDC) operating uniformly over a wide range of wavelength (ideal OBW$\sim \infty$).

1.3 Thesis Organization

The rest of this thesis is organized with the description of design aspects of various devices (DC based), important experimental results and their analyses. They are discussed chapter-wise as follows:

In chapter 2, we have discussed about the design and demonstration of WIDCs
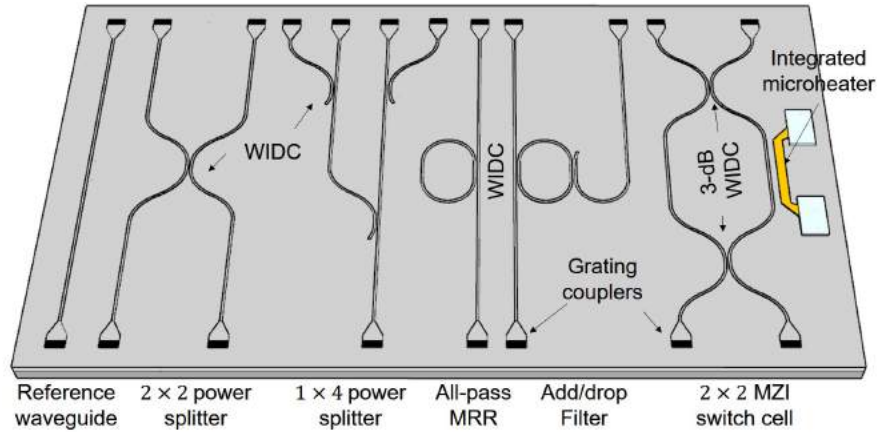
Figure 1.13: Proposed layout for experimental demonstration of integrated photonics circuit building blocks designed with WIDCs.

with scalable power splitting ratios. We started with theoretical understanding of polarization dependent single-mode waveguide design on a 220-nm SOI platform followed by waveguide dispersion characteristics using numerical simulations. A condition for wavelength independent coupling has been established by solving the guided supermodes of a DC. The device fabrication process with optimized parameters are presented in detail. Finally, performances of experimentally demonstrated broadband power splitters (2×2 and 1×4) are analyzed and validated with theoretical predictions.

In Chapter 3, we have presented the design and demonstration of broadband all-pass and add-drop microring resonators. The chapter begins with the general theory and working principle of ring resonators. The transmission characteristics of a wavelength dependent DC based and a WIDC based MRR are numerically evaluated including the effect of bend loss and bend induced coupling at the curved regions of the ring. The devices are fabricated and the experimental resonance characteristics such as extinction ratio, Q-factor, free-spectral range, fineness, etc., are compared with simulation results. In addition to that, the demonstration of compact MRRs (radius ~ 25 μm) are also presented.

Chapter 4 is reserved for broadband MZIs integrated with WIDCs. Working principle and transfer function of balanced/unbalanced MZIs have been presented along with simulation results. The experimental demonstration and broadband transmission characteristics of broadband MZIs are presented along with theoretical validation. This section also includes the demonstration of more compact broadband MZIs fabricated in

two step lithography and etching steps.

In chapter 5, we have presented the design and demonstration of a MZI based switch cell integrated with thermo-optic phase-shifters. The switching characteristics of metal-integrated waveguide phase-shifters in different configurations were analyzed numerically in terms of switching power, switching time and metal absorption loss. Experimental demonstration including the fabrication details of microheater integration and four-probe thermo-optic characterization are discussed. In the end, various performance figure of merits of demonstrated balanced/unbalanced MZI thermo-optic switches are compared with that of earlier reported results.

A summary of the research carried out within the scope of this thesis and possible extensions of the work have been briefly outlined in Chapter 6.

CHAPTER 2

Directional Coupler: Design and Demonstration

In this chapter we have studied the coupling characteristics of a conventional 2×2 DC structure in SOI towards the design and demonstration of wavelength independent DC (WIDC) operating near $\lambda \sim 1550$ nm. Typical layout of a 2×2 DC is shown in Figure 2.1(a) (x-z plane). The cross- and bar-ports are indicated with respect to one of the input ports. The two waveguides are assumed to be identical and separated by a small gap G over a coupling length (along z-axis) of L_{DC} as shown. However, the effective
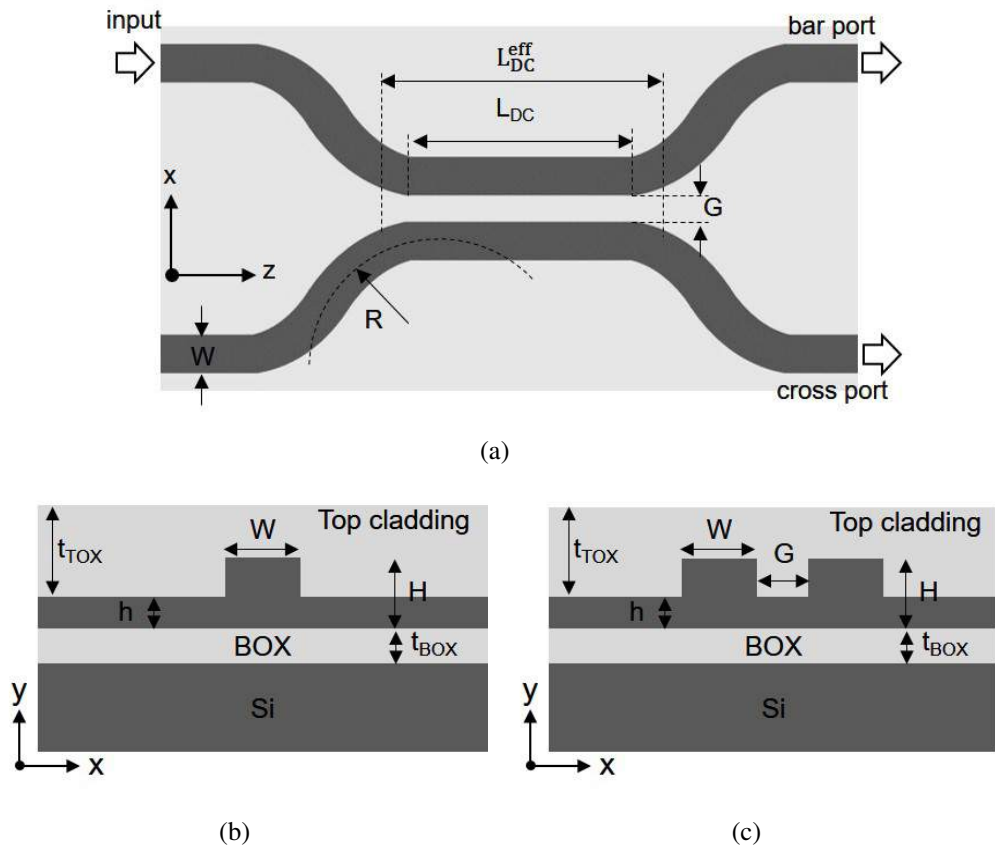
Figure 2.1: (a) Top view of a 2×2 DC, (b) and (c) are cross-sectional views of input/output waveguide and DC respectively in SOI substrate. L_{DC}: DC length, W: rib width, h: slab height, G: gap, H: device layer (rib) height and R: waveguide bend radius, t_{BOX}: buried oxide thickness and t_{TOX}: top oxide thickness.

coupling length of DC must be longer than L_{DC}, as the input/output waveguides approach adiabatically through S-bends (with bending radius of R) and hence contribute additional couplings in both sides of the parallel coupled section. A sharper S-bends (or a smaller R) may be desired for compact device footprint as well as to limit couplings in the bend regions. The gap G controls the mode overlap and coupling strength of DC for any fixed waveguide geometry. A cross-sectional view (in x-y plane) of individual waveguides and DC region in SOI substrate along with important design parameters are shown in Figures 2.1(b) and 2.1(c), respectively. The waveguide geometry is defined by rib width W, height H and slab height h. Following the standards of silicon photonics foundries, we have considered a 220-nm thick device layer (H) SOI substrate with buried oxide layer (SiO$_2$) thickness (t_{BOX}) of 2 μm and handle silicon layer of thickness of ~ 500 μm. The waveguides may be assumed to be covered with a top cladding layer of air/oxide/nitride. Since the refractive index of silicon core is very large (~ 3.4775), the values of W, h, G and H are in sub-wavelength scale for a single mode propagation. This in turn makes the conventional DC strongly wavelength sensitive (dispersive). However, with suitable choice of design parameters it is possible to engineer the dispersion characteristics of waveguides and hence the DC design towards wavelength independent operation over a given wavelength range.

In following sections we have investigated the polarization dependent criteria for single-mode guidance, wavelength dependent coupling characteristics of coupled single-mode waveguides and S-bends for input/output access waveguides. Finally, WIDCs were experimentally demonstrated using the best design parameters obtained from simulation results.

2.1   Waveguide Design

The cross-sectional geometry of a SOI waveguide with design parameters (W, h, H) has been shown previously in Figure 2.1(b). Total internal reflection of light waves with an incident angle of $\sim 60°$ inside the waveguide is satisfied by the high refractive index contrast Δ $\left(= \frac{n_{Si}^2 - n_{SiO_2}^2}{2 \cdot n_{si}^2} \sim 40\% \right)$ between silicon ($n_{Si} \approx 3.4775$) and oxide ($n_{SiO_2} \approx 1.4447$) in the telecommunication wavelength range ($\sim$1300 nm - 1600

nm). Thus light is confined both vertically and horizontally in the silicon core region (x-y plane). The index contrast increases with etch depth ($d = H - h$), but the rough sidewalls increase the propagation loss due to sidewall scattering. In our theoretical discussions, we have considered loss-less waveguides with smooth and vertical sidewalls. In general, waveguides are designed for single-mode operation except for some application like mode-division multiplexing (MDM) [97]. In other words, the phase velocity difference between the guided modes cause inter-modal dispersion in multi-mode waveguides. However, in single mode waveguides due to the tighter confinement of modes in submicron waveguides, the effective index (n_{eff}) of guided mode varies significantly with wavelength. This is called intra-modal (structural) dispersion, resulting in wavelength dependent group index, ($n_g(\lambda) = n_{eff}(\lambda) - \lambda \cdot \frac{dn_{eff}(\lambda)}{d\lambda}$). Therefore, it is important to estimate the valid range of W and h (fixed $H = 220$ nm) for single-mode guidance and their polarizations over a desired wavelength range ($\lambda \sim 1550$ nm).

2.1.1 Single-Mode Guidance

At any operating wavelength λ, the number of guided modes and their polarizations are decided by waveguide geometry (W, h and H). The polarization of supporting modes inside the waveguide can be ether TE-like (dominant electric field component parallel to the substrate) or TM-like (dominant electric field component perpendicular to the substrate). The difference between effective indices of these two orthogonally polarized modes is called birefringence. Due to the geometrical asymmetry, the structural birefringence is relatively large in submicron photonic wire waveguides compared to that of large cross-section waveguides [98, 99]. The birefringence is zero for symmetric square waveguide ($W = H$, $h = 0$, and surrounded by oxide). The possible supporting modes of a waveguide of certain geometry are calculated by solving the Maxwell's equation with appropriate boundary conditions. Commercial *finite difference eigen-mode solver* (FDE) of Lumerical MODE Solutions [100] is used to calculate the geometry dependent effective index (n_{eff}) and polarization fraction of mth ($m = 0,\ 1,\ 2..$) order guided modes for various W (300 nm $\leq$ W $\leq$ 700 nm) and h ($0 \leq$ h $\leq$ 200 nm) at an operating wavelength $\lambda \sim 1550$ nm. The degree of polarization of the guided modes are defined
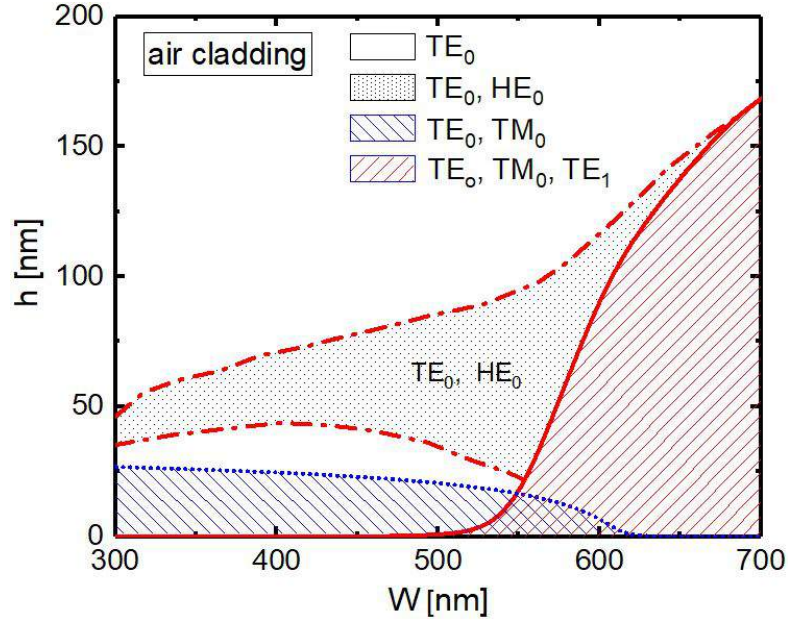
(a)
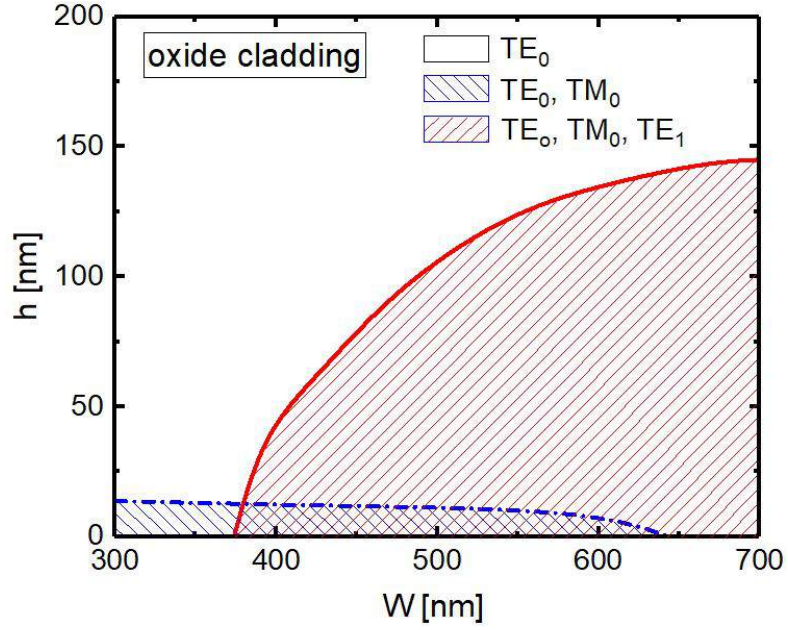
(b)

Figure 2.2: Allowed guided modes defined by $TE_{0,1}$, TM_0 and HE_0 (see text for definitions) shown in W-h plane for (a) air top-cladding and (b) oxide top-cladding. The calculations are carried out for H = 220 nm and $t_{BOX} = t_{tox}$ = 2 μm, at an operating wavelength λ = 1550 nm.

by comparing the fraction of transverse electric field component along x-direction:

$$\gamma_x = \frac{\int |E_x|^2 dxdy}{\int \left(|E_x|^2 + |E_y|^2\right)dxdy} \qquad (2.1)$$

20

where, E_x and E_y are the transverse electric field components of a guided mode. For convenience, we have assumed a guided mode to be TE-polarized if $\gamma_x \geq 0.6$, TM-polarized if $\gamma_x \leq 0.4$ and hybrid or HE-polarized for $0.4 < \gamma_x < 0.6$; and accordingly demarcated in Figs. 2.2(a) (air-cladding) and 2.2(b) (oxide-cladding). Besides single-mode guiding condition, we also observe that TE_0 mode is supported for all values of h when W is kept below 500 nm (375 nm) for air (SiO_2) top-cladding. Both TE_0 and TM_0 modes are supported for $h \leq 30$ nm (15 nm) for air (oxide) top-cladding. Note that, HE-polarized modes ($0.4 \leq \gamma_x \leq 0.6$) are absent in waveguides with oxide cladding, due to the symmetric vertical and horizontal boundary conditions (oxide cladding).

In order to understand the geometry dependent distribution of modes along the waveguide cross-section, we have considered a few waveguide geometries and plotted E_x field distribution at $\lambda = 1550$ nm. For example, the waveguide geometry in

(a)   (b)
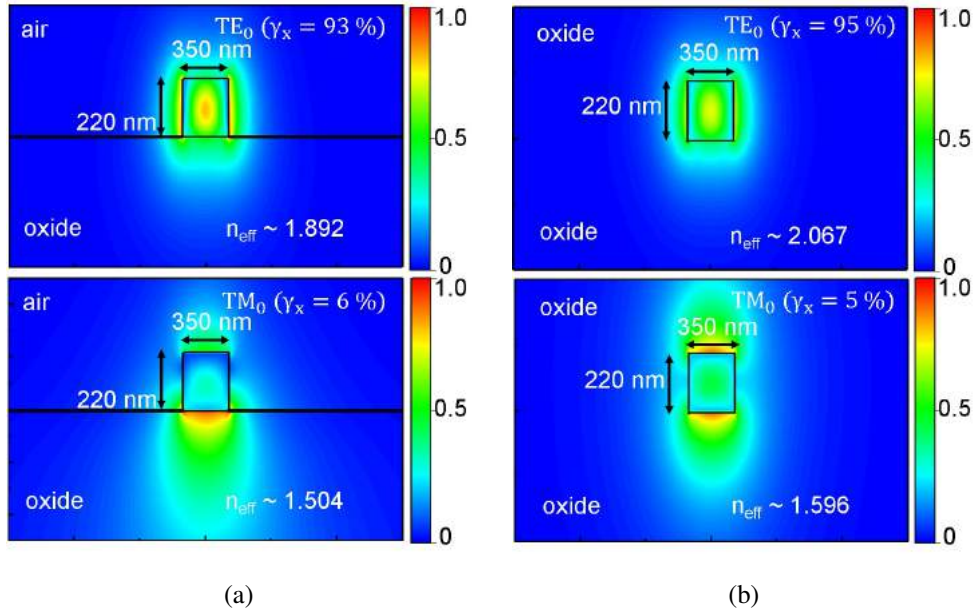
Figure 2.3: Electric field intensity distribution of TE_0 (top) and TM_0 (bottom) modes of a SOI waveguide of $W = 350$ nm, $h = 0$ nm and $H = 220$ nm calculated at $\lambda = 1550$ nm with (a) air cladding and (b) oxide cladding.

Figure 2.3 ($W = 350$ nm, $h = 0$ nm, $H = 220$ nm) support two orthogonally polarized modes: TE_0 and TM_0, and does not support higher order modes of same polarization (Figure 2.3(a) for air cladding and Figure 2.3(b) for oxide cladding). Also, a waveguide ($W = 400$ nm, $h = 50$ nm, $H = 220$ nm) that supports fundamental TE_0 mode and an HE_0 mode is shown in Figure 2.4. Here HE_0 mode is the first order mode ($m = 1$) of

the waveguide with nearly equal E_x and E_y polarization fractions ($0.4 \leq \gamma_x \leq 0.6$).

(a)   (b)
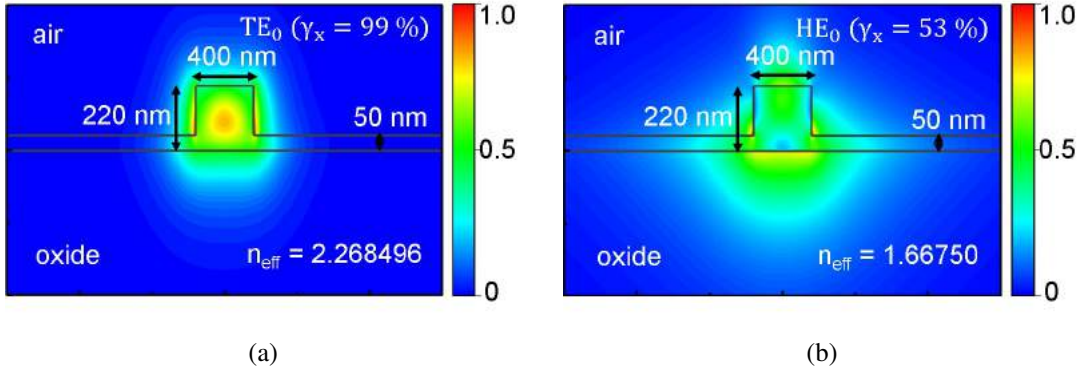
Figure 2.4: Electric field intensities of TE_0 ($\gamma_x = 99\%$) and HE_0 ($\gamma_x = 53\%$) guided modes of a SOI waveguide of $H = 220$ nm, $W = 400$ nm and $h = 50$ nm calculated at $\lambda = 1550$ nm with air as top cladding.

2.1.2 Modal Dispersion

The n_{eff} of a SOI waveguide is not only a function of waveguide geometry but also a function of wavelength. The wavelength dependent effective index of a guided mode results in structural dispersion. To calculate the $n_{eff}(\lambda)$, we have included the ma-
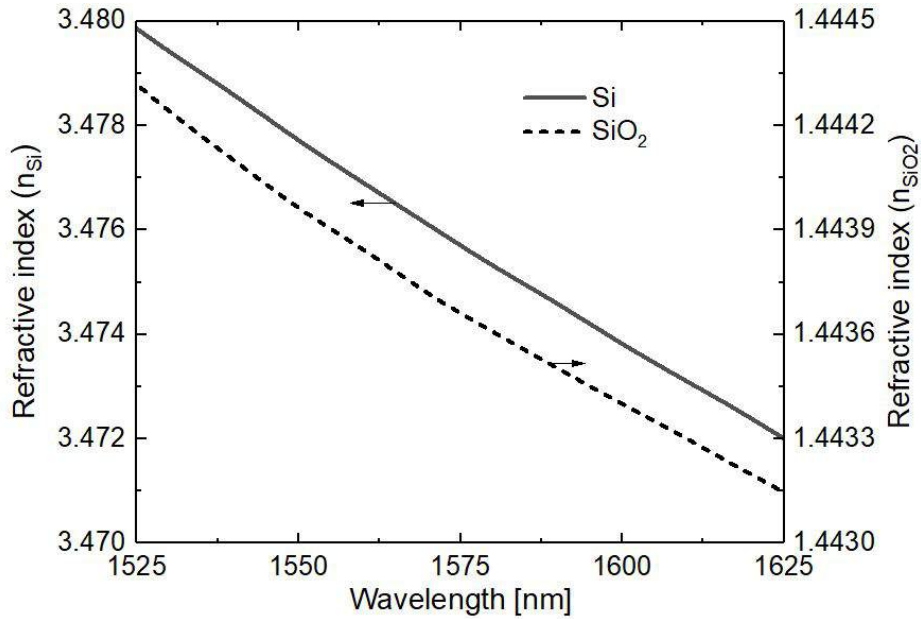
Figure 2.5: Wavelength dependent refractive index (material dispersion) curves for Si [101] (solid) and SiO$_2$ [100] (dotted) used to calculate modal dispersion of SOI waveguides.
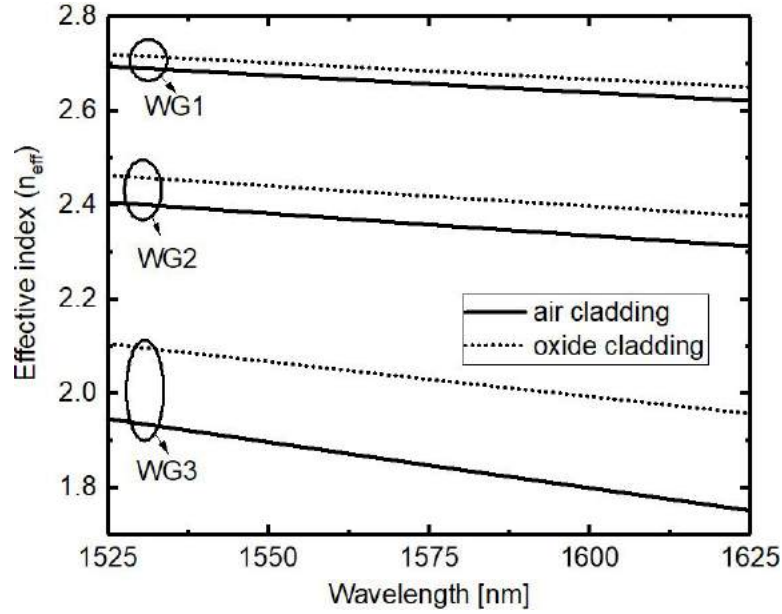
Figure 2.6: Wavelength dependent effective index of fundamental TE_0 mode calculated for three different waveguide geometries (WG1: $W = 550$ nm, $h = 150$ nm, $H = 220$ nm, $W = 350$ nm, WG2: $h = 100$ nm, $H = 220$ nm, WG3: $W = 350$ nm, $h = 0$ nm, $H = 220$ nm) with air cladding (solid lines) and with oxide cladding (dashed lines).

terial dispersion parameters of silicon and SiO_2 given in [101] in Lumerical MODE Solutions for 1525 nm $\leq \lambda \leq$ 1625 nm. The calculated $n_{eff}(\lambda)$ as a function of λ for three waveguide geometries (WG1: $W = 550$ nm, $h = 150$ nm, $H = 220$ nm, WG2: $W = 350$ nm, $h = 100$ nm, $H = 220$ nm, WG3: $W = 350$ nm, $h = 0$ nm, $H = 220$) over a wavelength span of 100-nm (1525 nm $\leq \lambda \leq$ 1625 nm) are shown in Figure 2.6. The solid lines represent air cladding and dotted lines represent oxide cladding. Note that, irrespective of the waveguide geometry and cladding, n_{eff} reduces as wavelength increases. Again, n_{eff} is a strong function of λ for smaller core area waveguides (WG3). Thus deeply etched waveguides are highly dispersive than shallow etched waveguides.

Since n_{eff} reduces with wavelength, the evanescent tail of the modes penetrate more into the cladding region and hence the power confinement in the core region reduces. The confinement factor of a mode quantifies the fraction of optical power in the waveguide core ($-W/2 \leq x \leq W/2$, $0 \leq y \leq H$) for a particular polarization, and is defined

by,

$$\Gamma = \frac{\int_{-W/2}^{W/2} \int_0^H |E_x|^2 \, dy dx}{\int_{-\infty}^{\infty} \int_{-\infty}^{\infty} |E_x|^2 \, dy dx} \tag{2.2}$$

In submicron waveguides, the modal confinement and evanescent field distributions
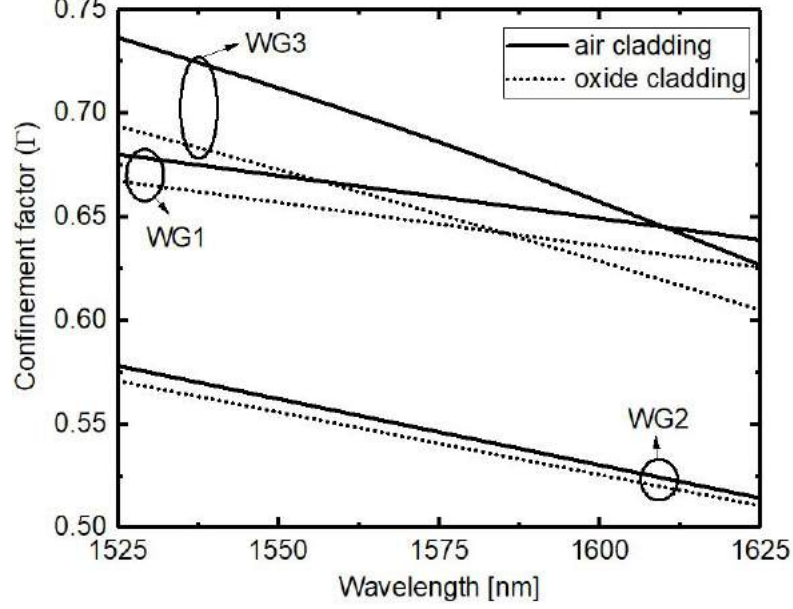
Figure 2.7: Wavelength dependent confinement factor (Γ) of fundamental TE$_0$ mode calculated for three different waveguide geometries (WG1: $W = 550$ nm, $h = 150$ nm, $H = 220$ nm, WG2: $W = 350$ nm, $h = 100$ nm, $H = 220$ nm, WG3: $W = 350$ nm, $h = 0$ nm, $H = 220$ nm) with air cladding (solid lines) and with oxide cladding (dashed lines).

are strong functions of wavelength. Since the effective index reduces with wavelength (Figure 2.6), evanescent tail penetrates more into the slab region and hence Γ_x reduces with wavelength. The wavelength dependent variation of Γ for above mentioned three different waveguide cross-sections (supporting TE$_0$ mode), calculated over 1525 nm $\leq \lambda \leq 1625$ nm are shown in Figure 2.7 for air cladding (solid lines) as well as oxide cladding (dashed lines). The magnitude and slope of Γ are found to be relatively large for deeply etched waveguide (WG3) compared to shallow etched waveguide (WG2). This is because, the deeply etched waveguides confine more light in the waveguide core due to high refractive index contrast in the horizontal ($x-$) direction. On the other hand, Γ increases with core size of shallow etched waveguides (WG1 and WG2) and reduces at a slower rate w.r.t λ. It is to be noted that, though $n_{eff}(\lambda)$ is more with oxide cladding (see Figure 2.6), the modal confinement reduces with oxide cladding since the refractive

index contrast Δ between the core and cladding reduces as the cladding index increases. Confinement factor is an important parameter in DC design as it measures the coupling strength between coupled waveguides. Higher the confinement factor, lower will be the DC length for a given power splitting ratio. Moreover, lower confinement increases the bend induced losses and hence limits the bending radius of S-bends. This is explained in more details with simulation results while considering the design aspects of WIDCs to be discussed later.

2.2 Dispersion in Coupled Waveguides

To understand the dispersion in coupled waveguides we first discuss the working principle of a DC and thereafter the wavelength dependent propagation of its guided eigenmodes (supermodes).

2.2.1 Coupled Waveguides: Working Principle

The coupling characteristics of a 2×2 DC of length L_{DC} (length of parallel coupled region) can be explained using supermode analysis [102], where the coupled waveguides are modeled as a composite structure supporting higher order modes. Figure 2.8(a) shows two single-mode waveguides with field amplitudes $E_1(x, y, z)$ and $E_2(x, y, z)$ propagating along $z-$ direction with propagation constants $\beta_1 = 2\pi n_{eff1}/\lambda$ and $\beta_2 = 2\pi n_{eff2}/\lambda$, respectively. The gap (G) is such that their field amplitudes are non-overlapping and hence waveguides are uncoupled. Whereas in case a of coupled waveguide system, as shown in Figure 2.8(b), the evanescent tails of the two guided modes can overlap in the small gap. If the two single-mode waveguides are identical, one can expect two lowest supermodes (symmetric supermode and antisymmetric supermode) which are the linear combination of the individual uncoupled waveguide modes E_1 and E_2. This has been schematically shown in Figure 2.8(b) and mathematically expressed
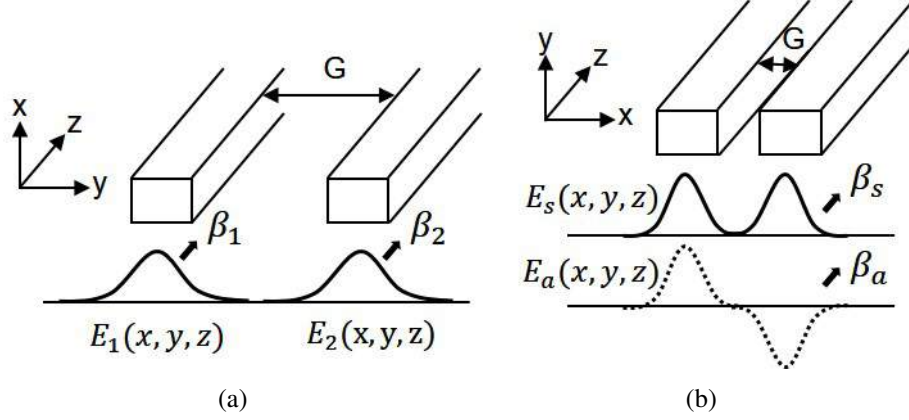
Figure 2.8: Schematics of (a) uncoupled waveguides and (b) directional coupler (DC); $E_1(x, y, z)$ and $E_2(x, y, z)$ are the electric field distributions of individual waveguides; $E_s(x, y, z)$ and $E_a(x, y, z)$ are the electric field distributions of two lowest order modes (symmetric and antisymmetric supermodes) of a DC.

as:

$$E_s(x, y, z) = E_s(x, y) \exp(j\beta_s z) \tag{2.3a}$$

$$E_a(x, y, z) = E_a(x, y) \exp(j\beta_a z) \tag{2.3b}$$

where E_s and E_a are the cross-sectional electric field profiles of the symmetric supermode (or fundamental mode) and antisymmetric supermode (or first order mode) respectively. The propagation constants β_s and β_a of the two modes are given by:

$$\beta_s = \frac{2\pi}{\lambda} n_{eff}^s(\lambda) \quad \text{and} \quad \beta_a = \frac{2\pi}{\lambda} n_{eff}^a(\lambda) \tag{2.4}$$

where n_{eff}^s and n_{eff}^a are the effective indices of symmetric and antisymmetric supermodes respectively. Since $n_{eff}^a < n_{eff}^s$, both modes travel with different velocities and hence their relative phase difference ($\phi = (\beta_s - \beta_a)z$) decides the fraction of power coupled from one waveguide to other waveguide at any distance along the coupled region. Figure 2.9(a) schematically shows the electric field distribution in symmetric (solid line) and antisymmetric supermodes (dashed line) and their relative phase difference at three different locations along the length of DC, when input power is launched to the top waveguide ($P_{in} = |E_1|^2$ and $P_2 = 0$ at $z = 0$). Here we assume that the two waveguides are identical such that $\beta_1 = \beta_2$ and lossless propagation.

26
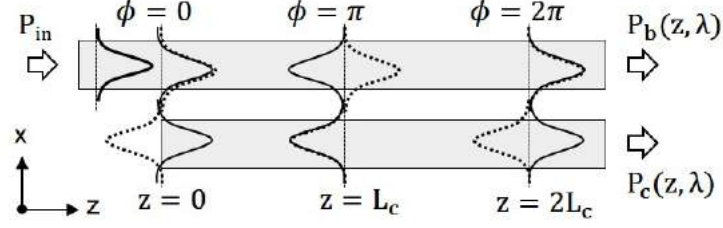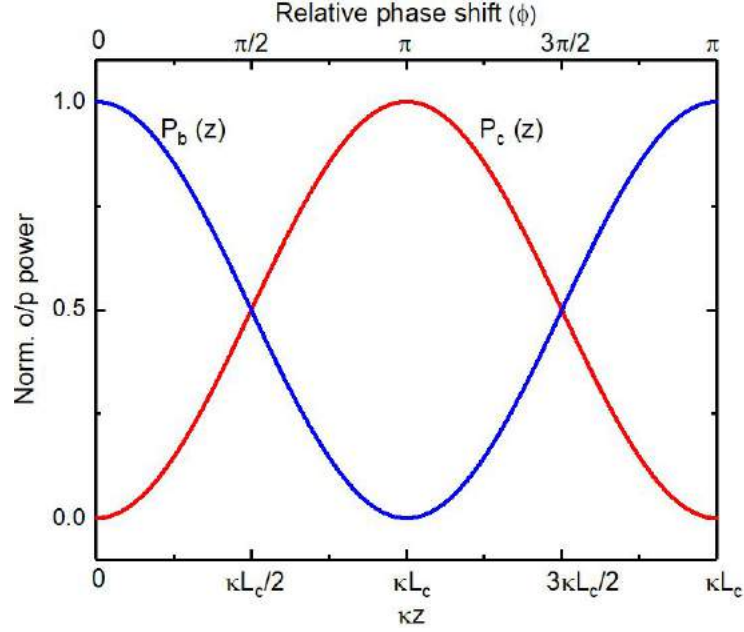
Figure 2.9: (a) Electric field profiles of symmetric (solid line) and antisymmetric (dotted line) modes along the length of the waveguide at $z = 0$, $z = L_c$ and $z = 2L_c$, where L_c is the cross coupling length; (b) normalized output power at the bar port ($P_b(z)$) and cross port ($P_c(z)$) calculated along the DC length using Eq. 2.5 (assuming loss-less waveguides) as a function of κz. where κ is the coupling strength. The relative phase shift between two ports is shown in the top x axis.

At $z = 0$ ($\phi = 0$) input power couples to both the supermodes, however, the total field will get canceled at the cross port and appear only in the bar port (see Figure 2.9(a)). As it propagates (assuming loss-less waveguides) at some distance $z = L_c$, the relative phase difference becomes $\phi = \pi$ where the two filed amplitudes constructively interfere at the cross port and destructively interfere at the bar port resulting in $P_b = 0$ and $P_c = P_{in}$. Again at $z = 2L_c$ the situation becomes similar to $z = 0$ ($\phi = 2\pi$), where $P_b = P_{in}$ and $P_c = 0$. Thus L_c is defined as the cross-coupling length (interaction length of DC required for the complete exchange of power from one waveguide to other). Thus

the sinusoidal distribution of P_b and P_c at $z = L_{DC}$ can be derived from Eq. 2.3 as [99]:

$$P_b(\lambda) = \cos^2(\kappa L_{DC}) \cdot P_{in}(\lambda) = |t^2|\, P_{in}(\lambda) \tag{2.5a}$$

$$P_c(\lambda) = \sin^2(\kappa L_{DC}) \cdot P_{in}(\lambda) = |k^2|\, P_{in}(\lambda) \tag{2.5b}$$

where the self coupling coefficient t and cross coupling coefficient k are defined as [102]:

$$t = \cos(\kappa L_{DC}) \quad \text{and} \quad k = e^{-j\pi/2} \sin(\kappa L_{DC}) \tag{2.6}$$

respectively. The term $e^{-j\pi/2}$ represents that the relative phase difference between field amplitudes. The term κ is the coupling strength, as given by:

$$\kappa(\lambda) = \frac{\beta_s(\lambda) - \beta_a(\lambda)}{2} = \frac{\pi \Delta n(\lambda)}{\lambda} \tag{2.7}$$

and $\Delta n(\lambda) = n_{eff}^s(\lambda) - n_{eff}^a(\lambda)$.

In general, the amplitude transfer function of a 2×2 DC can be expressed as [103]:

$$\mathcal{T}_{DC}(\lambda) = \begin{bmatrix} \cos[\kappa(\lambda)L_{DC}] & -j\sin[\kappa(\lambda)L_{DC}] \\ -j\sin[\kappa(\lambda)L_{DC}] & cos[\kappa(\lambda)L_{DC}] \end{bmatrix} \tag{2.8}$$

For any fixed Δn and λ (i.,e, κ constant) the power coupling efficiencies at the cross port and bar port and their relative phase difference are plotted in Figure 2.9(b) along the length of DC. At every successive L_c distance, power transfers completely from one port to other port, thus L_c is called cross coupling length or beat length. The 3-dB coupling length of DC can be estimated as:

$$L_{3dB}(\lambda) = \frac{L_c(\lambda)}{2} = \frac{(2m+1)\pi}{4\kappa(\lambda)} \tag{2.9}$$

where m = 0, 1, 2, 3.... Thus for any coupling length the power splitting ratio of a DC is highly wavelength dependent. Length dependent dispersion was discussed in detail in the Ph.D. thesis of Sujith [99]. In the following section, we will focus on the dispersion engineering of supermodes by varying waveguide design parameters (within TE$_0$ propagation regime), especially W and h for a given H (device layer thickness) and G

(physical separation between coupled waveguides). In fact G is important parameters for dispersion engineering. However, we have restricted it's value to a minimum possible value which could achieved uniformly using e-beam lithography process. Smaller the value of G, one can design a smaller footprint of DC for a desired coupling (splitting) ratio. However, smaller value of G makes the DC more dispersive.

2.2.2 Supermode Dispersion: Simulation Results

The wavelength dependent performance of a SOI based DC (see Figure 2.1) is better understood by calculating the dispersion characteristics of its supermodes. The symmetric and anti-symmetric supermodes of a DC are evaluated numerically using Lumerical's Eigenmode Solver including the material dispersion parameters for Si core and SiO_2 cladding [100, 101]. We start with three different DC cross-sections (DC1, DC2 and DC3) with waveguide design parameters similar to that of WG1, WG2 and WG3 respectively (fixed G and H). The corresponding electric field (E_x) distributions of TE-like guided modes (λ = 1550 nm) for; DC1 ($W = 550$ nm, $h = 100$ nm, $G = 150$ nm), DC2 ($W = 350$ nm, $h = 100$ nm, $G = 150$ nm), and DC3 ($W = 350$ nm, $h = 0$ nm, $G = 150$ nm) are shown in Figs. 2.10(a), 2.10(b), and 2.10(c), respectively.

As discussed earlier, the waveguide parameters (W, H, h) chosen for all the three DCs are such that they support only the fundamental modes (TE-like) for a wide band of wavelength range (e.g., 1520 nm $\leq \lambda \leq$ 1630 nm). However, because of wavelength dependent mode-field distributions, the waveguide modes as well as symmetric and antisymmetric supermodes of the DCs are expected to be dispersive. The calculated effective indices corresponding to symmetric and anti-symmetric supermodes (n_{eff}^s and n_{eff}^a) as a function of wavelength for the above mentioned three DCs (DC1, DC2, and DC3) are shown in Fig. 2.11(b). It is now evident from the plots that the values of $\Delta n(\lambda) = n_{eff}^s(\lambda) - n_{eff}^a(\lambda)$ and the slope $\frac{d}{d\lambda}[\Delta n(\lambda)]$ of the SOI based DCs can be engineered appropriately by controlling the design parameters such as W, H, h, and G. In the following discussion, we are going to establish how the wavelength dependent transmission characteristics of a DC can be analytically evaluated by employing the coupled mode theory with knowledge of numerically obtained values of $\Delta n(\lambda)$ and
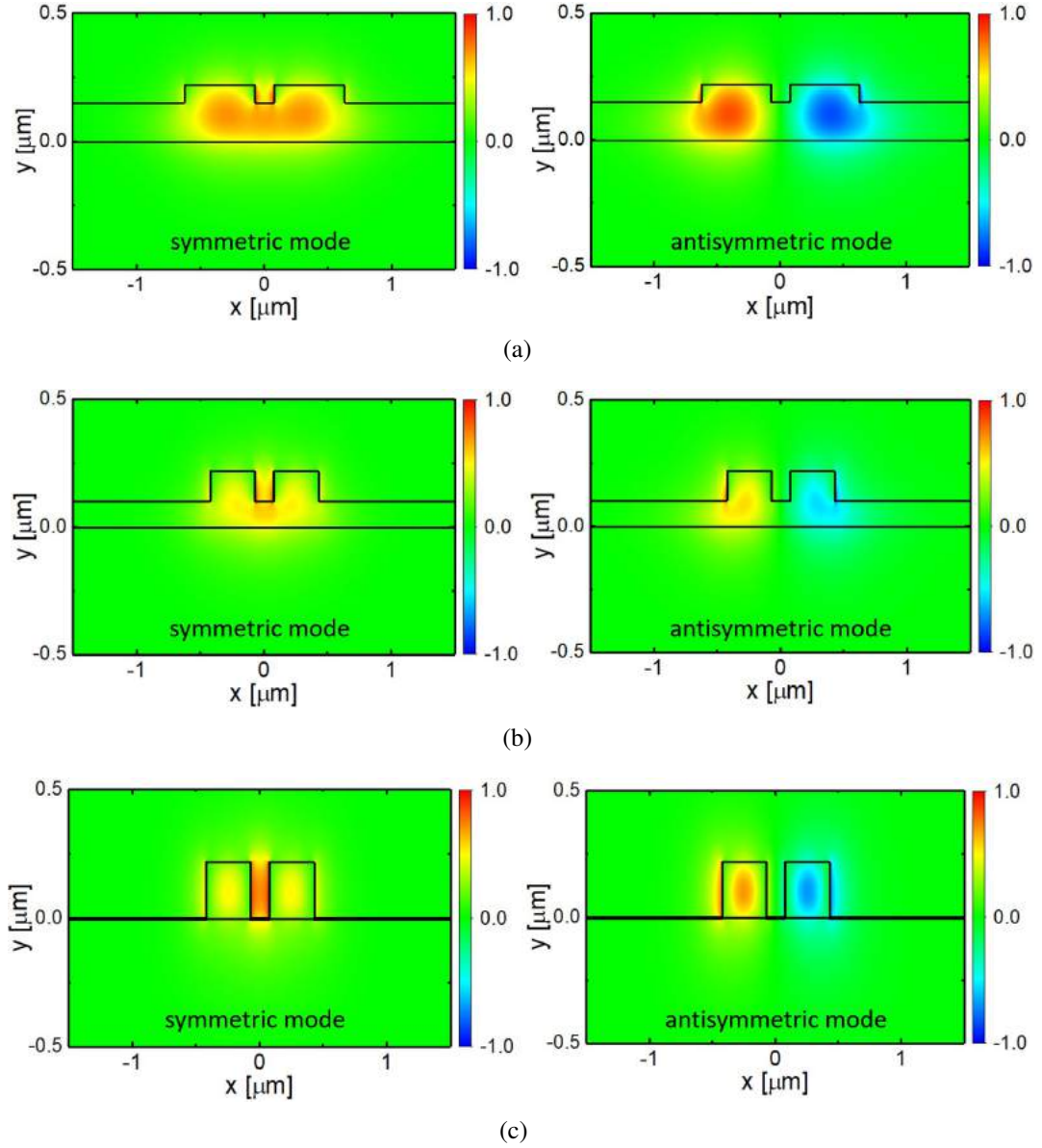
Figure 2.10: Electric field distribution of TE-like (symmetric and antisymmetric) modes calculated for an operating wavelength $\lambda = 1550$ nm: (a) DC1 with $W = 550$ nm, $H = 220$ nm, $h = 150$ nm, $G = 150$ nm; (b) DC2 with $W = 350$ nm, $H = 220$ nm, $h = 100$ nm, $G = 150$ nm; and (c) DC3 with $W = 350$ nm, $H = 220$ nm, $h = 0$ nm, $G = 150$ nm.

$\frac{d}{d\lambda}[\Delta n(\lambda)]$.

Typical transmission characteristics of a DC (DC1) of length $L_{DC} = 25$ µm is shown in Figure 2.12. Using Eq. 2.5, the free spectral range (FSR) of the transmitted light waves at both the output ports can be derived as:

$$\Delta\lambda = -\frac{\lambda^2}{L_{DC}\,\Delta n_g} \qquad (2.10)$$

30
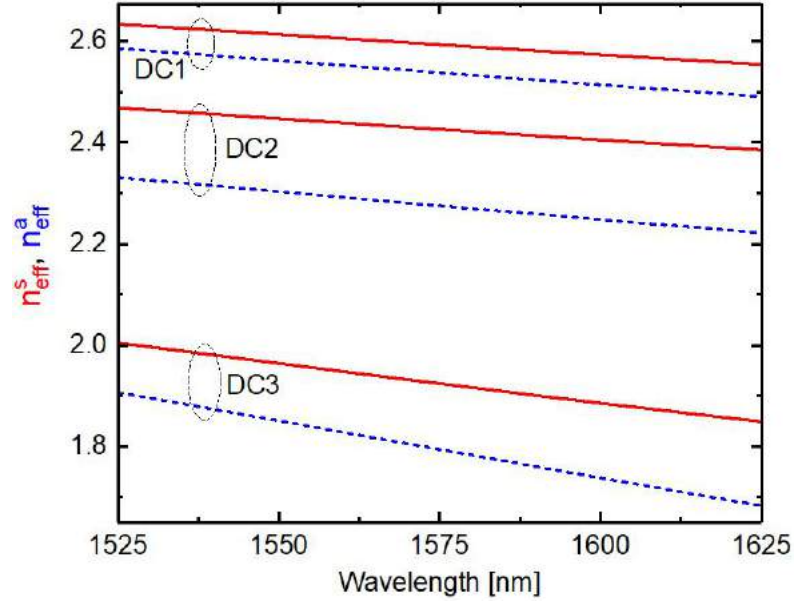
(a)
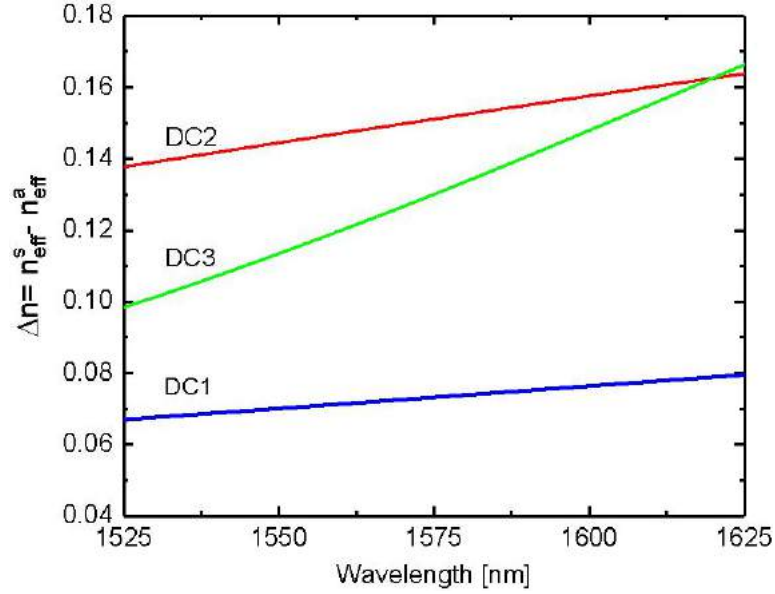
(b)

Figure 2.11: (a) n_{eff}^s (solid line) and n_{eff}^a (dashed line) and (b) Δn calculated for three DC geometries; DC1 (W = 550 nm, h = 150 nm), DC2 (W = 350 nm, h = 100 nm), and DC3 (W = 350 nm, h = 0 nm). The calculations are carried out for TE-polarization and for fixed H = 220 nm and G = 150 nm.

where

$$\Delta n_g(\lambda) = n_g^s(\lambda) - n_g^a(\lambda) = \Delta n(\lambda) - \lambda \frac{d}{d\lambda}[\Delta n(\lambda)] \qquad (2.11)$$

is the *differential group index* of DC supermodes. This infers that if a DC is designed such that $\Delta n_g \to 0$ over a range of wavelength, it exhibits wavelength independent transmission characteristics within the band. This is in fact similar to the design of zero
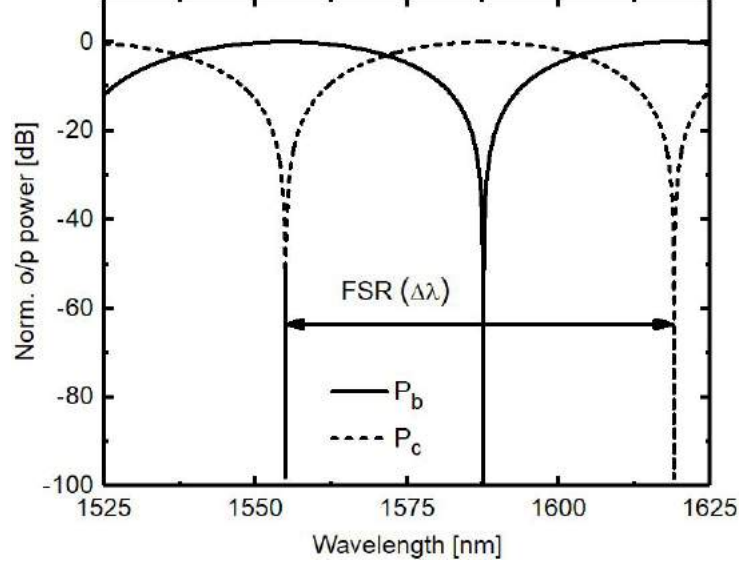
Figure 2.12: Typical transmission characteristics at the output ports of a DC of length $L_{DC} = 25$ μm and cross-section corresponding to DC1 (W = 550 nm, h = 150 nm, $G = 150$ nm, $H = 220$ nm).

differential group delay (DGD) in multi-core fiber as proposed earlier [104] and [105].

2.2.3   Condition for Wavelength Independent Coupling

A wavelength independent DC (WIDC) is characterized by $\Delta n_g(\lambda) \sim 0$ (zero dispersion) for which FSR ($\Delta\lambda$) $\to \infty$. In other words, using Eq. 2.5 we can write:

$$\frac{d\kappa(\lambda)}{d\lambda} = -\frac{\pi}{\lambda^2}\Delta n_g(\lambda) \sim 0 \qquad (2.12)$$

Hence the condition for a WIDC is as follows:

$$\boxed{\Delta n_g(\lambda) = 0 \Rightarrow \quad \kappa(\lambda) \text{ constant for all } \lambda\text{s}} \qquad (2.13)$$

This means that coupling strength κ is wavelength independent for any non-dispersive DC geometry over the entire range of operating wavelengths.

In order to find out the optimized WIDC geometries we first evaluated the geometry dependent values of Δn_g by varying the values of W and h (ensuring single-mode guidance in TE-like propagation at $\lambda \sim 1550$ nm), keeping constant values of $H = 220$ nm and $G = 150$ nm. A contour plot of Δn_g as a function of W and h shown
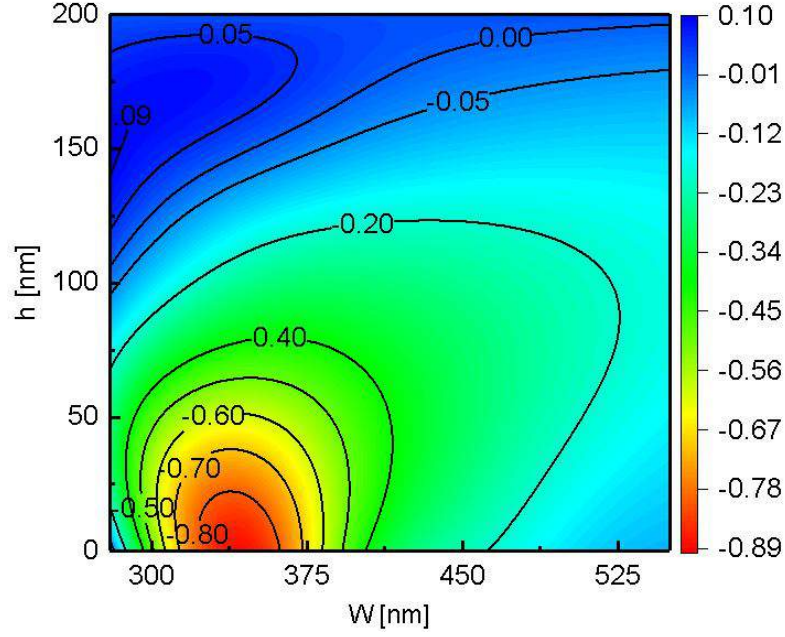
Figure 2.13: Contour plot of Δn_g in W - h plane calculated for $H = 220$ nm, $G = 150$ nm and TE polarization at $\lambda = 1550$ nm.

in Fig. 2.13 reveals that a DC can be indeed designed and fabricated with $\Delta n_g \to 0$ and $FSR \to \infty$ (refer Eq. 2.10 and Figure 2.12). Thus one can optimize the design parameters of a WIDC operating over a broad wavelength range for which Δn_g can be considered non-dispersive.

Fig. 2.14(a) shows the calculated Δn_g as a function of wavelength (1525 nm $\leq \lambda \leq$ 1625 nm) for a DC design DC4 ($W = 375$ nm, $H = 220$ nm, $h = 160$ nm, $G = 150$) along with DC1, DC2, and DC3 (design parameters given earlier). Among four designs, Δn_g variation for DC4 is relatively small, around zero ($-0.02 \leq \Delta n_g \leq +0.02$) within the given wavelength range and it is likely to fulfill the design of a WIDC. Again, Δn_g is relatively large and highly dispersive for DC3 ($0.75 \leq |\Delta n_g| \leq 1.03$); the design can be used for a wavelength dependent DC (WDDC). Nonetheless, κ plays an important role in determining the length of a WIDC or WDDC for the desired values of coupling co-efficients t and k. As given in Eq. 2.13, the value of $\kappa(\lambda)$ must remain constant over the wavelength range of interest for WIDC operation (DC4) and it should be reasonably large for the sake of compact footprint of the device (lower value of L_{DC}). Figure 2.14(b) shows the estimated values $\kappa(\lambda)$ for all the above DC geometries (DC1-DC4). As expected, $\kappa(\lambda)$ is a strong function of λ for DC3, whereas it is nearly wavelength independent for DC4. Moreover, using Δn_g plot in Figure 2.13 and Eq.

33
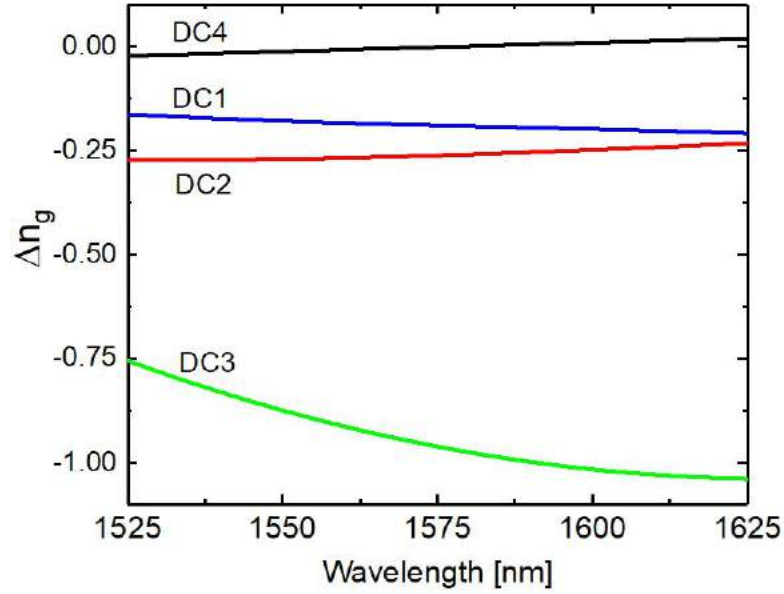
(a)
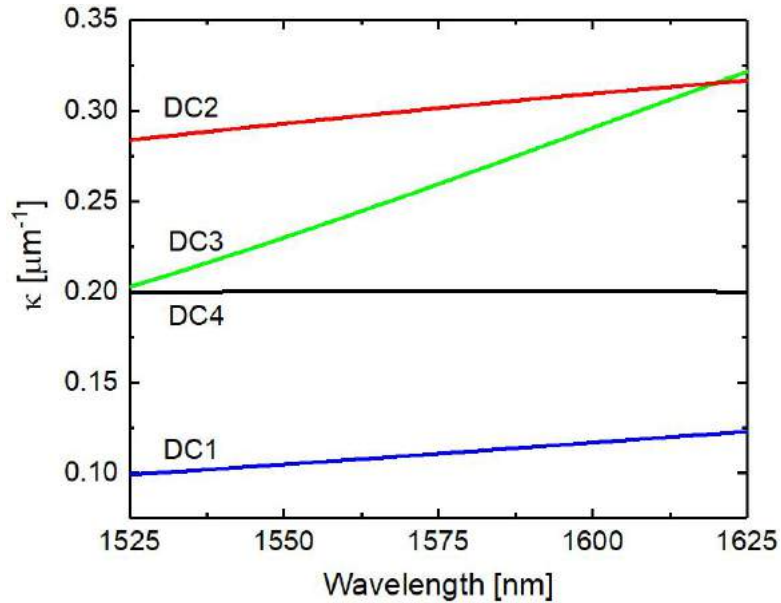
(b)

Figure 2.14: Calculated (a) Δn_g and (b) κ as a function of wavelength for four different DC geometries: DC1 with $W = 550$ nm, $h = 150$ nm; DC2 with $W = 350$ nm, $h = 100$ nm; DC3 with $W = 350$ nm, $h = 0$ nm; and DC4 with $W = 375$ nm, $h = 160$ nm. In all cases $H = 220$ nm, $G = 150$ nm and calculated for TE-polarization.

2.12 one can estimate the tolerance in design parameters (W and h) for which the κ is nearly wavelength independent. In other words, a ± 30 nm variations in DC4 geometry ($W = 375$ nm, $h = 160$ nm) introduce a maximum of $\pm 5\%$ change in power splitting ratio over the entire wavelength range of operation.
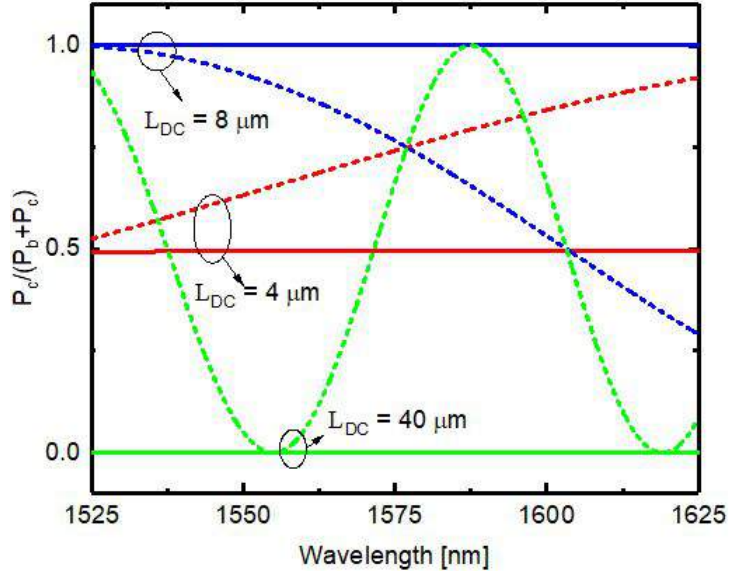
Figure 2.15: Power splitting ratio calculated at cross port ($P_c/(P_c + P_b)$)) as a function of wavelength for the designs of DC3 (dashed line) and DC4 (solid line) for three different device lengths ($L_{DC} = 4$ μm, 8 μm, 40 μm).

Figure 2.15 shows the power splitting ratio (fraction of output power at the cross-port, $P_c/(P_c + P_b)$) of DC3 (dashed lines) and DC4 (solid lines) against λ for three different coupler lengths ($L_{DC} = 4$ μm, 8 μm, and 40 μm). As expected, DC4 design (WIDC) offers nearly wavelength independent transmission characteristics for all lengths and its 3-dB coupling length is only 4 μm, which is acceptable for the development of compact integrated silicon photonics circuits for broadband operations. On the other hand, the DC3 design is highly wavelength dependent which may be useful for sensing [85] and WDM application. A dispersive DC based 1×4 wavelength de-multiplexer has been presented in Appendix A. It is worth mentioning here that DC designs with shallower etched rib waveguides ($h \rightarrow H$) should be avoided for a WIDC design, as the waveguide bend loss becomes enormously high for lower modal confinements within rib waveguide structures. This has been confirmed by calculating mode-field distributions and bend-induced loss estimations.

2.2.4   S-bend Design

As discussed in the previous section, a WIDC can be designed with relatively shallower etched coupled waveguides with parameters corresponding to DC4. However,

designing the access waveguides with S-bend structures (see Figure 2.1(a)) is somewhat critical as one needs to take care of bend-induced losses and additional couplings between the input/output access waveguides. Typically, the S-bend waveguides are designed by connecting equal arc lengths taken from externally touching two identical ring waveguides of radius R. Thus the bending loss and coupling between two access waveguides (both input and output sides) can be analyzed by the use of geometrical top view as shown in Figure 2.16.
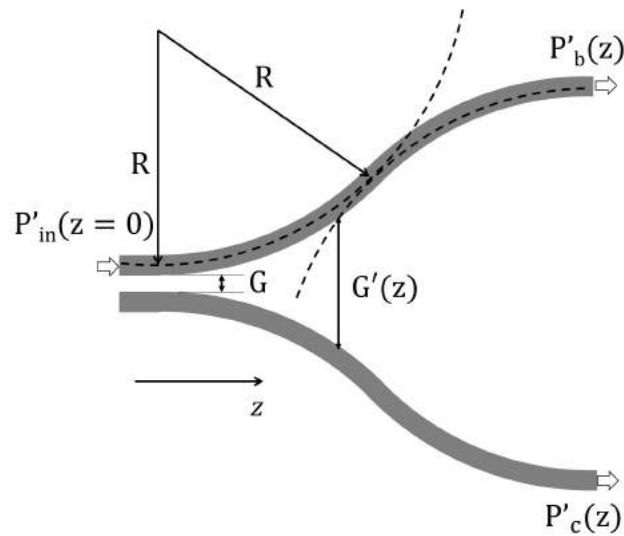
Figure 2.16: Geometrical top view of the S-bend and branching region of approach waveguides of DC.

Bend Induced Loss

Though the performance of a shallower etched parallel coupled rib waveguides (DC4) is described earlier as WIDC, it is also important to ensure the wavelength independent bend induced losses and couplings in the coupled S-bend waveguide regions. Figure 2.17 shows the calculated (using Lumerical MODE Solutions solver) losses per $90°$ bend as a function of bending radius R for three different wavelengths ($\lambda =$ 1525 nm, 1575 nm, 1625 nm). For shorter bending radii, longer wavelengths exhibit higher bending losses. However, for $R > 90$ μm, the bending losses are negligibly small and nearly wavelength independent. In case of deeply etched waveguides (DC4), the bend loss for $R \sim 5$ μm is calculated to be in the order of $\sim 10^{-2}$ dB/cm for 1525 nm $\leq \lambda \leq$ 1625 nm.
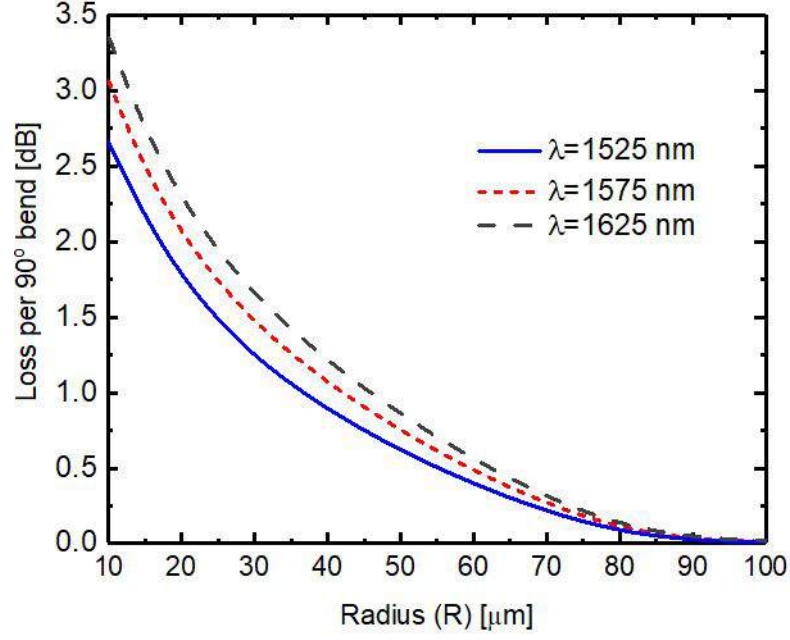
Figure 2.17: Loss per 90° bend for a waveguide of $W = 375$ nm, $h = 160$ nm and $H = 220$ nm as a function of bending radius R calculated for three wavelengths.

Bend Induced Coupling

In presence of bend induced coupling the bar- and cross-port powers in Eq.2.5 can be modified as:

$$P_b(\lambda) = P_{in} \ \cos^2\left[\kappa(\lambda)L_{DC} + C_{bend}(\lambda)\right] \tag{2.14a}$$

$$P_c(\lambda) = P_{in} \ \sin^2\left[\kappa(\lambda)L_{DC} + C_{bend}(\lambda)\right] \tag{2.14b}$$

where $C_{bend}(\lambda)$ is the correction term which accommodates the effective wavelength dependent bend induced coupling at both sides of the DC. Thus the condition for WIDC in Eq. 2.13 has to be redefined as:

$$\boxed{\kappa(\lambda) \ \textbf{constant} \ \forall \ \lambda\text{s} \ \ \text{and} \ \ C_{bend}(\lambda) \ \textbf{constant} \ \forall \ \lambda\text{s}} \tag{2.15}$$

The couplings in both side bend regions of a DC are to be accounted for estimating the value of effective coupling length L_{DC}^{eff}, which can be expressed as:

$$L_{DC}^{eff} = L_{DC} + 2\Delta L_b \tag{2.16}$$
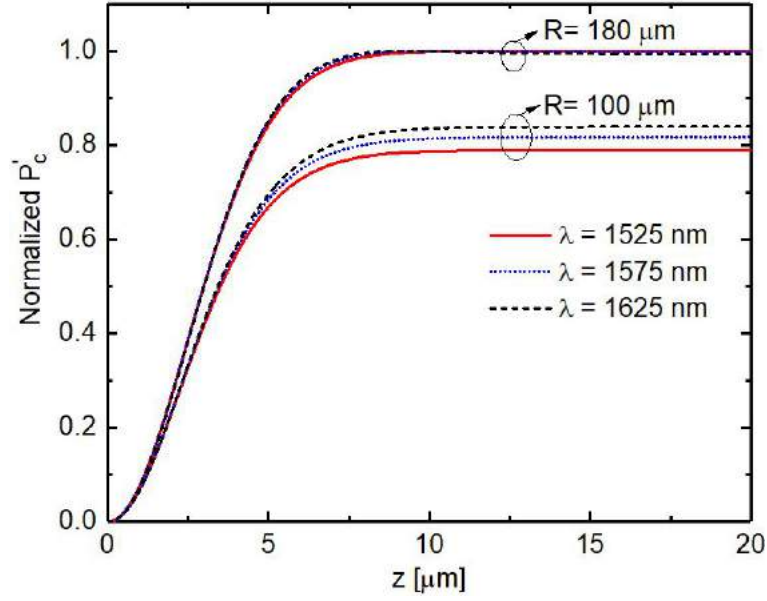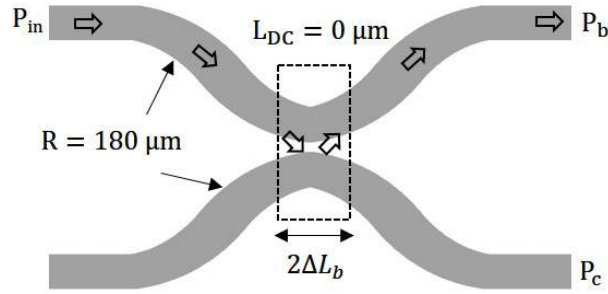
Figure 2.18: (a) Power coupling to cross port as a function of bend induced coupling length (z) for two different bend radii ($R = 100\,\mu$m and $180\,\mu$m) and for the given WIDC geometry (DC4); (b) schematic illustration of $2\Delta L_b \equiv 2L_c$ with $R = 180\,\mu$m hence power couples back to bar port.

where ΔL_b accommodates coupling in one side of the bend region and depends on DC geometry and bending radius. This can be modeled using the expression given for ring resonator in Ref. [85] :

$$\Delta L_b = \frac{1}{\Delta n(G, \lambda)} \int_{z=0}^{z=R} \Delta n\left(\lambda, G(z')\right) dz \qquad (2.17)$$

where the gap between waveguides at any z in the branching region $G'(z)$ can be calculated using the geometry given in Figure 2.16:

$$G'(z) = G + 2\left(R - \sqrt{R^2 - z^2}\right) \qquad (2.18)$$

For a low bending loss ($R > 100$ µm), shallow etched DC geometry (DC4), ΔL_b may be significantly higher than that of 3-dB length and hence the power splitting ratio at the output ports deviates from the expected values. We first estimated the $\Delta n(\lambda, G'(z))$ in the DC branching region along z for a fixed DC cross-section (DC4) and for different R, which is further used to calculate the normalized coupled power P'_c (see Figure 2.16). The calculated results for $R = 100$ µm and 180 µm are shown in Figure 2.18(a). It indicates again that the power couplings for lower values of R are wavelength dependent. However, higher values of R exhibit longer interaction lengths (z) but tending towards wavelength independent couplings. We find nearly wavelength independent and 100% cross coupling only in one side of DC4 design with R = 180 µm. Thus it is possible to design a WIDC with nullified bend-induced couplings in both side access waveguides, as they jointly provide two times cross coupling length of the DC ($2\Delta L_b \equiv 2L_c$). This has been shown schematically in Figure 2.18(b) and can be expressed mathematically as:

$$\cos^2\left(C_{bend}(\lambda)\right) = 1 \;\; \text{and} \;\; \sin^2\left(C_{bend}(\lambda)\right) = 0 \tag{2.19}$$

WIDC with compact S-bends

The WIDC design including its access S-bend waveguides discussed above has relatively large footprint because of larger bending radius ($R = 180$ µm). Moreover, the proposed shallower etched waveguide design needs to be integrated for a compact designs of functional MZI, MRR, etc. which demand for a deeply etched waveguide geometry with tightly confined guided modes. A 3D scheme of the proposed WIDC for compact silicon photonics devices has been shown in Figure 2.19. In this design, the shallow-etched slab of the WIDC is adiabatically tapered towards access S-bend waveguides to reduce its insertion loss, ensuring the effective L_{DC} is unchanged. This is possible by two-step etching process. The first etching is for the shallow etched waveguide definition compatible to WIDC design and then the second etching to facilitate deeply etched waveguide for sharper bends masking WIDC appropriately. The fabrication process steps has been explained in section 2.3.1.

Alternative to the WIDC geometry discussed so far ($W \sim 350$ nm and $h \sim 160$ nm), one can choose another deeply etched WIDC using the contour plot of Δn_g given in
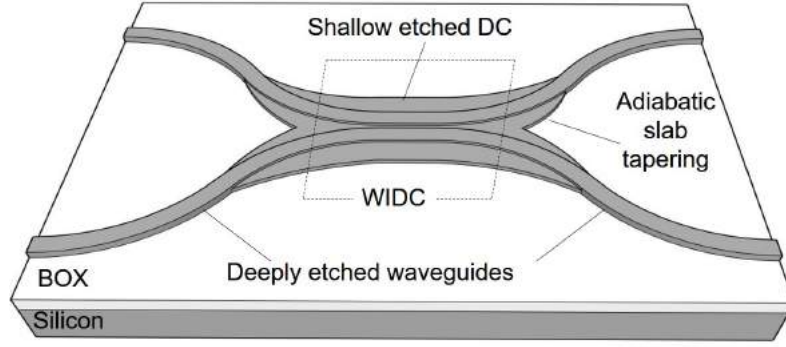
Figure 2.19: 3D scheme of the proposed WIDC design with deeply etched access waveguides for compact silicon photonics devices.

Figure 2.13. One such WIDC geometry is $W = 310$ nm, $h = 110$ nm, $G = 150$ nm and $H = 220$ nm. The calculated κ (~ 0.35) and Δn_g ($|\Delta n_g| < 0.6$) are found to be nearly wavelength independent as shown in Figure 2.20(a). The simulated wavelength

(a)

(b)
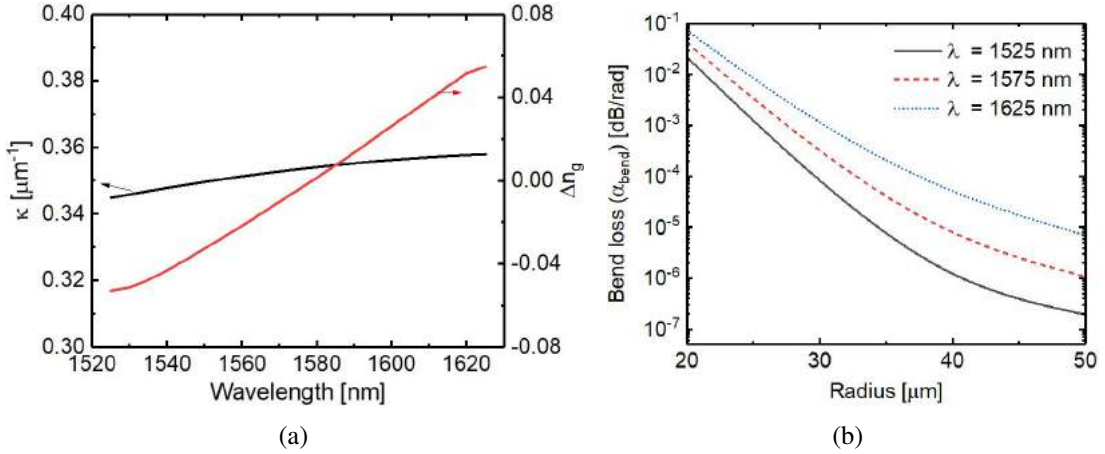
Figure 2.20: (a) Wavelength dependent κ and Δn_g calculated for a relatively deeply etched WIDC geometry of $W = 310$ nm and $h = 110$ nm.

dependent bend loss (α_{bend}) of the waveguide as a function of bend radius is shown in Figure 2.20(b). It is clear from the plot that, for $R \geq 30$ μm the wavelength dependent bend loss is negligibly small, whereas for $R < 30$ μm bend loss is considerably high and wavelength dependent, since the modal confinement is relatively weaker at higher wavelengths ($\lambda \sim 1625$ nm). However, this particular geometry is less fabrication tolerant compared to DC4 ($W = 375$ nm, $h \sim 160$ nm). A ± 10 nm variation in W or h may introduce wavelength dependency ($|\Delta n_g| > 0.06$) in the transmission characteristics. Hence, for broadband power splitters we fixed the WIDC geometry as that of DC4. However, later in chapter 3 we have discussed compact microring

resonators based on this particular WIDC geometry with relatively deeply etched ($h \sim$ 110 nm) waveguides.

2.3 Experimental Results and Discussion

The proposed WIDC design with a set of optimized design parameters ($W \sim 375$ nm, $h \sim 160$ nm, $G \sim 150$ nm and $H = 220$ nm) has been experimentally demonstrated using in-house facilities available at IIT Madras. The devices were fabricated on a commercially available 220-nm device layer SOI (specifications are given in Appendix B) using electron beam lithography (EBL) and inductively coupled plasma reactive ion etching (ICPRIE). Both wavelength dependent and independent 2×2 DCs of various device lengths (L_{DC}s) were prepared in separate samples. The detailed fabrication process flow and characterization results are discussed in the following sections.

2.3.1 Device Fabrication

Typical mask layout (GDS II format designed in RAITH Nanosuit) of DCs along with reference waveguide and alignment markers is shown in Figure 2.21. For stitch-free patterning of longer waveguides (2-3 mm) we used fixed beam moving stage (FBMS) exposure scheme available with RAITH 150 TWO system. However, gratings and tapers were defined as conventional elements (CE) where the electron beam expose the elements within the pre-defined write field (WF) area [99]. Both input and output waveguides were terminated with grating couplers (GC) for efficient light coupling. The grating region (gratings of $\sim$610 nm period and 50% duty cycle) has been defined over 12 µm $\times$12 µm area and tapered towards the waveguide over a length of 100 µm. More detailed design parameters of GCs are found in [99, 106]).

The fabrication process flow is schematically given in Figure 2.22. We prepared a few SOI samples using standard silicon cleaning procedures as outlined in Appendix B. The samples were then coated with negative tone e-beam resist (HSQ -Hydrogen silsesquioxane) with spin parameters as listed in Table 2.1. The choice of negative resist HSQ (XR-1541) is to minimize design complexity and patterning time by ex-
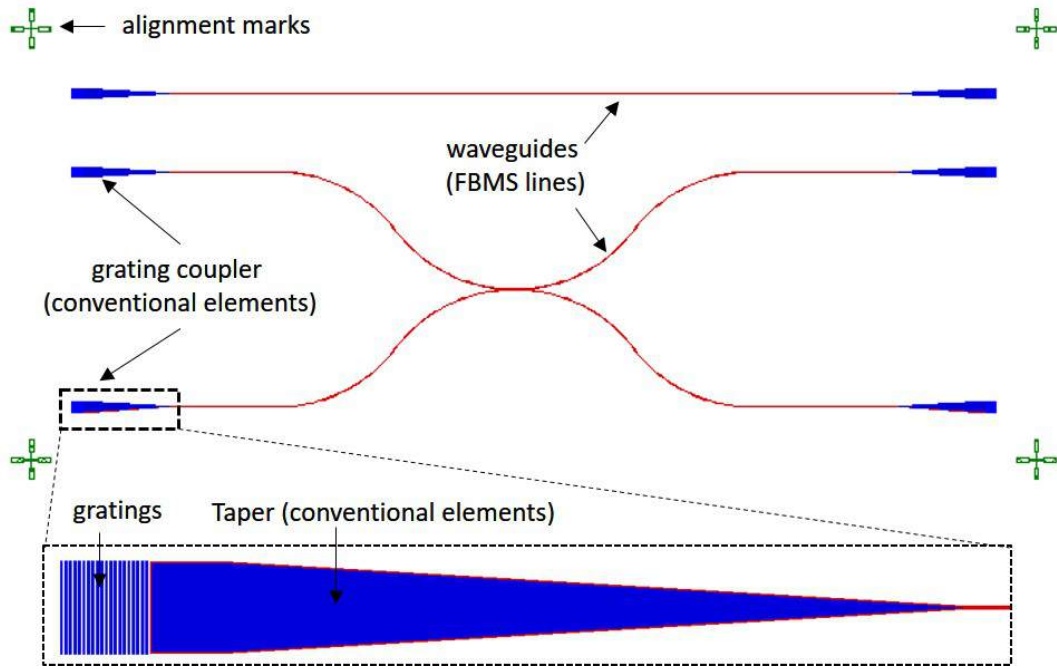
Figure 2.21: Typical mask layout of DCs along with reference waveguide and alignment markers (designed using RAITH Nanosuit). The GC region (both gratings and taper) and waveguides are defined using conventional elements and FBMS lines respectively. A zoomed-in view of the GC is shown in inset.

posing only the waveguide region. Subsequently, the mask patterns were transferred

Table 2.1: Spin coat parameters for HSQ electron beam resist optimized for two different uniform thicknesses.

Step 1 (spread)	Step 2 (coat)	Thickness
Speed: 100 rpm Acceleration: 100 rpm/sec Time:10 sec	Speed: 3000 rpm Acceleration: 1500 rpm/sec Time:30 sec	100 nm

to the resist using EBL (Raith 150 TWO System) with optimized e-beam parameters as given in Table 2.2. After lithography, the samples were developed using commercially available MF319 (Microposit $^{®}$) developer solution for 6 min and then baked (post-bake) at 300 °C for 3 min. The patterns were subsequently transferred to silicon using SF_6:CHF_3 chemistry in inductively coupled plasma environment. Optimized IC-PRIE (Oxford PlasmaLab System 100) chemistry listed in Table 2.3 has been used for nearly smooth and vertical sidewalls. The devices were etched for ~ 60 nm etch depth ($h = 160$ nm) in 8 seconds.
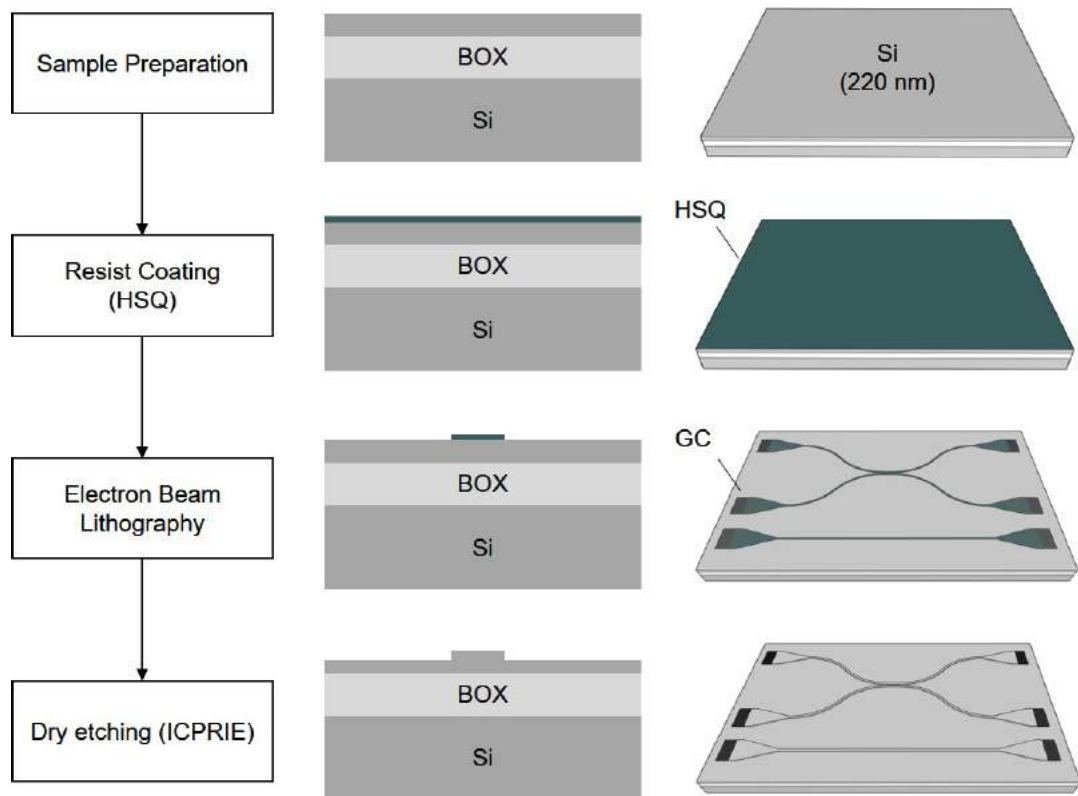
Figure 2.22: Fabrication process flow (left) with cross-sectional 2D (middle) and 3D schematics (right). GC - grating coupler, HSQ - Hydrogen silsesquioxane, ICPRIE - inductively coupled plasma reactive ion etching.

Table 2.2: Optimized EBL parameters in Raith 150 TWO system for conventional patterning and FBMS patterning over HSQ.

System Parameters	Patterning parameters
Acceleration Voltage = 20 kV Aperture = 20 μm Write Field = 100 μm × 100 μm Working distance = 10 mm	Max CE dose = 240 μC/cm^2 FBMS dose = 350 μC/cm^2 Area step size = 10 nm Developing time (MF319) = 6 min

Table 2.3: Optimized ICPRIE parameters silicon etching.

Parameter	Value
Gas flow rate	SF_6:CHF_3::5:18 sccm
ICP power	1000 W
RF power	30 W
Pressure	15 mTorr
Temperature	20 °C
Etch rate	540 nm/min

A SEM image of fabricated WIDC with input/output GCs is shown in Figure 2.23. The total device length is around 1-2 mm. Separate SEM images of top view of DC region, tilted view of DC region, tilted view of cleaved end facet showing the sidewall angle, and tilted view of bend waveguide are shown in Figures 2.24(a) - 2.24(d) respectively. The side wall angle is nearly vertical ($\sim 95°$) with roughness in the order of ~ 10 - 20 nm (see Appendix B). SEM images of the GC region and a zoomed-in view of the gratings are shown in 2.24(e) and 2.24(f) respectively. Table 2.4 shows the designed
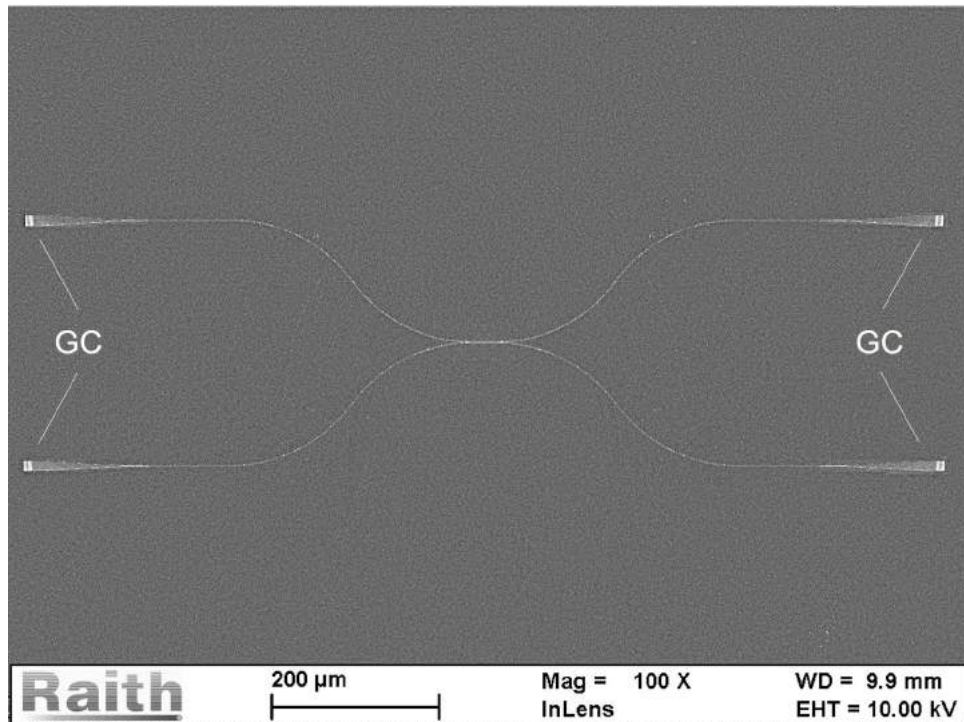
Figure 2.23: SEM image of the fabricated WIDC with input/output grating couplers.

and measured device dimensions of WIDC and DC regions. A ± 20 nm variation in design parameters were measured which may be attributed to fabrication induced errors (proximity effects, electron-beam current variations, etching non-uniformity, etc.).

Adiabatic Slab Tapering

The proposed compact WIDC design with deeply etched access waveguides discussed in section 2.2.4 was fabricated in two-step etching process. In the first step, devices with shallow etched rib waveguides of 160 nm thick slab (etch depth $\sim$ 60 nm) were fabricated as discussed in the previous section. Without removing the HSQ mask over
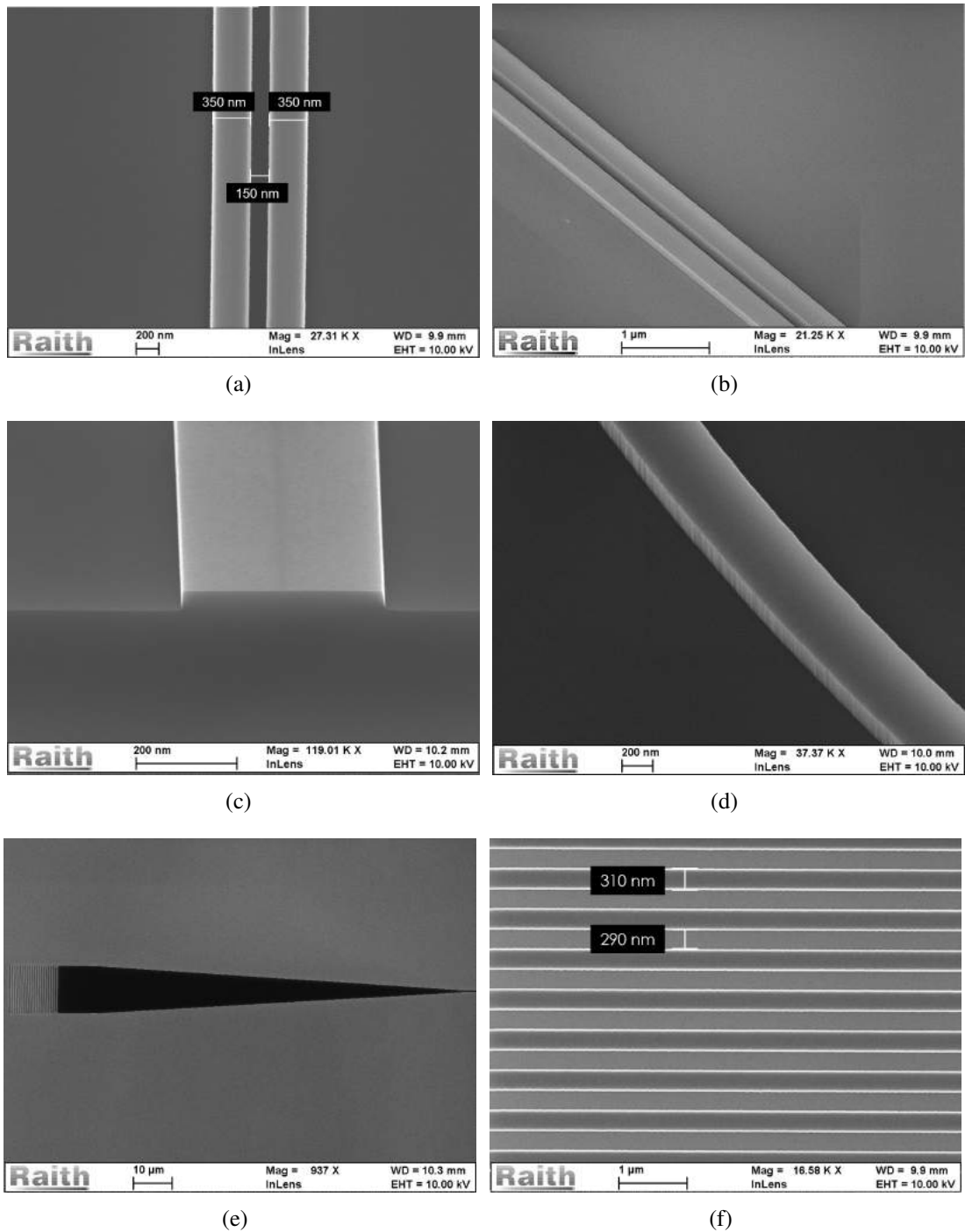
Figure 2.24: SEM images of (a) top view of DC region, (b) tilted of view DC region, (c) cleaved end-facet of waveguide, (d) tilted view of bend waveguide, (e) input/output grating coupler (GC) and (f) a zoomed-in view of grating region.

the waveguides, a second layer of HSQ has been coated over the sample. The DC and GC masks shown in Figures 2.25(a) and 2.25(b) were critically aligned over the waveguides using the three-point alignment procedure available with RAITH Nanosuite

45

Table 2.4: Designed and measured (using SEM) device dimensions of WIDC and GC.

Parameter	Designed	Measured
Rib width (W)	375 nm	350 ± 20 nm
Etch depth ($H - h$)	60 nm	60 ± 10 nm
Gap (G)	150 nm	150 ± 20 nm
GC period (Λ)	610 nm	610 nm
GC duty cycle (δ)	50%	48-52%

(a)   (b)

(c)   (d)
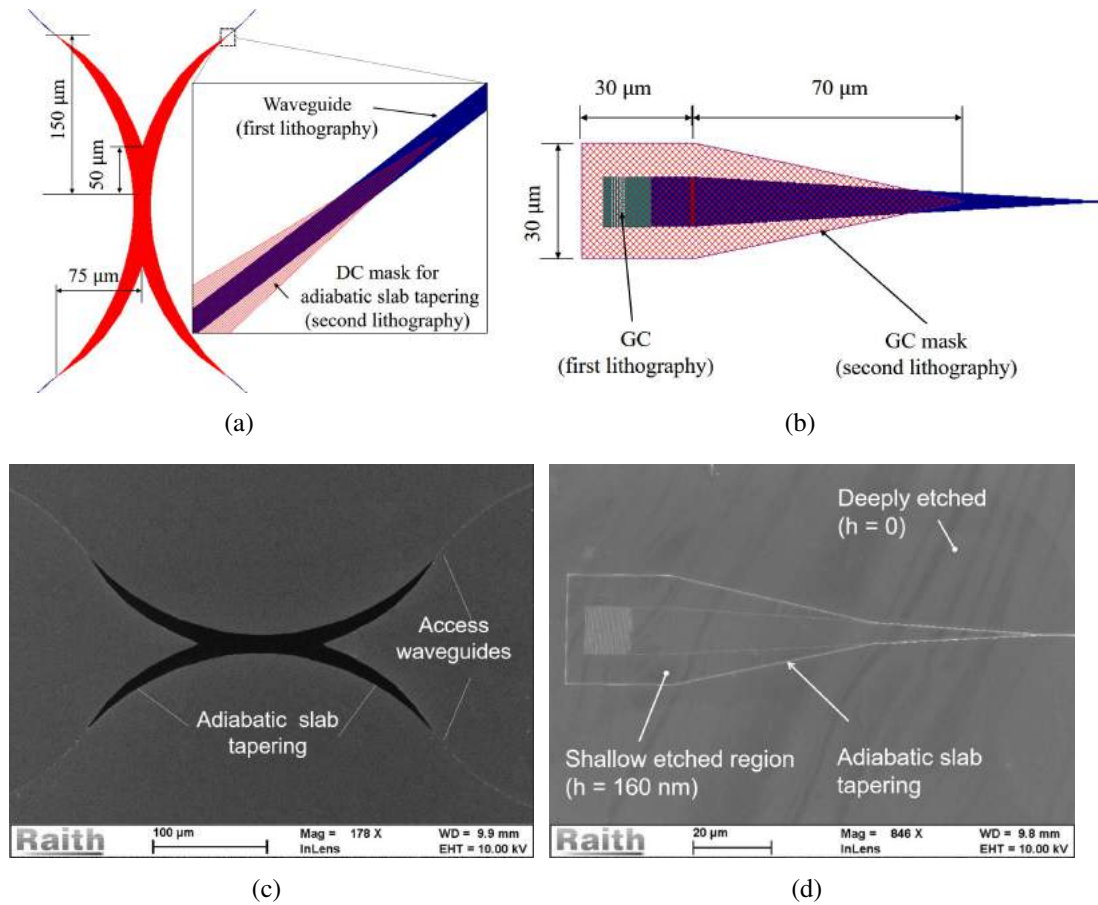
Figure 2.25: (a) and (b) are mask layouts of DC and GC regions respectively for second lithography; (c) and (d) are corresponding SEM images of DC and GC showing the deeply etched access waveguides and adiabatically tapered slab regions.

[107] software. The maximum misalignment was measured to be ≤ 50 nm, due to unavoidable fabrication errors like drift in stage positioning, beam current, etc. The unmasked waveguide slab regions (h = 160 nm) were then deeply etched for zero slab height with the same ICPRIE parameters as listed in Table 2.3. During this step, the

unmasked waveguides were protected by the existing HSQ layer (after first step) over the waveguides. Figures 2.25(c) and 2.25(d) are the SEM images of DC and GC with deeply etched access waveguides and shallow etched adiabatically tapered slab. We later verified that this additional fabrication step neither contribute additional loss nor change the device performance.

A list of fabricated samples are given in Table 2.5. To estimate the value of Δn_g experimentally from the transmission characteristics, we fabricated longer devices of both wavelength dependent (S1) and wavelength independent (S2 and S3) DC geometry. Moreover, WIDC devices are also fabricated in different sample (S3) to validate the reproducibility and tolerance. Cascaded WIDCs in 1×2 configurations are also used to demonstrate broadband 1×4 power splitters.

Table 2.5: Summary of fabricated samples.

Sample	W, h	L_{DC}	Remarks
S1	$W = 500$ nm $h = 130$ nm $G = 150$ nm	50, 100, 500 µm	Wavelength dependent DC to estimate Δn_g
S2	$W = 350$ nm $h = 160$ nm $G = 150$ nm	0, 5, 10,...30 µm 50, 100, 500, 1000 µm	Shorter WIDCs for power splitters and longer WIDCs for Δn_g estimation
S3	$W = 350$ nm $h = 160$ nm $G = 150$ nm	0, 2, 4,...20 µm 50, 100, 500 µm	2×2, 1×4 WIDCs and compact WIDCs

2.3.2 Device Characterization

All the demonstrated devices were characterized using a broadband (1520 nm $\leq \lambda \leq$ 1630 nm) tunable laser source (TLS) and an optical spectrum analyzer (OSA). Both TLS and OSA are inbuilt with Apex-AP2043B high resolution optical spectrum analyzer (OSA). Figures 2.26(a) and 2.26(b) respectively show the schematic and photograph of fiber-optic grating coupler probe station for passive device characterization. The device under test (DUT) is tightly held on a sample holder using a vacuum pump. Light input from TLS is launched directly to the input GC through a single-mode fiber (SMF) and collected from output GC through another SMF and fed to the spectrum
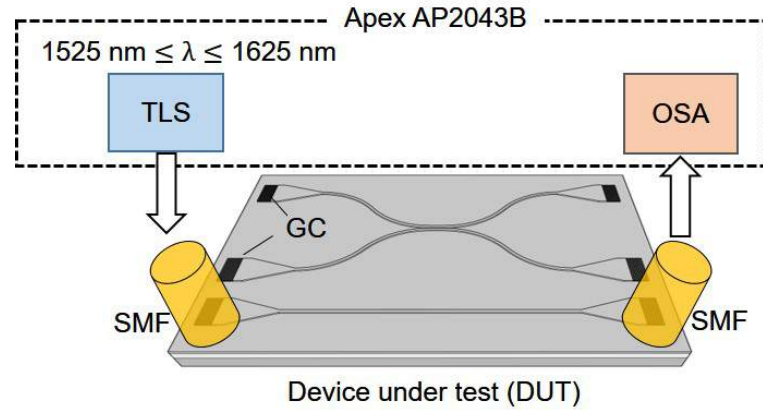
(a)
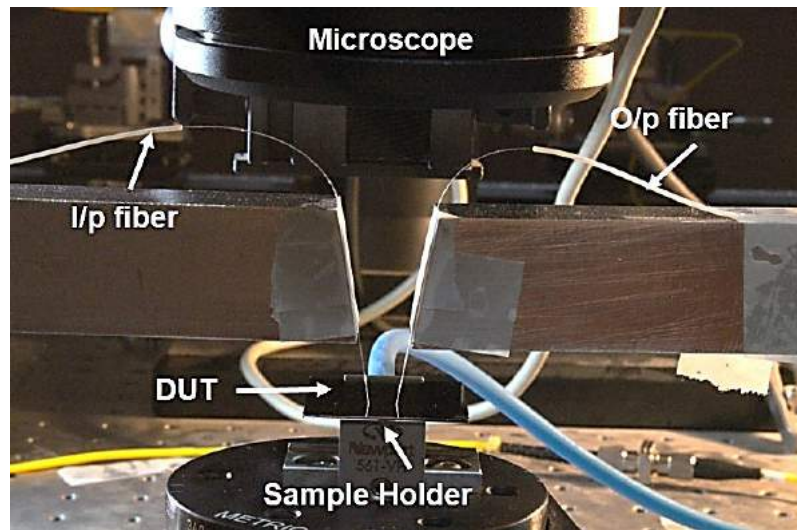
(b)

Figure 2.26: (a) Scheme of characterization setup; (b) photograph of fiber-optic grating coupler probe station. DUT - device under test, TLS - tunable laser source, OSA - optical spectrum analyzer, SMF - single-mode fiber.

analyzer (OSA). Both input and output SMFs are aligned $10°$ vertically to the GCs for maximum coupling efficiency [85]. A microscope is used to precisely align the fibers to the input/output GCs. The input laser power is measured to be ~ 125 μW (-9 dBm) and uniform over 100 nm (1525 nm$\leq \lambda \leq$1625 nm). Figure 2.27 shows the wavelength dependent transmission characteristics of a reference waveguide along with the TLS output spectrum.

Grating Coupler Response

The wavelength dependent transmission characteristics of reference straight waveguides (RWs) terminated with input/output GCs were obtained first which were used

later to normalize transmission characteristics of the WIDCs. However, we observed significant difference in the transmission characteristics of GCs fabricated in the three different sets of samples listed Table 2.5. Figure 2.27 shows the measured transmission
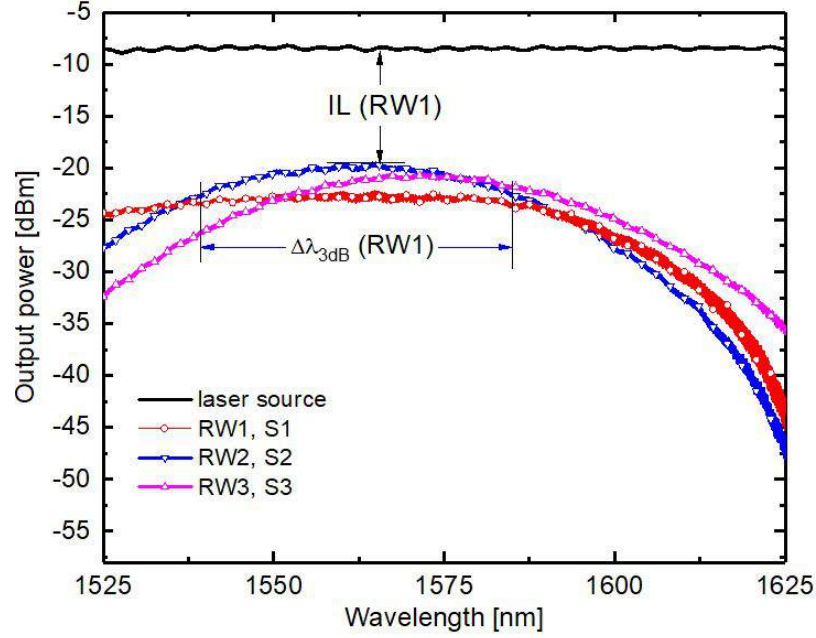
Figure 2.27: Transmission characteristics of different reference waveguides (RWs) fabricated in four different samples (See Table 2.6 for device details) along with the TLS spectrum. $\Delta\lambda_{3dB}$ - 3-dB bandwidth, IL - insertion loss.

characteristics of a few RWs with input/output GCs. The measured 3-dB bandwidth ($\Delta\lambda_{3dB}$) and IL along with design parameters are tabulated in Table 2.6. RW1 (etch depth, $d = 90$ nm) show nearly flat response at lower wavelengths with a 3-dB bandwidth of 74 nm. Note that, the coupling efficiency reduces at longer wavelengths due to relatively large scattering loss. Although RW2 (S2) and RW3 (S3) have the same design parameters, their responses slightly vary from sample to sample. This is attributed to the variation in design parameter due to fabrication errors such as etching non-uniformity, width and duty cycle variations due to proximity effects, device layer thickness variations, etc. Great care must be taken while aligning the fibers with the input/output GCs to maximize the coupling efficiency. RW1 has maximum coupling efficiency at $\lambda \sim 1564$ nm and gives a minimum IL of 11 dB. RW3 gives nearly flat response with $\Delta\lambda_{3dB} \sim 74$ nm and IL~ 14.5 dB. This includes coupling and waveguide (3-mm) loss. Nevertheless, we did not observe much difference in spectra of RWs fabricated in same sample (S2) at different locations (RW1 and RW4)

Table 2.6: $\Delta\lambda_{3dB}$ and IL measured for different RWs with input/output GCs fabricated in four different samples. The design parameters of waveguides and GC are also given: Λ - period of grating, δ - duty cycle, d - etch depth (H-h), $\Delta\lambda_{3dB}$ - 3-dB bandwidth, IL - insertion loss, λ_p - peak wavelength.

#	GC design parameters	$\Delta\lambda_{3dB}$ (Exp.)	Input to output fiber coupling loss (Exp.)
RW1, S1	$\Lambda = 610$ nm $\delta = 0.5$, d = 90 nm	74 nm	~ 14.5 dB $\lambda_p = 1564$ nm
RW2, S2	$\Lambda = 610$ nm $\delta = 0.5$, d = 60 nm	46 nm	~ 11 dB $\lambda_p = 1564$ nm
RW3, S3	$\Lambda = 610$ nm $\delta = 0.5$, d = 60 nm	43 nm	~ 12 dB $\lambda_p = 1572$ nm
RW4, S2	$\Lambda = 610$ nm $\delta = 0.5$, d = 60 nm	45 nm	~ 11 dB $\lambda_p = 1562$ nm

Estimation of Differential Group Index (Δn_g)

To validate our wavelength independent/dependent DC designs and theoretical predictions, we fabricated few test structures of 2×2 DCs. The experimental transmission characteristics of two different test device structures, $D1$ ($W \sim 550$ nm, $h \sim 130$ nm) and $D2$ ($W \sim 350$ nm, $h \sim 160$ nm) each with $L_{DC} = 500$ μm (sufficiently long) were
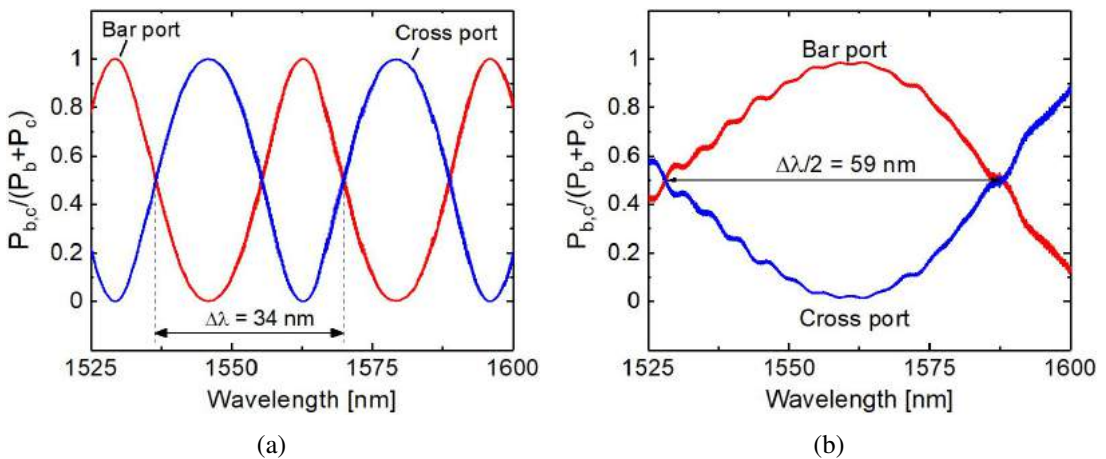
Figure 2.28: Normalized transmission characteristics at bar and cross ports of two dispersive DCs each with $L_{DC} = 500$ μm: (a) $D1$ (S1) and (b) $D2$ (S2). See Table 2.7 for device specifications and Δn_g comparison.

used to estimate the values of Δn_g from experimental results and compared with theoretical calculations (see Fig. 2.13). Figures 2.28(a) and 2.28(b) show the normalized $(P_{b,c}/(P_b + P_c))$ bar port (P_b) and cross port (P_c) transmission characteristics of $D1$ and $D2$ respectively. First, the values of FSR $(\Delta\lambda)$ were extracted from the experimental transmission characteristics (at the bar or cross port) centering at $\lambda \sim 1550$ nm and then they were used to evaluate Δn_g using Eq. 2.10. The experimental results shown in Table 2.7 are consistent with the values corresponding to the evaluated simulation results and Eq. 2.11. Slight deviations may be attributed to the fabrication/measurement related errors in estimating W, h and G. It must be noted that the longer DC lengths were used to estimate Δn_g so that at least one FSR could be captured within our available wavelength range (1525 nm $\leq \lambda \leq$ 1625 nm) used for the experiments. Longer the FSR of a DC, better is the wavelength independent performance one may expect for its shorter lengths.

Table 2.7: Comparison of experimental and theoretical values of Δn_g.

Device#	H [nm]	W [nm]	h [nm]	G [nm]	L_{DC} [μm]	$|\Delta n_g|$ (Exp.)	$|\Delta n_g|$ (Theo.)
$D1$ (S1)	220	550	130	150	500	0.14	0.155
$D2$ (S2)	220	350	160	150	500	0.036	0.042
$D3$ (S3)	220	350	160	150	1000	0.051	0.042

WIDC based 2×2 Power Splitters

Since device $D2$ and $D3$ exhibits a large FSR ($\Delta\lambda >$100 nm) and smaller group velocity mismatch between supermodes ($|\Delta n_g|$ = 0.036), we have studied it further for shorter lengths to obtain desired wavelength independent power splitting ratio (0 to 1), over a wavelength span of 100 nm (1525 nm $\leq \lambda \leq$ 1625 nm). We first measured the power splitting ratios at the cross port of WIDCs for various DC lengths ($L_{DC} : 0 - 30$ μm, from S1 and S2) at $\lambda \sim 1550$ nm. Experimentally observed power splitting ratio at the cross port defined by $P_c/(P_b + P_c)$, where P_b and P_c are in linear scale, at $\lambda = 1550$ nm as a function of L_{DC} (0 μm $\leq L_{DC} \leq$ 30 μm) has been shown in Figure 2.29. The
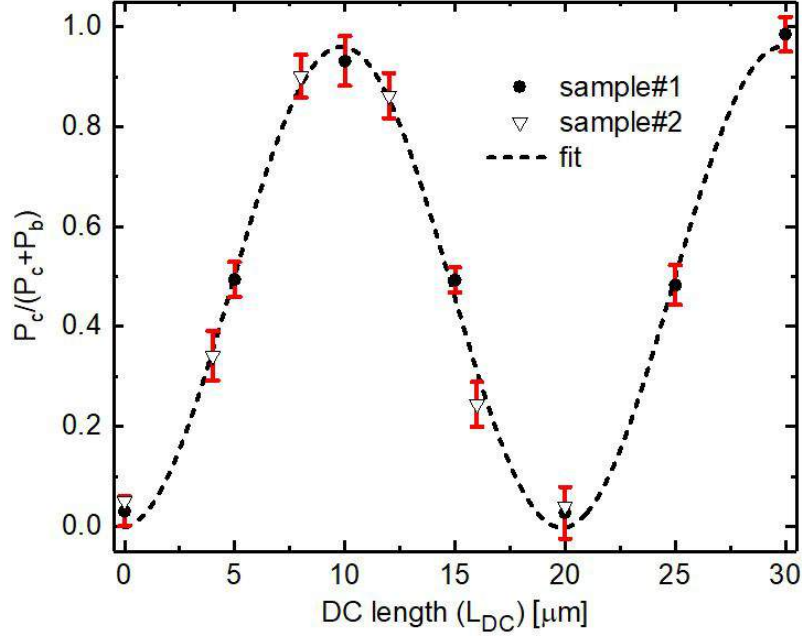
Figure 2.29: Power splitting ratio measured at cross port of WIDCs (fabricated in S2 and S3) at $\lambda = 1550$ nm as a function of L_{DC}.

measured values are fitted with theoretical curve which goes well with the analytical expressions given in Eq. 2.5. However, we have observed $2 - 5\%$ variation (error bars in Figure 2.29) in power splitting ratio because of the uncertainty in coupling efficiency between input/output single-mode fibers and GCs. It is interesting to note that for $L_{DC} = 0$ µm, the launched power appears only at bar port. This ensures coupling in S-bend access waveguides ($R = 180$ µm) exhibiting two times full power couplings between cross and bar ports which satisfies well with the theoretical prediction (though actual values of W, h, G might have varied slightly after fabrication). Again, the measured 3-dB coupling length is 5 µm, which is found to be a little longer than corresponding simulation result (4.0 µm). This $\sim 20\%$ difference in 3-dB coupling length may be attributed to the fabrication induced errors in the design parameters (see Table 2.3.1) and as well as the coupling in the bend regions. The power splitting ratio of a DC may be obtained more accurately using MZI configuration as described by Bogaerts et al. [69].

Figure 2.30 shows the cross port and bar port transmission characteristics of a 2×2 WIDC of length $L_{DC} = 5$ µm (S2), when input is launched at one of the input GCs. Both the output powers are nearly equal (3-dB power splitter) and follows the response of the neighboring reference waveguide. This confirms the wavelength independent
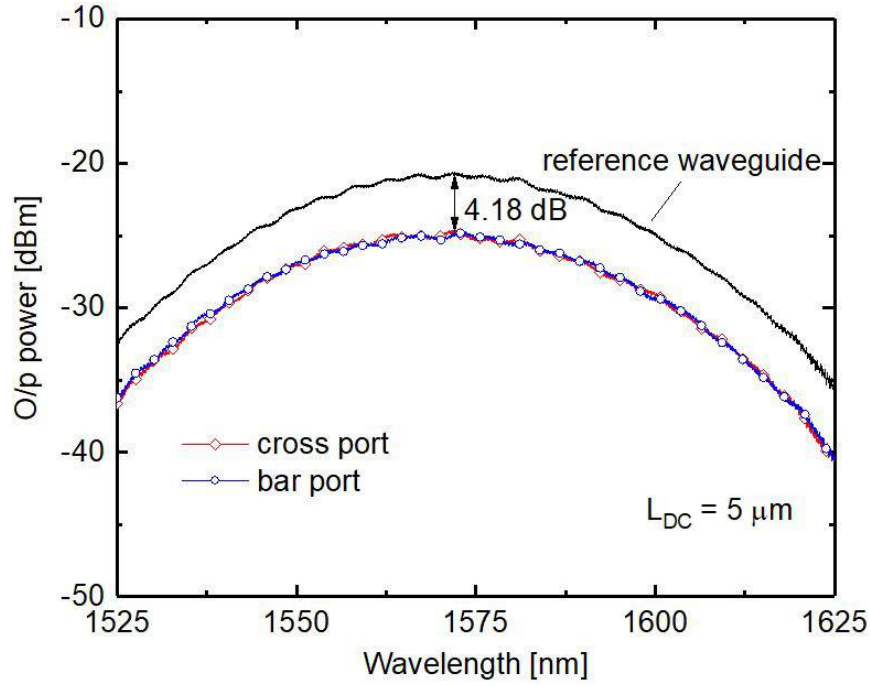
Figure 2.30: Measured wavelength dependent transmission characteristics at the output ports (P_b and P_c) of a 3-dB WIDC ($L_{DC} = 5$ μm, S2) and a reference waveguide fabricated very close to the WIDC.

performance of fabricated WIDC which is closely agreeing with the theory. The device exhibits nearly wavelength independent insertion loss of 1.18 dB.

We further investigated the power splitting characteristics of WIDCs in terms of coupling length L_{DC} (S2 and S3). Figures 2.31(a) - 2.31(f) show normalized power splitting ratios at the bar- and cross-ports as a function of wavelength for $L_{DC} = 0$ μm, 5 μm, 10 μm, 12 μm, 15 μm and 20 μm. As expected, all the devices are exhibiting nearly wavelength independent performances with non-uniformity in splitting ratio $<$ $\pm 5\%$ over the entire wavelength range. Note that, the non-uniformity in the power splitting characteristics $L_{DC} = 15$ μm (3-dB) WIDC is $> 5\%$ which is attributed to the poor response of GCs of that particular device.

Transmission Characteristics of Compact WIDCs

As discussed earlier (also see Figure 2.19), we carried out second etching by protecting the DC region and rib of the access waveguides by HSQ mask as shown in Figure 2.25(c). The normalized wavelength dependent transmission characteristics of a WIDC
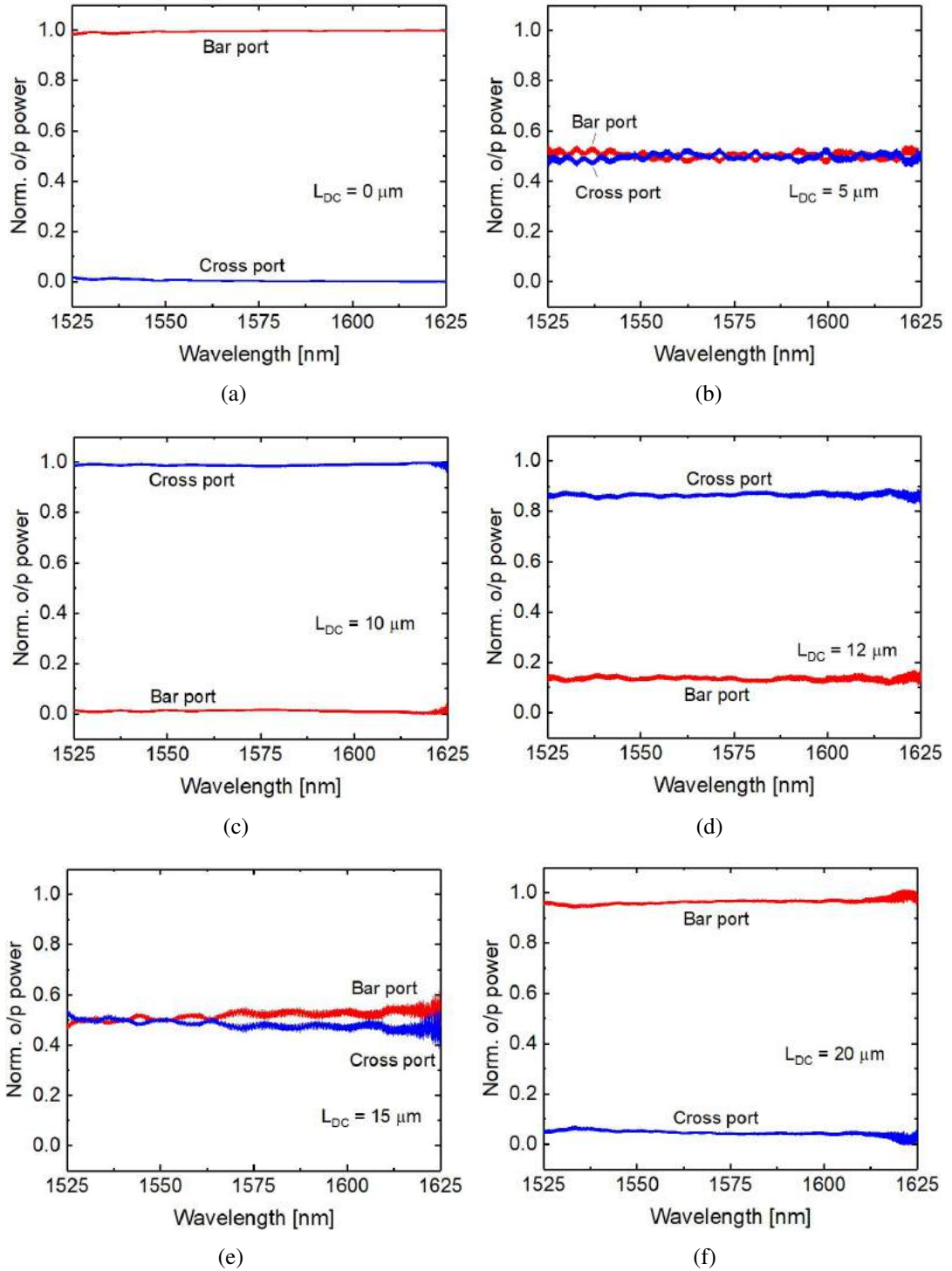
Figure 2.31: Normalized transmitted powers at cross- and bar-ports as a function of wavelength for (a) $L_{DC} = 0$ μm, (b) $L_{DC} = 5$ μm, (c) $L_{DC} = 10$ μm, (d) $L_{DC} = 12$ μm, (e) $L_{DC} = 15$ μm and (f) $L_{DC} = 20$ μm.

with shallow etched access waveguides, a WIDC with deeply etched access waveguides, and a deeply etched DC device have been shown in Figure 2.32. All the three devices have same $L_{DC} = 8$ μm and the transmission characteristics were normalized with their
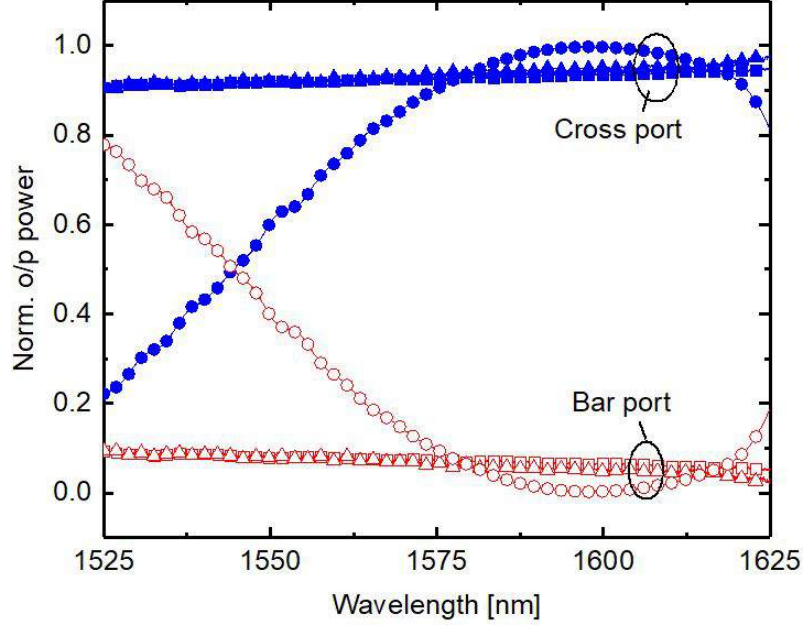
Figure 2.32: Normalized wavelength dependent transmission characteristics at bar and cross ports of a WIDC without deeply etched access waveguides (squares), a WIDC with deeply etched access waveguides (triangles) and a deeply etched DC (circles).

respective reference waveguides. It is evident that the normalized transmission characteristics of WIDCs with and without deeply etched access waveguides are identical; a little deviation in longer wavelength region may be due to bend induced dispersion in deeply etched waveguide. Normalized transmitted power of the deeply etched DC is found to be wavelength dependent in spite of its shorter L_{DC} of 8 μm. Thus we infer that the proposed WIDC design with deeply etched access waveguides can be safely used for designing compact integrated silicon photonics circuits which may be operated over a broad wavelength range.

Excess Loss Estimation

We estimated the excess loss (EL) of individual devices by taking ratio of the sum of transmitted powers at cross (P_c) and bar (P_b) ports to the transmitted power at reference waveguides (P_s).

$$EL = 10 \times \log \left[\frac{P_b + P_c}{P_s} \right] \tag{2.20}$$

The extracted EL for WIDC with shallow etched access waveguide and deeply etched access waveguide are shown in Figure 2.33. It is found to be varying between 1 dB to

1.5 dB (with shallow etched access waveguides). Since length of the coupled waveguide section of a WIDC is much lower than that of S-bend access waveguides, major portion of EL is attributed to the losses in the bend region. However, the average EL of WIDCs with deeply etched access waveguide is reduced by 0.4 dB near $\lambda = 1550$ nm. However, this seems to be relatively higher than the earlier reported values, since our loss estimation completely depends on the coupling efficiency of the I/O grating couplers and the quality of waveguides.
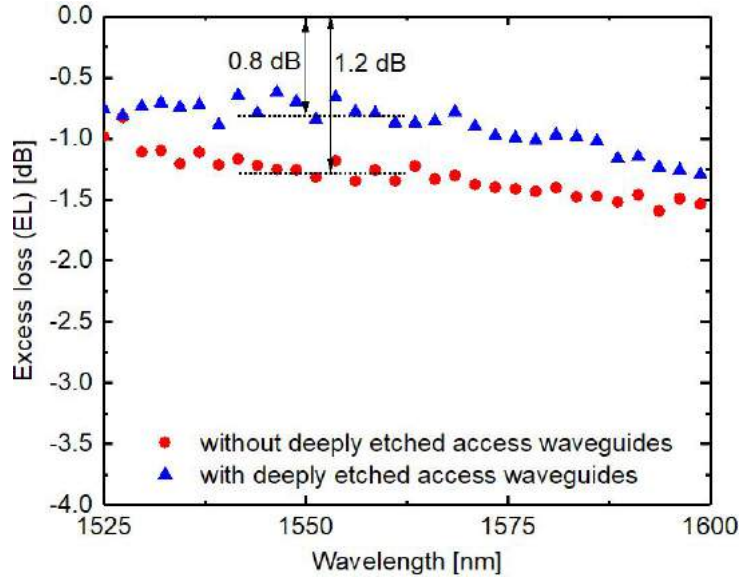
Figure 2.33: Excess loss of WIDC without (circles) and with deeply etched access waveguides (triangles) measured using Eq. 2.20.

2.3.3   WIDC based 1×4 Power Splitters

We have demonstrated broadband 1×4 power splitters by cascading WIDCs in 1×2 configuration (S3). The details of fabricated 1×4 power splitters are listed in Table 2.8. SEM image of a fabricated 1×4 power splitter is shown in Figure 2.34 where all the three WIDCs are designed for identical splitting ratio.   We have designed a

Table 2.8: Details of fabricated 1×4 power splitters in S3.

Sample	W, h	L_{DC}	Remarks
S2	$W \sim 350$ nm $h \sim 160$ nm	0, 1, 2, . ..10 μm	1×4 splitter

little modified 1×2 WIDCs, where S-bends (R = 180 μm) are used only in one of

56
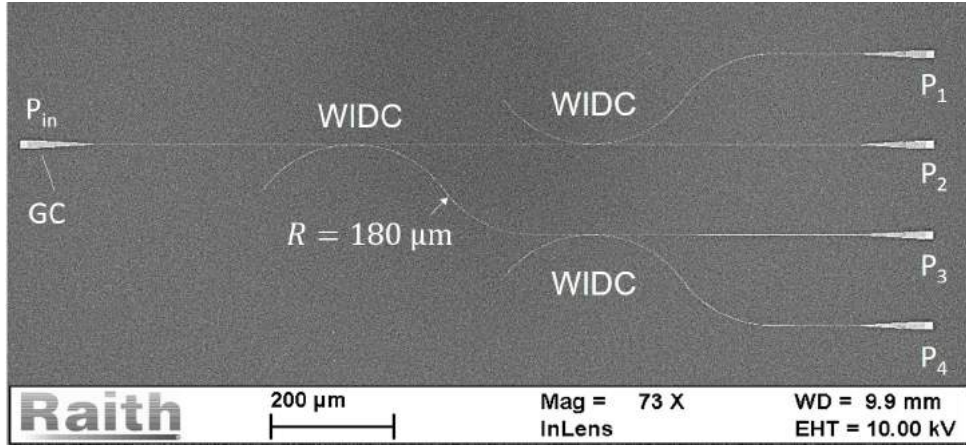
Figure 2.34: (SEM image of a 1×4 power splitter

the coupled waveguides. This is to facilitate compact design of the device with equal spacings among output waveguides. Typical normalized transmission characteristics at the four output ports (P_1, P_2, P_3 and P_4) of a demonstrated 1×4 power splitter obtained with $L_{3dB} = 5$ µm is shown in Figure 2.35(a) which gives $\sim 50\% : 20\% : 22\% : 8\%$ splitting ratio at $\lambda = 1550$nm . These results indicate that the splitting ratio of a single stage 1×2 WIDC with $L_{DC} = 5$ µm is approximately $70\% : 30\%$. The measured splitting ratios of another 1×4 splitter with $L_{DC} = 7$ µm ($\sim 50\% : 55\%$) is shown in Figure 2.35(b) where the power splitting ratio is measured as $\sim 25\% : 25\% : 25\% : 25\%$ at $\lambda = 1550$nm (6-dB power splitter). We further designed a suitable
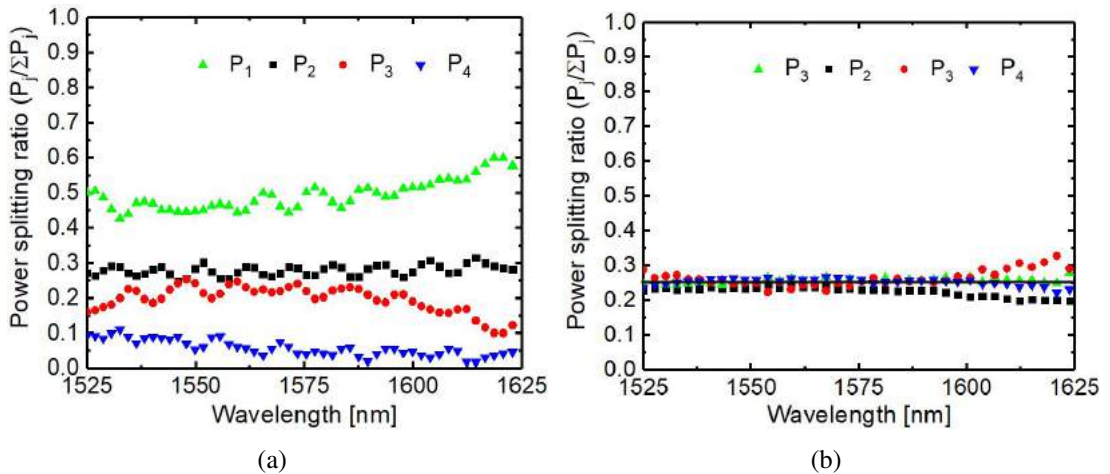
Figure 2.35: Normalized transmission characteristics ($P_j/\Sigma P_j$) at the four output ports (P_1, P_2, P_3, P_4) of 1×4 power splitters of (a) $L_{DC} = 5$ µm and (b) $L_{DC} = 7$ µm.

mask for the WIDC region as in Figure 2.36(a) and fabricated more compact 1×4

power splitters with deeply etched access waveguides in a two step etching process. The transmission characteristics of a typical 6-dB power splitter (L_{DC} = 7 μm) is shown in Figure 2.36(b). We observed a $\sim \pm 10\%$ wavelength dependent variation in power splitting ratios of all the above discussed 1×4 power splitters. The deviation is slightly more towards longer wavelengths (contradicting theoretical prediction) which may be attributed to the poorer response of the GCs.

<div align="center">(a)   (b)</div>
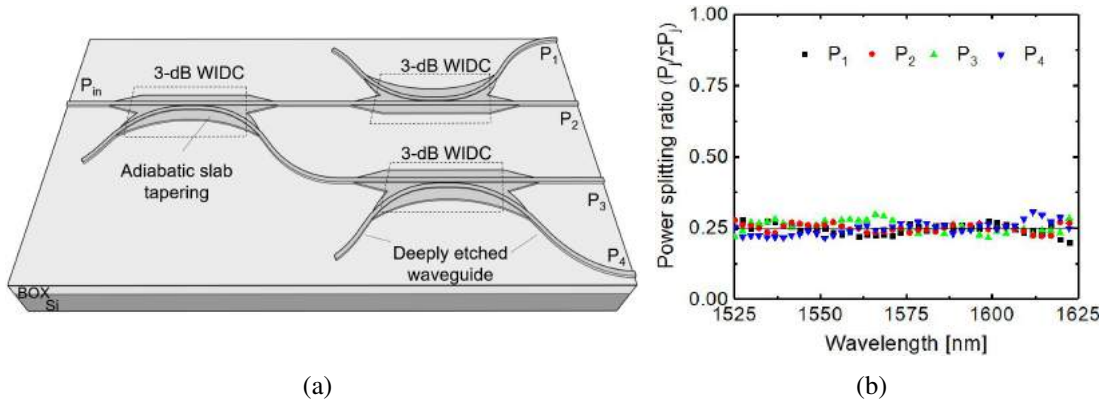
Figure 2.36: (a) 3D scheme of 1×4 power splitter using 3-dB WIDCs with deeply etched access waveguides and (b) the corresponding normalized transmission characteristics at the four output ports obtained with $L_{DC} = 7$ μm.

2.4 Summary

The polarization dependent single-mode guidance geometries and dispersion characteristics of sub-micron waveguides on a 220-nm SOI have been discussed. We have formulated a simple design rule for a WIDC by solving the two propagating supermodes of a DC. The proposed WIDC design with optimized waveguide parameters on a 220-nm SOI substrate exhibits uniform coupling characteristics over a broad wavelength range in communication window (1525 nm $\leq \lambda \leq$ 1625 nm) in TE-polarization. Broadband 2×2 WIDCs with various power splitting ratios were fabricated and experimental results are validated with theoretical predictions. The access waveguides of the proposed WIDC geometry is designed with S-bends of radius 180 μm to suppress the effect of bend region in coupling length and coupling characteristics. The experimentally measured 3-dB coupling length (5 μm) is slightly more than the theoretical

predictions (4 µm) due to fabrication induced errors in device dimensions. The maximum non-uniformity in splitting ratio is measured to be $\sim \pm 0.5$ dB over the entire operating wavelength range. A compact WIDC design deeply etched access waveguides has been proposed and demonstrated in two step etching steps. The excess loss of the demonstrated WIDC is measured to be ~ 1.2 dB. Broadband 1×4 power splitters also demonstrated by cascading WIDCs in 1×2 architecture. The measured transmission characteristics are consistent with the theoretical predictions. Thus WIDCs can be suitably integrated in MRRs and MZIs to improve their optical bandwidth. Following chapters discuss about broadband MRRs and MZIs.

CHAPTER 3

Microring Resonators with WIDCs

Microring resonators (MRRs) are used in various photonics applications like, add-drop filters [108, 109, 110], nonlinear optics [54], delay lines [111, 112], biomedical sensing [85, 113, 114, 115] etc. As discussed in chapter 1, the optical bandwidth of a conventional DC based MRR is limited by the wavelength dependent coupling between the ring and bus waveguide. However, a broadband MRR with uniform extinction ratio (ER) is highly desired for some applications like optical WDM and switching. Thus our WIDC design discussed in chapter 2 is a suitable candidate to improve the operating bandwidth of MRRs.

In this chapter, we have discussed the design and demonstration of broadband MRRs integrated with WIDCs. For completeness, we first discuss the working principle and resonance characteristics of an all-pass and add-drop MRRs. The wavelength dependent transmission characteristics of a typical conventional DC based and WIDC based MRRs are presented with numerical simulations. To validate the theory, we fabricated a few MRRs of different radii and coupling lengths and the resonance characteristics have been analyzed.

3.1 Theory of MRR: Working Principle

The working principle of MRR is extensively discussed in literatures [69, 102]. For completeness, in this section we briefly discuss about the design parameters and resonance characteristics of all-pass and add-drop MRRs. Schematics of directional coupler based all-pass and add-drop MRRs are shown in Figures 3.1(a) and 3.1(b) respectively. In both cases, E_i and E_t are the mode amplitudes at the input and output (through port) of the bus waveguide. Similarly E_a and E_d are the field amplitudes at the add- and drop- ports respectively. The couplers (symmetric DC) are characterized by the self
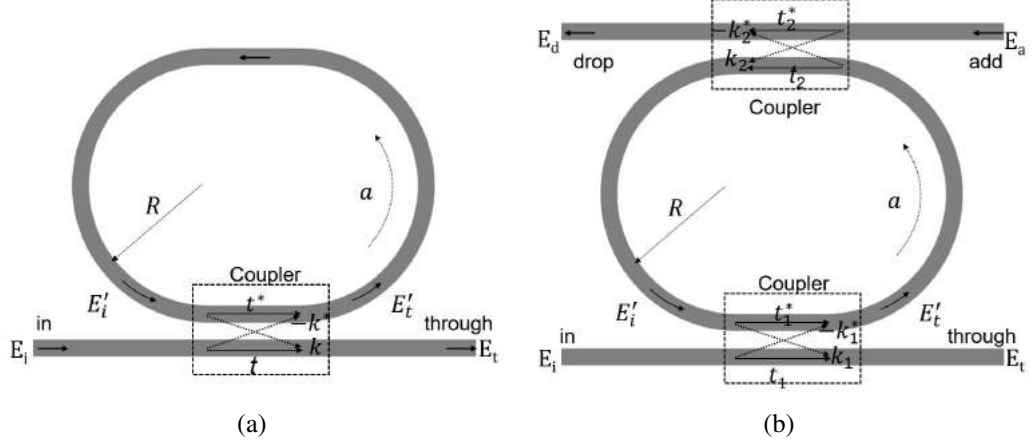
Figure 3.1: Schemes of (a) all-pass and (b) add-drop microring resonators. t - self coupling coefficient, k - cross-coupling coefficient, a - single pass transmission coefficient, R - the radius and $E_{i,t,a,d}$ - electric field amplitudes at input-, through-, add- and drop-ports, respectively.

coupling coefficients (t, t_1, t_2) and cross coupling coefficient (k, k_1, k_2). The round trip amplitude transmission is defined by a, which includes the total round trip loss in the ring as given by:

$$a = \exp\big[- (\alpha_{\text{bend}} \cdot 2\pi R + \alpha_{\text{wg}} L)\big] \tag{3.1}$$

where α_{bend} and α_{wg} are the power attenuation coefficients due to bend induced loss and propagation loss respectively and L is the total perimeter of the ring ($L = 2\pi R + 2L_{DC}$). Assuming no loss in the coupler section i.e., $t^2 + k^2 = 1$, the through-port transmission power of an all-pass MRR is expressed as [69]:

$$P_t^{ap} = \frac{a^2 + t^2 - 2at\cos(\theta + \phi_t)}{1 + a^2 t^2 - 2at\cos(\theta + \phi_t)} \tag{3.2}$$

where $\theta = 2\pi n_{eff} L/\lambda$ is the round trip phase accumulation in the ring and ϕ_t is the phase of the coupler. At resonance, $(\theta + \phi_t) = 2m\pi$, where m is an integer, the above equation becomes:

$$P_t^{ap} = \frac{(a - t)^2}{(1 - at)^2} \tag{3.3}$$

Similarly the though-port (P_t^{ad}) and drop-port (P_d^{ad}) transfer functions of an add-drop MRR are given by:

$$P_t^{ad} = \frac{t_2^2 a^2 + t_1^2 - 2at_1 t_2\cos(\theta + \phi_t)}{1 + a^2 t_1^2 t_2^2 - 2at_1 t_2\cos(\theta + \phi_t)} \tag{3.4}$$

$$P_d^{ad} = \frac{(1 - r_1^2)(1 - r_2^2)a}{1 + a^2 t_1^2 t_2^2 - 2t_1 t_2 \cos(\theta + \phi_t)} \tag{3.5}$$

Typical resonant characteristics at the output ports of all-pass and add-drop ring resonators are shown in Figures 3.2(a) and 3.2(b) respectively, assuming wavelength independent values of $n_{eff} = 2.7$, $a = 0.95$ and $|t| = |t_1| = |t_2| = 0.9$. In both cases, the through port transmission at resonance drops to minimum (ideally to 0) under critical coupling condition, i.e., $|t| = a$ in Eq. 3.3. The resonant wavelengths which are circulating in the ring can be dropped at the drop port. The free spectral range (FSR)
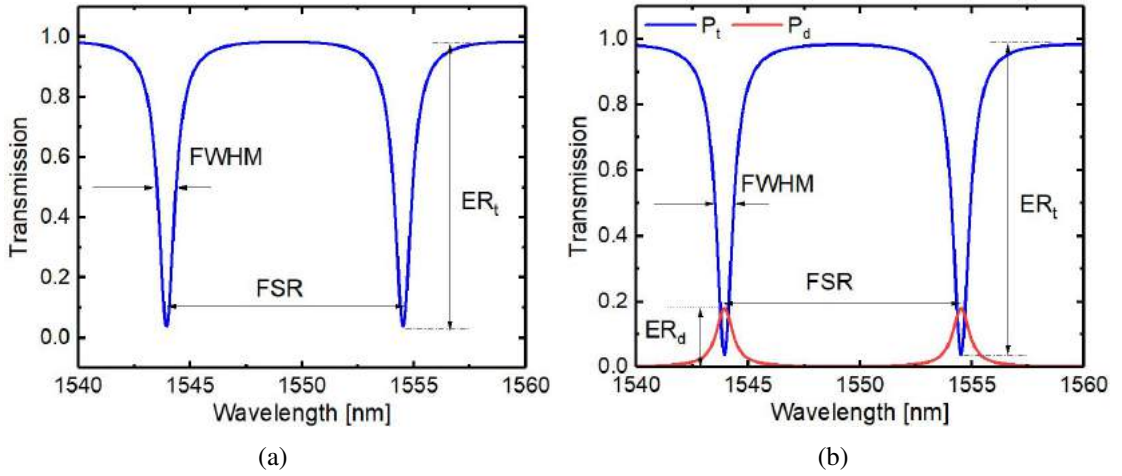
Figure 3.2: Normalized transmission characteristics of MRRs: (a) all-pass configuration, and (b) add-drop configuration. The calculations were carried using Eqs. 3.2, 3.4 and 3.5 assuming $n_{eff} = 2.7$, $a = 0.95$ and $|t| = |t_1| = |t_2| = 0.9$). ER - extinction ratio, FSR - free spectral range, FWHM - full width half maximum.

and full width half maximum of the resonance are given by [69]:

$$\text{FSR} = \frac{\lambda_{r,m} \lambda_{r,m+1}}{n_g L} \tag{3.6}$$

$$\text{FWHM (all-pass)} = \frac{(1 - ta)\lambda_r^2}{\pi n_g L \sqrt{ta}} \tag{3.7}$$

$$\text{FWHM (add-drop)} = \frac{(1 - t_1 t_2 a)\lambda_r^2}{\pi n_g L \sqrt{t_1 t_2 a}} \tag{3.8}$$

where $\lambda_{r,m}$, $\lambda_{r,m+1}$ are two successive resonant wavelengths of order m and $m + 1$ respectively. The extinction ratio (ratio of maximum transmission to minimum transmission) of the spectrum depends on the coupling coefficient (t) and the loss in the

waveguide. The ER at the through port of the two configurations can be expressed as [69]:

$$\text{ER (all-pass)} = \frac{(t+a)^2}{(t-a)^2} \times \frac{(1-ta)^2}{(1+ta)^2} \tag{3.9}$$

$$\text{ER (add-drop)} = \frac{(t_2 a + t_1)^2}{(t_2 a - t_1)^2} \times \frac{(1 - t_1 t_2 a)^2}{(1 + t_1 t_2 a)^2} \tag{3.10}$$

Q-factor (λ_r/FWHM) is another important parameter which quantifies the amount of energy stored at resonance and around resonance wavelength, as given by:

$$\text{Q (all-pass)} = \frac{\pi n_g L \sqrt{ta}}{\lambda_r (1 - ta)} \tag{3.11}$$

$$\text{Q (all-drop)} = \frac{\pi n_g L \sqrt{t_1 t_2 a}}{\lambda_r (1 - t_1 t_2 a)} \tag{3.12}$$

Similarly, finesse = FSR/FWHM measures the sharpness of the resonance with relative to the resonance spacing. In the following section, we will compare the transmission characteristics of MRRs designed with a conventional DC and a WIDC using numerical simulations.

3.1.1 Transmission Characteristics: Simulation Results

In general, the coupler parameters (t, k, ϕ_t) and waveguide parameters (a, n_{eff}) are wavelength dependent since the waveguides under consideration are highly dispersive. To understand the wavelength dependent transmission characteristics of MRRs, we have considered two different waveguide geometries similar to that of $DC3$ ($W = 350$ nm, $h = 0$ nm, $G = 150$ nm) and $DC4$ ($W = 375$ nm, $h = 160$ nm, $G = 150$ nm) in Figure 2.14. The wavelength dependent n_{eff}, α_{bend}, and t are extracted using Lumerical MODE Solutions (for TE-polarization) and the transfer functions of all-pass MRRs are simulated using MATLAB. In calculations, we have included the effect of bend induced coupling at the two sides of the DC for a given radius R. We also assumed the average loss of the waveguide is ~ 5 dB/cm. Figures 3.3(a) and 3.3(b) show the simulated transmission characteristics of MRRs ($R = 100$ µm, $L_{DC} = 4$ µm) designed with $DC3$ and $DC4$, respectively. It is clear from 3.3(a), that the ER (~ 55 dB to ~ 5 dB) and Q (~ 8000 to 10000) are highly nonuniform over the entire range of wavelength due to the
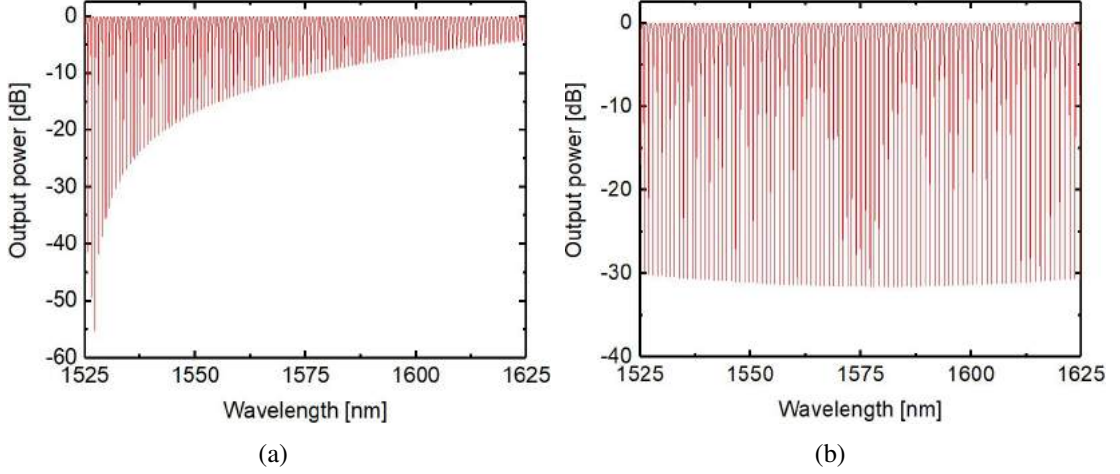
Figure 3.3: Simulated transmission characteristics of all-pass MRRs of radius $R = 100$ µm and designed with (a) a wavelength dependent DC (W = 350 nm, $h = 0$ nm, $H = 220$ nm, $G = 150$ nm) and (b) a WIDC (W = 350 nm, h = 160 nm, $H = 220$ nm, $G = 150$ nm) of $L_{DC} = 4$ µm. Calculations are carried out for TE polarization and assuming the waveguide loss 5 dB/cm.

strong wavelength dependency of κ ($DC3$). On the other hand a WIDC ($DC4$) based MRR as shown in Figure 3.3(b), exhibits nearly wavelength independent ER (30 dB) over more than 100 nm wavelength range (1525 nm $\leq \lambda \leq$ 1625 nm). The extinction and Q of a MRR can be improved by suitably designing the coupling length L_{DC} of DC region (Eq. 3.9). The minimum radius of MRR is limited by the bend loss associated with shallow etched S-bends of WIDC.

3.1.2   Compact MRR Design with WIDC

Since the above discussed WIDC waveguides are shallow etched, the bend loss associated with the ring waveguide limits the performance of micro-ring resonator. From our previous calculations, the minimum bend radius of WIDC waveguide was shown to be 100 µm, below which α_{bend} is significant and wavelength dependent. In such cases ($R < 100$ µm) the ring operates in deep under-coupling region ($a << |t|$) [69], and hence $P_t \approx |t|^2$, using Eq. 3.3. In order to demonstrate compact MRRs we followed the same methods discussed under section 2.2.4; (i) MRR with adiabatically tapered WIDC waveguides and (ii) MRR with deeply etched WIDC waveguides.

(i) MRR with adiabatically tapered WIDC access waveguides

It is bit tricky to design a compact MRR especially with shorter ring radius as it requires deeply etched ring waveguides for reduced bending loss and shallow etched bus waveguide for WIDC. Figure 3.4(a) shows a 3-D schematic of compact MRR with shallow

<table>
<tr><td>(a)</td><td>(b)</td></tr>
</table>
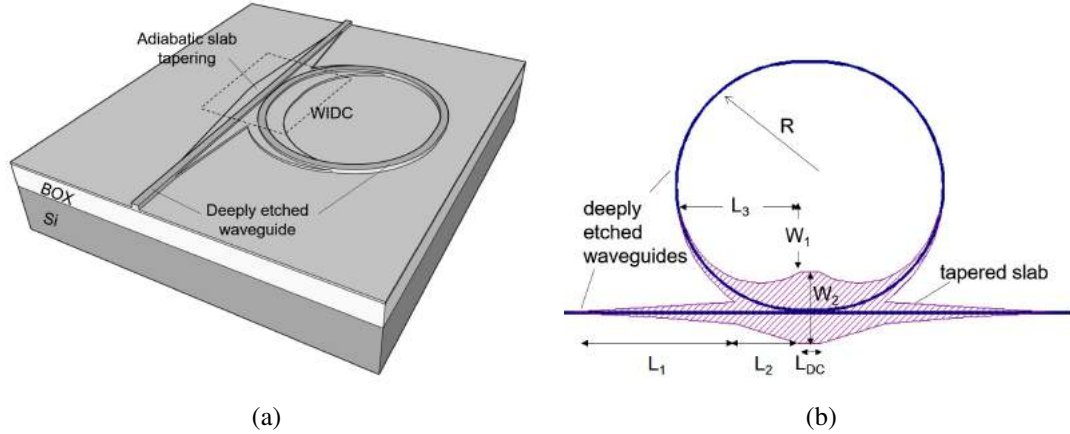
Figure 3.4: (a) 3-D scheme of an all-pass deeply etched waveguide ring resonator designed with shallow etched WIDC and deeply etched access waveguides; (b) Typical layout of the mask used in second step lithography. L_1, L_2, L_3, W_1 and W_2 are appropriately chosen to maintain the WIDC characteristics as well as to minimize the mode-mismatch loss.

etched WIDC and deeply etched waveguides. The scheme is similar to that of WIDCs with deeply etched waveguides as discussed under section 2.2.4 and requires two steps of fabrication process. First, the shallow etched devices are fabricated and then the waveguides are further etched by selectively masking the DC region in lithography. Typical layout of the mask used in second step lithography is shown in Figure 3.4(b). L_1, L_2, L_3, W_1 and W_2 are appropriately chosen to maintain the WIDC characteristics as well as to minimize the mode-mismatch loss. A wider taper of width W_2 (~ 10 µm) is provided at the WIDC region in order to accommodate the evanescent tails of the shallow etched WIDC supermodes ($2 - 3$ µm to one side). Then the slab is adiabatically tapered towards the waveguide (bus and ring) region covering the bend induced coupling region (L_2) followed by much narrower and adiabatic taper (L_1, L_3, W_1) to minimize the mode mismatch loss. However, the sharp transition from shallow etched WIDC waveguide region to deeply etched bend waveguide region may introduce significant mode-mismatch loss. Thus, this type of slab tapering scheme is not suitable for smaller ring radii since it requires sufficiently long taper length for adiabatic transition

of modes, which covers the major portion of the bend.

(ii) MRR with deeply etched WIDC

One can design a broadband MRR with tighter bends (radius close to 30 μm) with a deeply etched WIDC geometry of $W \sim 300$ nm and $h \sim 110$ nm (see Figure 2.20). Fig-
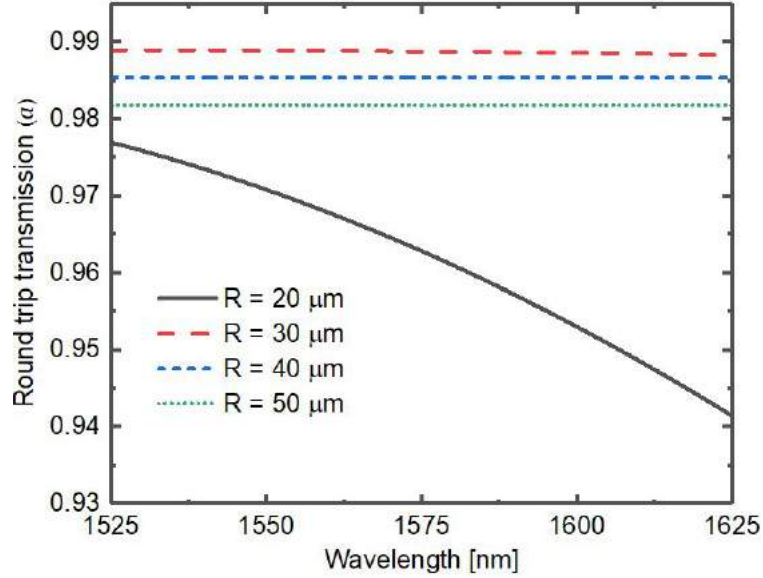
Figure 3.5: Round trip transmission coefficient (a) calculated using Eq. 3.1 for four different ring radii (R) and for a given WIDC geometry of $W = 310$ nm, $h = 110$ nm (assuming typical values for $\alpha_{\mathrm{wg}} = 5$ dB/cm and $L_{DC} = 4$ μm).

ure 3.5 shows the single-pass transmission coefficients (a) calculated for four different ring radii ($R : 20,\ 30,\ 40,\ 50$ μm) assuming an over estimated value of $\alpha_{\mathrm{wg}} = 5$ dB/cm (experimentally 3 dB/cm for shallow etched waveguides [85]). It is to be noted that a is highly wavelength dependent for $R = 20$ μm and nearly wavelength independent for $R \geq 30$ μm. However, the broadband performance of such WIDC geometry is less tolerant to fabrication errors in design parameter variation.

3.2 Experimental Results and Discussions

The above discussed MRRs were experimentally demonstrated on a 220-nm device layer SOI with same fabrication process flow discussed under 2.3.1. Two different sam-

ples were fabricated one (S3) with shallower etched WIDC geometry ($W = 350$ nm, $h = 160$ nm, $G = 150$ nm) and the other (S4) with deeply etched WIDC geometry ($W = 310\ nm$, $h = 110$ nm, $G = 150$ nm). A list of fabricated devices on two set of samples are given in Table 3.1. The experimental results are discussed in the following section.

Table 3.1: List of fabricated devices on two sets of samples.

Sample	$W,\ h,\ G$	$L_{DC},\ R$	Remarks
S3	W = 350 nm h = 160 nm G = 150 nm	L_{DC}: 0, 2, 4 µm R: 25, 100 µm	WIDC with shallow/deeply etched ring and access waveguides
S4	W = 310 nm h = 110 nm G = 150 nm	L_{DC}: 0, 2, 4 µm R: 20, 30, 40, 50 µm	All-pass and add-drop MRRs

3.2.1 Demonstration of All-pass MRRs with Shallow etched WIDC

First, we characterized the WIDC integrated MRRs ($R = 25$ µm and $R = 100$ µm) of sample S3. Figure 3.6 shows the SEM image of a MRR of $R = 100$ µm with input/output GCs. The measured transmission characteristics (normalized to 0 dBm) of
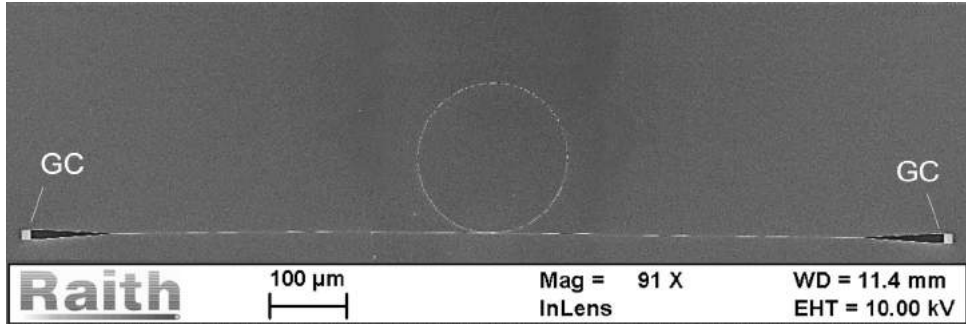
Figure 3.6: SEM image of a WIDC based MRR of $R = 100$ µm fabricated with a single-step lithography (GC - grating coupler).

$R = 100$ µm MRRs with $L_{DC} = 0$ µm, $L_{DC} = 2$ µm and $L_{DC} = 4$ µm are shown in Figures 3.7(a), 3.7(b) and 3.7(c) respectively. In all cases, MRR exhibits nearly wavelength independent ER over the entire wavelength range. This clearly indicates the signature of the WIDCs. Since WIDC waveguides are shallow etched ($h = 160$ nm), the round trip optical loss is negligibly small as ring waveguide has large bending radius which is consistent with the simulation results shown in Fig. 3.3(b). A zoomed-in view

67
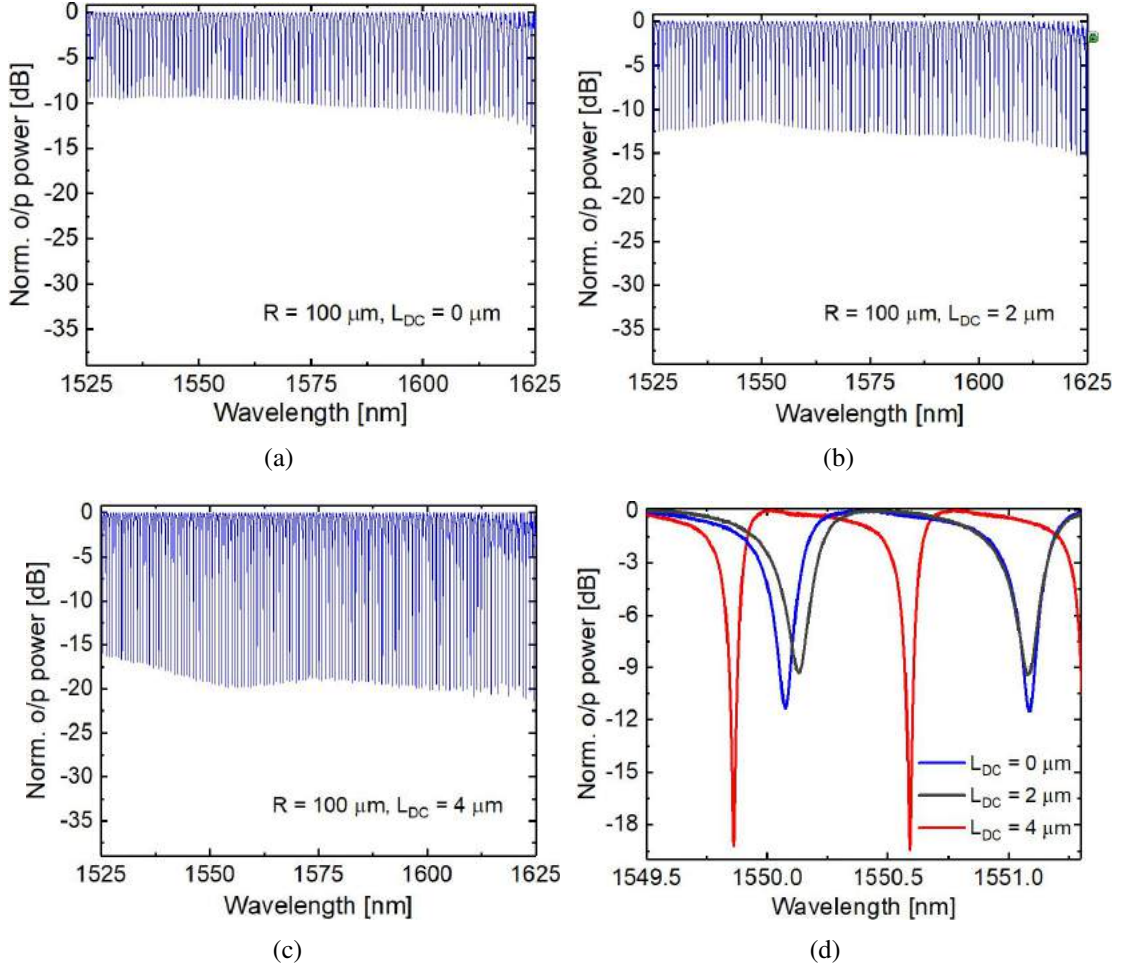
Figure 3.7: Normalized transmission characteristics $R = 100$ µm MRRs with (a) $L_{DC} = 0$ µm, (b) $L_{DC} = 2$ µm and (c) $L_{DC} = 4$ µm; (d) zoomed in view of the resonances in (a), (b) and (c) near $\lambda = 1550$ nm.

of the resonances of MRRs near $\lambda = 1550$ nm are shown in Figure 3.7(d). Note that, the ER of the spectra are different for $L_{DC} = 0$ µm (~ 10 dB), $L_{DC} = 2$ µm (~ 13 dB) and $L_{DC} = 4$ µm (~ 20 dB) as shown in Figure 3.8(a). This is because the ER increases as t approaches a (Eq. 3.9). The measured ER values are fitted with theoretical values (calculated by considering the additional coupling length in the bend region $2\Delta L_b = 15$ µm) as shown in Figure 3.8(a). Theoretical ERs are found to be a little less than that of measured data, which may be attributed to the deviations in estimated values of a and $2 \times L_b$. Also we have estimated the FSR ($\Delta \nu = c\Delta\lambda/\lambda^2$, where $\Delta\lambda$ is the FSR in wavelength domain) for the above two MRRs as shown in Figure 3.8(b). The wavelength dependent variation in $\Delta\nu$ is due to the wavelength dependent group index of the waveguide ($\Delta n_g = 3.78$ at $\lambda \sim 1550$ nm). Similarly, the wavelength dependent Q-factor measured for all the three MRRs discussed above are shown in Figure 3.8(c).

68
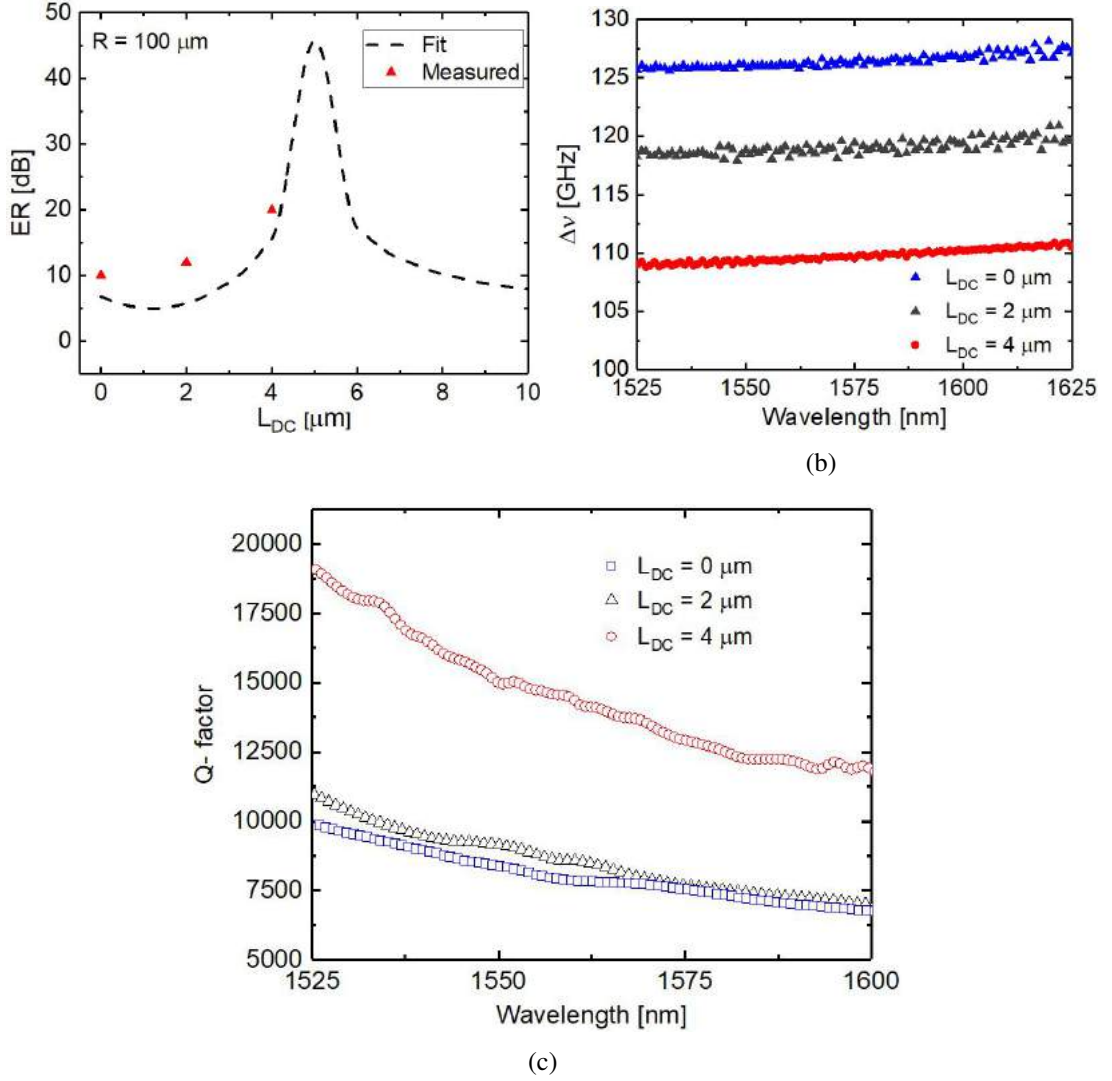
Figure 3.8: (a) Measured ER values and theoretical fit. (b) Measured wavelength dependent FSR ($\Delta\nu = c\Delta\lambda/\lambda^2$, where $\Delta\lambda$ is the FSR is wavelength domain). (c) Measured wavelength dependent Q-factor.

Since, n_g of the waveguide is wavelength dependent, the Q- factor (Eq. 3.12) is also found be wavelength dependent. The experimentally (theoretical) measured Q values of the above three MRRs are 8500 (9200), 8750 (12000) and 15200 (20500), respectively (near $\lambda = 1550$ nm). Again, the Q of the ring can be improved by suitably choosing the coupling length L_{DC} for desired coupling coefficient t. However, our primary goal was experimental validation of the broadband resonance characteristics of MRRs integrated with WIDCs.

Interestingly, MRR with $R = 25$ μm shows no resonances for any L_{DC}s as shown in Figure 3.9. The tighter bend of shallow etch waveguide introduces higher bend loss
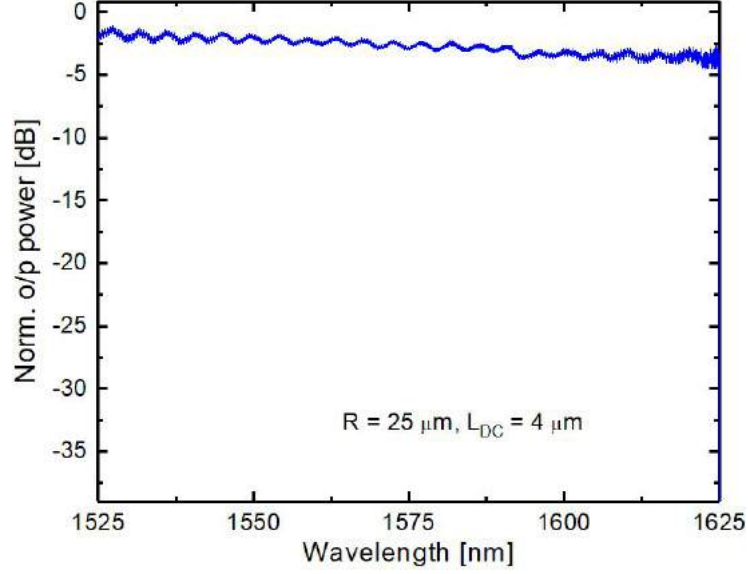
Figure 3.9: Normalized transmission characteristics $R = 25$ μm MRRs with shallow etched WIDC of $L_{DC} = 4$ μm. The spectrum shows no resonance since $a << |t|$.

(α_{bend}) resulting in $a << |t|$ and hence $P_t \approx |t|^2$ (similar to bar port transmission of DC). Thus, in order to have a resonance cavity one need to reduce the bend loss which is possible by deeply etching the ring waveguide region without altering the coupling characteristics of WIDC region as discussed in section 3.1.2.

3.2.2 Demonstration of Compact MRRs

We have demonstrated compact all-pass MRRs with adiabatically tapered WIDC access waveguides as discussed under section 3.1.2. The DC region of a MRR of $R = 25$ μm (sample S3) is selectively masked (see SEM image in Figure 3.10(a)) and the access waveguides are further etched deeply to a slab height of ~ 20 nm. The transmission characteristics MRRs ($R = 25$ μm) with $L_{DC} = 0$ μm and $L_{DC} = 4$ μm are shown in Figures 3.10(b) and 3.10(c), respectively. In both cases, resonances with nearly uniform extinction over the entire wavelength span of 100 nm are distinctly observed. However, the measured Q is ~ 1500 due to relatively large mode-mismatch loss in the taper region. These results suggest that a better design of tapered slab is required for a WIDC based compact MRR. More importantly, the same ring waveguide with deeply etched (wavelength dependent) DC bus waveguide exhibits non-uniform resonance extinctions
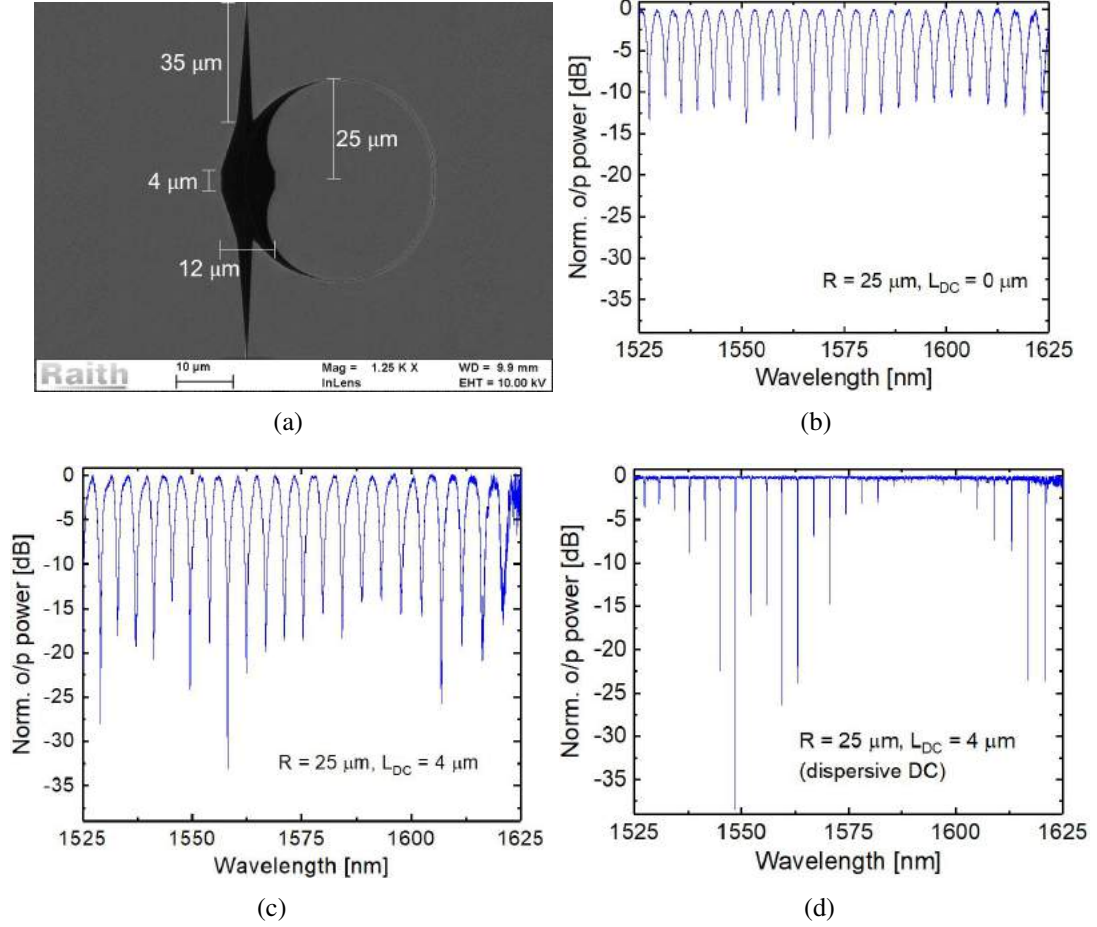
Figure 3.10: SEM image of the masked WIDC of MRR ($R = 25$ μm) prepared for second etching in (a) and the corresponding normalized transmission characteristics measured for $L_{DC} = 0$ μm in (b) and $L_{DC} = 4$ μm in (c). Transmission characteristics of a MRR with dispersive DC ($W \sim 350$ nm, $h \sim 20$ nm) of $L_{DC} = 4$ μm in (d).

and with relatively high Q-values (25000) near critically coupled wavelengths as shown in Figure 3.10(d).

The transmission characteristics of compact MRRs fabricated (sample S4) with deeply etched WIDC geometry ($W = 310$ nm, $h = 110$ nm) were also validated. Figures 3.11(a) and 3.11(b) show the normalized transmission characteristics of MRRs of $R = 20$ μm and $R = 40$ μm respectively, each with $L_{DC} = 4$ μm. Though the devices are deeply etched, the bend loss for $R = 20$ μm is relatively large and wavelength dependent resulting in wavelength dependent ER (Figure 3.11(a)). The noise modulation at higher wavelength is due to the poor coupling efficiency of the GCs (of this particular device). However, a clean and uniform resonance spectrum is observed for

71

$R = 40$ µm since the bend loss is relatively small and nearly wavelength independent. These results are consistent with our numerical calculations (see Figure 3.5). The best measured spectral characteristics are FSR ~ 2.67 nm, Q$\sim 3600 \pm 400$ at $\lambda \sim 1550$ nm and ER ~ 25 dB over 1525 nm $\leq \lambda \leq 1625$ nm.
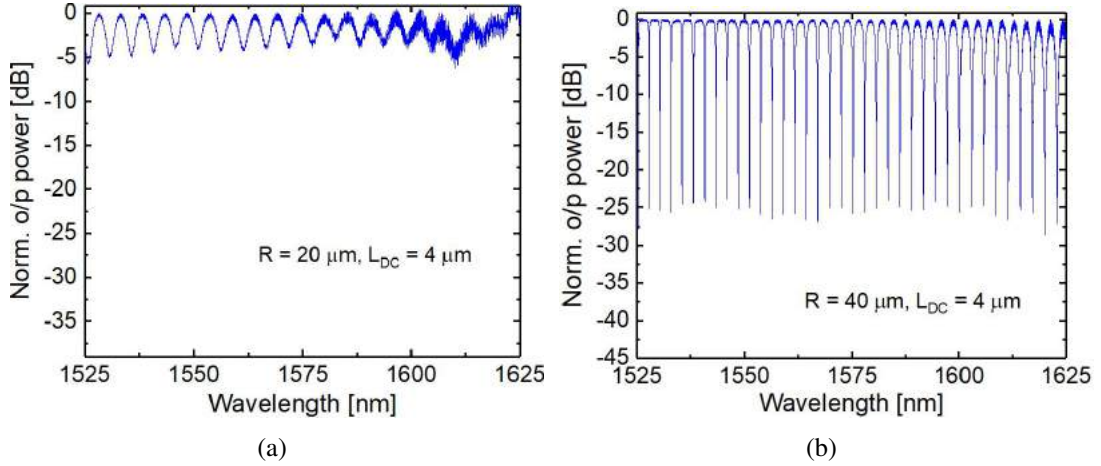
Figure 3.11: Normalized transmission characteristics deeply etched WIDC based compact MRRs of (a) $R = 20$ µm, $L_{DC} = 4$ µm and (b) $R = 40$ µm, $L_{DC} = 4$ µm.

Finally, we characterized an add-drop MRR fabricated in the same sample S4 with deeply etched WIDC. A SEM image of fabricated add-drop MRR of radius $R = 40$ µm and $L_{DC} = 4$ µm (fabricated in S4) is shown in Figure 3.12(a) and a zoomed-in SEM image in Figure 3.12(b). The measured through port and drop port transmission characteristics are shown in Figure 3.12(c) and a more close-up view near $\lambda = 1550$ nm is shown in Figure 3.12(d). Both through- and drop-port spectra are modulated with unwanted oscillations due to the poor coupling efficiency of GCs at longer wavelengths. This was observed in a few more devices which were fabricated near to the edge of the sample (S4). We observed that, non-uniform extinctions in the through port (25-40 dB) and drop port (12-15 dB) of the add-drop MRR which is mainly due to the less fabrication tolerance in deeply etched WIDC geometry ($W = 310$ nm, $h = 110$ nm). However, the major goal of nearly wavelength independent characteristics have been validated.
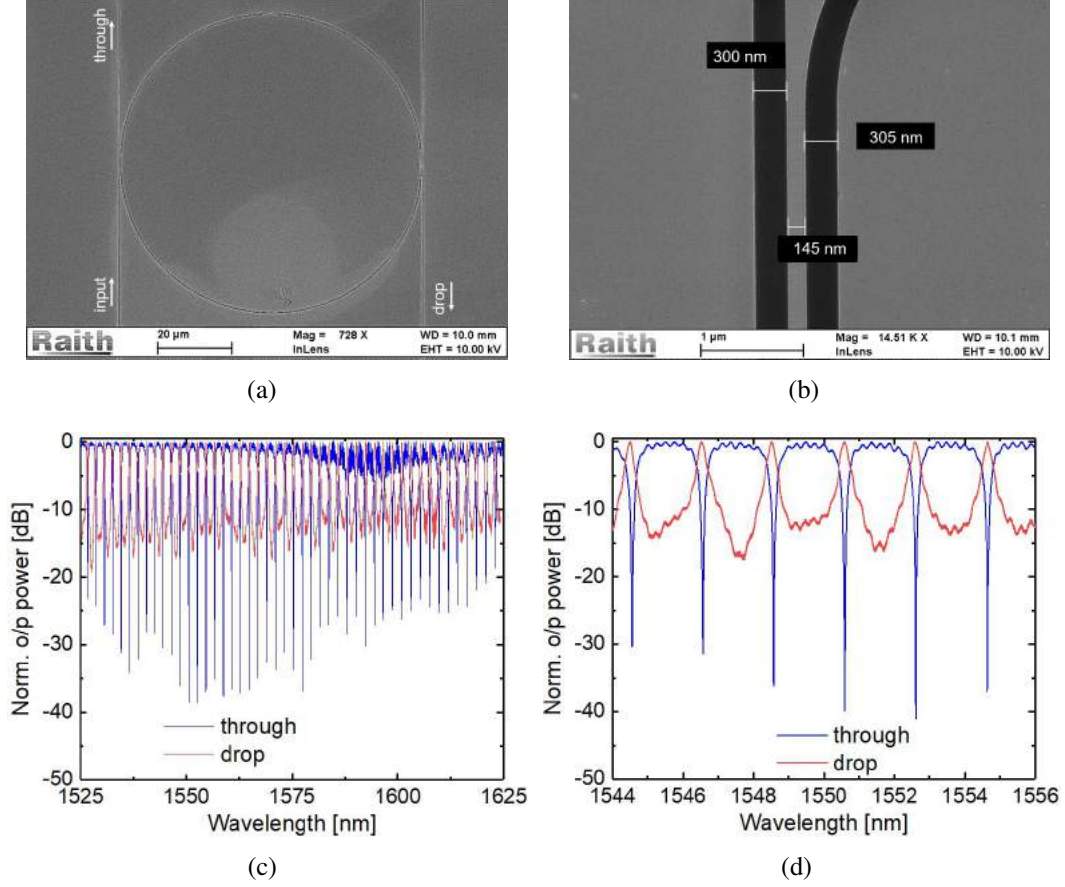
Figure 3.12: SEM images of (a) add-drop microring resonator of $R = 40$ μm; and (b) zoomed-in view of the WIDC region ($W = 310$ nm, $G = 150$ nm); (c) the corresponding through-port and drop port responses with zoomed-in view in (d).

3.3 Summary

The broadband transmission characteristics of WIDC based MRRs were studied numerically and experimentally validated. The fabricated MRR of radius $R = 100$ μm exhibits uniform extinction ratio (20 dB) over the entire wavelength range of interest. The extinction ratio can be improved by suitably designing the couping length of WIDC for any desired coupling coefficient. Since the WIDC waveguides are shallow etched ($h = 160$ nm) the minimum ring radius is limited by the bend loss. Compact MRRs with radius $R = 25$ μm with shallow etched WIDC design were demonstrated in two step fabrication process with deeply etched access waveguides. Such MRRs also exhibit uniform extinction ratio, however, the estimated Q values are relatively small (2000) compared to that of $R = 100$ μm MRR fabricated in single step process

(18000). This corresponds to significant mode-mismatch loss in the taper section and thus one needs to further optimize the taper region to improve the performance of compact MRRs $R < 100$ μm. We found that a deeply etched WIDC is another solution to demonstrate compact MRRs of $R > 30$ μm, in single step process. The experimental transmission spectrum of all-pass rings exhibit an ER ~ 25 dB and $Q \sim 4000$ over the entire 100-nm wavelength range of interest. Add-drop MRRs ($R = 40$ μm) were also demonstrated and the broadband performance has been validated. It is worth mentioning that, our primary design concern was to demonstrate uniform extinction ratio MRRs using WIDCs, however, one can appropriately choose the design parameters (coupler length L_{DC}, ring radius R and controlling the waveguide propagation loss α) for desired Q and FSR values.

CHAPTER 4

Mach-Zehnder Interferometers with WIDCs

Mach-Zehnder interferometers (MZIs) are widely used for various silicon photonics applications such as modulation, switching, filtering, sensing, (de-)multiplexing, etc. As discussed in chapter 1, the optical bandwidth of conventional (dispersive) DC based MZIs are limited to a few tens of nanometers [116]. However, MZI based modulators and switches operating over a broad wavelength range ($\lambda \sim 1550$ nm) is essential for on-chip switching and routing of a large number of WDM channels [117, 118]. In this chapter, we discuss the design and demonstration of broadband (balanced and unbalanced) MZIs designed with two identical 3-dB WIDCs.

4.1 MZI: Working Principle and Simulation Results

Figure 4.1 shows the schematic layout of a 2×2 MZI comprised of two cascaded DCs. The transmission characteristics of MZI depends on the power splitting/combining ratio of the DCs and the optical phase difference of light travelling in two arms. The phase difference between two arms of MZI at any given λ is given by:

$$\Delta\phi = \beta_1 l_1 - \beta_2 l_2 = \frac{2\pi}{\lambda}\big[n_{eff1}l_1 - n_{eff2}l_2\big] \tag{4.1}$$

where n_{eff1} and n_{eff2} are the effective indices of the upper and lower arms of lengths l_1 and l_2 respectively.

The transmitted signal amplitudes at bar port (S_b) and cross-port (S_c) of MZI can be expressed in matrix equation for a launched signal at one of the input ports (S_{in}) [119]:

$$\begin{bmatrix} S_b(\lambda) \\ S_c(\lambda) \end{bmatrix} = \mathcal{T}_{DC_2}(\lambda) \cdot \mathcal{T}_M(\lambda) \cdot \mathcal{T}_{DC_1}(\lambda) \begin{bmatrix} S_{in} \\ 0 \end{bmatrix} \tag{4.2}$$
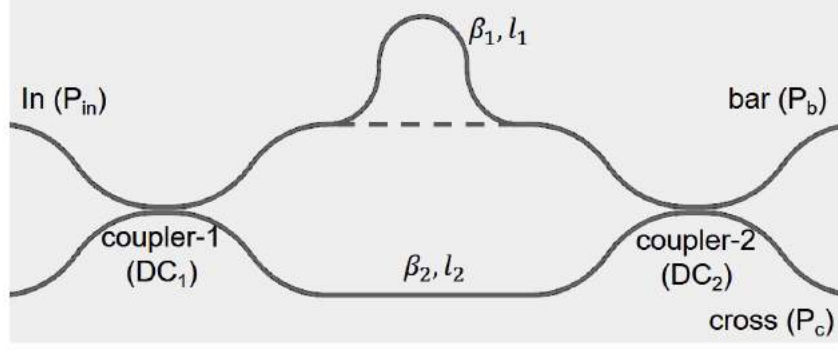
Figure 4.1: Schematic layout of a DC based (un)balanced Mach-Zehnder interferometer ($\beta_1 l_1 \neq \beta_1 l_2$) in SOI. $\beta_{1,2}$ are the propagation constants, and $l_{1,2}$ are the lengths of the upper and lower arms.

where, $\mathcal{T}_{DC_1}$ and $\mathcal{T}_{DC_2}$ are the transfer matrices for input and output directional couplers respectively (Eq. 2.8). The wavelength dependent propagation matrix for MZI arms can be expressed as:

$$\mathcal{T}_M(\lambda) = e^{-j\phi_2} \begin{bmatrix} e^{-j\Delta\phi} & 0 \\ 0 & 1 \end{bmatrix} \tag{4.3}$$

Eq. 4.2 reveals that the MZI transfer function strongly depends on the wavelength dependent splitting/combining ratio of the two directional couplers.

We have studied the performance of wavelength dependent (dispersive) DCs ($W = 350$ nm, $h = 0$ nm, $G = 150$ nm and $H = 220$ nm) based MZIs and WIDCs ($W = 375$ nm, $h = 160$ nm, $G = 150$ nm and $H = 220$ nm) based MZIs with balanced and unbalanced arms. The wavelength dependent DC parameters (t and k) and waveguide parameters (n_{eff}) are calculated (TE-polarization) using Lumerical MODE Solutions and the corresponding transfer functions of P_b and P_c are simulated in MATLAB using Eq. 4.2. In calculations, we have considered the effect of bend (bend induced loss and bend induced coupling length).

MZI with balanced arms ($\beta_1 l_1 = \beta_2 l_2$)

A balanced MZI has two identical arms such that $\Delta\phi = 0$. The calculated splitting ratio of 3-dB couplers designed with dispersive DC and WIDC are shown in Figures 4.2(a) and 4.2(b) (top). Since both the DCs are assumed to be identical and designed for coupling lengths of $L_{3dB} = 3.4$ μm (4 μm) for dispersive DC (WIDC) at $\lambda = 1550$ nm,

maximum transmission is expected in the cross port for both MZIs. However, the over all splitting ratio of the MZI with dispersive DCs (Figure 4.2(a), bottom) is found to be wavelength dependent since splitting ratio (k^2) of individual DCs varies significantly ($0.3 \leq k^2 \leq 0.7$) over the entire wavelength range of interest (1525 nm $\leq \lambda \leq$ 1625 nm). On the other hand, WIDC ($k^2 \sim 0.5$) based MZI exhibits wavelength independent splitting ratio throughout the operating bandwidth as shown in Figure 4.2(b) (bottom).
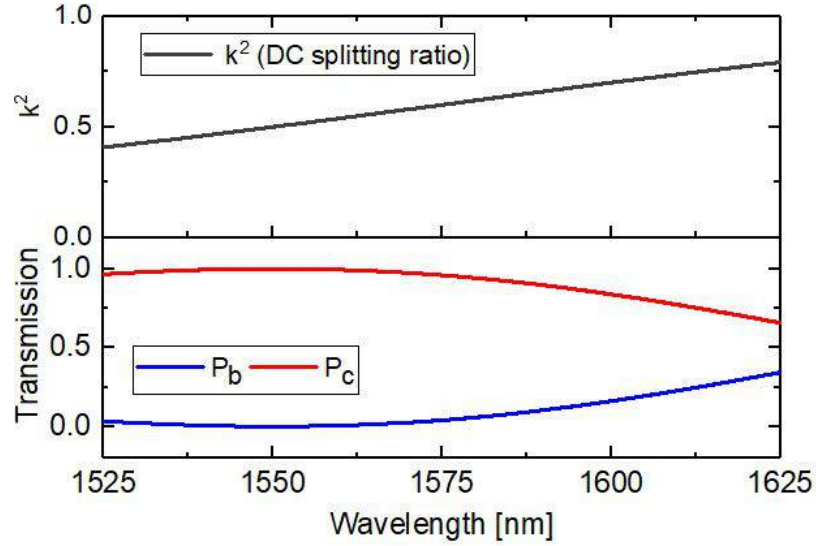
(a)
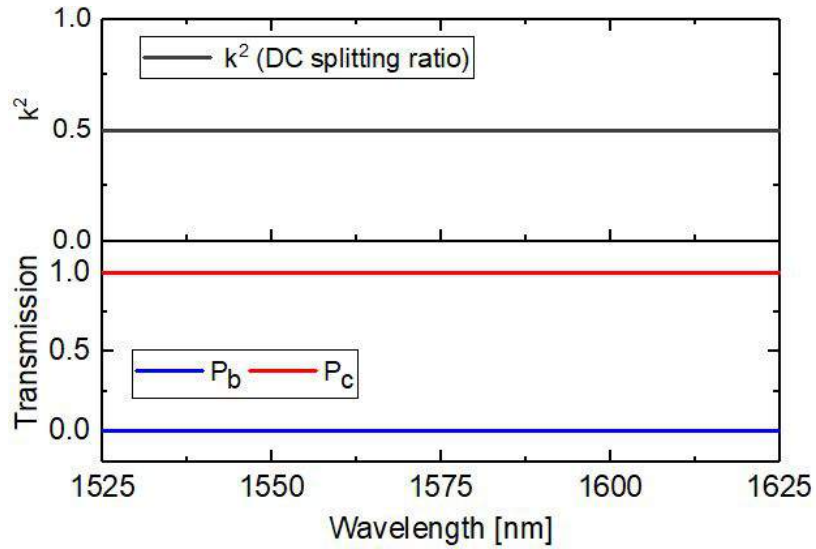
(b)

Figure 4.2: Splitting ratio (k^2) of 3-dB coupler and MZI transmission characteristics at the output ports calculated for (a) dispersive DC ($W = 350$ nm, $h = 0$ nm, $G = 150$ nm and $H = 220$ nm) based balanced MZI and (b) WIDC ($W = 375$ nm, $h = 160$ nm, $G = 150$ nm and $H = 220$ nm) based balanced MZI. The calculation are carried out for TE-polarization.

MZI with unbalanced arms ($\beta_1 l_1 \neq \beta_2 l_2$)

In this case we assume $n_{eff1} = n_{eff1}$ and $l_1 - l_2 \neq 0$. Similar transmission characteristics calculated for unbalanced MZIs ($\Delta l = 100 \, \mu$m) are shown in Figure 4.3. Note that,
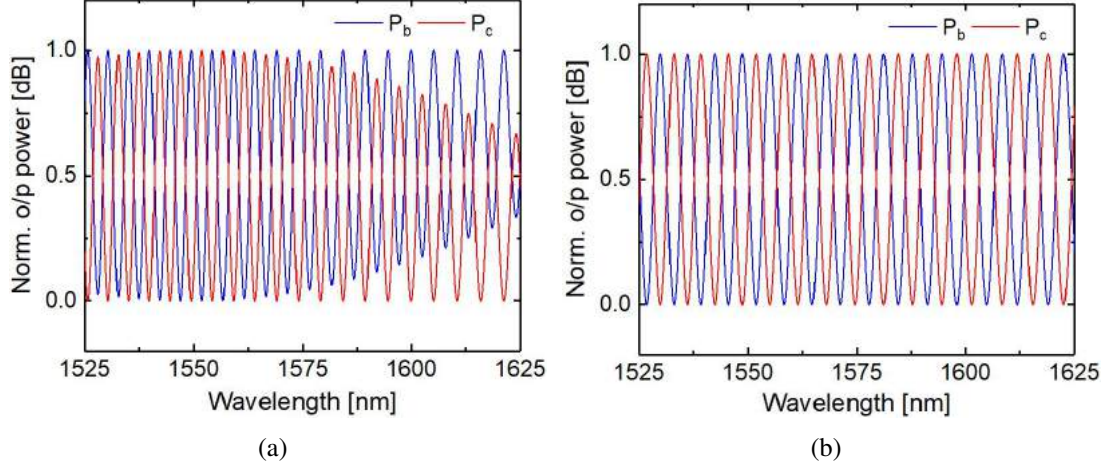
Figure 4.3: Normalized transmission characteristics at the output ports of (a) dispersive DC based unbalanced MZI and (b) WIDC based unbalanced MZI with $\Delta l = 100 \, \mu$m. The calculations were carried out for TE-polarization.

the extinction ratio of the interference patters are non-uniform for dispersive DC based MZI (Figure 4.3(a)) and nearly wavelength independent for WIDC based MZI (Figure 4.3(b)). The FSR ($\Delta\lambda$) at any of the output ports (P_b or P_c) is defined as [76]:

$$\Delta\lambda = \frac{\lambda_i \lambda_{i+1}}{n_g \Delta l} \tag{4.4}$$

where λ_i and λ_{i+1} are two adjacent constructive or destructive interfering wavelengths and n_g is the group index of the waveguide, which is calculated to be 3.87 for shallow etched waveguides ($W = 375$ nm, $h = 160$ nm, $H = 220$ nm) and 5.05 for deeply etched waveguides ($W = 350$ nm, $h = 0$ nm, $H = 220$ nm) at $\lambda \sim 1550$ nm so that FSR $\sim$ 3 nm and $\sim$ 4 nm respectively.

MZIs with unbalanced WIDCs

In the previous section we have considered MZIs with identical 3-dB WIDCs, which is an ideal situation. In practice, the splitting ratios of the two WIDCs (SR$_1$ and SR$_2$) may
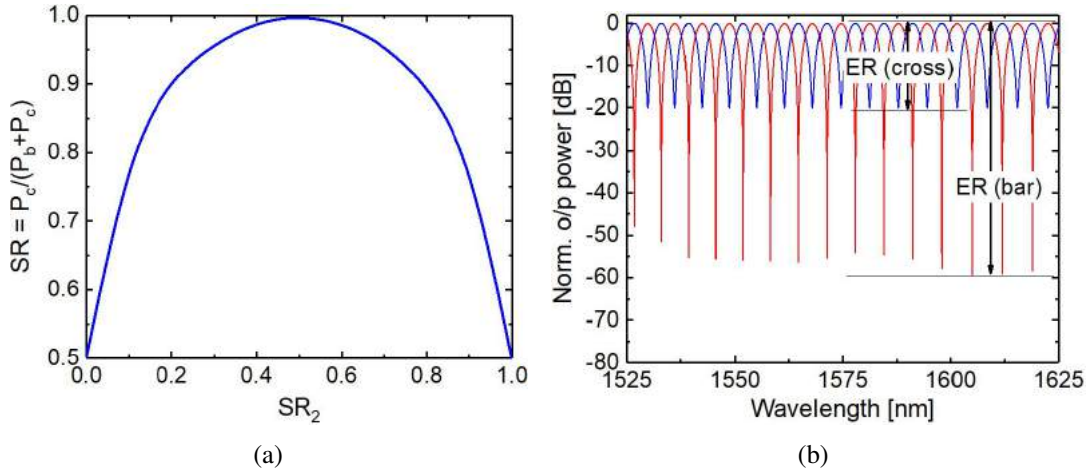
Figure 4.4: (a) Splitting ratio (SR) of WIDC based balanced MZI as a function of SR_2, assuming $SR_1 = 0.5$, and (b) Transmission characteristics at the output ports (P_b and P_c) of WIDC based unbalanced MZI ($\Delta l = 100$ μm) calculated for $SR_1 = 0.55$ and $SR_2 = 0.45$.

differ due to unavoidable fabrications errors. In order to quantify the overall splitting ratio variations with respect to the variations in SR_1 and SR_2, we first assume $SR_1 = 0.5$ (at the cross port) and calculate the overall splitting ratio at the cross port of MZI (SR = $P_c/(P_c + P_b)$) for various values of SR_2 as plotted in Figure 4.4(a). As expected, SR = 1 only if $SR_1 + SR_2 = 1$, otherwise SR < 1 for all other values of SR_2 ($SR_1 = 0.5$). A similar plot can be obtained if SR_1 and SR_2 are interchanged in Figure 4.4(a). In case
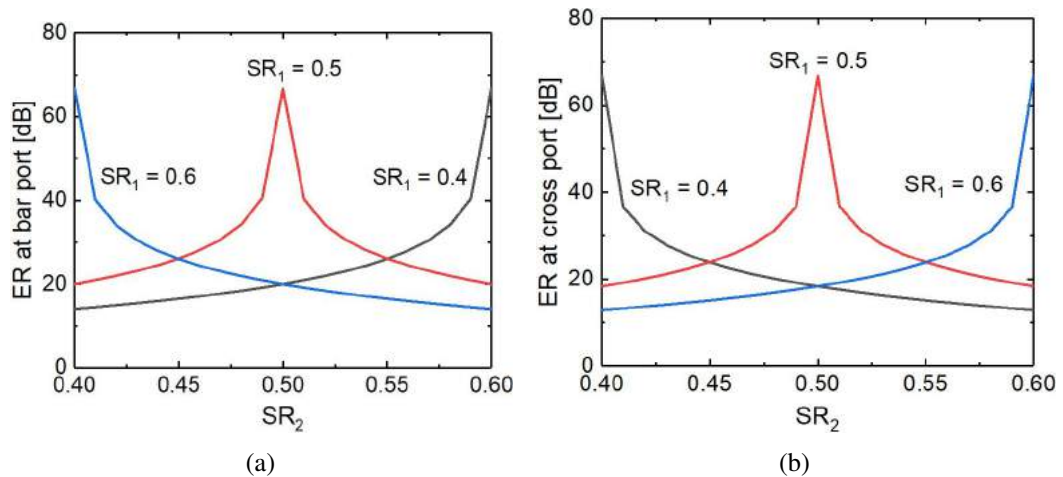
Figure 4.5: Extinction ratio (ER) at (a) the bar port and (b) cross port of an unbalanced MZI calculated as a function of SR_1 and SR_2.

of unbalanced MZI, any imbalance in 3-dB splitting ratios of the two WIDCs results in unequal extinction ratio (ER) at the two output ports (P_b and P_c). For example, Figure

4.4(b) shows the transmission characteristics calculated the bar- and cross-ports of MZI ($\Delta l = 100$ μm) for $SR_1 = 0.55$ and $SR_2 = 0.45$. To account this, we calculated the ERs as a function of SR_1 and SR_2 as shown in Figures 4.5(a) for bar port and 4.5(b) for cross port. These calculation helps to quantify the fabrication induced deviation in splitting ratios of MZIs.

4.2 Experimental Demonstration

We have demonstrated both balanced and unbalanced MZIs with input/output grating couplers (GCs) on a 220-nm SOI substrate. The fabrication details have been discussed earlier under section 2.3.1. Table 4.1 shows the list of fabricated MZIs in a sample S5. Different sets of devices were fabricated separately for balanced and unbalanced MZIs on the same sample (S5). A few devices (fabricated near the sample edges) were found to be defective due to over dose and other fabrication errors. In the following section, we discuss experimental results of some of the best devices.

Table 4.1: List of fabricated devices on sample (S5).

Sample	W, h, G	L_{DC}, Δl	Remarks
S5	W = 350 nm h = 160 nm G = 150 nm	L_{DC} = 4, 5, 6, 7 μm $\Delta l = 0$	Balanced MZI (WIDC with shallow/deeply etched access waveguides.
S5	W = 350 nm h = 160 nm G = 150 nm	L_{DC} = 4, 5, 6, 7 μm $\Delta l = 275$ μm	Unbalanced MZI (WIDC with shallow/deeply etched access waveguides.

Balanced MZI

The SEM images of fabricated 2×2 balanced MZI with 3-dB WIDCs (sample S5) are shown in Figures 4.6(a) (with shallow etched WIDC and waveguides defined in single step lithography) and 4.6(b) (with shallow etched WIDC and deeply etched waveguides fabricated in two step process). The two 3-dB WIDCs ($W \sim 350$ nm, $h \sim 160$ nm and $G \sim 150$ nm) of $L_{3dB} = 5$ μm, are expected to have nearly wavelength independent and identical splitting ratio (see Figure 2.31(b)). The access waveguides are designed with a bending radius of 180 μm so that the bend induced coupling can be ignored. The

measured power splitting characteristics (normalized with respect to reference waveguide) are found to be nearly wavelength insensitive over a broad range of wavelength as shown in Figure 4.6(c) (WIDC with shallow etched access waveguides) and 4.6(d) (WIDC with deeply etched access waveguides). The results are closely matching with

(a)

(b)

(c)

(d)
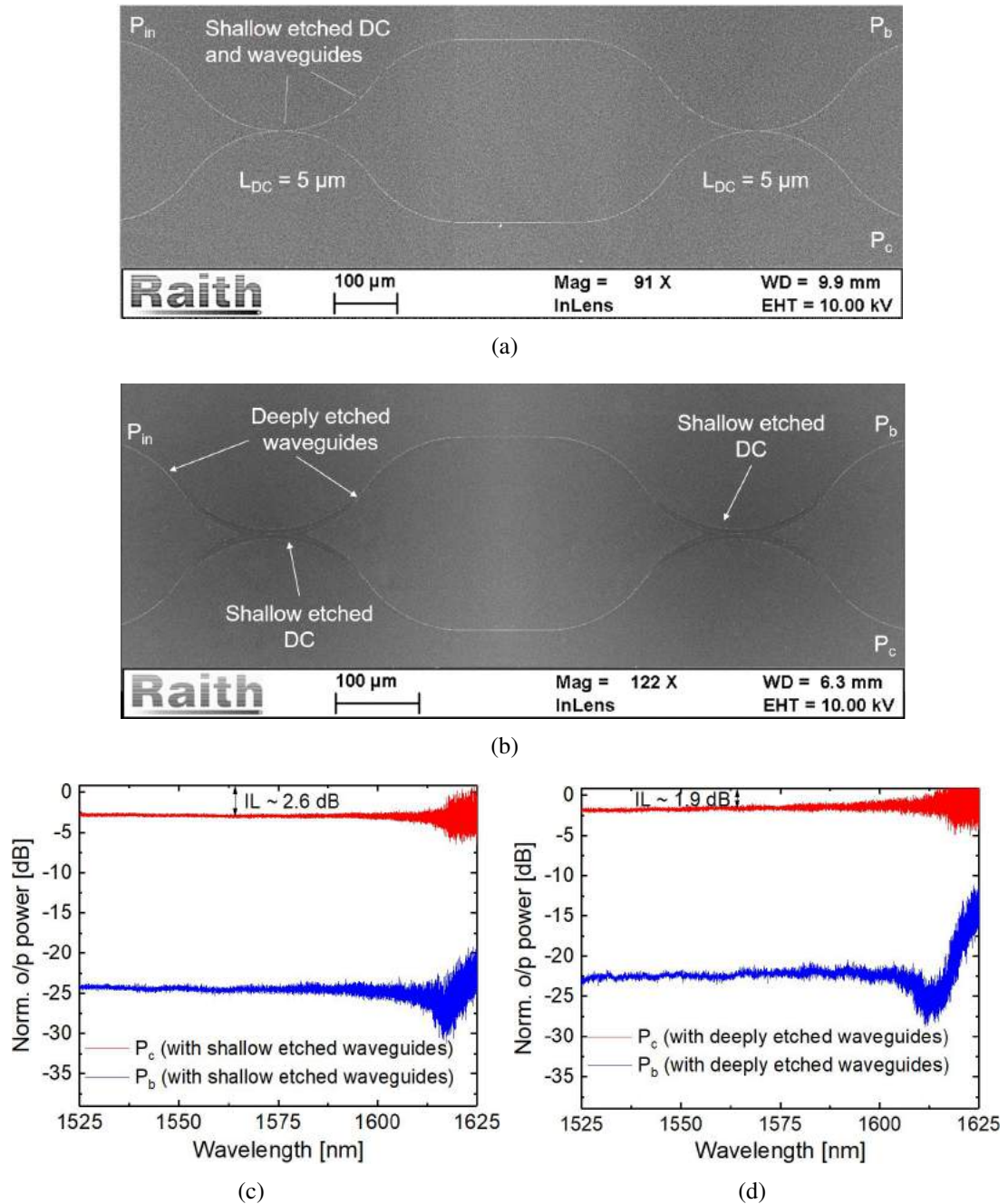
Figure 4.6: SEM images of balanced MZIs; (a) shallow etched WIDC and access waveguides ($h = 160$ nm) and (b) shallow etched WIDC and deeply etched access waveguides ($h \sim 0$ nm). (c) and (d) are normalized (with reference waveguide) transmission characteristics at the output ports (P_b, P_c) of MZIs in (a) and (b) respectively.

the simulated transmission characteristics. The maximum ER is measured to be not more than 25 dB, due to the slight imbalance in the splitting ratios of 3-dB WIDCs ($SR_1 + SR_2 < 1$) as discussed in the previous section 4.1. As we have observed earlier, the spectrum is modulated with increased oscillations at the longer wavelengths ($\lambda > 1610$ nm) because of the weaker coupling efficiency of input/output GCs, resulting into noise level detection limit of the photodetector. The demonstrated MZIs exhibit nearly wavelength independent insertion loss of $\sim 2.4 - 2.6$ dB in comparison to the reference waveguide. This is in accordance to the ~ 1.2 dB excess loss from each DCs as shown previously in Figure 2.33.

Unbalanced MZI

(a)

(b)   (c)
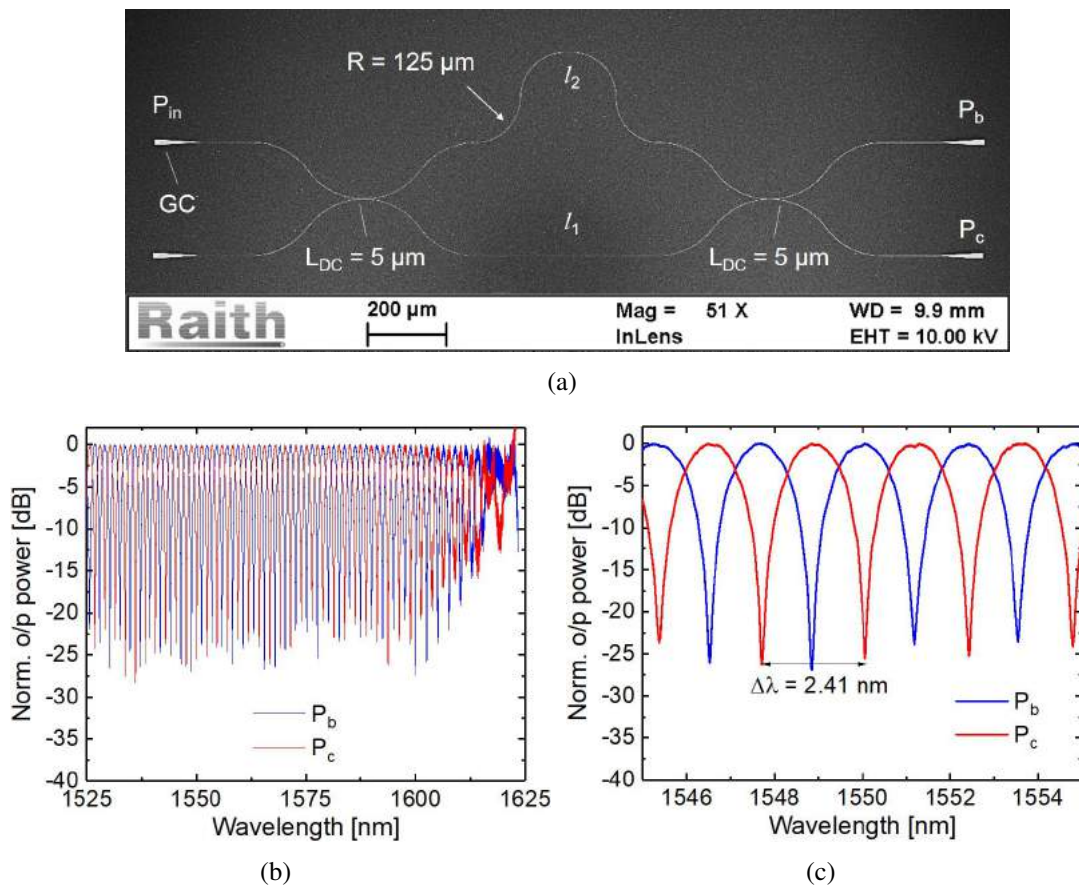
Figure 4.7: (a) SEM image and (b) normalized (to 0 dBm) transmission characteristics at the output ports of an unbalanced MZI ($\Delta l = 275$ μm) fabricated with 3-dB WIDCs; (c) zoomed-in view of (b) near $\lambda = 1550$ nm. GC - grating coupler.

The SEM image of fabricated WIDC ($L_{DC} = 5$ µm) based MZI with input and output grating couplers is shown in Figure 4.7(a). A minimum bend radius of $R = 125$ µm is provided to the semi-circular waveguide of the longer arm ($\Delta l = 275$ µm) for negligible bend induced loss. The normalized (to 0 dBm) transmission characteristics at the bar port and cross port are shown in Figure 4.7(b) with a zoomed-in view in Figure 4.7(c). The spectrum has unwanted noise modulations at longer wavelengths as seen in Fig, 4.6 due to poor coupling efficiency of input/output GCs. Interestingly, the ER at both the ports are measured to be nearly equal, i.e., ~ 25 dB. This confirms that the splitting ratio of both the WIDCs are nearly 3 dB. A similar transmission charac-

(a)   (b)
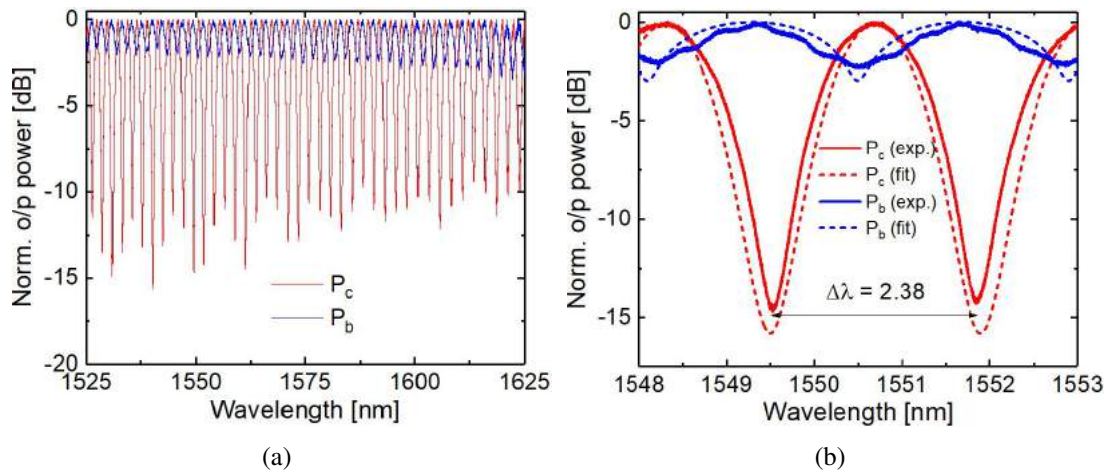
Figure 4.8: (a) Normalized transmission characteristics measured at the output ports of an unbalanced MZI with $L_{DC} = 7$ µm and $\Delta l = 275$ µm and zoomed-in view in (b) with theoretical fit to estimate the splitting ratios of WIDCs and n_g of waveguide near $\lambda = 1550$ nm.

teristics measured for an unbalanced MZI with $L_{DC} = 7$ µm (SR$_1$, SR$_2 > 3$ dB) is shown in Figure 4.8(a). Since $L_{DC} = 7$ µm corresponds to SR$_1$ = SR$_2 \sim 0.8$ (from Figure 2.29), one can expect maximum ER in cross port ($10 - 15$ dB) according to the theoretical calculations given in Figure 4.5. The transmission characteristics has been theoretically fitted using Eq. 4.2. The splitting ratio and n_g are extracted to be 0.75 and 3.76 (Eq. 4.4), respectively, which are consistent with the theoretical calculations. The FSR of the spectrum is measured to be ~ 2.4 nm which is closely matching with the theoretical calculations (2.48 nm) using Eq. 4.4. The wavelength dependent FSR ($\Delta\lambda$ and $\Delta\nu = c\Delta\lambda/\lambda^2$) measured at the cross (or bar) port of the above discussed MZI is shown in Figure 4.9. Note that, $\Delta\lambda$ increases with wavelength (since n_g is a function

of wavelength) while $\Delta\nu$ is nearly constant ($\sim$ 295 GHz).
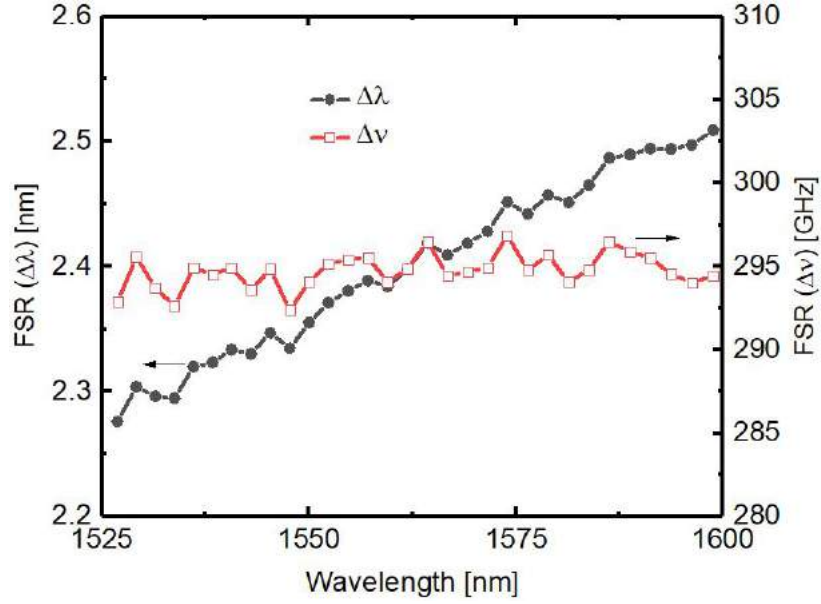
Figure 4.9: Wavelength dependent FSR ($\Delta\lambda$ and $\Delta\nu$) measured at the cross (or bar) port of MZI discussed in Figure 4.8.

More compact MZIs can be demonstrated with deeply etched access waveguides after selectively masking the GC and DC region as discussed in section 2.2.4. A SEM image of 3-dB WIDC based MZI with deeply etched waveguides is shown in Figure 4.10(a). The corresponding normalized (with 0 dBm) transmission characteristics at the output ports are shown in Figure 4.10(b). A close-up view of the spectrum near $\lambda = 1550$ nm is shown in Figure 4.10(c). A nearly uniform and high interference extinctions over the entire wavelength band is observed, which bears the signature of the properties of WIDCs. It is to be noted that, the ER at the bar port ($\sim$ 35 dB) and cross port ($\sim$ 20 dB) are differs by $\sim$ 15 dB, due to the imbalance in splitting ratios of the two WIDCS as discussed in section 4.1. Further optimization is needed at the bend regions of the WIDC mask during second step fabrication process to reduce the non-uniformity in extinction ratio. As expected, the measured FSR ($\sim$ 2.01 nm) is lower than that of MZI with shallow etched waveguides since deeply etched waveguide has higher Δn_g (4.7).
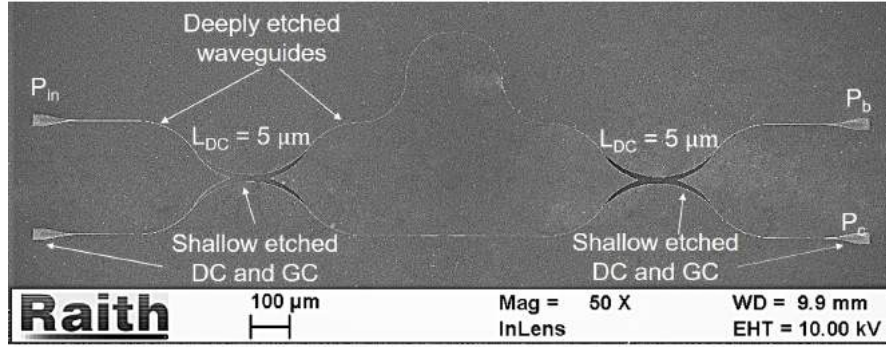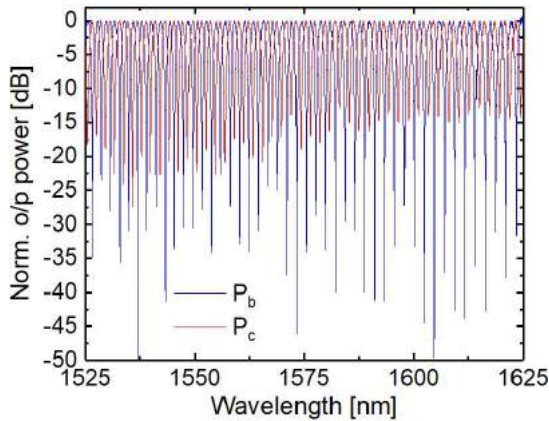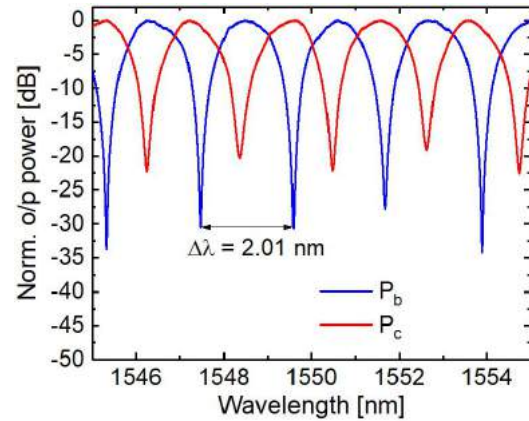
Figure 4.10: a) SEM image of a fabricated WIDC based unbalanced MZI ($\Delta l = 275$ μm) with deeply etched ($h \sim 0$ nm) access waveguides; (b) normalized (to 0 dBm) transmission characteristics at the output ports; (c) zoomed-in view of (b) near $\lambda = 1550$ nm.

4.3 Summary

The transmission characteristics of MZIs (balanced and unbalanced) with WIDCs have been studied theoretically as well as experimentally. Both balanced and unbalanced MZIs exhibit a nearly wavelength independent extinction ratio of ~ 25 dB with an excess loss of 2.2 dB over a broad wavelength range (1525 nm $\leq \lambda \leq$ 1625 nm). The performance of deeply etched waveguide based broadband MZIs demonstrated in a second step fabrication process has been evaluated and compared with shallow etched waveguide based broadband MZIs.

These devices can be employed in various applications like on-chip $N \times N$ MZI based optical switches and routers where wide optical bandwidth is required to accommodate multiplexed WDM channels from different on-chip servers. In such ap-

plications, the transmission characteristics are controlled actively by integrating micro-heaters in any one of the MZI arms. We have presented the design and demonstration of a basic wavelength insensitive MZI switching cell in the following chapter.

CHAPTER 5

Broadband Thermo-optic Switches

The importance of broadband switches and two important switch configurations using MRR and MZI have been discussed in chapter 1. In this chapter we discuss about the design and demonstration of thermo-optic switches designed with broadband MZIs and metal-integrated waveguide phase-shifters. In general, integrated optical MZI switches are realized by integrating a phase-shifter in one of the arms of the balanced MZI. The phase of the propagating optical mode can be controlled by changing the refractive index of the waveguide core by thermo-optic effect (microheaters) or plasma dispersion effect (p-n junction diodes) [120]. The plasma dispersion effect is relatively faster (> 10 GHz) [121] compared to the thermo-optic effect in silicon, but intrinsic free-carrier absorption makes it unsuitable for some applications . On the other hand, thermo-optic effect in silicon is inherently loss-less and can be implemented easily with a metal strip or doped p/n resistive heaters [122]. Since the WIDC based MZI devices under discussion are designed with shallow-etched waveguide geometry (h = 160 nm) supporting only the TE-polarized fundamental mode and thus it has been possible to take advantage of direct heating of one of the MZI arms by depositing a metal-microheater directly on the slab but with a safe distance from the guided mode so that metallic absorption is minimized. Prior to the discussion of our proposed thermo-optic switches, we briefly review some of the demonstrated thermo-optic switches with integrated metal-microheaters and their figure of merits (FOMs).

Integrated metal-strip microheaters are widely used for reconfigurable silicon photonics devices because of large thermo-optic coefficient (TO) in bulk silicon crystal ($dn/dT = 1.86 \times 10^{-4}$ K^{-1}) [123] and they can be implemented easily by front-end integration. Some important applications are reconfigurable wavelength filtering [124, 125, 126], wavelength interleavers [127], tunable directional couplers [128], large scale optical switch matrices for WDM systems [129, 130, 131], etc. In all these examples, metallic microheater strip lines are suitably integrated close to waveguides, acting

as waveguide thermo-optic phase-shifters. The phase shift is directly proportional to the temperature rise in the waveguide and its effective length [132]. Again, the temperature rise in the waveguide is proportional to the electrical power consumed as Joule heating effect in metallic microheater. Therefore, the power efficiency is greatly improved by clever design of waveguide phase-shifter system. Typically, waveguide core is heated through the top cladding oxide using metallic (Ti, TiN, CrAu, NiCr, etc) microheater strip-line integrated directly above the waveguide [133, 134]. Recently, 2D material (graphene) is also used for low power and faster thermo-optic tuning [135]. However, the technology described in case of graphene based microheater is not suitable for large-scale wafer-level integration. An attractive meander-type metal microheater design over the oxide cladding of spiraled long waveguide (Figure 5.1(a)) was reported earlier exhibiting lower switching power (Pπ = 6.5 mW) and extremely small switching temperature (ΔT_π = 0.67K) [136]. However, the reported switching time (τ_{th} = 14 µs) and optical insertion loss in spiraled waveguide section (IL = 6.5 dB) are relatively large. A few other efforts in switching power reduction were reported by selectively removing the cladding oxide and giving undercuts to the waveguide [137, 138, 139]. An example of suspended waveguide with oxide undercuts is shown in Figure 5.1(b) [138] where the waveguide is heated by TiN microheater integrated in the top oxide. However, the switching time of those phase-shifter designs are in the order of few hundreds of microseconds. In contrast, metallic-microheaters integrated directly on the waveguide slab are shown to be relatively faster ($\tau_{th} \sim$ 5 µs), but at the cost of large switching power (P$_\pi \sim$ 50 mW) [126, 132].

Therefore, it remains a challenging task to design a silicon photonics thermo-optic switch fulfilling all desired features, viz. broad optical bandwidth, lower on-state switching power and switching time, compact design for large scale integration, lower optical insertion loss, etc. There is a little effort seen so far for a detail design and modeling of metallic microheater integrated waveguide phase-shifters. Very recently, Bahadori *et al.* reported a compact model describing detail dc and transient characteristics of microheater-ring resonator system in silicon photonics platform [15]. Atabaki *et al.* investigated earlier with numerical simulations followed by experimental demonstration estimating some figure of merits (FOMs) of metallic microheaters used for silicon photonics applications [134]. However, the authors in their model concentrated only on the
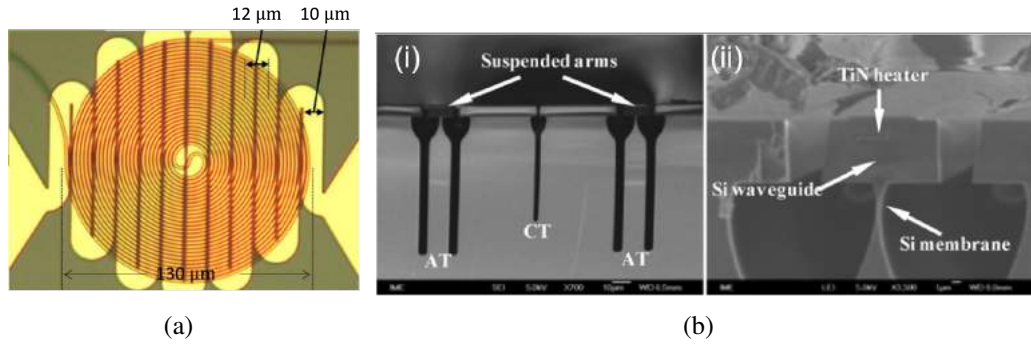
Figure 5.1: (a) Double spiral waveguide geometry with thin-film folded metallic micro-heater deposited over the top oxide cladding [136]. (b) Cross-sectional SEM images of the thermo-electric optical switch with suspended arms (AT: arm trenches; CT: central trench) in (i) and cross-section of the suspended arm in (ii) [138]

width of microheater strip-line and the effect of cladding oxide thicknesses.

In this chapter, we are presenting an MZI based 2×2 thermo-optic switching cell designed with WIDCs for 3-dB power splitters and a slab integrated metal-microheater in one of the MZI arms. Detailed theoretical analysis and performance optimization of various metal-microheater integrated waveguide phase-shifter configurations have been presented in 5.1. Switching characteristics of temperature insensitive WIDC based MZI switches are discussed in 5.2. In section 5.3, integration of microheaters with CMOS compatible process flow and experimental demonstration of different types of MZI based switches are discussed. The measured static and transient switching characteristics are also discussed in this section. In the end, a conclusion comparing earlier reported close results is outlined in Section 5.4.

5.1 Phase-Shifter Design and Analysis

In this section we discuss the design and theoretical analysis of waveguide phase-shifters integrated with metallic microheater. The FOMs of a thermo-optic phase-shifter (switching power, time and temperature, compactness, optical insertion loss, etc.) can be improved by optimizing the waveguide design parameters as well as positioning of the microheater and thermal insulation properties (heat capacity and conductance) of the system.

89

5.1.1 Thermo-optic phase shifter

In this work, Ti is preferred as the heating element because of its high melting point, high resistivity and ensures no serious electro-migration happens at higher temperatures.

The thermo-optic phase shift of light travelling through the waveguide is given by [136]:

$$\Delta\phi(\lambda, \Delta T) = \frac{2\pi}{\lambda} \cdot \frac{\partial n_{eff}(T, \lambda)}{\partial T} \cdot \Delta T \cdot L_w \tag{5.1}$$

where, n_{eff} is the effective index of the guided mode, and L_w is the length of waveguide which is heated to a uniform differential temperature of ΔT. Thus, for a given L_w, the rise in waveguide temperature for π phase-shift at an operating wavelength λ is given by:

$$\Delta T_\pi \cdot L_w = \frac{\lambda}{2} \cdot \left(\frac{\partial n_{eff}}{\partial T}\right)^{-1} \tag{5.2}$$

Since the value of $\frac{\partial n_{eff}}{\partial T}$ is nearly a constant ($\sim 1.79 \times 10^{-4}$ K^{-1} at $\lambda \sim 1550$ nm) for silicon photonic wire waveguide, the value of $\Delta T_\pi \cdot L_w$ is also constant ($\sim 4.33 \times 10^3$ K·µm). Thus the operating range of differential temperature in the waveguide can be kept lower by simply increasing waveguide length as described by Densmore *et al.* [136]. Further, the steady-state temperature rise (ΔT_s) in waveguide core is directly proportional to the Joule heating power consumption by a resistive/metallic microheater. The thermal sensitivity S_H of the phase shifter can be defined as:

$$\Delta T_s = S_H \cdot p_w \tag{5.3}$$

where p_w is the Joule heating power consumption by the microheater normalized to unit length of the waveguide phase-shifter. Thus the higher value of S_H ensures lower power consumption and/or shorter length of the waveguide phase-shifter for a desired phase-shift of the guided mode, but at the cost of higher operating temperature.

On the other hand, the transient waveguide temperature rise $\Delta T(t)$ can be expressed as:

$$\Delta T(t) = \Delta T_s(1 - e^{-t/\tau_{th}}) \tag{5.4}$$

In the above equation, the thermal response time $\tau_{th} = \mathcal{H}/\mathcal{G}$, where $\mathcal{H}$ is the thermal capacity and $\mathcal{G}$ is the conductance of the waveguide-microheater system. Since these parameters depend on waveguide core and cladding materials, waveguide cross-sectional geometry, microheater positioning relative to waveguide core, etc., the value of τ_{th} can be estimated numerically by solving Fourier's heat equation using FDTD method. However, for a given waveguide phase-shifter, one can estimate waveguide characteristic thermal parameters h_w ($= \mathcal{H}/L_w$) and g_w ($= \mathcal{G}/L_w$). This results into a new expression for waveguide thermal response time:

$$\tau_{th} = \frac{h_w}{g_w} \tag{5.5}$$

Further, for a steady-state temperature rise of ΔT_s of the waveguide-microheater system, the required electrical power is given by $P_e = \Delta T_s \cdot \mathcal{G}$. This again boils down to $p_w = \Delta T_s \cdot g_w$ according to our definitions. Thus the thermal sensitivity expressed in Eq. 5.3 can be re-written as:

$$S_H \cdot g_w = 1 \tag{5.6}$$

It is now obvious that for an efficient design of thermo-optic waveguide phase-shifter, we must assure higher thermal sensitivity S_H and lower thermal response time τ_{th}. Therefore, the corresponding figure of merit ($\mathcal{F}_H$) may be expressed as:

$$\mathcal{F}_H = \frac{S_H}{\tau_{th}} = \frac{\Delta T_s \cdot L_w}{P_e \cdot \tau_{th}} = \frac{1}{h_w} \Rightarrow \mathcal{F}_H \cdot h_w = 1 \tag{5.7}$$

Higher the value of S_H, one can ensure a shorter design of waveguide phase-shifter. In other words, a compact and efficient thermo-optic waveguide phase-shifter can be designed by simultaneously achieving lower effective thermal conductance g_w and higher effective heat capacity h_w. Moreover, closer proximity of microheater to the waveguide core ensures higher value of S_H. However, one must take care about additional optical attenuation of the guided mode due its evanescent tail overlap with the metallic microheater.
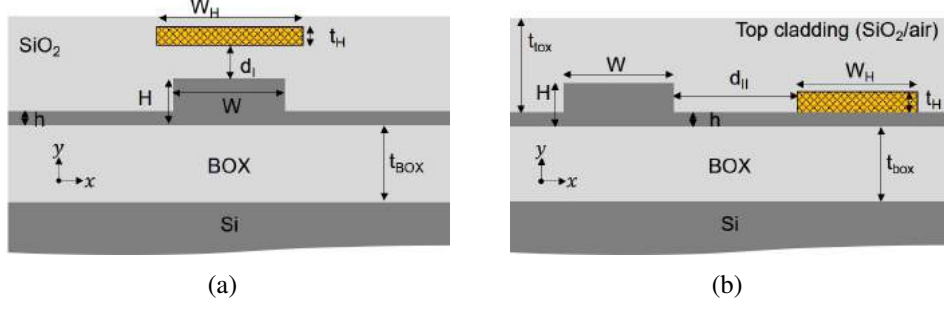
Figure 5.2: Schematic cross sectional views of two thermo-optic waveguide phase-shifter architectures along with important design parameters: (a) microheater directly integrated on top of the oxide cladding directly above the waveguide and (b) microheater directly integrated on the slab of the waveguide beneath the top oxide/air cladding.

5.1.2 Performance Analysis

For performance analysis, we have considered two different waveguide microheater configurations, commonly used for integrated optical thermo-optic phase-shifter in SOI platform as shown in Figure 5.2. According to Atabaki *et al.*, the two configurations shown in Figure 5.2(a) and Figure 5.2(b) are categorized as Type-I and Type-II architectures, respectively [140]. It was shown with detail analyses that the Type-II microheaters are superior than that of Type-I microheaters in terms of thermal response time of a micro-disk resonator. To analyze the performance of a Type-I or Type-II waveguide phase-shifter, we need to consider waveguide parameters like width W, slab height h, and the lateral distances of microheater to waveguide d_I (d_{II}) for Type-I (Type-II) as defined in the figures. As discussed earlier, the thermal power consumed per unit length of the waveguide phase shifter (p_w) is an important parameter, the width (W_H = 1 μm) and thickness (t_H = 100 nm) of a Ti metallic microheater strip is assumed same for both types of architectures [134]. Moreover, following the standards of silicon photonics foundries, we have considered device layer thickness of H = 220 nm and BOX layer (SiO$_2$) thickness of t_{BOX} = 2 μm.

For a given design of SOI waveguide geometry (W, H, and h) discussed above, the thermal properties (thermo-optic efficiency and response time) of the waveguide phase-shifter are mainly determined by the waveguide slab layer thickness h, lateral distance of microheater d_I or d_{II} and top cladding material SiO$_2$ or Air. In order to in-

vestigate thermo-optic FOMs like S_H and τ_{th} we have considered TE_0 mode guidance (refer Figure 2.2(a) and 2.2(b)) in waveguides with $W = 350$ nm and $0 \leq h \leq 200$ nm for both Type-I and Type-II architectures. The important properties of core Si, cladding SiO$_2$, and microheater Ti-strip used for numerical simulation are given in Table 5.1. The thickness dependent thermal conductivities (see Figure 5.3) [141] were appropriately considered for solving the heat transport equation [142] using COMSOL Multiphysics [143] with appropriate boundary conditions at the interfaces as described in Ref. [134]. To start with, we have simulated the steady-state values of tempera-

Table 5.1: The values of various thermal and electrical parameters like specific heat capacity (c_v), material mass density (ρ_m), thermal conductivity (k_T), electrical conductivity (σ), thermal expansion coefficient (α_c), refractive index (n) used for Ti, Si and SiO$_2$ in calculating thermo-optic effects. They are either taken as default values from the library of COMSOL Multiphysics simulator or from available literatures [141, 143, 144, 145].

Property	Ti	Si	SiO$_2$
c_v [J/(Kg.K)]	544	700	730
ρ_m [kg/m^3]	4506	2329	2200
k_T [W/(m.K)]	21.9	15-140	1.4
σ [S/m]	2.6×10^6	8.7	10^{-15}
α_c [1/K]	8.6×10^{-6}	2.6×10^{-6}	0.5×10^{-6}
n ($\lambda \sim$1550 nm)	$3.6848 + j4.6088$	3.4447	1.444

ture rise (ΔT_s) at the waveguide core (W = 350 nm, H = 220 nm, h = 100 nm) as a function of electrical power dissipation per unit length (p_w) of waveguide due to positioning of Ti strip microheaters (W_H = 1 μm and t_H = 100 nm) at $d_I = d_{II} = 1$ μm. The schematic layout (cross-section) of simulation region in COMSOL is shown in Figure 5.4 with necessary boundary conditions, assuming the initial condition of the device is $T_0 = 300$K. The simulated temperature distributions across the Type-I and Type-II (oxide cladding and air cladding) architectures are shown in Figure 5.5 for an applied microheater power. As expected, the ΔT_s vs. p_w plots shown in Figure 5.6(a) are following the linear relationship as defined in Eq. 5.3. It is evident that the sensitivity S_H for Type-I architecture (195 K·μm/mW) is reasonably higher than that of Type-II architectures ($\sim$130 K·μm/mW). This is expected due to the large thermal conductivity
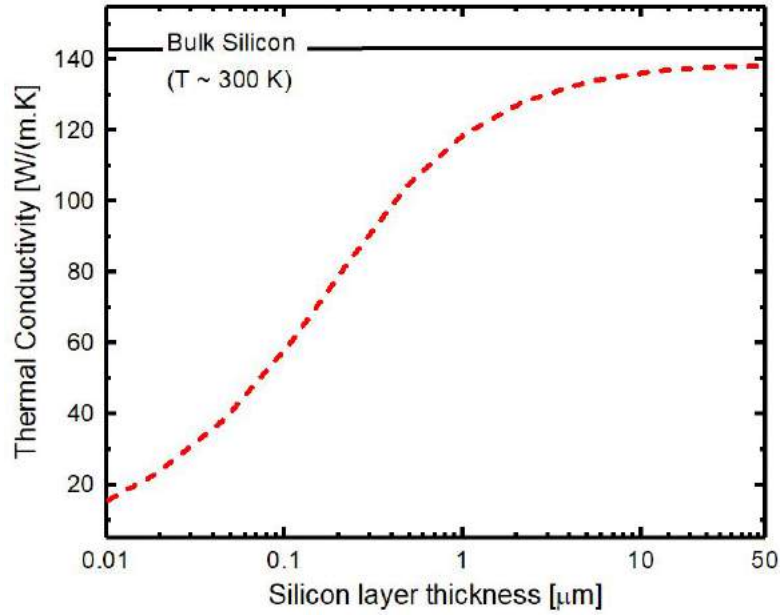
Figure 5.3: Thickness dependent thermal conductivity of silicon layers at room temperature [141].
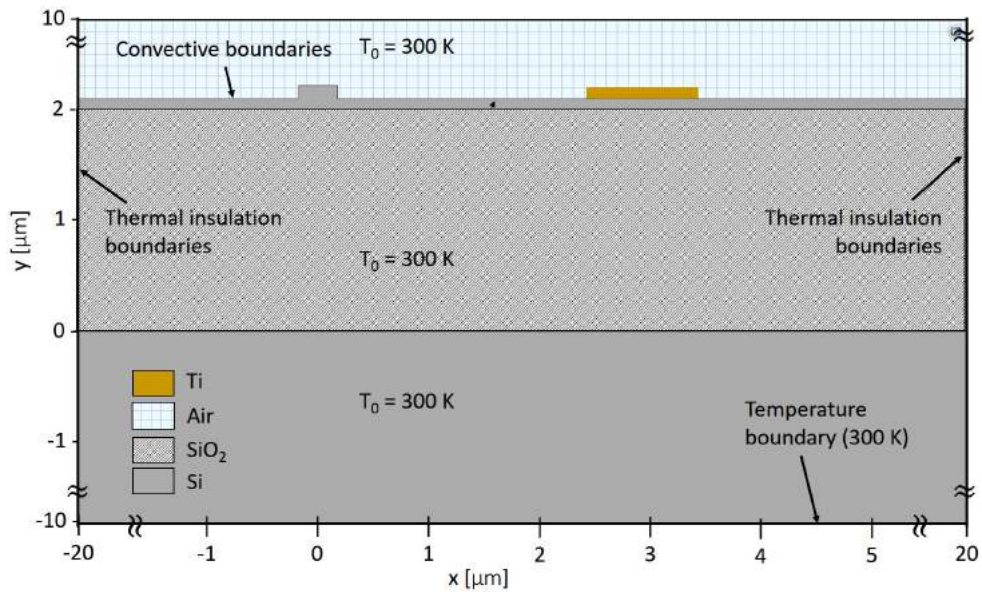
Figure 5.4: The schematic layout (cross-section) of simulation region in COMSOL with necessary boundary conditions, assuming the initial condition of the device is $T_0 = 300$K: convective heat flow to the top boundaries, thermal insulator boundaries to the side boundaries (> 20 µm away from the waveguide) and bottom of the substrate is at room temperature (300K).

of silicon slab ($h = 100$ nm) which increases the effective thermal conductance (g_w) of the slab-heating configuration and hence S_H reduces (Eq. 5.6) compared to oxide-heating. However, it is also observed that the value of S_H for Type-II (air cladding) is slightly higher than that of Type-II (oxide cladding). This is attributed to the lower
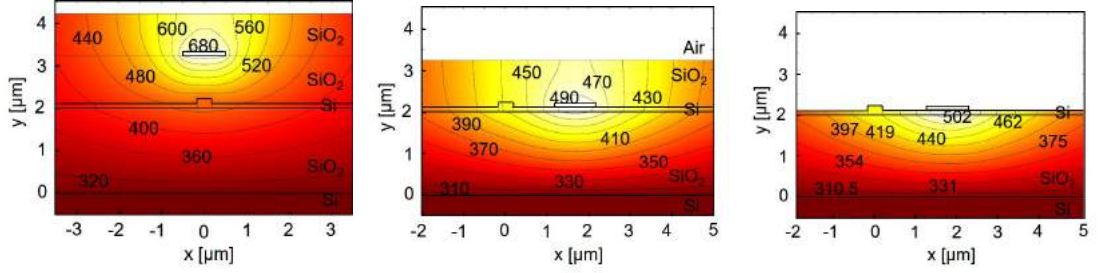
Figure 5.5: Steady state cross sectional temperature distribution (ΔT_s) extracted from 3-D simulation for Type-I, Type-II (oxide cladding), and Type-II (air cladding) waveguide phase-shifters calculated for an applied electrical power of (p_w) of 1 mW/μm ($W = 350$ nm, $H = 220$ nm, $h = 100$ nm, $t_H = 100$ nm, $W_H = 1.0$ μm and $d_{I,II} = 1$ μm).
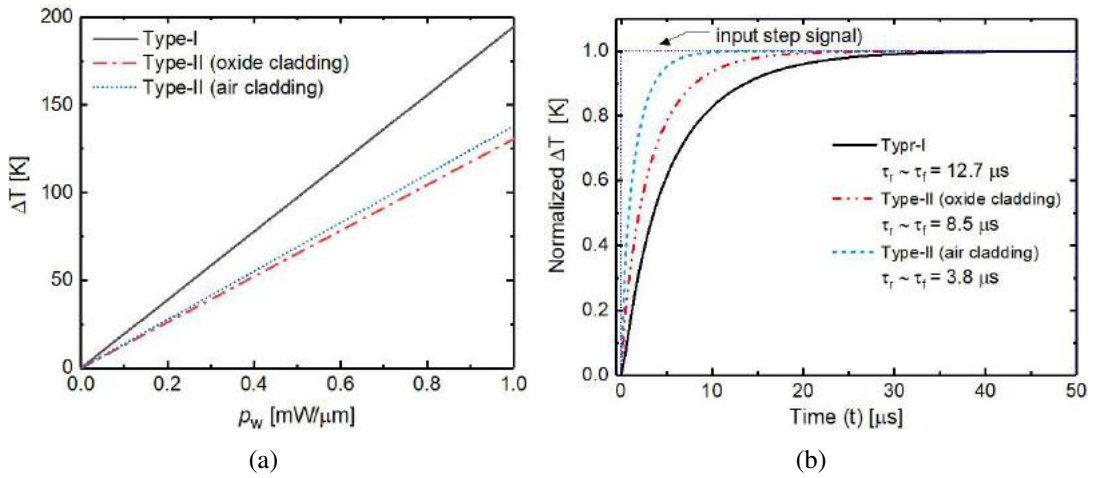
Figure 5.6: Simulation results for estimating thermal sensitivity S_H and response time τ_{th} for Type-I, Type-II (oxide cladding), and Type-II (air cladding) waveguide phase-shifters (see text for design parameters): (a) calculated steady-state temperature rise (ΔT_s) of the waveguide core as a function of electrical power dissipation per unit length of waveguide phase-shifter, and (b) transient temperature rise $\Delta T(t)$ normalized to ΔT_s as a function time for a unit step-function excitation of input voltage signal to the microheaters.

thermal conductivity of air cladding than that of SiO_2. The transient response of the temperature rise $\Delta T(t)$ in the waveguide core is evaluated by exciting the microheater with a step input voltage signal at $t = 0$. The simulated results (with ΔT_s normalized to unity) for the above mentioned Type-I and Type-II architectures are shown in Figure 5.6(b). The thermal response time τ_{th} estimated for Type-I, Type-II (oxide cladding), and Type-II (air cladding) are 12.7 μs, 8.5 μs, and 3.8 μs, respectively. Thus the above simulation results confirm that top oxide cladding results into an effective increase of thermal conductance (g_w) and/or effective decrease of thermal capacitance (h_w). The

95
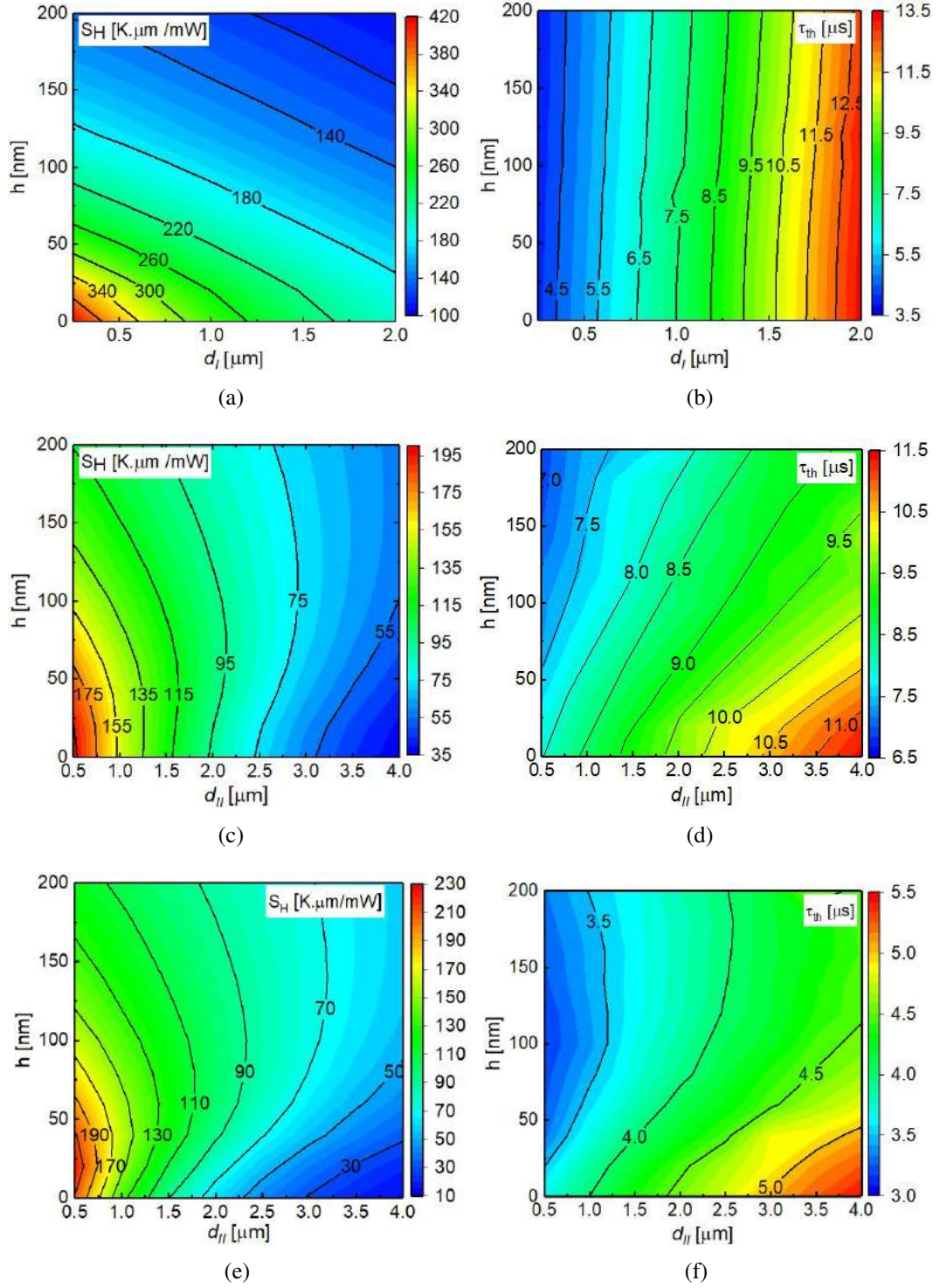
Figure 5.7: Contour plots of S_H in K·μm/mW and τ_{th} in μs calculated in the $d_{I,II} - h$ plane for (a, b) Type-I, (c, d) Type II (oxide cladding) and (e, f) Type-II (air cladding) heater architectures.

proximity of microheater to the waveguide core also play a role in reducing the value of τ_{th} as well as increasing S_H.

A more detailed simulation results for S_H and τ_{th} as a function of both h and d_I or d_{II} are shown in color contour plots in Figure 5.7. Note that, irrespective of the heater configuration (oxide-heating or slab heating), S_H reduces with respect to $d_{I,II}$ and h because of the increase in effective thermal conductance (g_w). In contrast, τ_{th} increases with $d_{I,II}$. Though g_w of the system increases with h, the value of τ_{th} remains unaffected w.r.t. h for oxide-heating, since the waveguide core is heated right from the top at a constant distance of d_I. We notice that the value of S_H can be as high as 350 K·μm/mW and τ_{th} is as low as 4.5 μs for a Type-I configuration with $h < 25$ nm and $d_I < 250$ nm. On the other hand, they are > 190 K·μm/mW (> 220 K·μm/mW) and < 8.0 μs (< 4 μs) for a oxide clad (air clad) Type-II configuration with $h < 50$ nm and $d_{II} < 500$ nm. Thus the studies help for maximizing the figure of merit $\mathcal{F}_H$ of the waveguide phase-shifter defined by S_H/τ_{th}. In doing so, one needs to minimize the value of d_I or d_{II}. However, closer proximity of metal microheater to the waveguide introduces optical attenuation of the guided mode because of plasma dispersion effect through evanescent field overlap. We have numerically estimated (using Lumerical's MODE Solutions) the optical loss co-efficient (α_h) for TE_0 guided mode as a function of $d_{I,II}$ (considering h as a parameter) with complex refractive index of Ti-strip (W_H = 1 μm, t_H = 100 nm) as $3.6848 + j4.6088$ at $\lambda = 1550$ nm [145]. This has been shown in Figs. 5.8(a) and 5.8(b) for Type-I and Type-II (oxide cladding, air cladding) respectively. As expected α_h (expressed in dB/mm) increases as the value of d_I or d_{II} decreases. However, for type-II configuration (with a given d_{II}), α_h increases with slab height due to poor confinement of the optical mode inside waveguide core. Whereas, for type-I (with a given d_I), the evanescent field-strength along y direction reduces with h and hence α_h reduces. It must be noted that the α_h is nearly same for oxide cladding and air cladding in Type-II configuration. Nevertheless, the metallic losses are negligibly small ($\alpha_h < 0.1$ dB/mm) for $d_{I,II} > 0.5$ μm.

It is worth mentioning here that we have restricted our above numerical studies for a straight waveguide phase-shifter where both waveguide and metallic microheater strip-line are parallel to each other for both Type-I and Type-II architectures. However, one can extend this study to spiraled waveguide geometry and meander-type metallic microheater in Type-I configurations as described in Ref. [136]. From their experimental results, we estimate the value of S_H as large as ~ 640 K·μm/mW. Similarly, for a bend
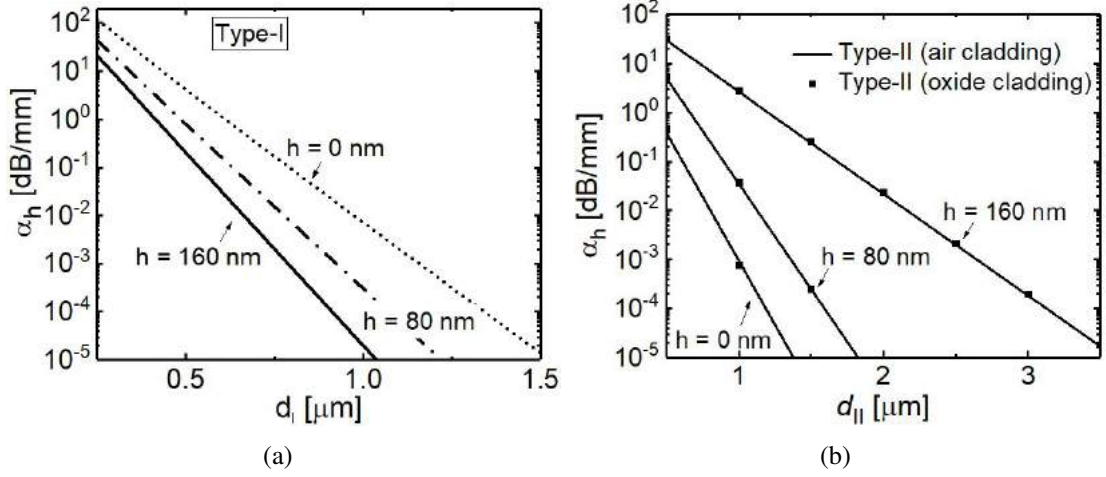
Figure 5.8: Calculated optical loss coefficient α_h of TE_0 mode in dB/mm (λ = 1550 nm) due to interaction between evanescent field and metallic microheater as a function of d_I for Type-I and d_{II} for Type II with h as a parameter: (a) Type-I and (b) Type-II (oxide cladding and air cladding). The calculations are carried out for W = 350 nm and H = 220 nm.

or folded waveguide (and microheater) design in Type-II configuration, the value of S_H can be enhanced significantly. This has been validated with numerical simulations as well as experimental results described in following section.

5.2 MZI based Thermo-optic Switch Design

As a case study we have evaluated the performance of Type-II phase shifter integrated MZI switches. Three variants of the MZI based 2×2 thermo-optic switches have been investigated (i) balanced MZI with straight waveguide phase-shifter (balanced S-MZI), (ii) balanced MZI with folded waveguide phase-shifter (balanced F-MZI), and (iii) unbalanced MZI with folded waveguide phase shifter (unbalanced F-MZI). The topological architecture of all the three variants are shown in Figures 5.9(a), 5.9(b) and 5.9(c) respectively. All the three device architectures are designed with identical pair of single-mode rib waveguides and identical pair of WIDCs for 3-dB couplers. The values of design parameters ($W \sim 350$ nm, $H = 220$ nm, $h \sim 160$ nm, and $G \sim 150$ nm) have been chosen judiciously to avail a nearly wavelength independent coupling co-efficient κ within and beyond C-band.

In presence of the thermo-optic phase -shifter, the wavelength dependent propaga-

(a)

(b)

(c)
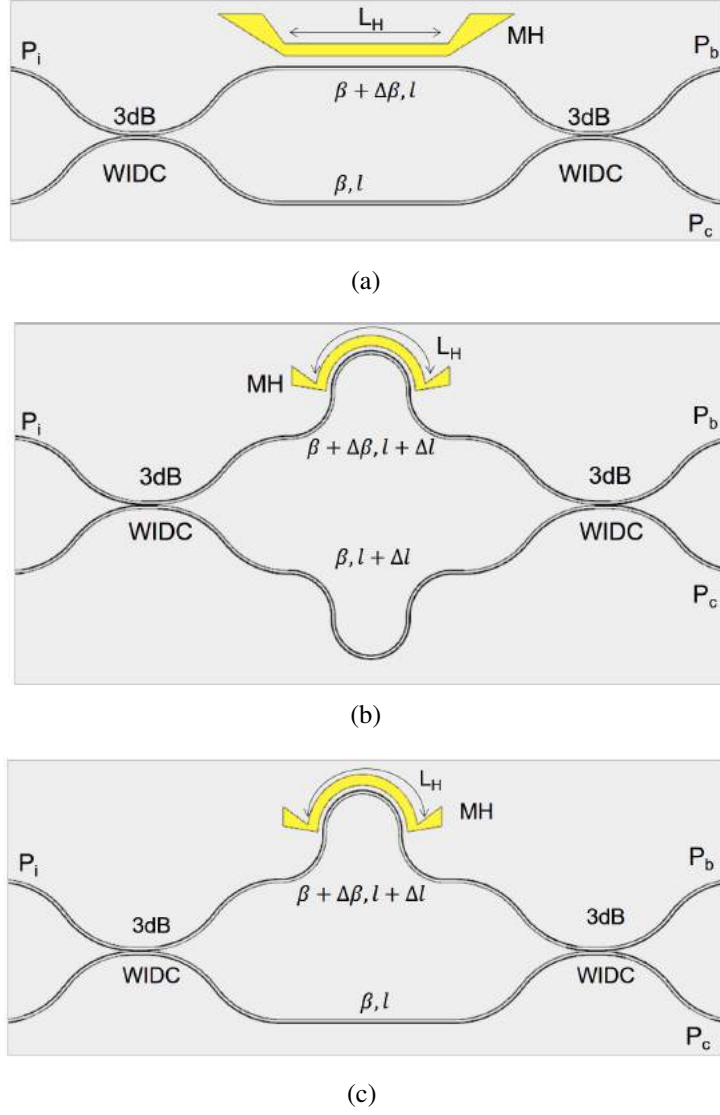
Figure 5.9: Schematic top views of the three variants of the proposed MZI based 2×2 thermo-optic switches: (a) balanced MZI with straight waveguide phase-shifter (balanced S-MZI), (b) balanced MZI with folded waveguide phase-shifter (balanced F-MZI), and (c) unbalanced MZI with folded waveguide phase shifter (unbalanced F-MZI).

tion matrix of MZI arms (Eq. 4.3) can be expressed as:

$$\mathcal{T}_M(\lambda, \Delta T) = e^{-j\phi(\lambda)} \begin{bmatrix} e^{-j\Delta\phi_t(\lambda, \Delta T)} & 0 \\ 0 & 1 \end{bmatrix} \qquad (5.8)$$

where $\phi(\lambda) = \beta l$ and $\Delta\phi_t(\lambda, \Delta T) = (\beta + \Delta\beta)(l + \Delta l) - \beta l$. Again $\beta = (2\pi/\lambda)n_{eff}(\lambda)$ and $\Delta\beta = (2\pi/\lambda)\Delta n_{eff}(\lambda, \Delta T)$ are the propagation constant at $\Delta T = 0$K and change in propagation constant due to thermo-optic effect, respectively. Thus the amplitude

transfer function of MZI given in Eq. 4.2 can be modified as:

$$\begin{bmatrix} S_b(\lambda, \Delta T) \\ S_c(\lambda, \Delta T) \end{bmatrix} = \mathcal{T}_{DC}(\lambda, \Delta T) \cdot \mathcal{T}_M(\lambda, \Delta T) \cdot \mathcal{T}_{DC}(\lambda, \Delta T) \begin{bmatrix} 1 \\ 0 \end{bmatrix} \tag{5.9}$$

However, the 3-dB DC design must be temperature insensitive, otherwise, the splitting ratio difference introduces power imbalance in the output. In the following section we discuss about the athermal property of our previously discussed rib waveguide DC geometry in SOI.

5.2.1 Thermal Stability of WIDCs

In particular, the temperature dependent effective index variation of SOI waveguides induces wavelength shift of resonant devices that limits the wavelength resolution in applications such as sensing, wavelength division multiplexing , spectroscopy, etc. Several active and passive thermal compensation techniques have been proposed for stabilizing the device performances. One active approach is heating silicon locally and thereby dynamically compensate the thermal fluctuations [146, 147]. However, active compensation techniques require extra power for cooling and controlling. Passive thermal compensation methods proposed in Ref. [148, 149] use a negative TO coefficient polymer over cladding, but not all polymers are CMOS compatible. An alternate solution for interference-based devices is employed in Ref. [150] by tailoring the optical confinement in the waveguide. However, all these thermal compensation methods contribute additional fabrication complexities or absorption loss or wavelength dependency. Interestingly, in addition to the wavelength independent transmission, our WIDC design is also found to be temperature insensitive.

The effective index variation of a SOI waveguide depends on the TO coefficients of core and claddings. For an asymmetric rib waveguide geometry with SiO_2 as bottom cladding (n_{SiO_2}) and air top cladding ($n_{air} = 1$) this can be expressed as [151]:

$$\frac{dn_{eff}}{dT}(\lambda) = \Gamma_{Si}(\lambda)\frac{dn_{Si}(\lambda)}{dT}(\lambda) + \Gamma_{SiO_2}(\lambda)\frac{dn_{SiO_2}}{dT}(\lambda) \tag{5.10}$$

where we assume that the confinement factor of core ($\Gamma_{Si}(\lambda)$) and cladding ($\Gamma_{SiO_2}(\lambda)$)

are assumed to be temperature independent. Also we can neglect the wavelength dependency on TO coefficients of SiO_2 cladding. Since dn_{SiO_2}/dT is an order of magnitude less than dn_{Si}/dT, we can write:

$$\frac{dn_{eff}}{dT}(\lambda) = \Gamma_{Si}(\lambda)\frac{dn_{Si}(\lambda)}{dT}(\lambda) \tag{5.11}$$

Figure 5.10 shows the temperature dependent effective index variation calculated for four different waveguide geometries using Lumerical MODE Solutions at $\lambda = 1550$ nm for TE polarization. Note that, these waveguide geometries correspond to our previous DC examples DC1, DC2, DC3 and DC4 in Figure 2.14: DC1 (H = 220 nm, W = 550 nm, h = 100 nm), DC2 (H=220 nm, W = 350 nm, h = 100 nm), DC3 (H = 220 nm, W = 350 nm, h = 0 nm) and DC4 (H = 220 nm, W = 375 nm, h = 160 nm). In this
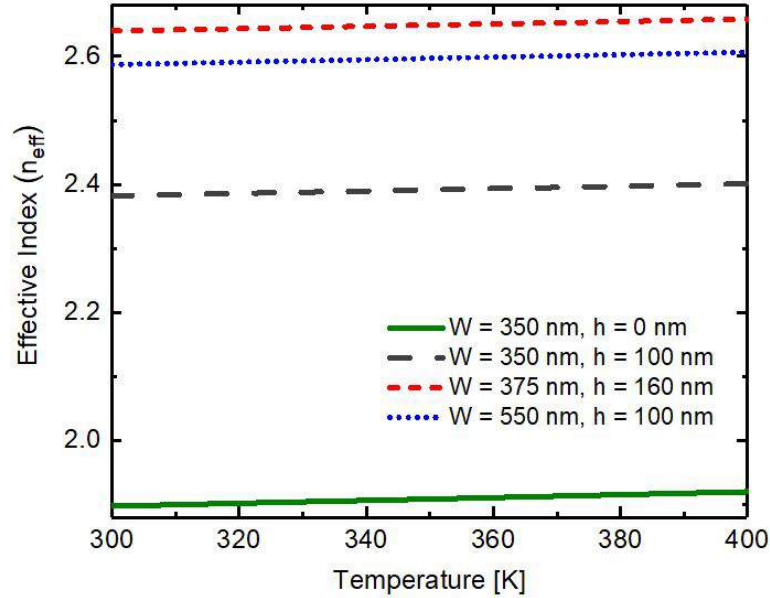
Figure 5.10: Effective index as a function of operating temperature calculated for four waveguide geometries corresponding to the DC geometries in Figure 2.14: DC1 (H = 220 nm, W = 550 nm, h = 100 nm), DC2 (H=220 nm, W = 350 nm, h = 100 nm), DC3 (H = 220 nm, W = 350 nm, h = 0 nm) and DC4 (H = 220 nm, W = 375 nm, h = 160 nm) and for TE polarization at $\lambda = 1550$ nm.

calculation, we have considered the thermo-optic co-efficients for silicon device layer and buried SiO_2 layer as 1.86×10^{-4} K^{-1} [152] and 1.0×10^{-5} K^{-1} [153], respectively. The TO coefficients (slope of the curves in Figure 5.10) of waveguides are estimated within $(1.78-2) \times 10^{-4}$ K^{-1}. In case of directional couplers, the temperature dependent

coupling constant can be expressed as:

$$\kappa(\lambda, T) = \frac{\pi}{\lambda} \left[n_{eff}^{s}(\lambda, T) - n_{eff}^{a}(\lambda, T) \right] \qquad (5.12)$$

and hence,

$$\frac{d\kappa(\lambda, T)}{dT} = \frac{\pi}{\lambda} \frac{d\Delta n(\lambda, T)}{dT} = \frac{\pi}{\lambda} \left[\frac{dn_{eff}^{s}(\lambda, T)}{dT} - \frac{dn_{eff}^{a}(\lambda, T)}{dT} \right] \qquad (5.13)$$

where $\frac{dn_{eff}^{s}}{dT}$ and $\frac{dn_{eff}^{a}}{dT}$ are the TO coefficients of symmetric and antisymmetric modes
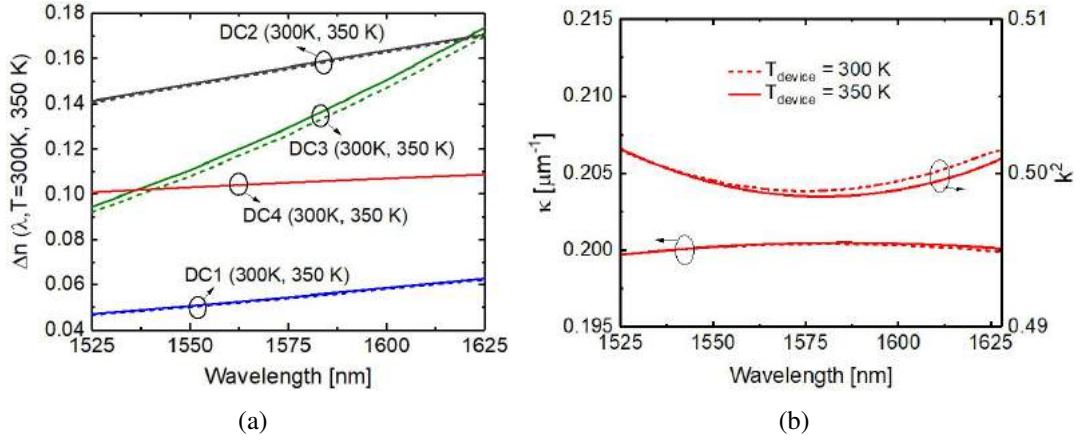
Figure 5.11: Calculated (a) $\Delta n(\lambda, T)$ as a function λ for four DC geometries (DC1, DC2, DC and DC4), and (b) cross coupling co-efficient ($\kappa(\lambda, T)$) and coupling strength ($k^2(\lambda, T)$) calculated for a WIDC (DC4) exhibiting 3-dB power splitting at $\lambda \sim 1550$ nm (TE-polarization) for two different operating temperatures (T_{device} = 300K, and 350K).

respectively. Since the electric field confinement of symmetric and antisymmetric modes are highly geometry dependent, the difference term in Eq. 5.13 decides the thermal stability of the DC transfer function. We have calculated $\Delta n(\lambda, T)$ for DC1, DC2, DC3, and DC4 (refer 2.2.3) as a function of λ and temperature T. Dashed lines in Figure 5.11(a) represent $\Delta n(\lambda)$ at T = 300K, and solid line represents that for T = 350K. It is to be noted that, out of this four DC geometries DC4 exhibits athermal characteristics, i.e.,$\Delta n(\lambda, T = 350$ K$) \approx \Delta n(\lambda, T = 300$ K$)$ over the entire range of wavelength. This means that, for this particular geometry (WIDC) the TO coefficients of supermodes are nearly same for all λs resulting in nearly athermal coupling coefficient (κ), in other words, DC4 gives temperature insensitive WIDC transfer function (k^2), as shown in Figure 5.11(b). In contrast, the TO coefficients of symmetric and antisym-

metric modes of DC3 are found to be unequal ($\frac{dn_{eff}^s}{dT} > \frac{dn_{eff}^a}{dT}$) for any λ, and hence $\Delta n(\lambda, T = 350\text{K}) - \Delta n(\lambda, T = 300\text{K}) > 0$, or $d\kappa/dT \neq 0$, resulting slightly thermally unstable transfer function. DC1 and DC2 designs can also considered as athermal since $d\kappa/d\lambda$ is close to zero in both cases; however both the geometries are wavelength dependent.

5.2.2 Switching Characteristics

Since the 3-dB WIDCs in Figure 5.9 are insensitive to both wavelength and temperature, the MZI response in Eq. 5.9 depends only on the $\mathcal{T}_M(\lambda, \Delta T)$. For a phase shifter length of l_w, the transfer functions at the bar port and cross port of balanced MZIs ($\Delta l = 0$) in Figures 5.9(a) and 5.9(b) can be written as (lossless case):

$$P_b = P_{in} \sin^2\left(\frac{\Delta\phi(\lambda, \Delta T)}{2}\right) \quad P_c = P_{in} \cos^2\left(\frac{\Delta\phi(\lambda, \Delta T)}{2}\right) \tag{5.14}$$

Thus by increasing temperature from $\Delta T = 0\text{K}$ to $\Delta T = T_\pi$, the input power can be switched from cross port to bar port. Similarly, the transfer function of an unbalanced MZI can be detuned (wavelength) within one FSR by adding thermo-optic phase $\Delta\phi(\lambda, \Delta T)$.

For the proposed thermo-optic waveguide phase-shifter (straight or folded) with WIDC waveguides ($\frac{\partial n_{eff}}{\partial T} = 1.79 \times 10^{-4} \text{ K}^{-1}$) one can estimate ΔT_π at $\lambda = 1550$ nm (using Eq. 5.2) as:

$$\Delta T_\pi = \frac{4.35}{L_H} \text{ mm-K} \tag{5.15}$$

Thus longer the microheater length smaller is the differential temperature required for a desired $\Delta\phi$. For example, if $L_H = 100$ μm, then $\Delta T_\pi = 43.5$K is required for π differential phase-shift between the MZI arms at $\lambda \sim 1550$ nm. However, a large ΔT_π may affect the performance of neighboring temperature sensitive electronic/photonic devices unless they are thermally insulated from the phase shifter. For our switch design, we have indeed used $L_H = 400$ μm to operate devices close to room temperatures ($\Delta T_\pi \sim 10.87$ K).

It must be also noted that the minimum waveguide bend radius of S-bends in direc-

tional couplers is kept at 180 µm to satisfy the WIDC design rule as described in section 2.2.4. Another important concern here is the bend induced loss as the confinement factor of guided mode in access rib waveguides (shallow etched) is relatively poor and hence the minimum bending radius for access waveguides is kept ~ 125 µm to minimize the bending loss (see Figure 2.17). This seems apparently detrimental for compact design, but it has been shown earlier in section 2.2.4 that the access waveguides can be in fact tightly bent by adiabatic etching of slab regions using a second lithographic definition. The wavelength dependent transmission characteristics at the bar port and cross
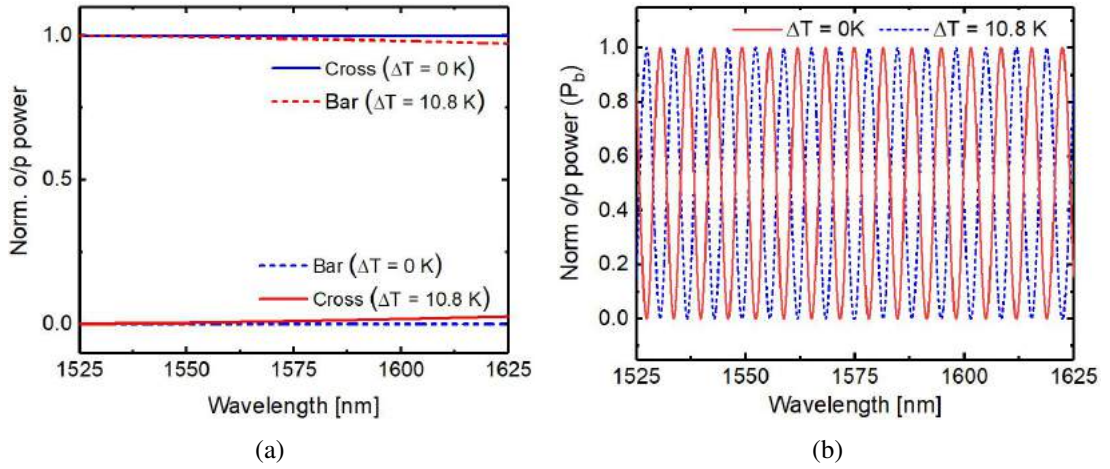
Figure 5.12: Wavelength dependent thermo-optic switching of power at cross- and/or bar port(s) of 2×2 MZIs designed with 3-dB WIDCs: (a) switching at cross and bar ports of a balanced MZI; and (b) microheater switching from OFF state to ON state at the bar port of an unbalanced MZI.

port of a balanced MZI calculated at $\Delta T = 0$ and $\Delta T = \Delta T_\pi = 10.8$K are shown in Figure 5.12(a). Similarly Figure 5.12(b) shows the cross port response calculated at $\Delta T = 0$ and $\Delta T = \Delta T_\pi = 10.8$K of an unbalanced MZI with $\Delta l = |l_1 - l_2| = 275$ µm. The calculations were carried out by including the wavelength dependent t, k, and n_{eff} values extracted using Lumerical MODE Solutions and assuming $\eta = 1$ in Eq. 5.9.

Next, we have studied the performance of slab integrated Type-II microheater in two different configurations: straight and folded. Figures 5.13(a) and 5.13(b) show typical layout of straight and curved waveguide microheaters used for experimental demonstration. The microheater terminals are flared towards the contact pads which allows to reduce the power dissipation throughout this region and hence improve the efficiency of the heater. The effective length of phase shifter can be modeled as $L_w = L_H + \Delta L$,

(a)

(b)
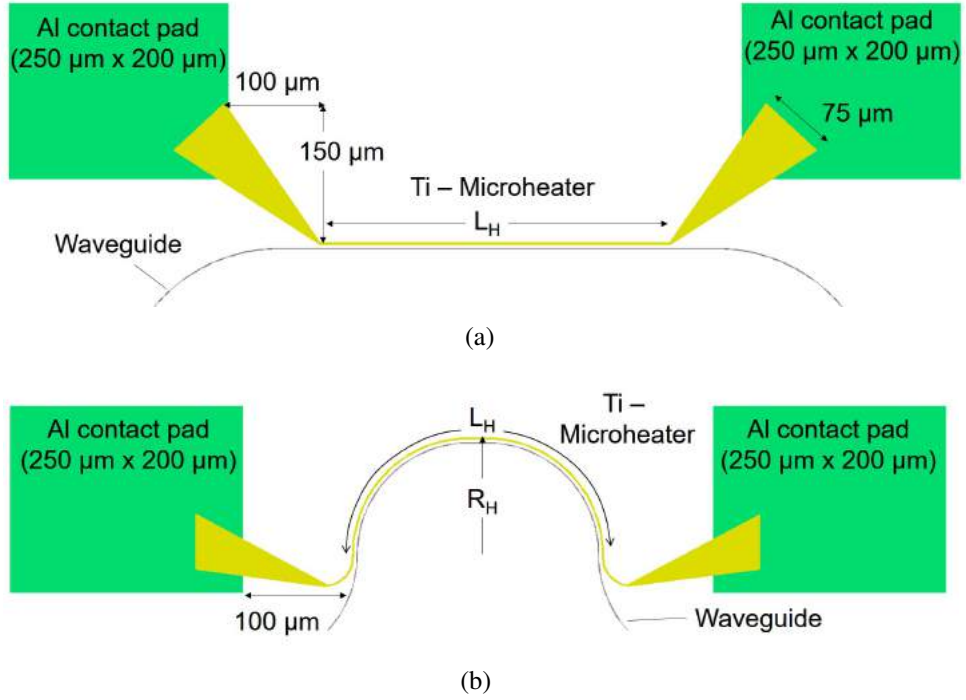
Figure 5.13: Top views of (a) straight and (b) curved (radius R) microheaters showing the flared microheater terminals towards the contact pads (Al).

where ΔL is differential length along the axis of the microheater due to temperature distribution of the flaring region at both ends. Longer waveguide microheater is especially preferred for keeping lower ON state temperature of the phase shifter ($\Delta T_\pi \sim$ 10.8K).

The extracted 2D temperature distribution (COMSOL simulations) along the plane of heater ($x - z$ plane at $y = h$) for straight and curved microheaters are shown in Figures 5.14(a) and 5.14(b) respectively, calculated for microheater driving power of $P_e = 30$ mW. Thickness dependent thermal conductivity of the silicon layers (device layer as well as handle layer) given in Figure 5.3 has been used for simulations. Our simulation results reveal that a curved waveguide microheater consumes less electrical power for the same temperature rise along the waveguide. This is expected as the Joule heating energy density increases because of the semi-circular bend waveguide microheaters of same length. The calculated $\Delta T \cdot L_w$ against the power dissipation P_e for straight and folded waveguide phase-shifters are shown in Figure 5.15. The power required for π-phase shift ($P_e = P_\pi$) has been estimated using Eq. 5.15. Nearly 1.2 times differential temperature rise from the room temperature (300 K) is observed for bend
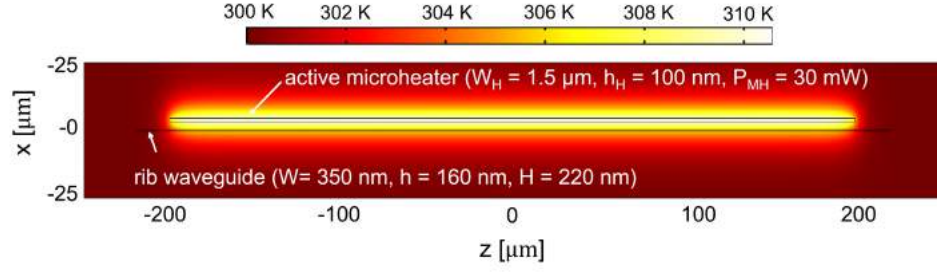
(a)
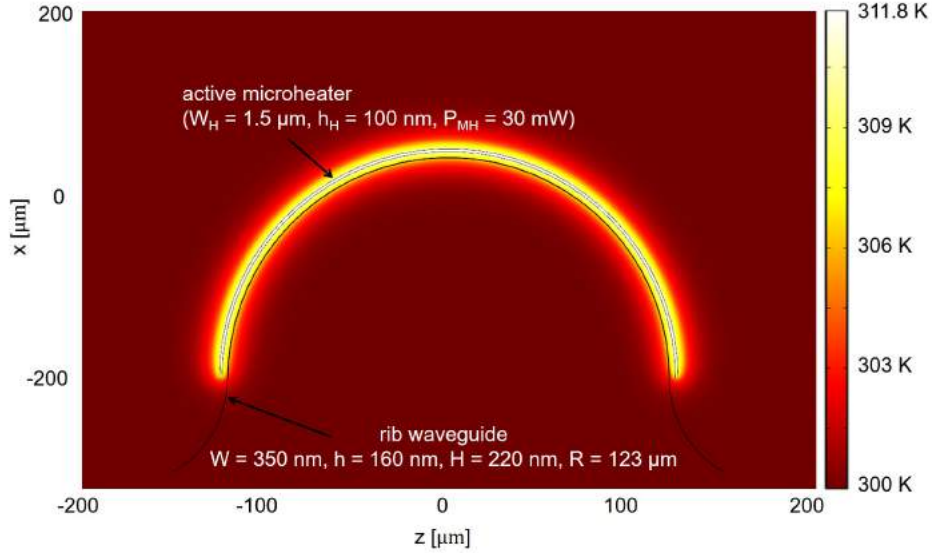
(b)

Figure 5.14: Temperature distribution (extracted form 3-D simulation) along the top surface ($x - z$ plane at $y = h$) for (a) straight waveguide microheater and (b) curved waveguide microheater, calculated for an applied $L_H = 400$ μm. In all cases waveguide ($W = 350$ nm, $H = 220$ nm, $h = 160$ nm) and heater ($t_H = 80$ nm, $W_H = 1.5$ μm) are separated by s = 3 μm.

waveguide microheater ($P_\pi \sim 40$ mW) of $R = 125$ μm in comparison to that of straight waveguide microheater ($P_\pi \sim 48$ mW). However there is no significant difference noticed in the calculated rise time and fall time of both the microheater configurations; $\tau_r \sim \tau_f = 4.2$ μs.

5.3   Experimental Results and Discussions

For experimental demonstration, the proposed devices (balanced S-MZI, balanced F-MZI, and unbalanced F-MZI) are fabricated on a 220-nm device layer SOI (BOX $\sim$ 2 μm, handle wafer ~ 500 μm). The WIDCs/MZIs including access waveguides and
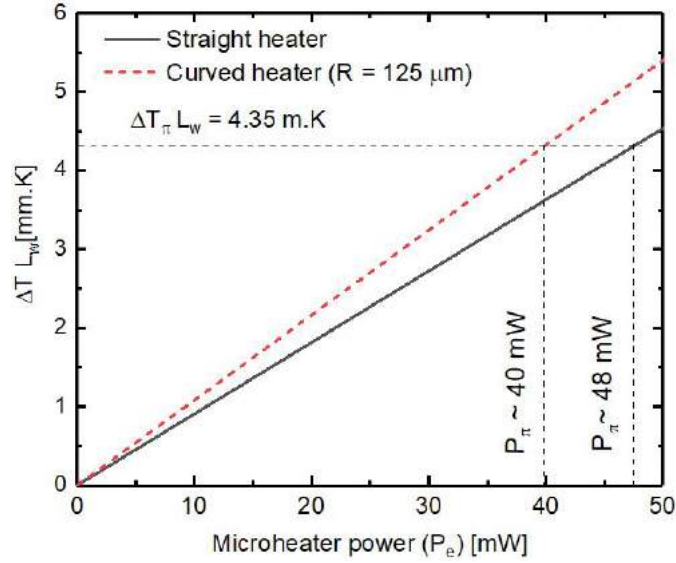
Figure 5.15: $\Delta T \cdot L_w$ calculated for straight waveguide microheater (solid lines) and semi-circular (R = 125 µm) waveguide microheater (dotted line) of effective phase shifter length L_w.

grating couplers were fabricated first with the same process steps as discussed under section 2.3.1. Here we will first discuss the integration of thermo-optic phase shifter followed by the line resistance extraction of the integrated Ti microheater. The static and transient optical transmission characteristics of the fabricated MZI switches are discussed in detail.

5.3.1 Microheater Integration

Ti microheaters are widely used for high temperature applications because of its high resistivity, high melting point and ensures no electro-migration at high temperature compared to Al and Au. Typical layout of the microheater along with Al contact pads have been shown earlier in Figure 5.13. Schematic flow charts of the process steps for Al contact pads and Ti microheater are shown in Figures 5.16(a) and 5.16(b) respectively. In both cases the positive electron beam resist is first patterned using EBL followed by metal deposition and lift-off. Al contact pads are integrated prior to Ti microheater, otherwise, Ti-strips may peel-off and re-deposit on top of the waveguide during the lift-off of Al.

Al contact pad integration

Figures 5.16(a) shows the process steps for Al-contact pads.

1. **Resist Coating:**
   Positive resist PMMA is uniformly coated over the sample with following spin parameters as listed in Table 5.2. As a rule of thumb, the resist thickness (300 nm) must be at least three times that of evaporated metal (100 nm) to ensure that the solvent will be able to lift the resist.
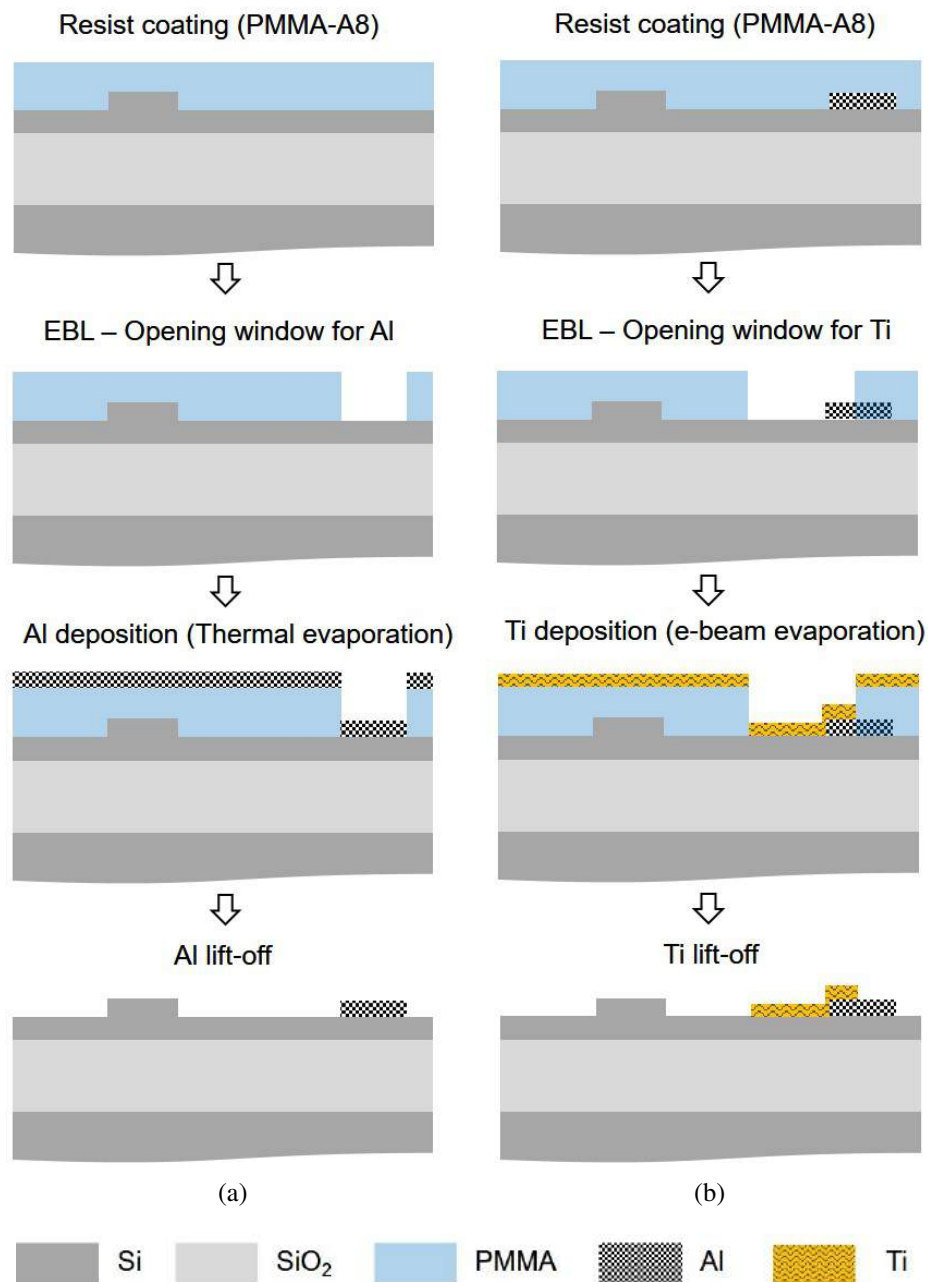
Figure 5.16: Fabrication process flow schematics for (a) Al contact pad and (b) Ti microheater integration (dimensions are not in scale).

Table 5.2: Spin coat parameters for PMMA-A8 electron beam resist optimized for uniform thickness of 300 nm.

Spin parameters	Thickness
Speed ~ 600 rpm Acceleration ~ 7000 rpm/sec Time:40 sec	300 nm

2. **Electron beam lithography:**
   Aluminum contact pad windows (250 µm $\times 200$ µm) are patterned over PMMA using electron beam lithography (RAITH 150 TWO). The exposed area is developed in MIBK:IPA (1:3) solution for 30 sec followed by 10 sec in IPA and then cleaned in DI water. The optimized electron beam parameters are given in Table 5.3.

Table 5.3: Optimized EBL (Raith 150 TWO system) parameters for patterning of contact pads over PMMA-A8.

System Parameters	Patterning/developing parameters
Acceleration Voltage 20 kV Aperture = 30 µm Write Field = 100 µm × 100 µm Working distance = 10 mm	Area dose = 150 µC/cm^2 Area step size = 10 nm Developing time: 30 sec in MIBK:IPA (1:3) and 10 sec in IPA.

3. **Al deposition:**
   Al layer is deposited by thermal evaporation (HPVT-305G) for a thickness of 100 nm (one third of resist thickness).

4. **Al lift-off:**
   The underlying resist layer is then removed and Al is lifted-off using Acetone solution. The sample is ultrasonic agitated in acetone at ~ 60 °C for ~ 10 min and then cleaned in DI water.

Ti Microheater Integration

The fabrication flow has been shown in Figure 5.16(b). Metal lines were also patterned with the same lithographic parameters listed in Tables 5.2 and 5.3. Ti is deposited (~ 80 nm) using ebeam evaporation (Hind Hi Vac BC-300T) and subsequently lifted-off using Acetone at 60 °C for 2 min. Care has to be taken to avoid the redeposition of Ti metal flakes over the waveguide during lift-off.

(a) (b) (c)
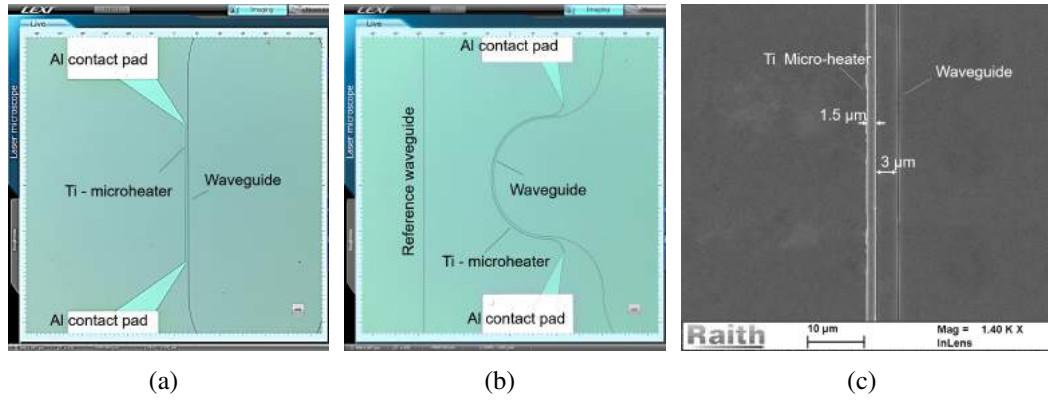
Figure 5.17: (a) and (b) are microscopic images of the straight and folded waveg-uide phase-shifters integrated with Ti-microheater and Al contact pads; (c) Zoomed-in SEM image of the microheater region.

Microscopic images of the integrated straight and folded waveguide phase-shifters ($L_H = 400\ \mu$m) along with Al contact pads are shown in Figures 5.17(a) and 5.17(b). A zoomed-in SEM image of the Ti-microheater which is integrated $3\ \mu$m away from the waveguide is also sown in Figure 5.17(c). The width W_H and height t_H of microheater are measured to be $1.5\ \mu$m and ~ 80 nm respectively. Figures 5.18(a)-5.18(c) show the microscopic images of fabricated balanced S-MZI, balanced F-MZI and unbalanced F-MZI (input/output grating couplers are not shown) respectively. Table 5.4 shows the list of fabricated MZI switches and their specifications

(a) (b) (c)
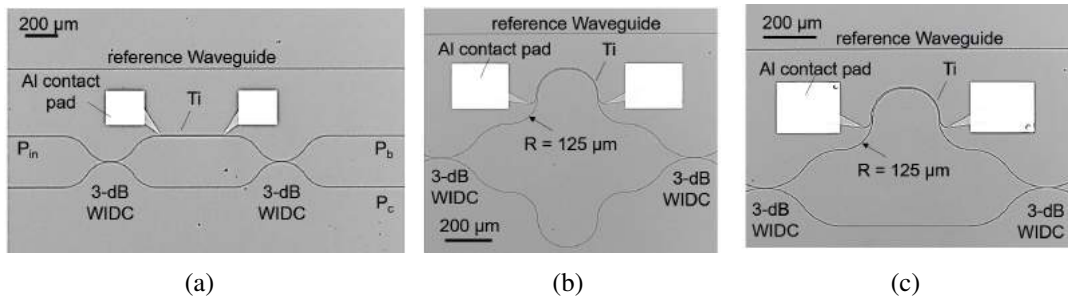
Figure 5.18: Microscopic images of fabricated (a) balanced S-MZI, (b) balanced F-MZI and (c) unbalanced F-MZI switches integrated with Ti microheater and Al contact pads.

Table 5.4: List of fabricated samples of broadband thermo-optic switches.

Sample	W, h	L_{DC}, L_H	Remarks
S6	W = 350 nm h = 160 nm W_H=1 μm h_H=100 nm	L_{DC}: 5 μm L_H: 100, 200, .. 500 μm	S-MZIs and F-MZIs

5.3.2   Line Resistance Measurement

Reference microheaters of various lengths (L_H = 100 μm to 500 μm) were fabricated to extract the line resistance using standard two-probe experimental setup and Ohm's law. Figure 5.19 shows the total resistance (R_H) of microheaters as a function of length L_H. The line resistance of fabricated microheaters is estimated from the slope as $r_H \sim$ 70 Ω/μm. The resistivity of deposited Ti film may vary significantly with that of bulk Ti material (film quality depends on the deposition temperature, pressure and material grade). By extrapolating the $L_H - R_H$ plot to L_H = 0, we extract the resistance of two flaring regions of each microheater as $\sim$ 4 kΩ (R_{CH}). This also includes the probe contact resistance which is of course not so significant in our measurement setup. Thus for a waveguide microheater of length L_H = 400 μm used for above mentioned three variants of MZI switches, the total resistance is $R_H (= r_H \cdot L_H + R_{CH}) \sim 32$ kΩ, which has been used to estimate the electrical power consumption for thermo-optic switching experiments for all fabricated devices: $P_e = I^2 R_H$, where I is the dc or rms value of current through the microheater. Since the operating temperature of the devices is not high, the temperature dependent change in microheater resistance is insignificant.

5.3.3   Thermo-optic Characterization setup

The schematic of experimental thermo-optic characterization setup and a photograph of the four probe station are shown in Figure 5.20(a) and 5.20(b) respectively. For thermo-optic switching characterizations of fabricated devices, we used two fiber-optic probes for input and output light coupling via GCs and simultaneously two electrical probes for driving the microheater. The two fiber probes and two electrical probes are accurately positioned over the sample using respective x-y-z stage micro-positioners. The micro-
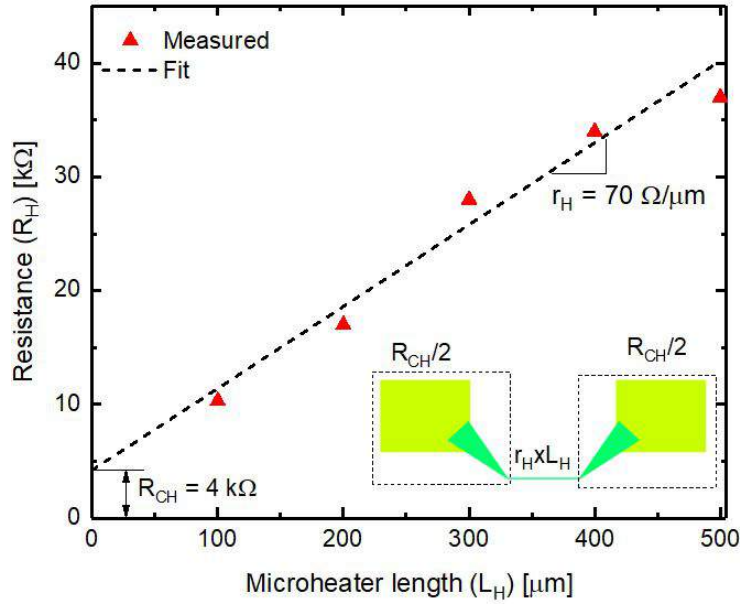
Figure 5.19: Measured resistance of fabricated microheaters as a function of their lengths. Inset shows the schematic of the microheater; $R_H = r_H \times L_H + R_{CH}$.

heaters were activated by connecting contact pads with a variable current source measuring unit (SMU). Additionally, for transient switching characteristics measurements, the SMU output is modulated with a square wave signal from a function generator (FG) and the optical output is detected using a photodetector (Thorlabs - PDA10CS InGaAs) and digital storage oscilloscope (Keysight - DSOX6002A). The setup is electrically and optically controlled using LabView programs installed in a computer. The wavelength dependent transmission characteristics of reference (shallow etched) straight waveguides terminated with input/output grating couplers were obtained first which were used later to normalize transmission characteristics of the MZI switches. Thus we eliminated the wavelength dependent response of the input/output grating couplers of fabricated MZI switches.

5.3.4 Static Characteristics

The static thermooptic characteristics of the devices were measured by sweeping the microheater driving current (I) and simultaneously measuring the transmission characteristics in OSA.
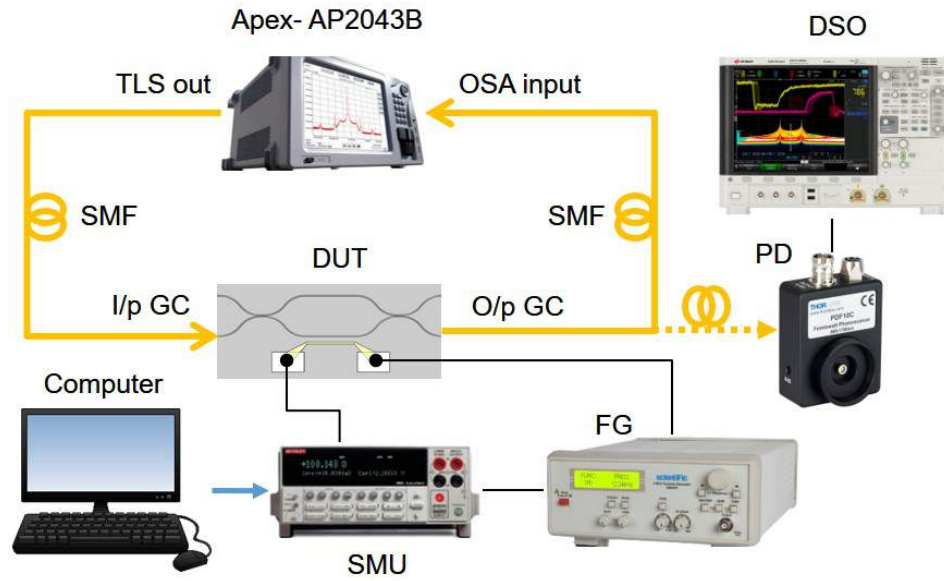
(a)
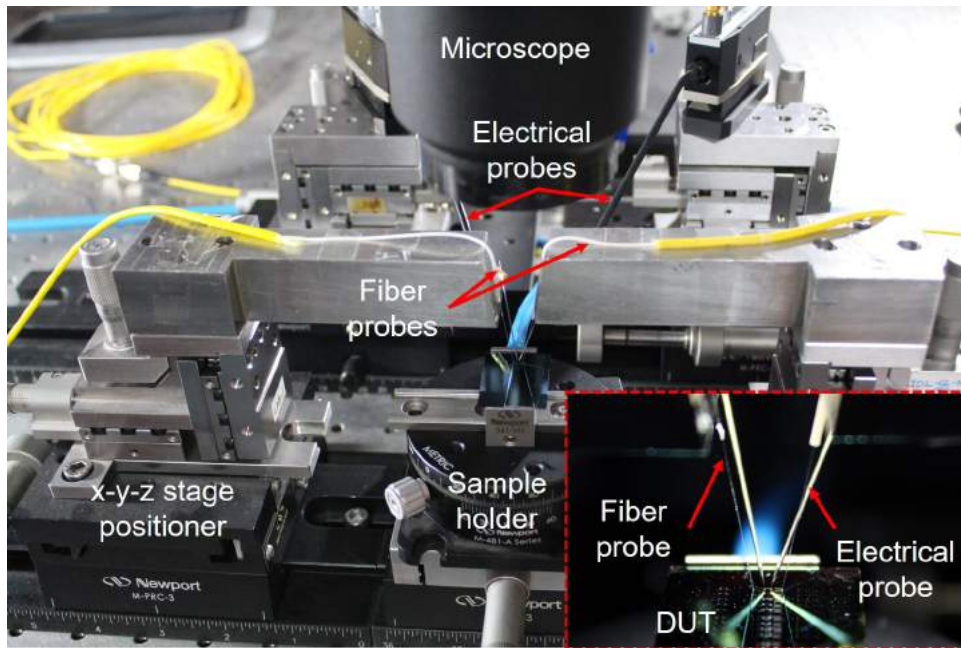
(b)

Figure 5.20: (a) Schematic of thermo-optic characterization set-up; (b) Photograph of the four-probe station with zoomed view of the DUT and probes in the inset; OSA - optical spectrum analyzer, TLS - tunable laser source, FG - function generator, SMU - source measuring unit, GC - grating coupler, DUT - device under test, PD - photodetector, DSO - digital storage oscilloscope.

Balanced MZI switches

The measured transmission characteristics (normalized with reference waveguide) at the bar- and cross-ports of balanced S-MZI and F-MZI switches are shown in Figure
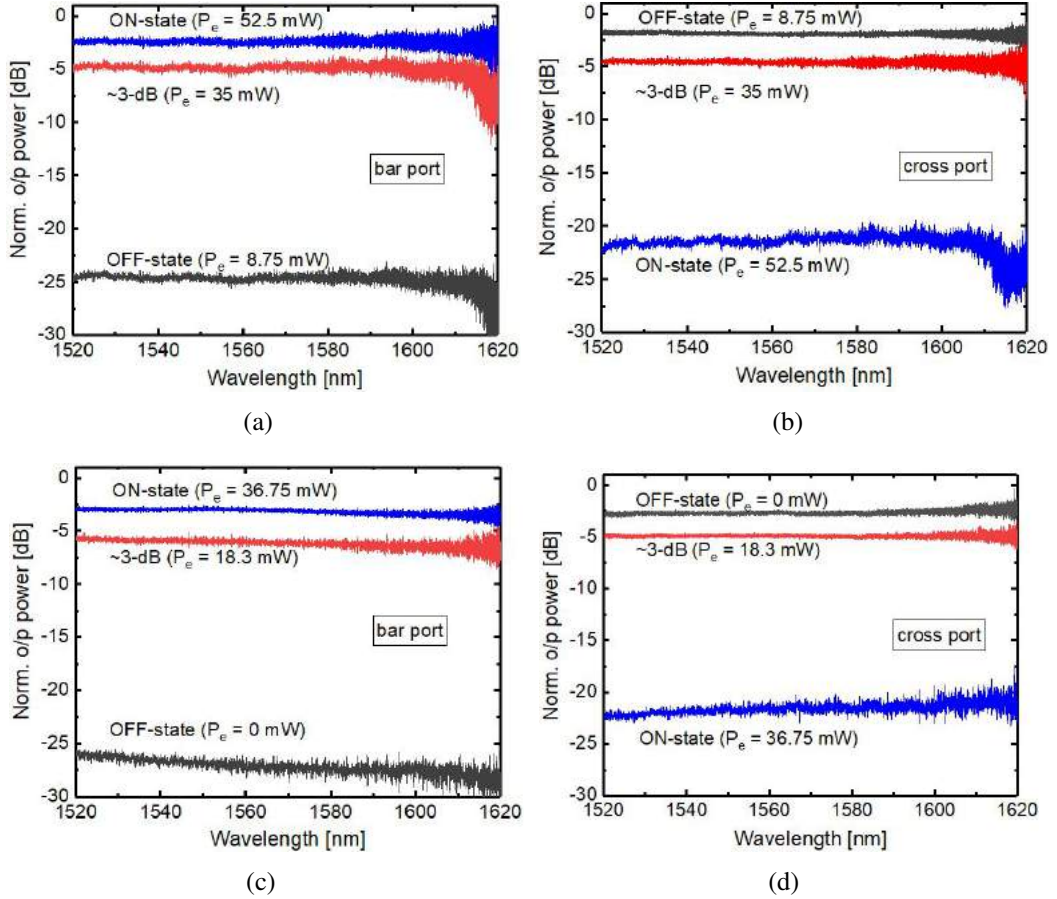
Figure 5.21: Wavelength independent transmission characteristics at the bar ports and cross ports measured for ON-state (maximum transmission), OFF-state (minimum transmission) and 3-dB switching power levels: (a and b) S-MZI, and (c and d) F-MZI.

5.21. Figures 5.21(a) and 5.21(b) represent transmission characteristics of S-MZI at the bar port and cross port respectively, measured for three different microheater driving powers corresponding to the OFF-state, 3-dB power splitting and ON-state of the switch. A similar transmission characteristics measured at the bar port and cross port of F-MZI device are shown in Figures 5.21(c) and 5.21(d) respectively. A wavelength independent insertion loss of ~ 2.5 dB is recorded for both S-MZI and F-MZI switches, which is mainly attributed to the total insertion loss of two 3-dB power splitters as shown previously in Figure 2.33. The increased fluctuations at longer wavelengths may be attributed to the error in photodetection, as the grating coupler exhibit poor coupling strengths at longer wavelengths. Typical electrical power required for switching optical signal from cross port to the bar port (with an extinction of > 20 dB) is $P_e \sim 52.5$ mW (~ 36.7 mW) for fabricated S-MZI (F-MZI) switches. The steady-state transmitted op-

114
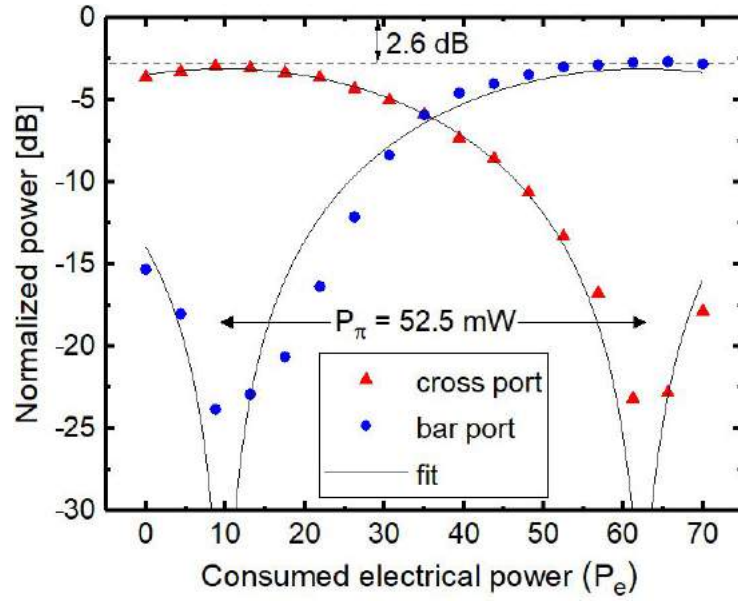
(a)
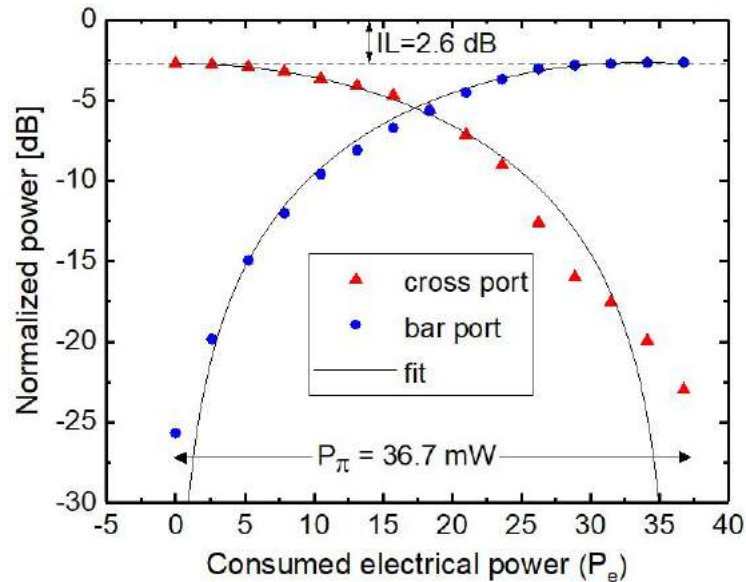
(b)

Figure 5.22: Switching characteristics measured at $\lambda = 1550$ nm: (a) transmission at cross and bar ports of an S-MZI, (b) transmission at cross and bar ports of an F-MZI.

tical signal ($\lambda = 1550$ nm) at the bar and cross ports of the above mentioned S-MZI and F-MZI as a function of electrical power dissipated/consumed by the microheaters are shown in Figs 5.22(a) and 5.22(b), respectively. Though both types of MZIs were designed with balanced arms, a little mismatch occasionally observed for some fabricated devices due to imbalance in splitting ratios of WIDCs (section 4.1). For example, an additional bias electrical power of $P_e = 8.75$ mW was required for achieving maximum

(minimum) transmission at the cross (bar) port of the S-MZI. Comparing the observed switching powers (P_π) between S-MZI (52.5 mW) and F-MZI (36.7 mW), we confirm that the curved waveguide microheater design is found to be more efficient than that of a straight waveguide microheater design of same length. This result is very much consistent with the theoretical prediction discussed earlier. It is also observed that as the transmitted power extinguishes in cross port, the transmitted power builds up at the bar port with equal strength for entire wavelength range of operation following the principle of 2×2 balanced MZI switch.

Unbalanced F-MZI switch

The transmission characteristics of passive (OFF-state) unbalanced MZIs were discussed in the previous chapter (section 4.2). The active unbalanced F-MZI switch shown in Figure 5.18(c) has been characterized for different values of microheater power. A zoomed-in (1540 nm $\leq \lambda \leq$ 1550 nm) transmission characteristics (normalized to 0 dBm) at the cross port for OFF-state ($P_e = 0$ mW) and ON-state ($P_e = 37$ mW) are shown in Figure 5.23(a). In this case, the OFF state and ON state of the switch are
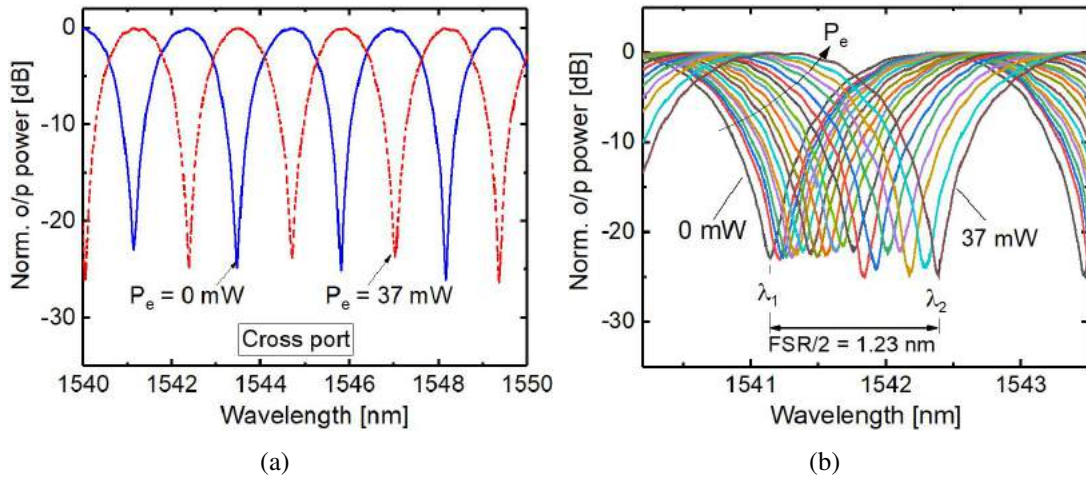
Figure 5.23: (a) OFF state ($P_e = 0$ mW) and ON state ($P_\pi = 37$ mW) transmission characteristics at the cross port of a fabricated unbalanced F-MZI switch (see Figure 4.7(b) for passive broadband characteristics); (c) wavelength tuning characteristics at the cross port against consumed electrical powers (0 mW to 37 mW). λ_1 and λ_2 are two wavelengths corresponding to cross port minimum at OFF state and ON state respectively.

corresponding to the maximum power transmission (for given operating wavelength) at

the cross port and bar port, respectively. Thus the transmission spectra corresponding to ON and OFF states are complimentary to each other for an unbalanced F-MZI. The signal extinction ratio at any of the output ports of the switch is found to be ~ 22 dB. Nevertheless, the wavelength tuning characteristics of transmission spectra within one FSR near $\lambda \sim 1542$ nm at the cross port for different driving powers (P_e) of the microheater are shown in figure 5.23(b). As the heater power increases from P_0 mW, the cross port optical power at λ_1 builds up and become maximum when $P_e = 37$ mW. The measured wavelength shift versus consumed electrical power has been plotted in 5.24. The wavelength tunability of the device is estimated as 33.2 pm/mW.
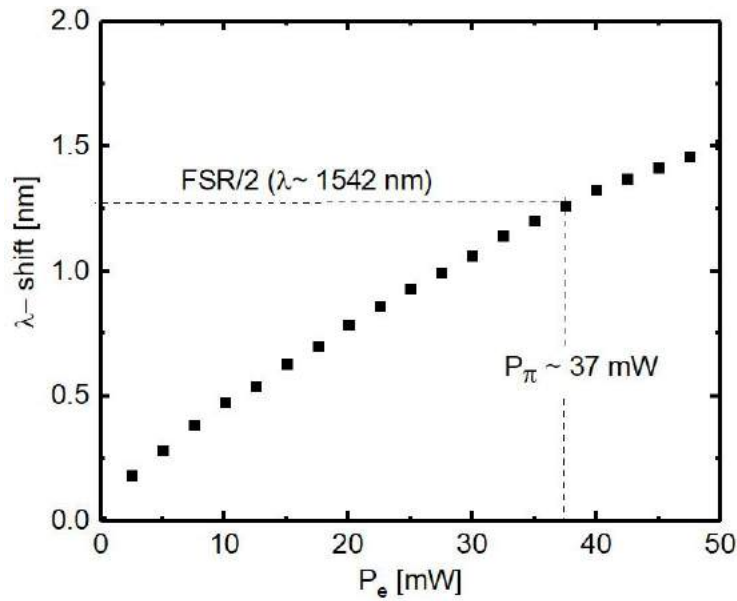
Figure 5.24: Measured wavelength shift versus consumed electrical power in the microheater (P_e).

5.3.5 Transient Characteristics

The transient characteristics of the switches were measured by modulating the heater bias voltage with a small signal ON-OFF voltage of 5V, 12 kHz from the function generator. The time-domain optical response at the bar port and cross port have been collected using a high speed photodetector (THORLABS PDA10CS InGaAs photodetector) and recorded in a digital storage oscilloscope (KEYSIGHT DSOX6002A). Typical transient response of optical transmission at both bar- and cross-ports of the MZI switch (straight or folded microheater) are shown in Fig. 5.25. The recorded rise/fall time for both
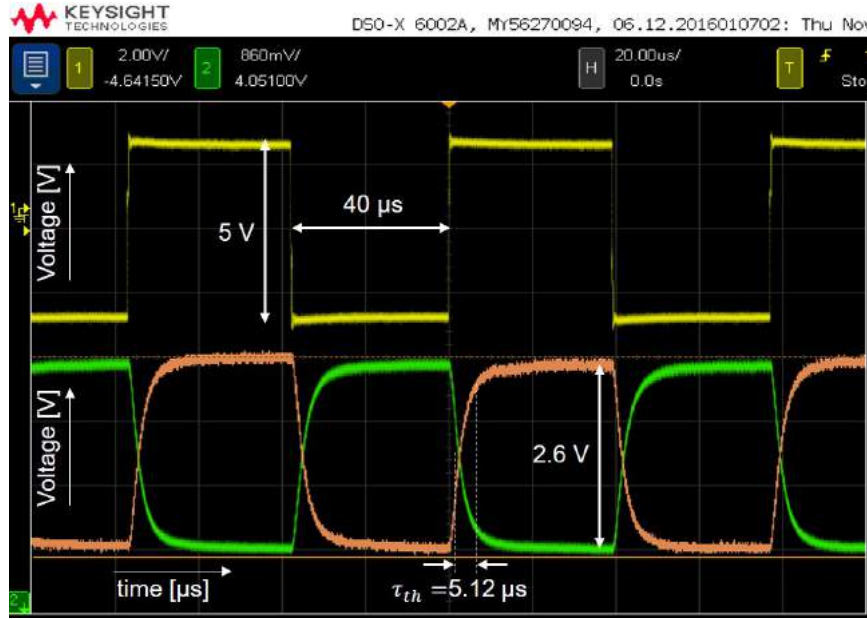
Figure 5.25: Transient characteristics measured at bar and cross ports of an S-MZI with the microheater driven by a square pulse (identical transient characteristics for F-MZI).

types of microheaters are measured to be nearly same ($\sim$5 µs) which is higher than the theoretical calculation (4.2 µs) as shown in Figure 5.7(f). This deviation may be due to the assumption of lower value of thermal conductivities and/or higher values of heat capacitances (for both core and claddings) in theoretical simulation.

5.3.6 Estimation of Figure of Merits (FOMs)

The steady-state switching characteristics obtained for S-MZI and F-MZI are fitted with appropriate analytical transfer functions (5.9) and we have extracted the values of ΔT_s (steady-state temperature in the waveguide core) vs. p_w (electrical power consumed per unit length of a waveguide phase-shifter) for both straight and folded waveguide phase-shifters as shown in Figure 5.26(a). The slope of ΔT_s vs. p_w is a measure of the sensitivity figure of merit S_H of the waveguide phase-shifter as defined earlier. The value of S_H extracted for an S-MZI is 82.4 K·µm/mW, which is slightly higher than that of theoretical prediction of 73.5 K·µm/mW. This may be attributed to the fact of our assumption $L_w = L_H$; a correction term is required for $L_w = L_{eff} = L_H + \Delta$, where $\Delta \sim$ 10 µm for $L_H > 100$ µm[132]. In other words, the effective conductance (g_w) of fabricated devices is slightly lower than that of theoretical calculations which is consistent
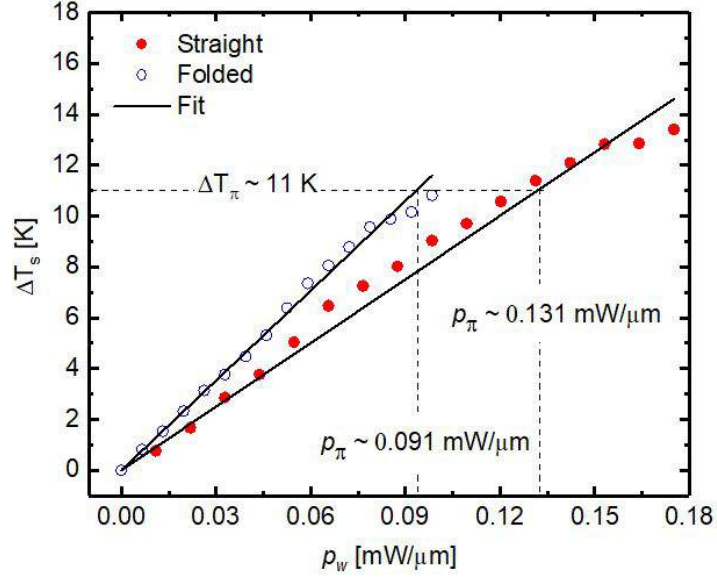
(a)
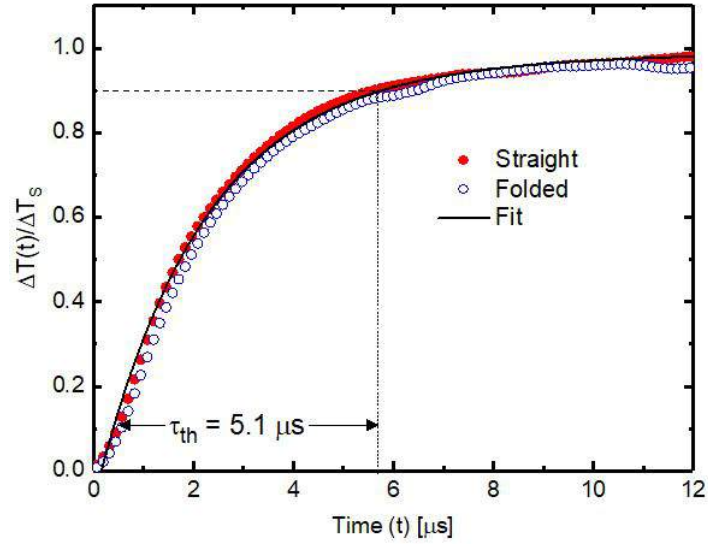
(b)

Figure 5.26: Steady-state and transient temperature characteristics of straight and folded waveguide phase-shifters used in S-MZI and F-MZI, respectively: (a) extracted steady-state temperature ΔT_s in the waveguide core as a function of dissipated electrical power per unit length of the phase-shifter (p_w), and (b) extracted transient temperature $\Delta T(t)/\Delta T_s$ in the waveguide core as a function of time t..

with the observed higher values of thermal response time (τ_{th}) of the fabricated devices discussed earlier. Nevertheless, we observed a significantly enhanced value of $S_H = 119$ K·µm/mW in case of folded waveguide phase-shifter as predicted earlier. The transient characteristics obtained for S-MZI and F-MZI are again fitted with the corresponding analytical functions to extract the temperature rise $\Delta T(t)$ in the waveguide core

of the phase-shifters (see Figure 5.26(b)); both straight and folded waveguide phase-shifters are shown to be following Eq.5.4 with τ_{th} = 5.1 µs. Thus the experimentally observed value of $\mathcal{F}_H$ in a folded waveguide phase-shifter (23.3 K·µm/mW·µs) is about 1.5 times higher than that of a straight waveguide phase-shifter (16.2 K·µm/mW·µs) for our fabricated devices. It is possible to improve the value of $\mathcal{F}_H$ further by designing more tightly folded waveguide phase-shifter with much closer proximity of micro-heater but one needs to take care of associated optical losses of the guided mode. Using Eqs. 5.6 and 5.7, we have extracted the thermal characteristic parameters g_w and h_w as 1.21×10^{-2} mW/K·µm (1.21×10^{-2} mW/K·µm) and 6.17×10^{-2} mW ·µs/K·µm (4.29×10^{-2} mW·µs/K·µm), respectively, for the fabricated straight (folded) design waveguide phase-shifters in Type-II (air cladding) architecture.

5.4 Summary

In summary, wavelength insensitive MZI based thermo-optic switches have been designed and demonstrated on a 220-nm SOI platform. A theoretical model for the performance analysis of a metallic strip-line microheater integrated waveguide phase-shifter has been developed. The model helps to define two important figure of merits such as temperature sensitivity S_H and $\mathcal{F}_H$ (= S_H/τ_{th}) following thumb-rules of $S_H \cdot g_w$ = 1 and $\mathcal{F}_H \cdot h_w$ = 1, respectively, where g_w and h_w are characteristic line conductance and line heat capacitance of the waveguide phase-shifter. These figure of merits were calculated for SOI waveguides (supporting TE_0 guided mode) integrated with Type-I and Type-II microheater architectures. It has been shown by numerical simulation that Type-II microheaters offer faster switching time than that of Type-I microheaters. It has been also shown that both S_H and $\mathcal{F}_H$ can be improved significantly by proper choices of waveguide design parameters, closer proximity of microheater to the waveguide core, and suitably folding the waveguide-microheater phase-shifter system. However, care must be taken to limit the bend induced waveguide loss and loss due to evanescent field overlap with metallic microheater. The theoretical model is further validated with experimental results by fabricating 2×2 MZI switches (wavelength independent) designed with Type-II microheaters in SOI platform. The demonstrated MZI switches

exhibit a nearly wavelength independent power splitting characteristics with ~ 22 dB extinction over 100-nm wavelength range (1525 nm $\leq \lambda \leq$ 1625 nm). The switching power (P_π) of balanced F-MZI is estimated to be 36.7 mW, which is ~ 1.4 times lower than that of S-MZI (52.5 mW) because of the folded waveguide architecture. However, straight and folded waveguide phase-shifters exhibit nearly same switching time, $\tau_{th} \sim 5$ µs. This corresponds to a FOM, $\mathcal{F}_H = 16.2$ K·µm/mW·µs for S-MZI and $\mathcal{F}_H = 23.3$ K·µm/mW·µs for F-MZI. Again, the wavelength tunability of folded waveguide-phase shifter is extracted as 33.2 pm/mW. Though the demonstrated MZI switches were not designed with the best possible values of figure of merits (S_H, τ_{th} and $\mathcal{F}_H$), the experimental technique described here helps to extract the characteristic parameters like g_w and h_w of a thermo-optic waveguide phase-shifter for its modeling and optimized design.

The important figure of merits of the demonstrated devices (S-MZI and F-MZI) are compared with earlier demonstrated directly waveguide heated thermo-optic MZI switch by Watts $et~al.$ [154] and spiral waveguide cladding microheater by Densmore $et~al.$ [136] in Table 5.5. It is evident that the MZI switching devices demonstrated in this work exhibit better FOM in terms of optical bandwidth and wavelength dependent non-uniformity. However, it is a bit inferior in terms of switching power and switching time. This is mainly because of longer microheater (400 µm) used for heating a larger volume of waveguide as well as slab regions. In contrast, Watts $et~al.$ used a very compact microheater of length 10 µm for heating only the core region of the waveguide. Nevertheless, the longer waveguide microheater costs for a higher switch-

Table 5.5: Comparison of FOMs of demonstrated two different switches with previously reported direct waveguide heating MZI switch by Watt $et~al.$ [154] and spiral waveguide heating MZI switch by Densmore $et~al.$ [136].

FOMs	Ref. [154]	Ref. [136]	S-MZI	F-MZI
Bandwidth (BW) [nm]	70	–	> 100	> 100
Extinction ratio (ER) [dB]	20	–	20	20
Non-uniformity (NU) [dB]	2.5	–	< 0.1	< 0.1
Insertion Loss IL [dB]	0.5	6.0	2.4	2.4
Switching power (P_π) [mW]	12.7	6.5	52.5	36.7
Rise time (τ_r) [µs]	2.2	14	5.0	5.0
Fall time (τ_f) [µs]	2.4	–	5.0	5.0
Phase-shifter length (L_w) [µm]	10	6300	400	400
Switching temperature (ΔT_π) [K]	433	0.67	10.8	10.8

ing power-time product but it enables operating the device at much lower temperatures ($\Delta T_\pi \sim 11$K). Densmore *et al.* [136] used a very long folded waveguide microheater ($L_H = 6.3$ mm) reporting much lower switching temperature ($\Delta T_\pi = 0.67$K) and much lower switching power ($P_\pi = 6.5$ mW). However, this device exhibits a much longer switching time ($\tau_r = 14$ μs) and very high optical insertion loss ($IL = 6.5$ dB). Moreover, this device was tested only at $\lambda = 1550$ nm - no information on optical bandwidth and extinction ratio are available. Nevertheless, the overall figure of merits of the proposed S-MZI/F-MZI switches can be further improved/optimized by a trench isolation between Mach-Zehnder arms. Moreover, the switching power can be reduced by increasing the thermal sensitivity of the heater by suitably positioning the microheater as discussed in section 5.1.2. This will give additional benefit to fold the longer waveguides tightly in a serpentine pattern to reduce the device footprint as well as to lower the switching power P_π. This is certainly possible if the MZI arms and/or WIDC access waveguides are deeply etched (see Figure 5.7 as described earlier in section 2.2.4. In addition to that, the switching time of the proposed device can be further reduced by replacing the integrated metal microheater with doped p/n resistive heaters or p-n junction diodes across the waveguides.

CHAPTER 6

Conclusions

The major research outcomes of this Ph.D. thesis are the design and demonstration of a wavelength independent directional coupler (WIDC) with scalable coupling ratio and some functional building blocks such as broadband MRRs, MZIs and switches operating uniformly over a wide range of wavelength. This chapter present a brief summary and outlook of the research work carried out in this thesis.

6.1 Thesis Summary

In summary, we have theoretically studied the coupling characteristics of a DC comprised of two single-mode waveguides in a 220 nm SOI platform and designed a WIDC with uniform coupling ratio over a broad wavelength range of more than 100-nm near $\lambda = 1550$ nm in TE polarization. The fundamental design rule is to optimize the DC cross-sectional design parameters such as rib width (W), slab height (h), and gap (G) for which the coupling strength κ is nearly wavelength independent. In order to find out the optimized WIDC geometry we first calculated the geometry dependent values of differential group index of the supermodes ($\Delta n_g(\lambda) = n_g^s - n_g^a$) by varying the values of W and h (ensuring single mode guidance and TE-polarization) near $\lambda \sim 1550$ nm for fixed values of $H = 220$ nm and $G = 150$ nm. The coupling ratio of a typical WIDC ($W \sim 375$ nm and $h \sim 160$ nm) is found to be nearly wavelength independent and is scalable to any desired value $0\% - 100\%$ just by changing the length of parallel coupling region (L_{DC}). The proposed WIDC is fabricated on a 220-nm device layer SOI using electron beam lithography and dry etching (ICPRIE). Experimentally demonstrated WIDC based power splitters (1×2 and 1×4) exhibit nearly uniform splitting ratio with ± 0.5 dB bandwidth ~ 100 nm (1525 nm $\leq \lambda \leq$ 1625 nm). Since the footprint of proposed WIDC is designed with shallow etched (60 nm) access waveguides the minimum S-bend radius is limited to ~ 100 µm and thus the overall footprint

exceeds hundreds of micrometers. In order to reduce the device footprint and to make the device more compact for MRRs and MZIs, we have proposed and demonstrated a compact WIDC with deeply etched access waveguides and selectively masking the shallow etched WIDC region in two step fabrication process. With proper optimization of the tapered slab region one can reduce the device footprint below 50×10 μm². We further demonstrated WIDC integrated MRRs and MZIs fort broadband applications. The fabricated MRR with $R = 100$ μm, shows resonances with nearly uniform FSR (~ 0.8 nm) and extinction ratio (~ 20 dB) with $Q \sim 18000$. Compact broadband MRRs ($R < 100$ μm) are also demonstrated in two step fabrication process with deeply etched access waveguides as well as with an alternate deeply etched WIDC geometry ($W \sim 300$ nm, $h \sim 110$ nm). Similarly, the broadband transmission characteristics of (un)balanced MZIs integrated with WIDCs are also validated experimentally. The bar port to cross port extinction of MZI is measured to be ~ 22 dB which is nearly uniform over the entire wavelength range of interest. Finally, broadband MZI based thermo-optic switches are designed and demonstrated by integrating Ti microheater in the slab region of the waveguide. The performance of metal-microheater integrated waveguide phase-shifter has been analyzed in terms of the figure of merit (FOM) $\mathcal{F} = S_H / \tau_{th}$ (S_H - thermal sensitivity, τ_{th} - thermal time constant). The demonstrated switches exhibit a broadband extinction ratio of ~ 20 dB with an insertion loss of 2.5 dB. A folded waveguide phase-shifter design integrated in a balanced MZI is characterized experimentally with $\mathcal{F}_H = 23.3$ K·μm/mW·μs ($S_H = 119$ K·μm/mW and $\tau_{th} = 5.1$ μs); which is shown to be ~ 1.5 times superior than that of straight waveguide phase-shifter of same waveguide cross-sectional geometry and length ($L_w = 400$ μm). Though the demonstrated MZI switches were not designed with the best possible values of figure of merits (S_H, τ_{th} and $\mathcal{F}_H$), the experimental results helps to extract the characteristic parameters like g_w (thermal conductivity per unit length of the waveguide phase-shifter) and h_w (heat capacitance per unit length of the waveguide phase-shifter) of a thermo-optic waveguide phase-shifter for its modeling and optimized design.

6.2 Thesis Outlook

The successful demonstration of WIDC based MZIs enabled us to demonstrate wavelength insensitive thermo-optic switches. Similarly, WIDC based MRRs can also be used for the demonstration of reconfigurable add-drop multiplexer operating over a broad operating wavelength range. Moreover, the concept can be extended to demonstrate more complex devices/components for various silicon photonics applications. For example, recently our group has demonstrated an add-drop filter by integrating sub-wavelength grating (SWG) structures in the two arms of a WIDC based balanced MZI as shown in Figure 6.1(a) [126]. The transmission characteristics measured for the OFF-state and ON-state of phase-shifter integrated with microheater H1 is also shown in Figures 6.1(c) and 6.1(b) respectively. The flat passband transmission characteristics of such filters are useful for on-chip multi-channel filtering of WDM channels [58].

(a)

(b)   (c)
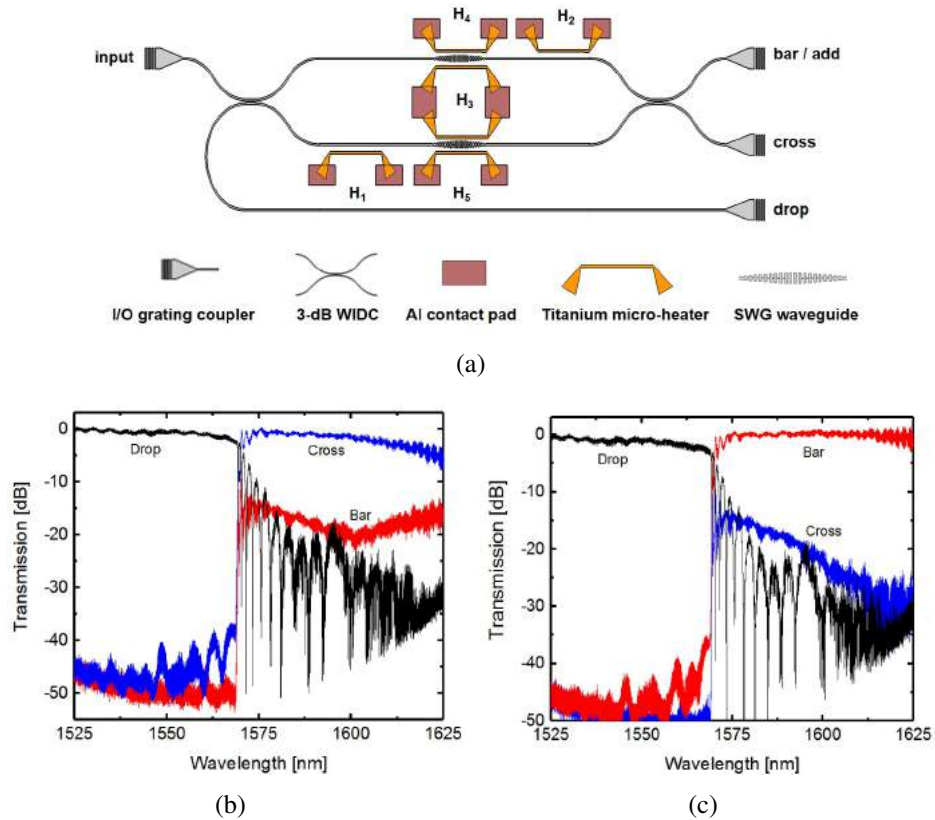
Figure 6.1: (a) Schematic illustration of the proposed 2×2 MZI based add-drop filter device integrated with five microheaters (H1-H5) at different locations; (b) and (c) are the transmission characteristics at the output ports corresponding to the OFF- and ON-state of heater H1 respectively [126].
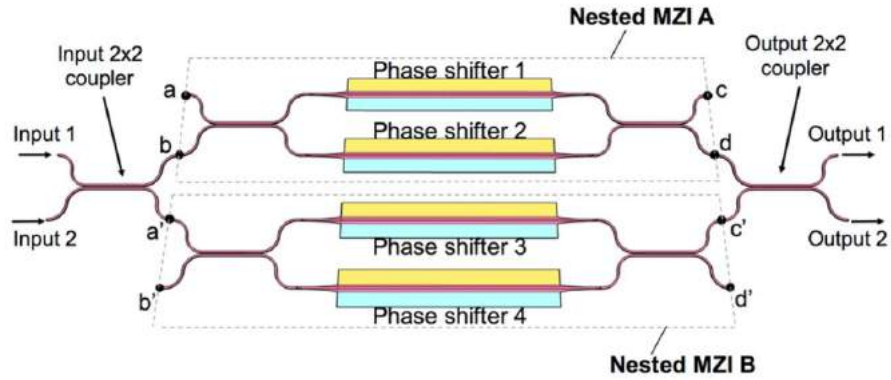
Figure 6.2: Schematic of the proposed balanced nested Mach-Zehnder interferometer (BNMZI) switch by Lu *et al.* in Ref. [155].

Very recently, Lu *et al.* [155] proposed a tri-state (cross/bar/blocking) switches with DC based MZI structures 6.2 as shown in Figure 6.2. These switches are designed for high-speed, broadband and low-cross talk performances and provides and extra blocking state which can be used for crosstalk suppression in $N \times N$ switch fabrics. The conventional DCs in the proposed model can be replaced with WIDCs to extend the bandwidth to C+L bands with improved crosstalk performance between the switching states.

The proposed WIDC design also enables slab integration of microheaters/p-n junction diodes for faster switching applications. The switching power can be reduced by appropriate positioning of thermo-optic/electro-optic phase-shifters and with suitable trench isolation. Moreover, we strongly believe the footprint of the proposed WIDC structures can be reduced further and it is possible to use them in a large scale silicon photonics switch matrix and for large number of channel add-drop multiplexing [58].

APPENDIX A

Directional Coupler based 4-channel WDM

(de-multiplexer)

In this section we discuss the application of dispersion enhanced conventional DCs as a 4-channel wavelength de-multiplexer.

A.1 Design and Demonstration

Typical layout of a 1×4 wavelength de-multiplexer is shown in Figure A.1(a), where all the three DCs (DC_a, DC_b and DC_c) are designed for highly dispersive transfer functions (see Figure 2.12). DC_a de-interleaves the four channels (λ_1, λ_2, λ_3 and λ_4) given at the

(a)   (b)
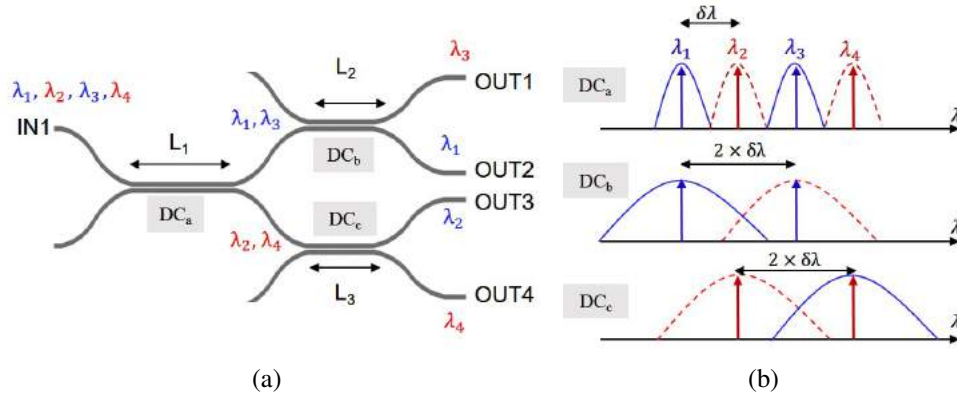
Figure A.1: Working principle of a 1×4 WDM (de-multiplexer); (a) schematic layout showing a cascaded 1×2 architecture of three interleavers DC_a, DC_b and DC_c with corresponding input and output channels at each output ports; (b) the transfer functions at the bar port (solid) and cross port (dashed) of DC_a (top), DC_b (middle) and DC_b (bottom). Vertical arrows indicate the location of four input channels.

input port such that λ_1 and λ_3 appear at the bar port and λ_2 and λ_4 appear at the cross port respectively. Again DC_b (DC_c) de-interleaves λ_1 (λ_2) to its bar port and λ_3 (λ_4) to its cross port respectively. The DCs are designed such that the transfer functions (bar

port and cross port) exactly match with the corresponding λs as shown in Figure A.1(b). For example the FSR (between the bar and cross ports) of DC_a is equal to the channel separation $\delta\lambda$ and that of DC_b and DC_c are $2\delta\lambda$. Also, the transfer function of DC_a and DC_b are relatively out-of phase by $\pi/2$ to drop the respective wavelength channels at the output ports. Thus for a fixed dispersive DC geometry, L_1, L_2 and L_3 are designed such that:

$$L_1 = \frac{\lambda_1\lambda_3}{2\delta\lambda \cdot \Delta n_g}, \quad L_2 = \frac{L_1}{2} \quad \text{and} \quad L_3 = \frac{L_1}{2} \pm L_{3dB} \tag{A.1}$$

where the additional length L_{3dB} ensures $\pi/2$ phase shift in transfer functions of DC_a and DC_b. For a given $\delta\lambda$, the minimum possible length of DC_a is decided by the maximum possible value of $|\Delta n_g|$ and which in turn depends on the the cross-sectional design parameters of DC (W, h, G and H). Note that the maximum possible $|\Delta n_g|$
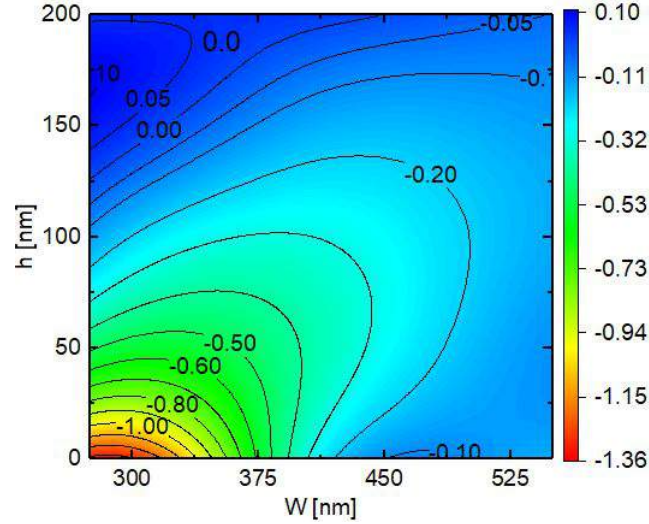
Figure A.2: Contour plots of Δn_g in W - h plane calculated for H = 250 nm, G = 150 nm and TE polarization at λ = 1550 nm.

(1.36) calculated with H = 250 nm SOI ($W = 300$ nm, $h = 0$ nm, $G = 150$ nm) is ~ 1.4 times more compared to that of $H = 220$ nm SOI ($W = 350$ nm, $h = 0$ nm, $G = 150$ nm) shown in Figure 2.13. Although dispersion is more for deeply etched DCs, the OBW is limited by the wavelength dependent slope of Δn_g. Thus shallow etched DCs with moderate $|\Delta n_g|$ gives relatively more OBW compared to that of shallow etched DCs (section 2.2). However, a lower $|\Delta n_g|$ results in longer DC length for a given channel separation $\delta\lambda$ as given in Eq. A.1. For example for a channel spacing of $\delta\lambda = 10$ nm, the calculated $L_1 \sim 106$ μm with deeply etched DC ($W = 300$ nm, $h = 0$ nm, $H = 250$ nm, $G = 150$ nm), and $L_1 \sim 1000$ μm for with shallow etched DC

$(W = 550$ nm, $h = 150$ nm, $H = 250$ nm, $G = 150$ nm$)$.

For experimental demonstration we have fabricated the proposed WDM device on a 250-nm device layer SOI with a relatively shallow etched DC with $W \sim 550$ nm, $h \sim 150$ nm and $G \sim 150$ nm [85]. The corresponding Δn_g is estimated to be $0.1 \leq |\Delta n_g| \leq 0.12$ over 1520 nm $\leq \lambda \leq 1570$ nm. The DC lengths L_1, L_2 and L_3 are calculated using Eq. A.1 and 2.9 as 1000 μm, 500 μm, and 506.5 μm respectively for a channel spacing of $\delta\lambda = 10$ nm. One can also fabricate more compact device with deeply etched DC $(W = 300$ nm, $h = 0$ nm, $G = 150$ nm$)$ in two step fabrication process, where shallow input/output GCs are fabricated in first defined followed deeply etched DC waveguides in a second step by properly masking the GC regions.

(a)

(b)   (c)
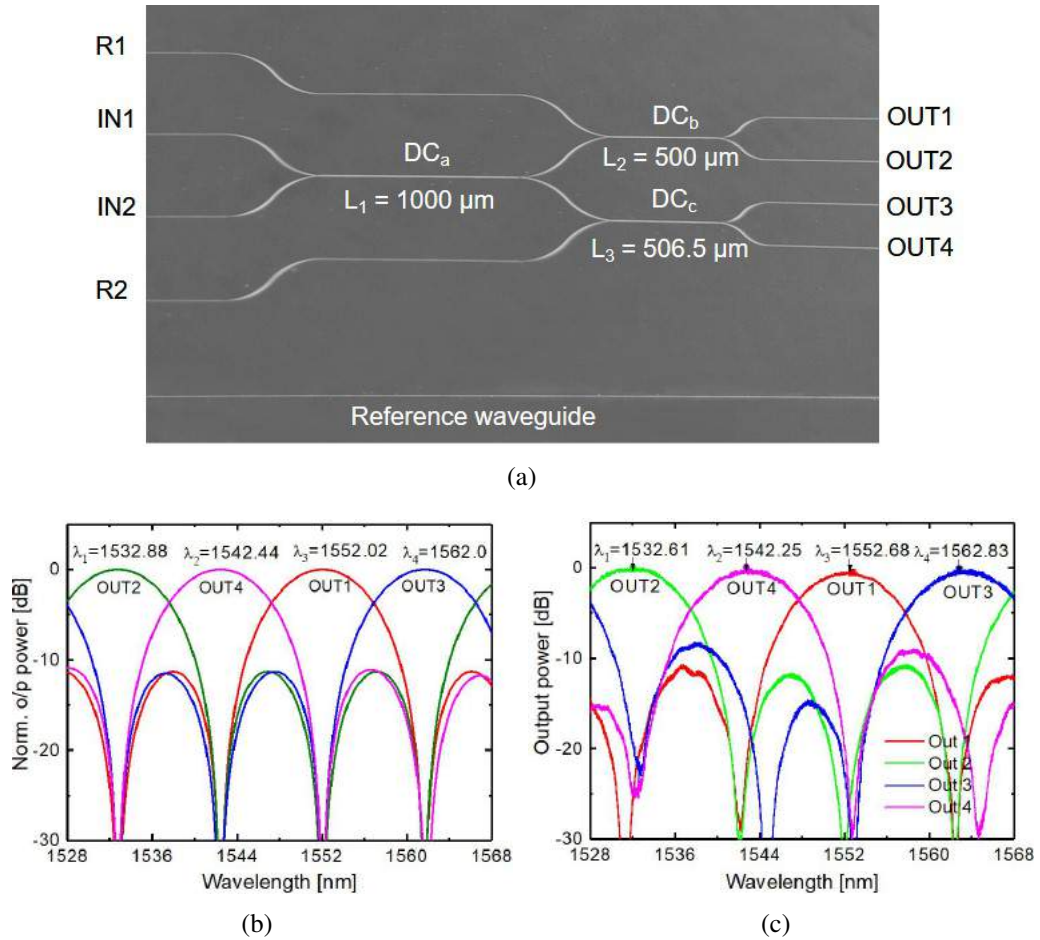
Figure A.3: (a) Microscopic photograph of a 4-channel WDM (de-multiplexer) device along with a reference straight waveguide; (b) and (c) are simulated and experimental transmission characteristics of the normalized with reference waveguide output.

A microscopic photograph of a fabricated 4-channel WDM (de-multiplexer) device

has been shown in Figure A.3(a) It has two identical input ports (IN1 and IN2) and four output ports (OUT1, OUT2, OUT3, and OUT4). The auxiliary inputs R1 and R2 are used to extract the transmission characteristics of of individual directional couplers (DC_b, and DC_c) The device is characterized by launching a broadband light source at port IN1 through input GC and the corresponding outputs are collected through corresponding GCs and recorded in OSA. Typical simulated and experimental transmission spectra (normalized to 0 dB) at individual output ports (OUT1, OUT2, OUT3 and OUT4) of the fabricated device are shown in Figures A.3(b) A.3(c) respectively. The channel separation is measured to be ~ 1.2 THz (10 nm) with cross talk < -16 dB. On chip insertion loss of the device is measured to be < 1 dB. The concept can be scaled to $1 \times N$ channel WDM device by cascading $(N - 1)$ number of DCs in a pyramidal architecture, which can be considered as an alternative solution of AWG devices requiring stringent design and process parameters.The FSR values as well as device footprints can be reduced by designing a highly dispersive DC (e.g. $\Delta n_g > 1$).

APPENDIX B

Additional Information on Fabrication

B.1 SOI Specifications (SOITEC)

Table B.1: Specifications of 220-nm device layer SOI.

Parameter	Device Layer	BOX	Handle Wafer
Thickness	220 nm	2 µm	500 µm
Doping	P-type	-	P-type
Crystal orientation	(100)	-	(100)
Resistivity	8.5-11.5 Ωcm	-	750 Ωcm

B.2 Silicon Cleaning Procedure

1. **TCE Cleaning** (TCE assay 99.5%): To remove organic contaminants
   - Ultrasonic agitation with TCE for 2 min
   - Heat up (60 °C) for 2 min

2. **Acetone Cleaning** (Acetone assay 99.5%): To remove residue formed by TCE
   - Ultrasonic agitation with acetone for 2 min (till bubbles come)
   - Heat up (60 °C) for 2 min
   - Take out sample and clean under running DI water
   - Dry with nitrogen air gun

3. **HNO_3 Cleaning** (HNO_3 assay 69 - 70%): To form metal oxides
   - Heat up (60 °C) for 2-3 min (till fumes come)
   - Rinse the sample with DI water and check for hydrophilic surface
   - Dry with nitrogen air gun

4. **HF Cleaning** (HF assay 48 - 52%): To remove metal oxides
   - Dip in dilute HF (HF:DI Water::1:10) for 30 sec
   - Rinse the sample with DI water and check for hydrophobic surface
   - Dry with nitrogen air gun

B.3 Spin Coating Procedure

1. **Resist Details**
   - **Resist:** HSQ - XR-1541 (6%), negative tone e-beam resist
   - **Chemical Formula:** $[HSiO3/2]_n$
   - **Features:** High resolution (~ 10 nm), minimum line edge roughness, excellent etch resistance and stability under SEM inspections[156]
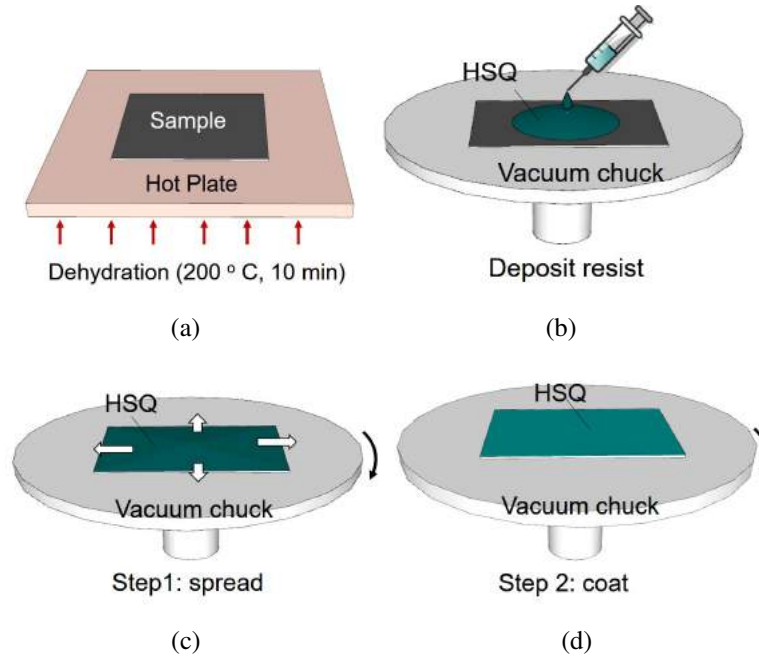
Figure B.1: Steps for spin coating: (a) dehydration (200 °C, 10 min), (b) deposit resist, (c) spread and (d) coat (see Figure B.2(a)).

2. **Two-Step Spin Coating (POLO - SPIN200i)**
   A schematic of the spin coating procedure is shown in Figure B.1.

   (a) Dehydration: 200°C, 10 min
   (b) Resist deposition: A few drops using a fresh syringe
   (c) Spread the resist: Spin at slow speed ($v_1 = 100$ rpm) and acceleration ($a_1 = 100$ rpm/s) for 10 sec (see Figure B.2(a))
   (d) coat the resist: Adjust spin speed (v_2), acceleration (a_2) and time t_2 for a desired resist thickness.

   Figure B.2(b) shows the HSQ film thickness versus spin speed v_2 for different acceleration of a_1 and a_2 keeping $v_1 = 100$ rpm, $t_1 = 10$ sec and $t_2 = 30$ sec. The thickness of the thin-film resist were measured using cross-sectional SEM images with an accuracy of $\sim \pm 20$ nm. Figures B.3(a) and B.3(b) show the SEM images of ~ 130 nm and ~ 300 nm HSQ layers respectively, over the silicon substrate.

3. **Prebake** After coating the sample is prebaked for 2 min at 180°C (hot plate).
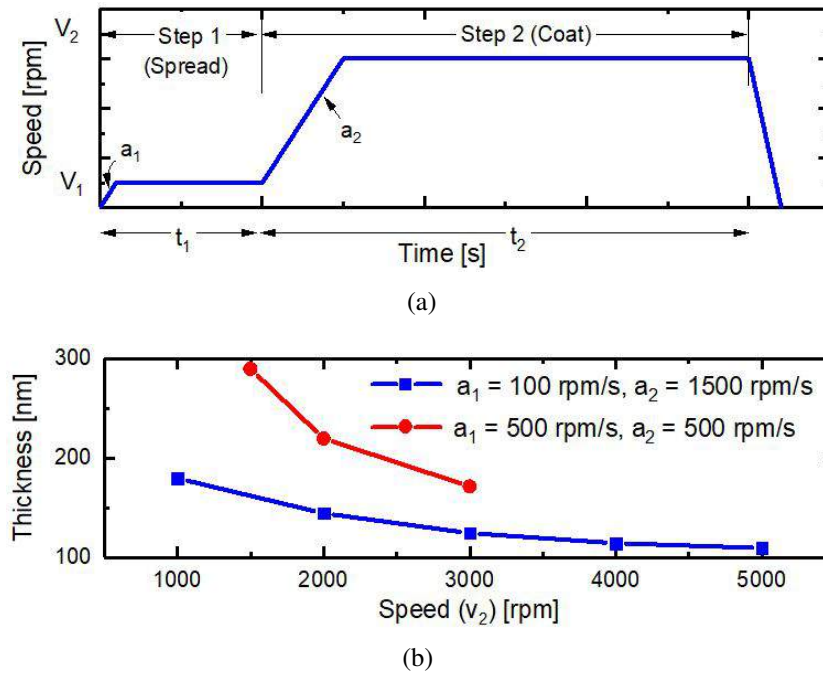
Figure B.2: (a) Spin speed versus time graph for coating HSQ over silicon sample in two steps; (b) Resist thickness versus spin speed ($v1$, $v2 = 100$ rpm) measured for two different combinations of a_1 and a_2: $a_1 = 100$ rpm/s, $a_2 = 1500$ rpm/s (blue squares), and $a_1 = 500$ rpm/s, $a_2 = 500$ rpm/s(red circles), and time (30 sec).
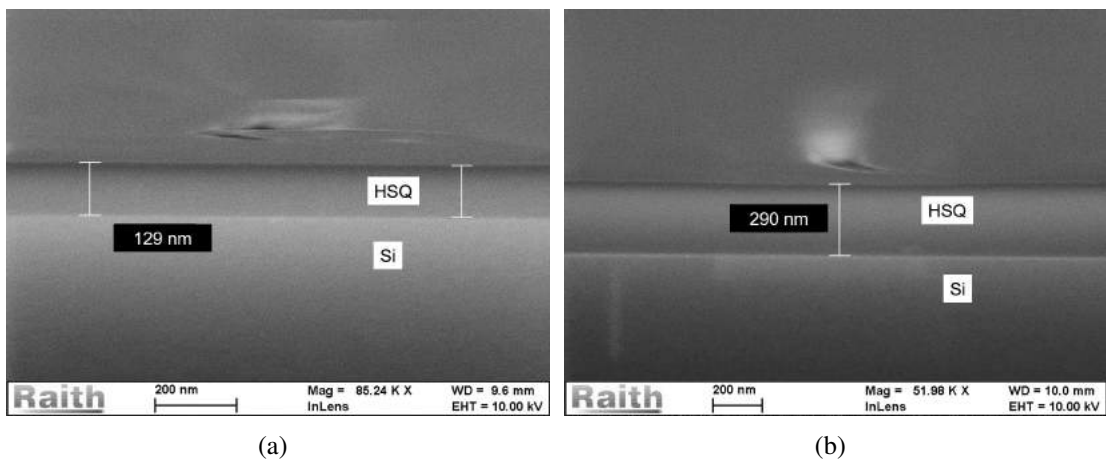
Figure B.3: SEM image showing the cross-section of HSQ layer of thickness (a) $\sim$ 130 nm and (b) $\sim$ 300 nm.

B.4   Patterning Parameters

1. **Mask Details**
   - **Mask Format:** GDS-II designed in Raith Nanosuit
   - **Device length:** 2-3 mm
   - **Waveguides:** Fixed Beam Moving Stage (FBMS) lines

133

- **GC and WIDC mask:** Conventional Elements (CE)

2. **System Specifications of RAITH-150 TWO**
   - **Acceleration Voltage (EHT):** Upto 30 kV
   - **Aperture sizes:** 7.5 μm, 10 μm, 20 μm, 30 μm, 60 μm and 120 μm
   - **Beam current:** Depends on EHT and aperture size (10 pA to 6000 pA)

3. **Optimized Dose Parameters**
   - **Write Field (WF) area:** 100×100 μm^2
   - **Working distance:** 10 mm
   - **Waveguides and GCs (single step):** EHT = 20 kV, Aperture size = 20 μm, beam current = 145 pA, FBMS dose = 350 μC/cm^2, CE dose = 240 μC/cm^2
   - **WIDC mask and Contact Pads:** EHT = 20 kV, Aperture size = 30 μm, beam current = 350 pA, CE dose = 90 μC/cm^2
   - **SEM measured waveguide width:** (Width of waveguide in mask - 100 nm) ± 20 nm
   - **SEM measured DC gap:** (Gap of DC in mask - 100 nm) ± 20 nm

4. **Development**
   - 6 - 7 min in MF319 developer (ambient temperature $\sim 24°$C)
   - Rinse with running DI water
   - Dry with nitrogen air gun
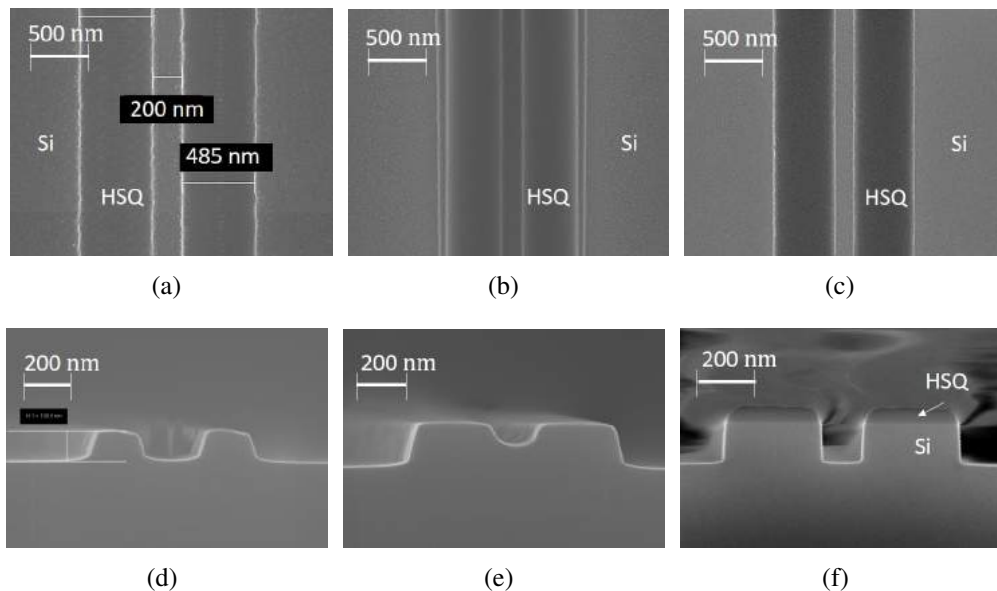
Figure B.4: (a)-(c) Top view SEM images of a DC after patterning, (d)-(e) cross-sectional SEM images of DC after etching. (a) & (d) under-dose, (b) & (e) over-dose, (c) & (e) optimum dose.

5. **Postbake:** 300 °C for 3 min (hot plate)

Figure B.4 shows the SEM images of DC region after patterning with different doses; (a) under-dose, (b) over-dose and (c) optimum-dose. The corresponding SEM images after etching are shown in (e) - (f) respectively.

B.5   ICPRIE Parameters (Oxford PlasmaLab System100)

The etch depth versus time graph of silicon and HSQ with an optimized ICPRIE chemistry is plotted in Figure B.5.   Figures B.6 shows the SEM images of a silicon waveg-
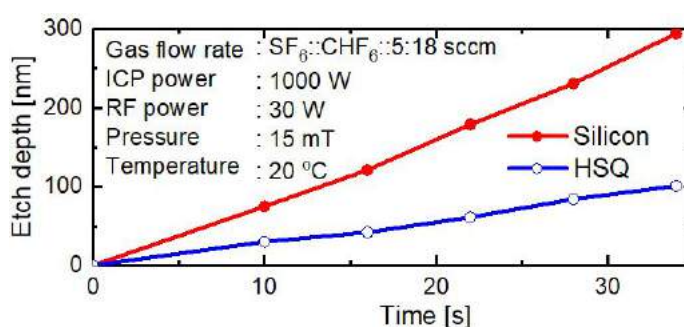
Figure B.5: Etch depth of a silicon and HSQ mask against etching time in optimized ICPRIE chemistry.
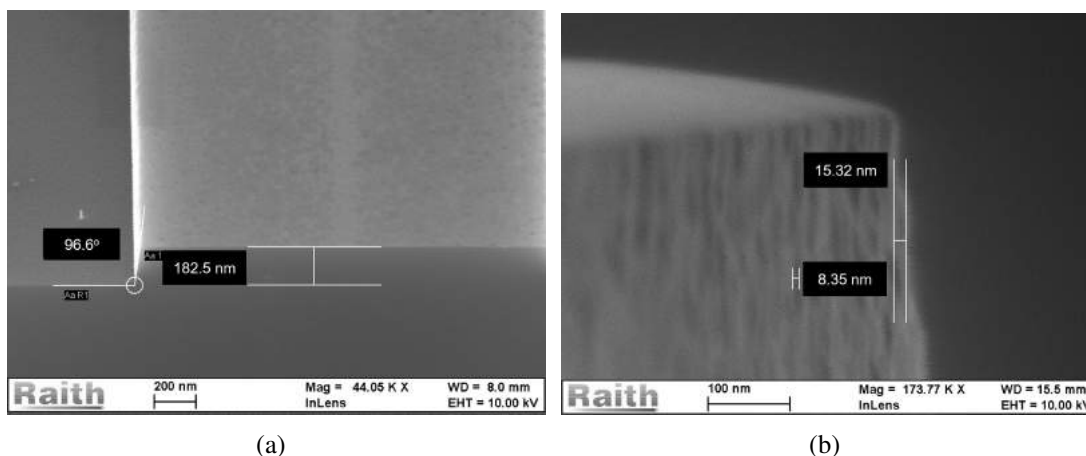
Figure B.6: Tilted SEM images of a silicon waveguide with nearly (a) vertical (96°) and (b) smooth sidewall (roughness $\sim$ 15 nm).

uide with nearly vertical (96°) and smooth sidewall (roughness $\sim$ 15 nm).

APPENDIX C

DOCTORAL COMMITTEE

CHAIR PERSON : Prof. Anil Prabhakar

Professor

Department of Electrical Engineering

Indian Institute of Technology, Madras

GUIDE : Prof. Bijoy Krishna Das

Professor

Department of Electrical Engineering

Indian Institute of Technology, Madras

MEMBERS : Prof. Amitava DasGupta

Professor

Department of Electrical Engineering

Indian Institute of Technology, Madras

: Dr. Ananth Krishnan

Assistant Professor

Department of Electrical Engineering

Indian Institute of Technology, Madras

: Dr. Manu Jaiswal

Assistant Professor

Department of Physics

Indian Institute of Technology, Madras

APPENDIX D

List of Publications Based on Thesis

Journals

1. **Ramesh K. Gupta** and Bijoy K. Das, "Performance Analysis of Metal-Microheater Integrated Silicon Waveguide Phase-Shifters", OSA Continuum, Vol. 1, Issue 2, pp. 703-714 (2018).

2. Sumi R., **Ramesh K. Gupta** and Bijoy K. Das, "Ultra Broadband Add-Drop Filter/Switch Circuit using Sub-Wavelength Grating Waveguides", IEEE Journal of Selected Topics in Quantum Electronics (2018), Vol. 25, No. 3, pp.1-11, May/June 2018.

3. **Ramesh. K. Gupta**, S. Chandran and B. K. Das, "Wavelength Independent Directional Couplers for Integrated Silicon Photonics," IEEE/OSA Journal of Lightwave Technology, Vol. 35, No. 22, pp. 4916-4923, November 2017.

4. **Ramesh K. Gupta** and Bijoy K. Das. "Multi-input and multi-output SOI (MIMO-SOI) platform for silicon photonics", CSI Transactions on ICT, Vol. 5, No. 2, pp. 189-193, June 2017.

5. S. Chandran, **Ramesh. K. Gupta** and B. K. Das, "Dispersion enhanced critically coupled ring resonator for wide range refractive index sensing", IEEE Journal of Selected Topics in Quantum Electronics, vol. 23, No. 2, pp.1-9, March 2017.

6. B K Das, N DasGupta, S Chandran, S Kurudi, P Sah, R Nandi, **Ramesh K.**, et. al, "Silicon Photonics Technology : Ten Years of Research at IIT Madras", Asian Journal of Physics, Vol. 25, No. 7, pp. 923 - 955, 2016.

Conference (Presentations / Proceedings/Workshop)

1. **Ramesh K. Gupta** and Bijoy K. Das, "Wideband MZI based Thermo-Optic Switch with Slab Integrated Microheater in SOI", 13th Pacific Rim Conference on Lasers and Electro-Optics (CLEO Pacific Rim, CLEO-PR 2018), 29 July to 3 August 2018, Hong Kong (poster).

2. R. Sumi, **Ramesh K Gupta**, Nandita DasGupta, and Bijoy K Das, "Integrated Optical Ultra-Broadband Add-Drop Filter in Silicon-On-Insulator Platform." Optical Fiber Communications Conference and Exposition (OFC), Optical Society of America, 2018 (pp. M4H-7).

3. **Ramesh. K. Gupta**, S. Chandran and B. K. Das, "Integrated silicon photonic directional couplers for WDM applications," 3rd International Conference on Microwave and Photonics (ICMAP), 9-11 February 2018, Dhanbad, India.

4. B.K. Das, **R.K. Gupta**, P. Sah, and S. Chandran, "Novel wavelength filter devices in SOI for optical interconnect applications," ICMAT 2017, Suntec Singapore, June 18- 23, 2017 (invited).

5. B. K. Das, S. Chandran, P. Sah, and **R. K. Gupta**, "Novel wavelength filter devices in SOI for sensing applications," Photonics 2016, IIT Kanpur, India, Dec. 04-08, 2017 (invited).

REFERENCES

[1] C. Gunn *et al.*, "CMOS photonics for high-speed interconnects," *IEEE micro*, vol. 26, no. 2, pp. 58–66, 2006.

[2] A. Liu, L. Liao, Y. Chetrit, J. Basak, H. Nguyen, D. Rubin, and M. Paniccia, "Wavelength division multiplexing based photonic integrated circuits on silicon-on-insulator platform," *IEEE Journal of Selected Topics in Quantum Electronics*, vol. 16, no. 1, pp. 23–32, 2010.

[3] M. Asghari and A. V. Krishnamoorthy, "Silicon photonics: Energy-efficient communication," *Nature Photonics*, vol. 5, no. 5, p. 268, 2011.

[4] Y. Ma, Y. Zhang, S. Yang, A. Novack, R. Ding, A. E.-J. Lim, G.-Q. Lo, T. Baehr-Jones, and M. Hochberg, "Ultralow loss single layer submicron silicon waveguide crossing for SOI optical interconnect," *Optics Express*, vol. 21, no. 24, pp. 29 374–29 382, 2013.

[5] S. Assefa, S. Shank, W. Green, M. Khater, E. Kiewra, C. Reinholm, S. Kamlapurkar, A. Rylyakov, C. Schow, F. Horst *et al.*, "A 90 nm CMOS integrated nano-photonics technology for 25 Gbps WDM optical communications applications," in *IEEE International Electron Devices Meeting (IEDM), 2012*. IEEE, 2012, pp. 33–8.

[6] C. Sun, M. Georgas, J. Orcutt, B. Moss, Y.-H. Chen, J. Shainline, M. Wade, K. Mehta, K. Nammari, E. Timurdogan *et al.*, "A monolithically-integrated chip-to-chip optical link in bulk CMOS," *IEEE Journal of Solid-State Circuits*, vol. 50, no. 4, pp. 828–844, 2015.

[7] L. Pavesi, D. J. Lockwood *et al.*, "Silicon Photonics III," *Topics in Applied Physics (Springer Berlin Heidelberg, 2016)*, vol. 122, 2016.

[8] A. E. Lim, T.-Y. Liow, J. Song, C. Li, Q. Fang, X. Tu, N. Duan, K. K. Chen, R. P. C. Tern, C. Peng *et al.*, "Path to silicon photonics commercialization: 25 Gb/s platform development in a CMOS manufacturing foundry line," in *Optical Fiber Communication Conference*. Optical Society of America, 2014, pp. Th2A–51.

[9] A. Khanna, Y. Drissi, P. Dumon, R. Baets, P. Absil, J. Pozo, D. L. Cascio, M. Fournier, J. Fédéli, L. Fulbert *et al.*, "Epixfab: the silicon photonics platform," in *Integrated Photonics: Materials, Devices, and Applications II*, vol. 8767. International Society for Optics and Photonics, 2013, p. 87670H.

[10] G. T. Reed, G. Mashanovich, F. Y. Gardes, and D. Thomson, "Silicon optical modulators," *Nature Photonics*, vol. 4, no. 8, p. 518, 2010.

[11] D. Marris-Morini, L. Vivien, G. Rasigade, J.-M. Fedeli, E. Cassan, X. Le Roux, P. Crozat, S. Maine, A. Lupu, P. Lyan *et al.*, "Recent progress in high-speed silicon-based optical modulators," *Proceedings of the IEEE*, vol. 97, no. 7, pp. 1199–1215, 2009.

[12] G. Cocorullo, M. Iodice, and I. Rendina, "All-silicon fabry–perot modulator based on the thermo-optic effect," *Optics Letters*, vol. 19, no. 6, pp. 420–422, 1994.

[13] G. Cocorullo, F. G. Della Corte, I. Rendina, and P. M. Sarro, "Thermo-optic effect exploitation in silicon microstructures," *Sensors and Actuators A: Physical*, vol. 71, no. 1-2, pp. 19–26, 1998.

[14] C. Qiu, X. Ye, R. Soref, L. Yang, and Q. Xu, "Demonstration of reconfigurable electro-optical logic with silicon photonic integrated circuits," *Optics Letters*, vol. 37, no. 19, pp. 3942–3944, 2012.

[15] M. Bahadori, A. Gazman, N. Janosik, S. Rumley, Z. Zhu, R. Polster, Q. Cheng, and K. Bergman, "Thermal rectification of integrated microheaters for microring resonators in silicon photonics platform," *Journal of Lightwave Technology*, vol. 36, no. 3, pp. 773–788, 2018.

[16] M. Dinu, F. Quochi, and H. Garcia, "Third-order nonlinearities in silicon at telecom wavelengths," *Applied physics Letters*, vol. 82, no. 18, pp. 2954–2956, 2003.

[17] R. Claps, D. Dimitropoulos, V. Raghunathan, Y. Han, and B. Jalali, "Observation of stimulated Raman amplification in silicon waveguides," *Optics Express*, vol. 11, no. 15, pp. 1731–1739, 2003.

[18] R. Dekker, A. Driessen, T. Wahlbrink, C. Moormann, J. Niehusmann, and M. Först, "Ultrafast kerr-induced all-optical wavelength conversion in silicon waveguides using 1.55 μm femtosecond pulses," *Optics Express*, vol. 14, no. 18, pp. 8336–8346, 2006.

[19] I.-W. Hsieh, X. Chen, X. Liu, J. I. Dadap, N. C. Panoiu, C.-Y. Chou, F. Xia, W. M. Green, Y. A. Vlasov, and R. M. Osgood, "Supercontinuum generation in silicon photonic wires," *Optics Express*, vol. 15, no. 23, pp. 15 242–15 249, 2007.

[20] I.-W. Hsieh, X. Chen, J. I. Dadap, N. C. Panoiu, R. M. Osgood, S. J. McNab, and Y. A. Vlasov, "Cross-phase modulation-induced spectral and temporal effects on co-propagating femtosecond pulses in silicon photonic wires," *Optics Express*, vol. 15, no. 3, pp. 1135–1146, 2007.

[21] R. Claps, D. Dimitropoulos, and B. Jalali, "Stimulated Raman scattering in silicon waveguides," *Electronics Letters*, vol. 38, no. 22, pp. 1352–1354, 2002.

[22] Y. Okawachi, M. A. Foster, J. E. Sharping, A. L. Gaeta, Q. Xu, and M. Lipson, "All-optical slow-light on a photonic chip," *Optics Express*, vol. 14, no. 6, pp. 2317–2322, 2006.

[23] H. Fukuda, K. Yamada, T. Shoji, M. Takahashi, T. Tsuchizawa, T. Watanabe, J.-i. Takahashi, and S.-i. Itabashi, "Four-wave mixing in silicon wire waveguides," *Optics Express*, vol. 13, no. 12, pp. 4629–4637, 2005.

[24] C. Bransley, I. Agha, and Y. Zhao, "Four-wave mixing in silicon waveguides," *Bulletin of the American Physical Society*, vol. 61, 2016.

[25] M. J. Heck, H.-W. Chen, A. W. Fang, B. R. Koch, D. Liang, H. Park, M. N. Sysak, and J. E. Bowers, "Hybrid silicon photonics for optical interconnects," *IEEE Journal of Selected Topics in Quantum Electronics*, vol. 17, no. 2, pp. 333–346, 2011.

[26] T. Komljenovic, M. Davenport, J. Hulme, A. Y. Liu, C. T. Santis, A. Spott, S. Srinivasan, E. J. Stanton, C. Zhang, and J. E. Bowers, "Heterogeneous silicon photonic integrated circuits," *Journal of Lightwave Technology*, vol. 34, no. 1, pp. 20–35, 2016.

[27] M. Watts, "Silicon photonics in high performance computing," in *Photonics in Switching*. Optical Society of America, 2010, p. PMC1.

[28] M. A. Taubenblatt, "Optical interconnects for high-performance computing," *Journal of Lightwave Technology*, vol. 30, no. 4, pp. 448–457, 2012.

[29] J. T. Robinson, L. Chen, and M. Lipson, "On-chip gas detection in silicon optical microcavities," *Optics Express*, vol. 16, no. 6, pp. 4296–4301, 2008.

[30] M.-S. Kwon and W. H. Steier, "Microring-resonator-based sensor measuring both the concentration and temperature of a solution," *Optics Express*, vol. 16, no. 13, pp. 9372–9377, 2008.

[31] S. M. Grist, S. A. Schmidt, J. Flueckiger, V. Donzella, W. Shi, S. T. Fard, J. T. Kirk, D. M. Ratner, K. C. Cheung, and L. Chrostowski, "Silicon photonic microdisk resonators for label-free biosensing," *Optics Express*, vol. 21, no. 7, pp. 7994–8006, 2013.

[32] V. Passaro, C. d. Tullio, B. Troia, M. L. Notte, G. Giannoccaro, and F. D. Leonardis, "Recent advances in integrated photonic sensors," *Sensors*, vol. 12, no. 11, pp. 15 558–15 598, 2012.

[33] D. Zhou and R. Biswas, "Photonic crystal enhanced light-trapping in thin film solar cells," *Journal of Applied Physics*, vol. 103, no. 9, p. 093102, 2008.

[34] E. Garnett and P. Yang, "Light trapping in silicon nanowire solar cells," *Nano Letters*, vol. 10, no. 3, pp. 1082–1087, 2010.

[35] H. Takesue, K.-i. Harada, H. Fukuda, T. Tsuchizawa, T. Watanabe, K. Yamada, Y. Tokura, and S.-i. Itabashi, "Silicon photonics in quantum communications," in *2009 Conference on Lasers and Electro-Optics and 2009 Conference on Quantum electronics and Laser Science Conference, CLEO/QELS*. IEEE, 2009, pp. 1–2.

[36] J. W. Silverstone, D. Bonneau, J. L. OâĂŹBrien, and M. G. Thompson, "Silicon quantum photonics," *IEEE Journal of Selected Topics in Quantum Electronics*, vol. 22, no. 6, pp. 390–402, 2016.

[37] M. Hochberg, N. C. Harris, R. Ding, Y. Zhang, A. Novack, Z. Xuan, and T. Baehr-Jones, "Silicon photonics: the next fabless semiconductor industry," *IEEE Solid-State Circuits Magazine*, vol. 5, no. 1, pp. 48–58, 2013.

[38] R. Soref and J. Larenzo, "All-silicon active and passive guided-wave components for λ= 1.3 and 1.6 μm," *IEEE Journal of Quantum Electronics*, vol. 22, no. 6, pp. 873–879, 1986.

[39] D. Dai, J. Bauters, and J. E. Bowers, "Passive technologies for future large-scale photonic integrated circuits on silicon: polarization handling, light non-reciprocity and loss reduction," *Light: Science & Applications*, vol. 1, no. 3, p. e1, 2012.

[40] D. H. Lee, S. J. Choo, U. Jung, K. W. Lee, K. W. Kim, and J. H. Park, "Low-loss silicon waveguides with sidewall roughness reduction using a $Sio_2 2$ hard mask and fluorine-based dry etching," *Journal of Micromechanics and Microengineering*, vol. 25, no. 1, p. 015003, 2014.

[41] A. W. Fang, H. Park, O. Cohen, R. Jones, M. J. Paniccia, and J. E. Bowers, "Electrically pumped hybrid algainas-silicon evanescent laser," *Optics Express*, vol. 14, no. 20, pp. 9203–9210, 2006.

[42] G. Roelkens, Y. De Koninck, S. Keyvaninia, S. Stankovic, M. Tassaert, M. Lamponi, G. Duan, D. Van Thourhout, and R. Baets, "Hybrid silicon lasers," in *Optoelectronic Integrated Circuits XIII*, vol. 7942. International Society for Optics and Photonics, 2011, p. 79420D.

[43] O. Boyraz and B. Jalali, "Demonstration of a silicon Raman laser," *Optics Express*, vol. 12, no. 21, pp. 5269–5273, 2004.

[44] H. Rong, R. Jones, A. Liu, O. Cohen, D. Hak, A. Fang, and M. Paniccia, "A continuous-wave Raman silicon laser," *Nature*, vol. 433, no. 7027, p. 725, 2005.

[45] H.-W. Chen, Y.-h. Kuo, and J. E. Bowers, "High speed silicon modulators," in *OptoElectronics and Communications Conference, 2009. OECC 2009. 14th.* Citeseer, 2009, pp. 1–2.

[46] A. Liu, L. Liao, D. Rubin, H. Nguyen, B. Ciftcioglu, Y. Chetrit, N. Izhaky, and M. Paniccia, "High-speed optical modulation based on carrier depletion in a silicon waveguide," *Optics Express*, vol. 15, no. 2, pp. 660–668, 2007.

[47] W. M. Green, M. J. Rooks, L. Sekaric, and Y. A. Vlasov, "Ultra-compact, low RF power, 10 Gb/s silicon Mach-Zehnder modulator," *Optics Express*, vol. 15, no. 25, pp. 17 106–17 113, 2007.

[48] S. Koester, G. Dehlinger, J. Schaub, J. Chu, Q. Ouyang, and A. Grill, "Germanium-on-insulator photodetectors," in *2nd International Conference on Group IV Photonics, 2005.* IEEE, 2005, pp. 171–173.

[49] M. Rouvière, L. Vivien, X. Le Roux, J. Mangeney, P. Crozat, C. Hoarau, E. Cassan, D. Pascal, S. Laval, J.-M. Fédéli *et al.*, "Ultrahigh speed germanium-on-silicon-on-insulator photodetectors for 1.31 and 1.55 μm operation," *Applied Physics Letters*, vol. 87, no. 23, p. 231109, 2005.

[50] M. Oehme, J. Werner, E. Kasper, M. Jutzi, and M. Berroth, "High bandwidth Ge p-i-n photodetector integrated on Si," *Applied physics Letters*, vol. 89, no. 7, p. 071117, 2006.

[51] A. Liu, H. Rong, M. Paniccia, O. Cohen, and D. Hak, "Net optical gain in a low loss silicon-on-insulator waveguide by stimulated Raman scattering," *Optics Express*, vol. 12, no. 18, pp. 4261–4268, 2004.

[52] Q. Xu, V. R. Almeida, and M. Lipson, "Demonstration of high Raman gain in a submicrometer-size silicon-on-insulator waveguide," *Optics Letters*, vol. 30, no. 1, pp. 35–37, 2005.

[53] H. Park, A. W. Fang, O. Cohen, R. Jones, M. J. Paniccia, and J. E. Bowers, "A hybrid AlGaInAs–silicon evanescent amplifier," *IEEE Photonics Technology Letters*, vol. 19, no. 4, pp. 230–232, 2007.

[54] Y.-h. Kuo, H. Rong, and M. Paniccia, "High bandwidth silicon ring resonator Raman amplifier," in *3rd International Conference on Group IV Photonics, 2006.* IEEE, 2006, pp. 228–230.

[55] R. Soref, "The past, present, and future of silicon photonics," *IEEE Journal of Selected Topics in Quantum Electronics*, vol. 12, no. 6, pp. 1678–1687, 2006.

[56] L. Kimerling, D. Ahn, A. Apsel, M. Beals, D. Carothers, Y.-K. Chen, T. Conway, D. Gill, M. Grove, C.-Y. Hong *et al.*, "Electronic-photonic integrated circuits on the CMOS platform," in *Silicon photonics*, vol. 6125. International Society for Optics and Photonics, 2006, p. 612502.

[57] J. S. Orcutt, B. Moss, C. Sun, J. Leu, M. Georgas, J. Shainline, E. Zgraggen, H. Li, J. Sun, M. Weaver *et al.*, "Open foundry platform for high-performance electronic-photonic integration," *Optics Express*, vol. 20, no. 11, pp. 12 222–12 232, 2012.

[58] Y. Li, Y. Zhang, L. Zhang, and A. W. Poon, "Silicon and hybrid silicon photonic devices for intra-datacenter applications: state of the art and perspectives," *Photonics Research*, vol. 3, no. 5, pp. B10–B27, 2015.

[59] C. Zhang and J. E. Bowers, "Silicon photonic terabit/s network-on-chip for datacenter interconnection," *Optical Fiber Technology*, vol. 44, pp. 2–12, 2018.

[60] "Intel® Silicon Photonics," https://www.intel.com.

[61] "IEEE standard for ethernet - amendment 10: Media Access Control Parameters, physical layers, and management parameters for 200 Gb/s and 400 Gb/s operation," *IEEE Std 802.3bs-2017*, 2017.

[62] A. Samani, D. Patel, M. Chagnon, E. El-Fiky, R. Li, M. Jacques, N. Abadía, V. Veerasubramanian, and D. V. Plant, "Experimental parametric study of 128 Gb/s PAM-4 transmission system using a multi-electrode silicon photonic Mach Zehnder modulator," *Optics Express*, vol. 25, no. 12, pp. 13 252–13 262, 2017.

[63] J. Verbist, M. Verplaetse, S. Srivinasan, P. De Heyn, T. De Keulenaer, R. Pierco, R. Vaernewyck, A. Vyncke, P. Absil, G. Torfs *et al.*, "First real-time 100-Gb/s NRZ-OOK transmission over 2 km with a silicon photonic electro-absorption modulator," in *Optical Fiber Communication Conference*. Optical Society of America, 2017, pp. Th5C–4.

[64] H. Zwickel, S. Wolf, C. Kieninger, Y. Kutuvantavida, M. Lauermann, T. De Keulenaer, A. Vyncke, R. Vaernewyck, J. Luo, A. K.-Y. Jen *et al.*, "Silicon-organic hybrid (SOH) modulators for intensity-modulation/direct-detection links with line rates of up to 120 Gbit/s," *Optics Express*, vol. 25, no. 20, pp. 23 784–23 800, 2017.

[65] J. Sun, M. Sakib, J. Driscoll, R. Kumar, H. Jayatilleka, Y. Chetrit, and H. Rong, "A 128 Gb/s PAM4 silicon microring modulator," in *2018 Optical Fiber Communications Conference and Exposition (OFC)*. IEEE, 2018, pp. 1–3.

[66] P. Dong, Y.-K. Chen, T. Gu, L. L. Buhl, D. T. Neilson, and J. H. Sinsky, "Reconfigurable 100 Gb/s silicon photonic network-on-chip," *Journal of Optical Communications and Networking*, vol. 7, no. 1, pp. A37–A43, 2015.

[67] P. Dong, "Silicon photonic integrated circuits for wavelength-division multiplexing applications," *IEEE J. Sel. Top. Quantum Electron.*, vol. 22, no. 6, pp. 370–378, 2016.

[68] Q. Fang, T.-Y. Liow, J. F. Song, K. W. Ang, M. B. Yu, G. Q. Lo, and D.-L. Kwong, "Wdm multi-channel silicon photonic receiver with 320 gbps data transmission capability," *Optics express*, vol. 18, no. 5, pp. 5106–5113, 2010.

[69] W. Bogaerts, P. De Heyn, T. Van Vaerenbergh, K. De Vos, S. Kumar Selvaraja, T. Claes, P. Dumon, P. Bienstman, D. Van Thourhout, and R. Baets, "Silicon microring resonators," *Laser & Photonics Reviews*, vol. 6, no. 1, pp. 47–73, 2012.

[70] Z. Fang and C. Z. Zhao, "Recent progress in silicon photonics: a review," *ISRN Optics*, vol. 2012, 2012.

[71] M. Rajarajan, B. Rahman, and K. Grattan, "A rigorous comparison of the performance of directional couplers with multimode interference devices," *Journal of Lightwave Technology*, vol. 17, no. 2, p. 243, 1999.

[72] M. T. Hill, X. Leijtens, G. D. Khoe, and M. K. Smit, "Optimizing imbalance and loss in 2×2 times/2 3-db multimode interference couplers via access waveguide width," *Journal of Lightwave Technology*, vol. 21, no. 10, pp. 2305–2313, 2003.

[73] S.-Y. Lee, S. Darmawan, C.-W. Lee, and M.-K. Chin, "Transformation between directional couplers and multi-mode interferometers based on ridge waveguides," *Optics Express*, vol. 12, no. 14, pp. 3079–3085, 2004.

[74] Y. Zhang, S. Yang, A. E.-J. Lim, G.-Q. Lo, C. Galland, T. Baehr-Jones, and M. Hochberg, "A compact and low loss y-junction for submicron silicon waveguide," *Optics express*, vol. 21, no. 1, pp. 1310–1316, 2013.

[75] P. Dumon, W. Bogaerts, V. Wiaux, J. Wouters, S. Beckx, J. Van Campenhout, D. Taillaert, B. Luyssaert, P. Bienstman, D. Van Thourhout *et al.*, "Low-loss SOI photonic wires and ring resonators fabricated with deep uv lithography," *IEEE Photonics Technology Letters*, vol. 16, no. 5, pp. 1328–1330, 2004.

[76] G. R. Bhatt, R. Sharma, U. Karthik, and B. K. Das, "Dispersion-free SOI interleaver for DWDM applications," *Journal of Lightwave Technology*, vol. 30, no. 1, pp. 140–146, 2012.

[77] A. W. Poon, X. Luo, F. Xu, and H. Chen, "Cascaded microresonator-based matrix switch for silicon on-chip optical interconnection," *Proceedings of the IEEE*, vol. 97, no. 7, pp. 1216–1238, 2009.

[78] N. Sherwood-Droz, H. Wang, L. Chen, B. G. Lee, A. Biberman, K. Bergman, and M. Lipson, "Optical 4×4 hitless silicon router for optical networks-on-chip (NoC)," *Optics Express*, vol. 16, no. 20, pp. 15 915–15 922, 2008.

[79] L. Yang, H. Jia, Y. Zhao, and Q. Chen, "Reconfigurable non-blocking four-port optical router based on microring resonators," *Optics Letters*, vol. 40, no. 6, pp. 1129–1132, 2015.

[80] L. Chen and Y.-k. Chen, "Compact, low-loss and low-power 8×8 broadband silicon optical switch," *Optics Express*, vol. 20, no. 17, pp. 18 977–18 985, 2012.

[81] B. G. Lee, A. V. Rylyakov, W. M. Green, S. Assefa, C. W. Baks, R. Rimolo-Donadio, D. M. Kuchta, M. H. Khater, T. Barwicz, C. Reinholm *et al.*, "Monolithic silicon integration of scaled photonic switch fabrics, CMOS logic, and device driver circuits," *Journal of Lightwave Technology*, vol. 32, no. 4, pp. 743–751, 2014.

[82] L. Yang, Y. Xia, F. Zhang, Q. Chen, J. Ding, P. Zhou, and L. Zhang, "Reconfigurable nonblocking 4-port silicon thermo-optic optical router based on Mach–Zehnder optical switches," *Optics Letters*, vol. 40, no. 7, pp. 1402–1405, 2015.

[83] B. E. Saleh, M. C. Teich, and B. E. Saleh, *Fundamentals of photonics*. Wiley New York, 1991, vol. 22.

[84] J. Van Campenhout, W. M. Green, S. Assefa, and Y. A. Vlasov, "Low-power, 2×2 silicon electro-optic switch with 110-nm bandwidth for broadband reconfigurable optical networks," *Optics Express*, vol. 17, no. 26, pp. 24 020–24 029, 2009.

[85] S. Chandran, R. K. Gupta, and B. K. Das, "Dispersion enhanced critically coupled ring resonator for wide range refractive index sensing," *IEEE Journal of Selected Topics in Quantum Electronics*, vol. 23, no. 2, pp. 424–432, 2017.

[86] K. Jinguji, N. Takato, A. Sugita, and M. Kawachi, "Mach-Zehnder interferometer type optical waveguide coupler with wavelength-flattened coupling ratio," *Electronics Letters*, vol. 26, no. 17, pp. 1326–1327, 1990.

[87] S.-L. Tsao, H.-C. Guo, and Y.-J. Chen, "Design of a 2×2 MMI MZI SOI electro-optic switch covering C band and L band," *Microwave and Optical Technology Letters*, vol. 33, no. 4, pp. 262–265, 2002.

[88] J. Van Campenhout, W. M. Green, and Y. A. Vlasov, "Design of a digital, ultra-broadband electro-optic switch for reconfigurable optical networks-on-chip," *Optics Express*, vol. 17, no. 26, pp. 23 793–23 808, 2009.

[89] M. Alam, J. N. Caspers, J. S. Aitchison, and M. Mojahedi, "Compact low loss and broadband hybrid plasmonic directional coupler," *Optics Express*, vol. 21, no. 13, pp. 16 029–16 034, 2013.

[90] J. N. Caspers and M. Mojahedi, "Measurement of a compact colorless 3 db hybrid plasmonic directional coupler," *Optics Letters*, vol. 39, no. 11, pp. 3262–3265, 2014.

[91] Z. Lu, H. Yun, Y. Wang, Z. Chen, F. Zhang, N. A. Jaeger, and L. Chrostowski, "Broadband silicon photonic directional coupler using asymmetric-waveguide based phase control," *Optics Express*, vol. 23, no. 3, pp. 3795–3808, 2015.

[92] R. Halir, A. Maese-Novo, A. Ortega-Moñux, I. Molina-Fernández, J. Wangüemert-Pérez, P. Cheben, D.-X. Xu, J. Schmid, and S. Janz, "Colorless directional coupler with dispersion engineered sub-wavelength structure," *Optics Express*, vol. 20, no. 12, pp. 13 470–13 477, 2012.

[93] Y. Wang, Z. Lu, M. Ma, H. Yun, F. Zhang, N. A. Jaeger, and L. Chrostowski, "Compact broadband directional couplers using subwavelength gratings," *IEEE Photonics Journal*, vol. 8, no. 3, pp. 1–8, 2016.

[94] G. F. Chen, J. R. Ong, T. Y. Ang, S. T. Lim, C. E. Png, and D. T. Tan, "Broadband silicon-on-insulator directional couplers using a combination of straight and curved waveguide sections," *Scientific Reports*, vol. 7, no. 1, p. 7246, 2017.

[95] H. Morino, T. Maruyama, and K. Iiyama, "Reduction of wavelength dependence of coupling characteristics using si optical waveguide curved directional coupler," *Journal of Lightwave Technology*, vol. 32, no. 12, pp. 2188–2192, 2014.

[96] F. Zhang, H. Yun, Y. Wang, Z. Lu, L. Chrostowski, and N. A. Jaeger, "Compact broadband polarization beam splitter using a symmetric directional coupler with sinusoidal bends," *Optics Letters*, vol. 42, no. 2, pp. 235–238, 2017.

[97] M. Greenberg and M. Orenstein, "Simultaneous dual mode add/drop multiplexers for optical interconnects buses," *Optics communications*, vol. 266, no. 2, pp. 527–531, 2006.

[98] D. Dai and S. He, "Analysis of the birefringence of a silicon-on-insulator rib waveguide," *Applied optics*, vol. 43, no. 5, pp. 1156–1161, 2004.

[99] S. Chandran, "Integrated optical microring resonator in SOI for wide range refractive index sensing," Ph.D. dissertation, Indian Institute of Technology Madras, Chennai, 2017.

[100] "Lumerical MODE Solutions," www.lumerical.com.

[101] C. D. Salzberg and J. J. Villa, "Infrared refractive indexes of silicon germanium and modified selenium glass," *JOSA*, vol. 47, no. 3, pp. 244–246, 1957.

[102] A. Yariv and P. Yeh, *Photonics: Optical electronics in modern communications (the Oxford series in electrical and computer engineering).* Oxford University Press, Inc., 2006.

[103] W.-P. Huang, "Coupled-mode theory for optical waveguides: an overview," *JOSA A*, vol. 11, no. 3, pp. 963–983, 1994.

[104] K. S. Chiang, "Intermodal dispersion in two-core optical fibers," *Optics Letters*, vol. 20, no. 9, pp. 997–999, 1995.

[105] Y. Wu and K. S. Chiang, "Compact three-core fibers with ultra-low differential group delays for broadband mode-division multiplexing," *Optics Express*, vol. 23, no. 16, pp. 20 867–20 875, 2015.

[106] P. Sah, "Integrated photonics filters with distributed Bragg reflector in silicon-on-insulator," Ph.D. dissertation, Indian Institute of Technology Madras, Chennai, 2018.

[107] "Raith nanofabrication," www.raith.com.

[108] S. J. Emelett and R. Soref, "Design and simulation of silicon microring optical routing switches," *Journal of Lightwave Technology*, vol. 23, no. 4, pp. 1800–1807, 2005.

[109] S. Xiao, M. H. Khan, H. Shen, and M. Qi, "Silicon-on-insulator microring add-drop filters with free spectral ranges over 30 nm," *Journal of Lightwave Technology*, vol. 26, no. 2, pp. 228–236, 2008.

[110] H. Guan, Z.-Y. Li, H.-H. Shen, and Y.-D. Yu, "Compact optical add-drop de-multiplexers with cascaded micro-ring resonators on SOI," *Chinese Physics Letters*, vol. 34, no. 6, p. 064201, 2017.

[111] J. K. Poon, J. Scheuer, Y. Xu, and A. Yariv, "Designing coupled-resonator optical waveguide delay lines," *JOSA B*, vol. 21, no. 9, pp. 1665–1673, 2004.

[112] F. Liu, Q. Li, Z. Zhang, M. Qiu, and Y. Su, "Optically tunable delay line in silicon microring resonator based on thermal nonlinear effect," *IEEE Journal of Selected Topics in Quantum Electronics*, vol. 14, no. 3, pp. 706–712, 2008.

[113] N. A. Yebo, D. Taillaert, J. Roels, D. Lahem, M. Debliquy, D. Van Thourhout, and R. Baets, "Silicon-on-insulator (SOI) ring resonator-based integrated optical hydrogen sensor," *IEEE photonics Ttechnology Letters*, vol. 21, no. 14, pp. 960–962, 2009.

[114] T. Claes, J. G. Molera, K. De Vos, E. Schacht, R. Baets, and P. Bienstman, "Label-free biosensing with a slot-waveguide-based ring resonator in silicon on insulator," *IEEE Photonics Journal*, vol. 1, no. 3, pp. 197–204, 2009.

[115] J. Liu, X. Zhou, Z. Qiao, J. Zhang, C. Zhang, T. Xiang, L. Shui, Y. Shi, and L. Liu, "Integrated optical chemical sensor based on an SOI ring resonator using phase-interrogation," *IEEE Photonics Journal*, vol. 6, no. 5, pp. 1–7, 2014.

[116] Y. Shirato, Y. Shoji, and T. Mizumoto, "Over 20-dB isolation with 8-nm bandwidth in silicon MZI optical isolator," in *10th International Conference on Group IV Photonics (GFP), 2013.*   IEEE, 2013, pp. 136–137.

[117] L. Qiao, W. Tang, and T. Chu, "32× 32 silicon electro-optic switch with built-in monitors and balanced-status units," *Scientific Reports*, vol. 7, p. 42306, 2017.

[118] M. J. Kobrinsky, B. A. Block, J.-F. Zheng, B. C. Barnett, E. Mohammed, M. Reshotko, F. Robertson, S. List, I. Young, and K. Cadien, "On-chip optical interconnects." *Intel Technology Journal*, vol. 8, no. 2, 2004.

[119] R. Aguinaldo, A. Forencich, C. DeRose, A. Lentine, D. C. Trotter, Y. Fainman, G. Porter, G. Papen, and S. Mookherjea, "Wideband silicon-photonic thermo-optic switch in a wavelength-division multiplexed ring network," *Optics Express*, vol. 22, no. 7, pp. 8205–8218, 2014.

[120] B. Jalali and S. Fathpour, "Silicon photonics," *Journal of lightwave technology*, vol. 24, no. 12, pp. 4600–4615, 2006.

[121] T. Baehr-Jones, R. Ding, Y. Liu, A. Ayazi, T. Pinguet, N. C. Harris, M. Streshinsky, P. Lee, Y. Zhang, A. E.-J. Lim *et al.*, "Ultralow drive voltage silicon traveling-wave modulator," *Optics express*, vol. 20, no. 11, pp. 12 014–12 020, 2012.

[122] N. C. Harris, Y. Ma, J. Mower, T. Baehr-Jones, D. Englund, M. Hochberg, and C. Galland, "Efficient, compact and low loss thermo-optic phase shifter in silicon," *Optics Express*, vol. 22, no. 9, pp. 10 487–10 493, 2014.

[123] G. Cocorullo and I. Rendina, "Thermo-optical modulation at 1.5 µm in silicon etalon," *Electronics Letters*, vol. 28, no. 1, pp. 83–85, 1992.

[124] H. Shen, M. H. Khan, L. Fan, L. Zhao, Y. Xuan, J. Ouyang, L. T. Varghese, and M. Qi, "Eight-channel reconfigurable microring filters with tunable frequency, extinction ratio and bandwidth," *Optics Express*, vol. 18, no. 17, pp. 18 067–18 076, 2010.

[125] J. Tao, H. Cai, Y. Gu, and A. Liu, "Demonstration of a compact wavelength tracker using a tunable silicon resonator," *Optics Express*, vol. 22, no. 20, pp. 24 104–24 110, 2014.

[126] R. Sumi, R. K. Gupta, N. DasGupta, and B. K. Das, "Ultra-broadband add-drop filter/switch circuit using subwavelength grating waveguides," *IEEE Journal of Selected Topics in Quantum Electronics*, vol. 25, no. 3, pp. 1–11, April/May 2019.

[127] L.-W. Luo, S. Ibrahim, A. Nitkowski, Z. Ding, C. B. Poitras, S. B. Yoo, and M. Lipson, "High bandwidth on-chip silicon photonic interleaver," *Optics Express*, vol. 18, no. 22, pp. 23 079–23 087, 2010.

[128] P. Orlandi, F. Morichetti, M. J. Strain, M. Sorel, A. Melloni, and P. Bassi, "Tunable silicon photonics directional coupler driven by a transverse temperature gradient," *Optics Letters*, vol. 38, no. 6, pp. 863–865, 2013.

[129] K. Suzuki, K. Tanizawa, S. Suda, H. Matsuura, T. Inoue, K. Ikeda, S. Namiki, and H. Kawashima, "Broadband silicon photonics 8×8 switch based on double-Mach–Zehnder element switches," *Optics Express*, vol. 25, no. 7, pp. 7538–7546, 2017.

[130] K. Tanizawa, K. Suzuki, M. Toyama, M. Ohtsuka, N. Yokoyama, K. Matsumaro, M. Seki, K. Koshino, T. Sugaya, S. Suda *et al.*, "Ultra-compact 32× 32 strictly-non-blocking Si-wire optical switch with fan-out LGA interposer," *Optics Express*, vol. 23, no. 13, pp. 17 599–17 606, 2015.

[131] C. Li, W. Zheng, P. Dang, C. Zheng, Y. Wang, and D. Zhang, "Silicon-microring-based thermo-optic non-blocking four-port optical router for optical networks-on-chip," *Optical and Quantum Electronics*, vol. 48, no. 12, p. 552, 2016.

[132] S. Kaushal and B. K. Das, "Modeling and experimental investigation of an integrated optical microheater in silicon-on-insulator," *Applied Optics*, vol. 55, no. 11, pp. 2837–2842, 2016.

[133] X. Wang, J. A. Martinez, M. S. Nawrocka, and R. R. Panepucci, "Compact thermally tunable silicon wavelength switch: modeling and characterization," *IEEE Photonics Technology Letters*, vol. 20, no. 11, pp. 936–938, 2008.

[134] A. Atabaki, E. S. Hosseini, A. Eftekhar, S. Yegnanarayanan, and A. Adibi, "Optimization of metallic microheaters for high-speed reconfigurable silicon photonics," *Optics Express*, vol. 18, no. 17, pp. 18 312–18 323, 2010.

[135] D. Schall, M. Mohsin, A. A. Sagade, M. Otto, B. Chmielak, S. Suckow, A. L. Giesecke, D. Neumaier, and H. Kurz, "Infrared transparent graphene heater for silicon photonic integrated circuits," *Optics Express*, vol. 24, no. 8, pp. 7871–7878, 2016.

[136] A. Densmore, S. Janz, R. Ma, J. H. Schmid, D.-X. Xu, A. Delâge, J. Lapointe, M. Vachon, and P. Cheben, "Compact and low power thermo-optic switch using folded silicon waveguides," *Optics Express*, vol. 17, no. 13, pp. 10 457–10 465, 2009.

[137] P. Sun and R. M. Reano, "Free-standing silicon-on-insulator strip waveguides for submilliwatt thermo-optic switches," in *Frontiers in Optics*.   Optical Society of America, 2010, p. FMH3.

[138] Q. Fang, J. F. Song, T.-Y. Liow, H. Cai, M. B. Yu, G. Q. Lo, and D.-L. Kwong, "Ultralow power silicon photonics thermo-optic switch with suspended phase arms," *IEEE Photon. Technol. Lett.*, vol. 23, no. 8, pp. 525–527, 2011.

[139] Z. Lu, K. Murray, H. Jayatilleka, and L. Chrostowski, "Michelson interferometer thermo-optic switch on SOI with a 50-µW power consumption," in *Photonics Conference (IPC), 2016 IEEE*.   IEEE, 2016, pp. 107–110.

[140] A. H. Atabaki, A. A. Eftekhar, S. Yegnanarayanan, and A. Adibi, "Sub-100-nanosecond thermal reconfiguration of silicon photonic devices," *Optics Express*, vol. 21, no. 13, pp. 15 706–15 718, 2013.

[141] M. Asheghi, M. Touzelbaev, K. Goodson, Y. Leung, and S. Wong, "Temperature-dependent thermal conductivity of single-crystal silicon layers in SOI substrates," *Journal of Heat Transfer*, vol. 120, no. 1, pp. 30–36, 1998.

[142] F. Kreith, R. M. Manglik, and M. S. Bohn, *Principles of heat transfer*.   Cengage learning, 2012.

[143] "COMSOL Multiphysics version 5.3," https://www.comsol.com.

[144] B. Singh and N. Surplice, "The electrical resistivity and resistance-temperature characteristics of thin titanium films," *Thin Solid Films*, vol. 10, no. 2, pp. 243–253, 1972.

[145] P. Johnson and R. Christy, "Optical constants of transition metals: Ti, V, Cr, Mn, Fe, Co, Ni, and Pd," *Physical Review B*, vol. 9, no. 12, p. 5056, 1974.

[146] S. Manipatruni, R. K. Dokania, B. Schmidt, N. Sherwood-Droz, C. B. Poitras, A. B. Apsel, and M. Lipson, "Wide temperature range operation of micrometer-scale silicon electro-optic modulators," *Optics Letters*, vol. 33, no. 19, pp. 2185–2187, 2008.

[147] M. R. Watts, W. A. Zortman, D. C. Trotter, G. N. Nielson, D. L. Luck, and R. W. Young, "Adiabatic resonant microrings (arms) with directly integrated thermal microphotonics," in *Conference on Lasers and Electro-Optics 2009 and Conference on Quantum electronics and Laser Science Conference 2009. CLEO/QELS 2009*.   IEEE, 2009, pp. 1–2.

[148] J.-M. Lee, D.-J. Kim, H. Ahn, S.-H. Park, and G. Kim, "Temperature dependence of silicon nanophotonic ring resonator with a polymeric overlayer," *Journal of Lightwave Technology*, vol. 25, no. 8, pp. 2236–2243, 2007.

[149] V. Raghunathan, N. Y. Winnie, J. Hu, T. Izuhara, J. Michel, and L. Kimerling, "Athermal operation of silicon waveguides: spectral, second order and footprint dependencies," *Optics Express*, vol. 18, no. 17, pp. 17 631–17 639, 2010.

[150] B. Guha, B. B. Kyotoku, and M. Lipson, "CMOS-compatible athermal silicon microring resonators," *Optics Express*, vol. 18, no. 4, pp. 3487–3493, 2010.

[151] N. Y. Winnie, J. Michel, and L. C. Kimerling, "Athermal high-index-contrast waveguide design," *IEEE Photonics Technology Letters*, vol. 20, no. 11, pp. 885–887, 2008.

[152] G. Cocorullo, F. Della Corte, and I. Rendina, "Temperature dependence of the thermo-optic coefficient in crystalline silicon between room temperature and 550 K at the wavelength of 1523 nm," *Applied Physics Letters*, vol. 74, no. 22, pp. 3338–3340, 1999.

[153] M. Kawachi, "Silica waveguides on silicon and their application to integrated-optic components," *Optical and Quantum Electronics*, vol. 22, no. 5, pp. 391–416, 1990.

[154] M. R. Watts, J. Sun, C. DeRose, D. C. Trotter, R. W. Young, and G. N. Nielson, "Adiabatic thermo-optic Mach–Zehnder switch," *Optics Letters*, vol. 38, no. 5, pp. 733–735, 2013.

[155] Z. Lu, D. Celo, H. Mehrvar, E. Bernier, and L. Chrostowski, "High-performance silicon photonic tri-state switch based on balanced nested Mach-Zehnder interferometer," *Scientific Reports*, vol. 7, no. 1, p. 12244, 2017.

[156] Z. Min, C. Baoqin, X. Changqing, L. Ming, and N. Jiebing, "Study of process of HSQ in electron beam lithography," in *5th International Conference on Nano/Micro Engineered and Molecular Systems (NEMS), 2010.* IEEE, 2010, pp. 1021–1024.